NANYANG TECHNOLOGICAL UNIVERSITY

LARGE N-HETEROACENE DERIVATIVES: SYNTHESIS, CHARACTERIZATION AND APPLICATIONS AS N-TYPE AND AMBIPOLAR SEMICONDUCTORS

WANG ZILONG

SCHOOL OF MATERIALS SCIENCE AND ENGINEERING

2017

[LARGE N-HETEROACENE DERIVATIVES: SYNTHESIS, CHARACTERIZATION AND APPLICATIONS AS N-TYPE AND AMBIPOLAR SEMICONDUCTORS]

WANG ZILONG

SCHOOL OF MATERIALS SCIENCE AND ENGINEERING

A thesis submitted to the Nanyang Technological University in partial fulfilment of the requirement for the degree of Doctor of Philosophy

2017

Statement of Originality

I hereby certify that the work embodied in this thesis is the result of original research and has not been submitted for a higher degree to any other University or Institution.

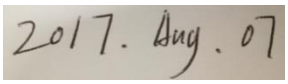

Date

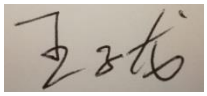

Student Name

Abstract

Organic π-conjugated materials have attracted much attention in recent years because these materials have already shown several great advantages over inorganic semiconductors, such as low-cost, flexibility, and variability of the properties. This is why organic low-bandgap compounds have been considered to be next generation semiconductors. Although great achievement in developing p-type organic semiconductors have been witnessed, the progress in searching n-type and ambipolar organic semiconductors has fallen behind the p-type ones. Thus, developing n-type and ambipolar organic semiconductors is of great significance.

N-heteroacenes, derived from the classic p-type semiconductors called oligoacenes, have been proven to be an efficient pathway to approach novel n-type and ambipolar organic semiconductors. Especially large N-heteroacene derivatives with longer conjugations can provide more possibilities for strong π-π interactions, and have come into the sight of scientists, recently. However, the research of large N-heteroacene derivatives is still far from sufficient to verify the potential and possibilities. Thus, this thesis mainly focuses on the research of large N-heteroacene derivatives, and it contains the following parts:

Firstly, two large N-heteroacene derivatives were designed and synthesized through employing a pyrene bridge and triisopropylsilyl substituents. These as-prepared two large N-heteroacene derivatives are easy to crystallize and have good stability as well as solubility. They show n-type semiconductor behaviors in photoelectrochemical (PEC) cells.

Secondly, a pyracyclene unit was employed as the bridge to build up stable large N-heteroacene derivative. This N-heteroacene derivative shows ambipolar semiconductor behaviors in the PEC cells for water splitting.

Thirdly, two extra-long large N-heteroacene derivatives were designed and synthesized with fifteen and twenty six-membered rings annulated in one row, respectively. The fifteen-ring one has been successfully confirmed by single crystal X-ray diffraction.

Fourthly, a quinone unit is employed as the bridge to extend the conjugation of the large N-heteroacene derivatives. Two large N-heteroacene derivatives are designed and synthesized with six and seven six-membered rings conjugated in one row. The extended conjugation can greatly change the molecules stacking structure without changing the molecular orbital energy levels. They have deep LUMO energy levels and show n-type semiconductor behavior in thin film transistors.

Finally, some reconnaissance research is also introduced in the last chapter. Some ideas and prospects are also presented.

In conclusion, this thesis focuses on the design and synthesis of large N-heteroacene derivatives and the characterization. Especially through the single crystal X-ray diffraction method, molecular structures, molecules stacking modes and the relationship between molecular structure and properties are well studied. As n-type or ambipolar semiconductors, the behaviors of the N-heteroacene derivatives in organic field-effect transistor and photoelectrochemistry cells are explored.

Acknowledgements

Firstly, the author would like to express gratitude to the financial support from the scholarship of MSE in the 4 years Ph.D study in NTU.

The author would like to express sincere gratefulness to his supervisor Assoc. Prof. Zhang Qichun for giving invaluable guidance and selflessly shares his knowledge through the entire research project, and also the guidance, solicitude and help in his life.

The author would like to thank the former group members: Dr. Li Gang, Dr. Gu Peiyang, Dr. Hu Benlin, Dr. Li Junbo, Dr. Xu Liang, Dr. Long Guankui, Dr. Wang Chengyuan, Dr. Zhou Yi et al for the kind guidance and assistance in the lab.

The author would like to thank Dr. Liu Guangfeng, Dr. Chen Wangqiao, Dr. Zhang Jing, Dr. Wang Zongrui, Dr. Zhan Xuejun, Dr. Ban Rui, Dr. Feng Jiansheng, Dr. Xu Wenjuan, Dr. Wang Ning, Mrs. Li'na Nie, Mr. Gu bin, Mr. Xie Jian, Mr. Zhao Kexiang, Mr. Ali Ahmed, Mr. Liu Wenbo, Mr. Li Yang, and all the research group members for the discussion, sharing experience and assistance all the way.

Lastly, the author would like to take this opportunity to thank his family and friends for the encouragement, care and continuous support.

Table of Contents

Table Captions

Scheme Captions

Figure Captions

density of **DQNDN** nanofibers under 0.61 V versus RHE; (f) Mott-Schottky plot of **DQNDN** nanofibers

Fig 5.8 (a) LSV of nanostructured **DQNDN** films under dark (black line) and under simulated solar light irradiation (AM 1.5, 100 mW/cm^2) (red line) in 0.5 M Na_2SO_4; (b) Corresponding current density-potential curve; (c) The transient photocurrent density of nanostructured **DQNDN** film under -0.20 V versus RHE. Inset: the picture showing the bubbles formed on the Pt plate; (d) The electrochemical impedance spectroscopy of **DQNDN** at -0.20 V versus RHE in the dark and under light irradiation

Fig 6.1 ^1H NMR spectrum of compound **6.5**, 300 MHz, $CDCl_3$, room temperature

Fig 6.2 ^{13}C NMR spectrum of compound **6.5**, 75 MHz, $CDCl_3$, room temperature

Fig 6.3 HR-MS(ESI) spectrum of compound **6.5**

Fig 6.4 ^1H NMR spectrum of compound **6.8**, 300 MHz, $CDCl_3$, room temperature

Fig 6.5 ^{13}C NMR spectrum of compound **6.8**, 75 MHz, $CDCl_3$, room temperature

Fig 6.6 HR-MS(ESI) spectrum of compound **6.8**

Fig 6.7 ^1H NMR spectrum of compound **6.9**, 300 MHz, $CDCl_3$, room temperature

Fig 6.8 ^{13}C NMR spectrum of compound **6.9**, 75 MHz, $CDCl_3$, room temperature

Abbreviations

IT	Information Technology
OFET	organic field-effect transistor
OPV	Organic Photovoltaic
OLED	Organic Light-Emitting Diode
PEC	Photoelectrochemical
N-heteroacenes	Nitrogen Doped Heteroacenes
TIPS	Triisopropylsilyl
SCXRD	Single Crystal X-ray Diffraction
LUMO	Lowest Unoccupied Molecular Orbital
HOMO	Highest Occupied Molecular Orbital
DCE	1,2-Dichloroethane
g-C_3N_4	Graphitic Carbon Nitride
IBX	2-Iodoxybenzoic Acid
$LiAlH_4$	Lithium Aluminium Hydride
THF	Tetrahydrofuran
MnO_2	Manganese Dioxide
TLC	Thin Layer Chromatography
R_f	Retardation Factor
NMR	Nuclear Magnetic Resonance
HRMS	High-resolution mass spectrometry
SCXRD	Single crystal X-ray diffraction
CV	Cyclic voltammetry
UV-Vis	Ultraviolet–Visible Spectroscopy
E_g	Energy Gap
PL	Photoluminescence
V_g	Gate Voltage
OANQ	Octaazanonacene-8,19-dione
OADA	2,15-di-*tert*-butyl-5,12,18,25-tetrakis((triisopropylsilyl)ethynyl)dibenzo[g_1h_1,lm]-

	4,6,11,13,17,19,24,26-octaazadecacene
TAOA	2,13-di-*tert*-butyl-5,10,16,21-tetrakis((triisopropylsilyl)ethynyl)dibenzo[a_1b_1,*jk*]-4,11,15,22-tetraazaoctacene
DCM	Dichloromethane
HR-MS	High-Resolution Mass Spectrum
FTO	Fluorine-Doped Tin Oxide
DI water	De-ionized Water
λ_{onset}	Onset Absorption
NICS	Nucleus-Independent Chemical Shift
MS	Mott-Schottky
BBL	Poly(benzimidazobenzophenanthr-oline
DQNDN	6,11,18,23-tetrakis((triisopropylsilyl)ethynyl) diquinoxalino[*g*,*g*']naphtha[1",8":3,4,5;4",5":3',4',5']-dicyclopenta[1,2-*b*:1',2'-*b*']diquinoxaline
TFA	CF_3COOD
TMS	Tetramethylsilane
TGA	Thermogravimetric Analysis
SEM	Scanning Electron Microscopy Analysis
EIS	The Electrochemical Impedance Spectroscopy
DFT	Density Functional Theory
ISC	Intersystem Crossing
BGTC	Bottom-gate Top-contact
OTS	Octadecyltrichlorosilane
Hept-CO	6,17-bis((triisopropylsilyl)ethynyl)naphtho[2,3-b]quinoxalino[2,3-i]phenazine-8,15-dione
Hex-CO	6,15-bis((triisopropylsilyl)ethynyl)benzo[b]quinoxalino[2,3-i]phenazine-8,13-dione
TMBDC	2,4,9,11-tetramethoxybenzo[1,2-c:4,5-c']dicinnoline
TCDO	2,3,8,9-tetrakis(decyloxy)-12H-cyclopenta[1,2-b:3,4-b']diquinoxalin-12-one (compound

PAF	Porous Aromatic Frameworks

Chapter 1

Introduction

In this chapter, background knowledge of this thesis is briefly introduced, followed by the discussion of the state-of-the-art research topic, namely, seeking high performance n-type organic semiconductor. In the past few decades, the large N-heteroacenes, although underdeveloped, have shown its immense potential as excellent n-type material. Based on this, the hypothesis and scope are proposed to achieve high-performance n-type semiconductors through designing and optimizing the structures of N-heteroacenes. Moreover, an overview of the whole thesis is briefly described chapter by chapter. Finally, the main findings and outcomes are listed at the end of this chapter.

1.1 Background and Hypothesis

In the past half-century, the semiconductor industry, as the cornerstone of the microelectronics technology and information technology (IT), has generated a great influence on the development of science and technology. With the microelectronics technology constantly breaking the limitations of information processing ability, the fast developing IT technology is playing a more and more important role in our lives. Since the first transistor was invented by John Bardeen, William Shockley and Walter Brattain in 1947,[1] the modern microelectronics technology is built on inorganic semiconductor (for example: Si, GaAs and GaN), However, the process of fabricating inorganic-semiconductor-based devices is very complicated and expensive.

	Organic	Silicon
Cost	$5/ft^2	$100/ft^2
Fabrication Cost	Low Capital	$1-$10 billion
Fabrication conditions	Ambient	Ultra Cleanroom
Device size	10 ft. x Roll to Roll	< 1m^2
Process	Continuous Direct Printing	Multi-step Photolithography
Material	Flexible and Stretchable Plastic Substrate	Rigid Glass or Metal

Fig 1.1 Organic semiconductors VS Silicon in electronic devices

In 1986, Tsumura and coworkers successfully made the first organic field-effect transistor (OFET).[2] Comparing with inorganic electronic devices, organic electronic devices are easier and cheaper to fabricate. The cost of production is expected to be 1% ~ 10% of that of silicon devices. Due to the good elasticity of organic materials, organic devices can be flexible. Moreover, different properties of organic electronic devices can be achieved through designing different organic molecule structures to meet the variety of applications. Because of these good characters, organic semiconductors have attracted more and more attentions and a lot of researches have been carried out. Especially in the past few decades, great progress has been made and the mobility of OFETs can be

comparable with or even higher than the polycrystalline silicon-based FET (~1.0 $cm^2V^{-1}S^{-1}$).[3] Until now, the highest hole mobility has reached 40 $cm^2V^{-1}S^{-1}$,[4] and the highest electron mobility has reached 11 $cm^2V^{-1}S^{-1}$.[5] Based on these achievements, OFETs have been widely considered to be the next generation transistors.

Other than in OFETs, organic semiconductor also have been expanded to a broad range of applications, including organic photovoltaics (OPVs),[6] organic light-emitting diodes (OLEDs)[7], organic memory devices[8], organic lasers[9], photoelectrochemical cells (PEC) for water splitting,[10], bio-image[11], etc.

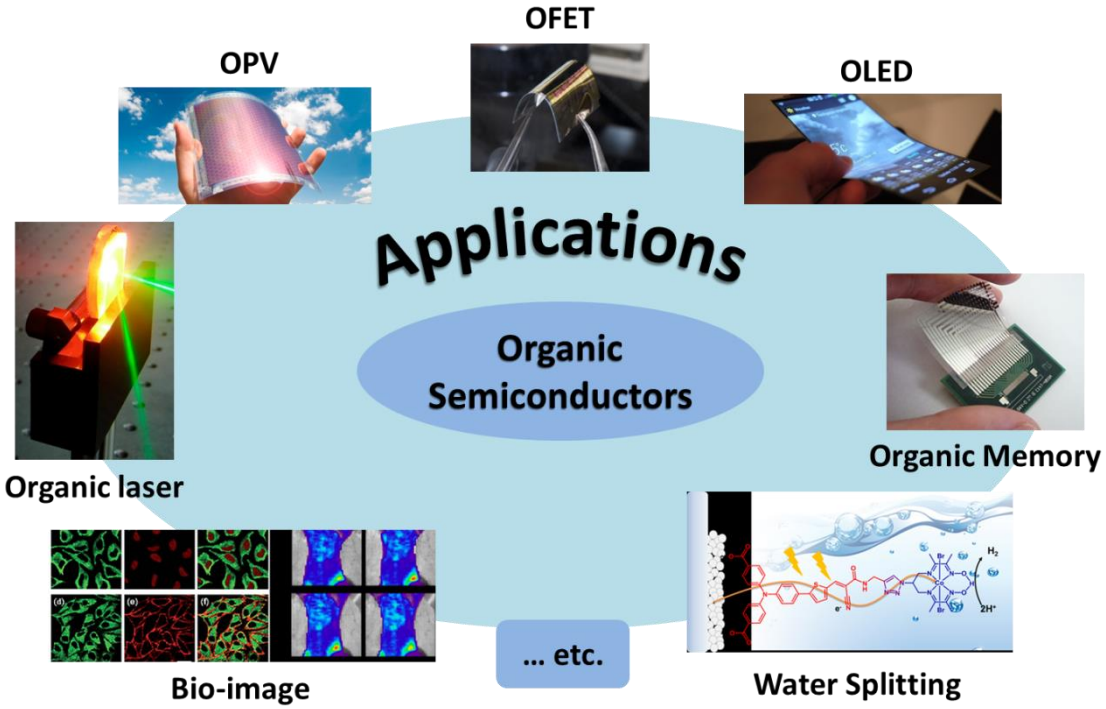

Fig 1.2 Broad applications of organic semiconductors

Although great achievements have been made in organic semiconductors, there are still many challenges, including the immature processing engineering of the devices and interface engineering theory. The most crucial problem is the imbalance between n-type and p-type semiconductors. Until now, most of the organic semiconductors are p-type ones. On the contrast, n-type organic semiconductors are quite few, and they normally have a poor performance, and/or a poor ambient stability. As for the ambipolar organic

semiconductors, the amount is even less. Considering that p-type and n-type semiconductors are equally important, developing high performance n-type and ambipolar organic semiconductor is of great significance.

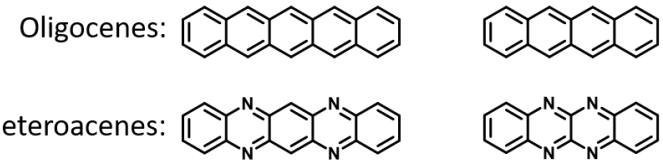

Fig 1.3 Molecular structures of typical oligoacenes and N-heteroacenes

Pentacene is a famous and well-studied molecule in OFET, and it holds the highest mobility record for p-type thin film OFET.[4] Rubrene also shows very good OFET performance, and its single crystals' mobility can reach as high as 43 $cm^2V^{-1}S^{-1}$.[12] By replacing carbon atoms with nitrogen atoms in the backbone of oligoacenes, nitrogen doped heteroacenes (N-heteroacenes or azaacenes) can be produced, as shown in Fig 1.3. N-heteroacenes are an important class of organic semiconductors. Normally replacing carbon atoms with unsaturated nitrogen atoms will lower the molecular orbital energy levels, this is why the unsaturated nitrogen atoms serve as electron-withdrawing centers. On the other hand, replacing carbon atoms with saturated nitrogen atoms will raise the molecular orbital energy levels, because saturated nitrogen atoms serve as electron-donating centers, and such replacement will lead to a p-type semiconductor. Thus, logically, ambipolar and n-type semiconductors can be obtained by purposely replacing the carbon atoms with the certain amount of nitrogen atoms in oligoacenes. Considering the high performance of acenes in p-type OFET, N-heteroacenes should have great potential as ambipolar and n-type semiconductors in organic electronic devices.

Recently, large N-heteroacenes have attracted much interest of scientists, especially the single crystal structure confirmed ones.[13] Because the large conjugations can offer more possibilities to ensure strong π-π interactions, which is conductive to the charge transfer. Therefore, good performance can be expected for large N-heteroacenes in organic electronic devices. Studying the single crystal structures is the most ideal method to understand the relationship between molecular structures and properties. Therefore crystal structures are very valuable and of great significance for designing novel

molecules for the improvement of performance in certain applications. However, large N-heteroacenes with single crystal structure are rarely reported.

Thus, the research in this thesis is mainly based on the several following hypotheses:

1) The real large N-heteroacenes with only one Clar's π-sextet are not stable. Embedding a π-conjugated bridge to interrupt the aromaticity is a useful method to build up large N-heteroacenes derivatives. Hence pyrene, pyracyclene and quinone units were employed as the bridges to build up novel large N-heteroacenes in this thesis. These novel large N-heteroacenes were expected to have good stability;

2) The spherical triisopropylsilyl (TIPS) groups are frequently attached onto the backbone of acenes to control the molecules stacking modes and crystallinity through the steric hindrance. On the other hand, the TIPS groups can also effectively enhance the solubility. Hence the TIPS groups were introduced into the large N-heteroacenes in this thesis. The large N-heteroacenes with TIPS groups were expected to have good solubility and crystallinity;

3) Based on above-mentioned two hypotheses, it is possible to challenge the record length of N-heteroacenes confirmed with the single crystal structure. Two large N-heteroacenes with fifteen and twenty rings fused in a row were designed by employing the pyrene bridges and TIPS groups. The as-designed large N-heteroacenes were expected to have sufficient solubility and crystallinity to afford high-quality crystal that can be studied through single crystal X-ray diffraction (SCXRD);

4) With nitrogen-doping in the conjugation backbone, the as-designed large N-heteroacenes were expected to have a low value of lowest unoccupied molecular orbital (LUMO) energy levels and narrow band gaps for n-type semiconductor applications. The applications of PEC cells for water splitting and OFET was explored. The as-designed large N-heteroacenes are expected to have good performance.

1.2 Objectives and Scope

In this thesis, the main objective and scope are:

1) To design and synthesize large N-heteroacenes as well as study the relationship between molecular structures and the properties;

2) To challenge the record length of the crystal-structure-confirmed large N-heteroacenes. To explore the limitation, observe and study what will happen when the conjugation backbones become ultra-long;

3) To explore and improve the performance of large N-heteroacenes in PEC cells for water splitting application;

4) To explore and improve the performance of large N-heteroacenes in OFET applications.

1.3 Dissertation Overview

This thesis mainly focuses on the design and synthesis of novel large N-heteroacenes, trying to obtain the crystal structures and study the relationship between molecule structure and property. This thesis also explores the applications as n-type and ambipolar semiconductors in OFET and PEC cells.

Chapter 1 provides a rationale to explain why large N-heteroacenes is focused on in this thesis. A brief research background and recent progress of N-heteroacenes and organic semiconductors are described firstly, in which the problems need to be solved are also discussed. Based on the background, the hypothesis is subsequently presented, following with the objectives and scope. After that, an overview of this dissertation is introduced chapter by chapter. Finally, findings and outcomes of the thesis are summarized.

Chapter 2 reviews the literature concerning N-heteroacenes. The background and recent progress of large N-heteroacenes are introduced and discussed in four parts: 1) The

history of N-heteroacenes is introduced; 2) The synthetic methods of N-heteroacenes are summarized; 3) The typical properties and applications are introduced; 4) Some research in other fields related to this thesis is also introduced.

Chapter 3 introduces the principles of experiment methods, including the synthetic routes and purification methods in obtaining all new compounds, the characterization method in confirming the molecular structures and studying the properties. Chapter 3 also introduces the testing methods in exploring the performance in certain applications. These introductions are all basic principles that have been widely accepted by scientists.

Chapter 4 elaborates the design and synthesis of two pyrene bridged large N-heteroacenes with eight and ten rings fused in one row. These two N-heteroacenes were fully characterized including SCXRD. The PEC performances of these two N-heteroacenes were studied, and both of them show n-type semiconductor behaviors.

Chapter 5 elaborates the design and synthesis of a pyracyclene bridged large N-heteroacene. This N-heteroacene showed ambipolar semiconductor behaviors in PEC cells with a max photocurrent density of 0.81 μA cm^{-2} as a photoanode and 0.13 mA cm^{-2} as a photocathode.

Chapter 6 describes the design and synthesis of extra-long π-conjugated pyrene-bridged large N-heteroacenes with fifteen and twenty six-membered rings fused in one row. The molecular structure of the fifteen one was successfully confirmed and studied by SCXRD.

Chapter 7 elaborates the design and synthesis of two quinone bridged large N-heteroacenes with six and seven rings fused in one row. They showed very different molecular stacking modes and almost the same molecular orbital energy levels. Finally, the performances in OFETs were studied.

Chapter 8 summarizes the whole thesis, firstly. Subsequently, some uncompleted

research is also introduced. Finally, the future of the large N-heteroacenes is proposed, and some specific ideas about the N-heteroacenes will be shared.

1.4 Findings and Outcomes

This research led to several novel outcomes:

1. Several large N-heteroacenes were designed and synthesized by using the moderate conjugation bridges including pyrene, pyracyclene and quinone.

2. A long single-crystal-structure-confirmed large N-heteroacenes was designed and synthesized. This further suggests that carefully arranging the TIPS substituents and employing moderate conjugation bridges to interrupt the aromaticity is an effective strategy to build up stable, soluble and crystallizable large N-heteroacenes.

3. The large N-heteroacenes are promising materials for PEC cells and water splitting.

4. The large N-heteroacenes are promising n-type semiconductor materials for OFET devices and other organic electronic devices.

References

[1] http://www.nobelprize.org/nobel_prizes/physics/laureates/1956/.

[2] A. Tsumura, H. Koezuka, T. Ando, *Applied Physics Letters* **1986**, *49*, 1210-1212.

[3] a) H. Klauk, U. Zschieschang, R. T. Weitz, H. Meng, F. Sun, G. Nunes, D. E. Keys, C. R. Fincher, Z. Xiang, *Advanced Materials* **2007**, *19*, 3882-3887; b)Y. Zhang, H. Dong, Q. Tang, Y. He, W. Hu, *Journal of Materials Chemistry* **2010**, *20*, 7029-7033; c) H. Ebata, T. Izawa, E. Miyazaki, K. Takimiya, M. Ikeda, H. Kuwabara, T. Yui, *Journal of the American Chemical Society* **2007**, *129*, 15732-15733; d) C. Liu, T. Minari, X. Lu, A. Kumatani, K. Takimiya, K. Tsukagoshi, *Advanced Materials* **2011**, *23*, 523-526; e) G. Giri, E. Verploegen, S. C. B. Mannsfeld, S. Atahan-Evrenk, D. H. Kim, S. Y. Lee, H. A. Becerril, A. Aspuru-Guzik, M. F. Toney, Z. Bao, *Nature* **2011**,

480, 504-508; f)H. Chen, Y. Guo, G. Yu, Y. Zhao, J. Zhang, D. Gao, H. Liu, Y. Liu, *Advanced Materials* **2012**, *24*, 4618-4622; g) R. Schmidt, J. H. Oh, Y.-S. Sun, M. Deppisch, A.-M. Krause, K. Radacki, H. Braunschweig, M. Könemann, P. Erk, Z. Bao, F. Würthner, *Journal of the American Chemical Society* **2009**, *131*, 6215-6228; h) H. Dong, C. Wang, W. Hu, *Chemical Communications* **2010**, *46*, 5211-5222.

[4] O. D. Jurchescu, M. Popinciuc, B. J. van Wees, T. T. M. Palstra, *Advanced Materials* **2007**, *19*, 688-692.

[5] H. Li, B. C. K. Tee, J. J. Cha, Y. Cui, J. W. Chung, S. Y. Lee, Z. Bao, *Journal of the American Chemical Society* **2012**, *134*, 2760-2765.

[6] a) H. S. Vogelbaum, G. Sauvé, *Synthetic Metals* **2017**, *223*, 107-121; b) H. Bildirir, V. G. Gregoriou, A. Avgeropoulos, U. Scherf, C. L. Chochos, *Materials Horizons* **2017**, *4*, 546-556; c) C. B. Nielsen, S. Holliday, H.-Y. Chen, S. J. Cryer, I. McCulloch, *Accounts of Chemical Research* **2015**, *48*, 2803-2812; d) J.-S. Wu, S.-W. Cheng, Y.-J. Cheng, C.-S. Hsu, *Chemical Society reviews* **2015**, *44*, 1113-1154.

[7] a) J.-H. Jou, S. Kumar, A. Agrawal, T.-H. Li, S. Sahoo, *Journal of Materials Chemistry C* **2015**, *3*, 2974-3002; b) X. Yang, X. Xu, G. Zhou, *Journal of Materials Chemistry C* **2015**, *3*, 913-944; c) Q. Chen, N. De Marco, Y. Yang, T.-B. Song, C.-C. Chen, H. Zhao, Z. Hong, H. Zhou, Y. Yang, *Nano Today* **2015**, *10*, 355-396.

[8] a) Y.-H. Chou, H.-C. Chang, C.-L. Liu, W.-C. Chen, *Polymer Chemistry* **2015**, *6*, 341-352; b) C. Wang, P. Gu, B. Hu, Q. Zhang, *Journal of Materials Chemistry C* **2015**, *3*, 10055-10065.

[9] a) I. D. W. Samuel, G. A. Turnbull, *Chemical reviews* **2007**, *107*, 1272-1295; b) A. J. C. Kuehne, M. C. Gather, *Chemical reviews* **2016**, *116*, 12823-12864.

[10] a) G. Zhang, Z.-A. Lan, X. Wang, *Angewandte Chemie International Edition* **2016**, *55*, 15712-15727; b) X. Zhang, T. Peng, S. Song, *Journal of Materials Chemistry A* **2016**, *4*, 2365-2402.

[11] X. Shi, Z. Xu, Q. Liao, Y. Wu, Z. Gu, R. Zheng, H. Fu, *Dyes and Pigments* **2015**, *115*, 211-217.

[12] M. Yamagishi, J. Takeya, Y. Tominari, Y. Nakazawa, T. Kuroda, S. Ikehata, M. Uno, T. Nishikawa, T. Kawase, *Applied Physics Letters* **2007**, *90*, 182117.

[13] a) B. Gao, M. Wang, Y. Cheng, L. Wang, X. Jing, F. Wang, *Journal of the American Chemical Society* **2008**, *130*, 8297-8306; b) B. Kohl, F. Rominger, M. Mastalerz, *Angewandte Chemie International Edition* **2015**, *54*, 6051-6056; c) A. H. Endres, M. Schaffroth, F. Paulus, H. Reiss, H. Wadepohl, F. Rominger, R. Krämer, U. H. F. Bunz, *Journal of the American Chemical Society* **2016**, *138*, 1792-1795.

Chapter 2

Literature Review

This chapter contains three parts. Firstly, history of N-heteroacenes is briefly introduced. Secondly, the main content of this chapter, in which the recent development of N-heteroacenes is reviewed, including synthetic method, novel large N-heteroacenes, characterisation methods and applications. Finally, other systems related to N-heteroncenes are briefly described. The background mentioned in this chapter lays the foundation of this thesis. Although N-heteroncenes have been intensively studied, the synthesis of large N-heteroacenes with excellent semiconductor properties remains challenging.

2.1 History of N-heteroacene

The first pentacene was synthesized by Clar and John in 1930s [1]. However, the first N-heteropentacenes with NH units were reported much earlier, which can be traced to the end of the 19th century according to Hinsberg's report[2] or Fischer and Hepp's research[3]. In the 1960s, Leete[4], Kummer and Zimmermann[5] found that the NH units in the N-heteropentacenes could be oxidized by chloranil, lead(IV) or copper(II), resulting in the "real" N-heteropentacenes with only one Clar's sextet. However, at that time, N-heteroacenes did not attract scientists' attention, until two reduced N-heteroacenes were employed as the hole transporting material in OFET by Miao, Nuckolls and coworkers, and showed a mobility approaching 10^{-2} $cm^2V^{-1}S^{-1}$.[6] After that, N-heteroacenes have been fastly developed and kept going, especially in OFET. Till now, the electron mobility of N-heteroacenes has reached 3.3 $cm^2V^{-1}S^{-1}$,[7] and even exceeded 10 $cm^2V^{-1}S^{-1}$ through optimizing the device fabrication process.[8] Besides in OFET,[9] N-heteroacenes also show good performance and prospect in many other applications[10], including OLED,[11] OPV devices[12], memory devices[13], sensors[14], photoelectrochemical cells[15], phototransistors[16], and molecular conductors[17].

2.2 Recent development in N-heteroacenes

2.2.1 Calculation

The calculation is a good guidance to design molecule structure. To design N-heteroacenes as organic semiconductors for certain applications, the most important factors need to be considered are the molecular orbital energy levels and molecules' stacking mode. Up to now, it is still difficult to calculate the molecules' stacking exactly. It can only be predicted based on experience. On the other hand, it is not difficult to calculate the molecular orbital energy levels. The molecule orbital energy levels determine the type of the organic semiconductors, as reported by Bao group in 2009.[18] A systemic study based on the data of 20 acenes was conducted. It was concluded that, in the acene system, the highest occupied molecular orbital (HOMO) energy level should be -5.60 eV or higher to achieve a p-type semiconductor and the LUMO energy level should be -3.15 eV or lower to achieve an n-type semiconductor.

Shuai's group has done a series of calculation on N-heteroacenes and made a comparison with pentacene. Several facts and trends about N-heteroacenes are found in the research, as shown in Fig 2.1. Firstly, replacing the CH fragments in the backbone of pentacene with NH units will increase both LUMO energy level and energy gap. Secondly, replacing the CH fragments with N atoms will lower both HOMO and LUMO energy levels, and the change of LUMO is more obvious than that of HOMO. This offers us a strategy to adjust the molecular orbital energy levels: LUMO level can be changed, meanwhile remaining HOMO energy level unchanged or changed a little, by doping N atoms in these acenes. Thirdly, the substituted group, TIPS-acetylene, does not affect the changing trend of molecular orbital energy levels. Meanwhile, it should be noted that TIPS-acetylene really makes a contribution to lower the molecule orbital levels, especially on the LUMO level. Lastly, the doping N atoms or NH units at the terminals have less effect on the molecular orbital energy levels than that in the middle of the acenes, concluded by comparing DAP-*2p* with DAP-*1p*, and DHDAP-2*p* with DHDAP-*1p*.

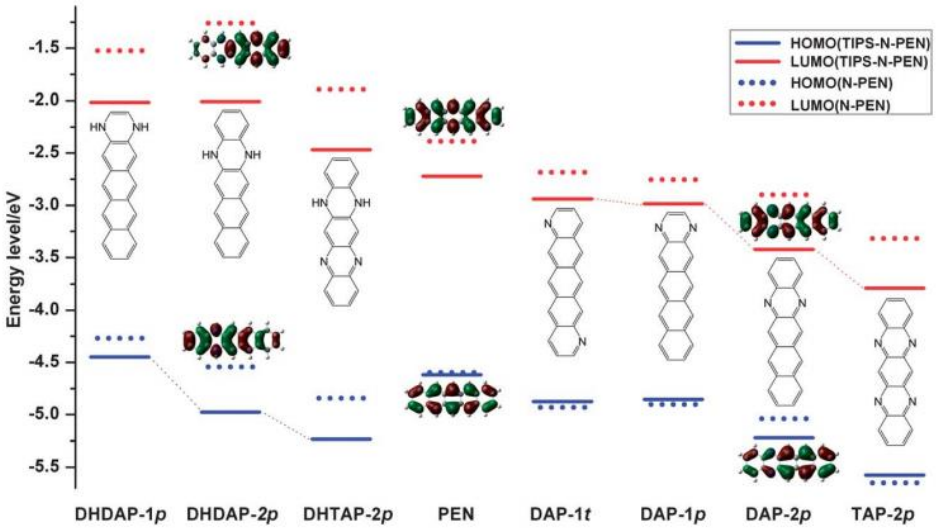

Fig 2.1 Calculation results for a series of N-heteroacenes and pentacene, done by Shuai group.[19] Reproduced from Ref. 19 with permission from The Royal Society of Chemistry.

The intermolecular interactions are critical factors for the molecular stacking. Winkler and Houk calculated a class of N-heteroacenes[20] with nitrile groups substituted at

different places, as shown in Fig 2.2 (bottom). These nitrile groups can significantly lower the LUMO energy levels, and they also contribute to self-assemble to a high ordered stacking structure. Along with a large amount of CH···N hydrogen bond, these N-Heteroacenes are predicted to exhibit a graphite-like 2D structure, as shown in Fig 2.2 (top). The strong intermolecular interactions can also increase the stability of the N-Heteroacenes in the air.

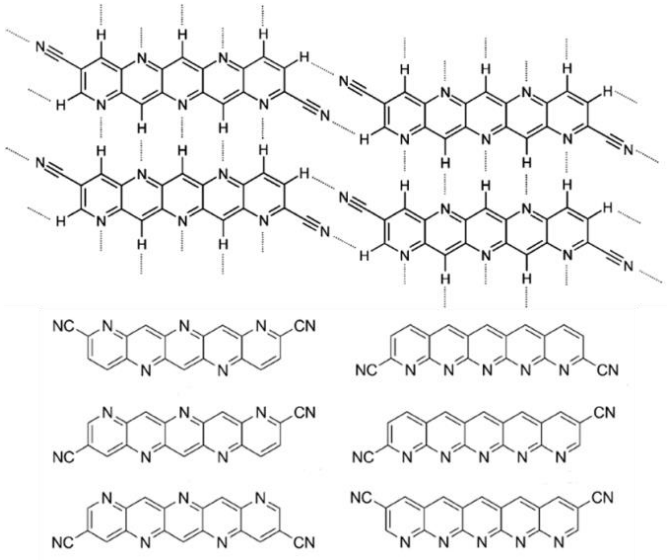

Fig 2.2 Theoretical studies of promising azaacenes by Winkler and Houk

2.2.2 Synthetic method

2.2.2.1. Condensation

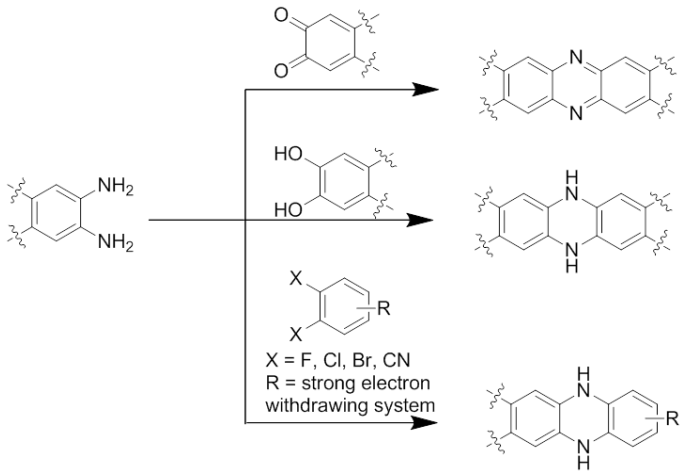

Fig 2.3 Synthesize N-heteroacenes through condensation reactions

N-heteroacenes can be synthesized by condensing *o*-diamine with *o*-quinone, *o*-diphenol, aryl-*o*-dihalides or aryl-*o*-dicyanide, as shown in Fig 2.3.

The condensation reaction between *o*-diamine and *o*-quinone is the most common method to synthesize N-heteroacenes. It can be easily carried out in high yield, and normally, this type of reactions is not sensitive to moisture and oxygen. While the only drawback of this method may be that *o*-quinone compounds are not easy to be synthesized and not stable sometimes. Fig 2.4 shows some examples of *o*-quinone compounds. Compounds **2-8**, **2-9a and 2-9b** are not stable, and they must be used as freshly prepared samples.

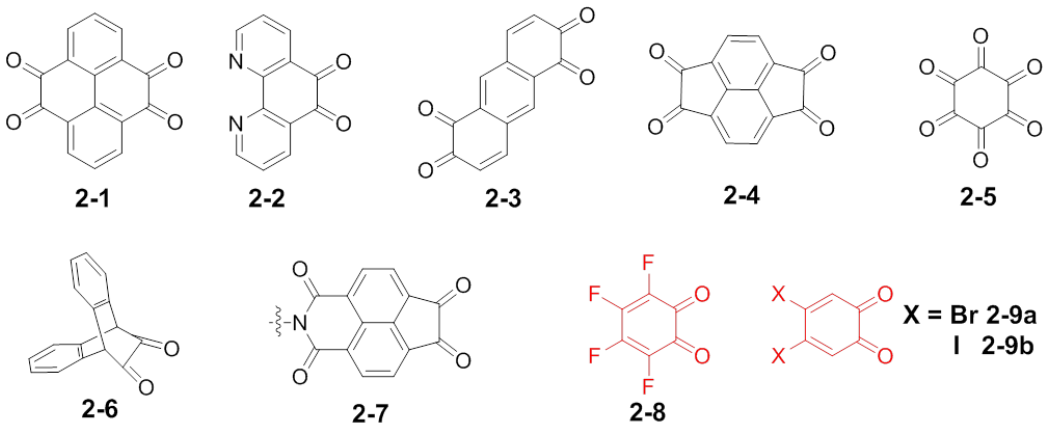

Fig 2.4 Examples of *o*-quinone compounds for synthesizing N-heteroacenes: **2-1**,[21] **2-2**,[22] **2-3**,[23] **2-4**,[24] **2-5**,[25] **2-6**,[11d] **2-7**,[26] **2-8**,[27] **2-9a**,[28] **2-9b**[28]

An effective method to synthesize *o*-quinone compounds through a double Friedel-Crafts acylation reaction in 1,2-dichloroethane (DCE) is reported recently as shown in Fig 2.5.[29] By using this method, new *o*-quinones can be synthesized, which offers more possibilities to design new N-heteroacenes.

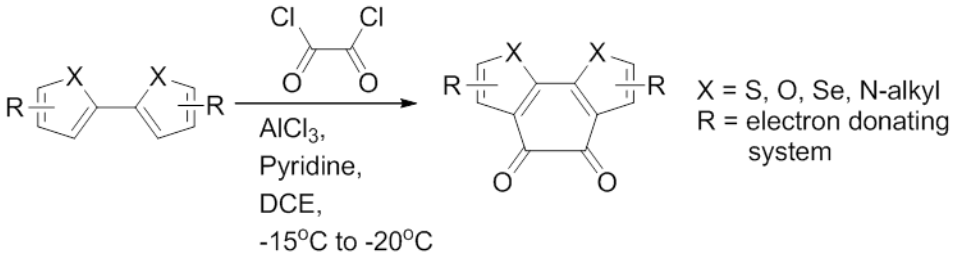

Fig 2.5 Synthesize *o*-quinone through double Friedel-Crafts acylation reactions

N-heteroacenes can be synthesized through condensing *o*-diamines with *o*-diphenols, as shown in Fig 2.3.[30] In this reaction, the *o*-diamines must not be in an electron withdrawing system to ensure that the reactivity remains high enough to condense with phenols. Electron-donating groups will make the *o*-diamines sensitive to oxygen and not stable in air, which might be the reason why this method is not so common to be used.

Aryl-*o*-dihalides[31] and aryl-*o*-dicyanide[32] can also be used to prepare N-heteroacene through condensing with *o*-diamines, as shown in Fig 2.3. In these reactions, the aryl-*o*-dihalides and aryl-*o*-dicyanide must be in a strong electron withdrawing system to ensure that the reactivity is high enough to condense with *o*-diamines, which is the limitation of this method.

Zhang and coworkers reported a method to synthesize N-heteroacene through aldol condensation, as shown in Fig 2.6.[33] This is a common method to synthesize acenes, however, rarely reported in the synthesis of N-heteroacene. The main reason is that this reaction does not dope new nitrogen atoms in the acenes and few building blocks containing nitrogen atoms can be used in this reaction. Designing and synthesizing new building blocks containing nitrogen atoms for aldol condensation could be a promising way to enlarge the family of N-heteroacenes.

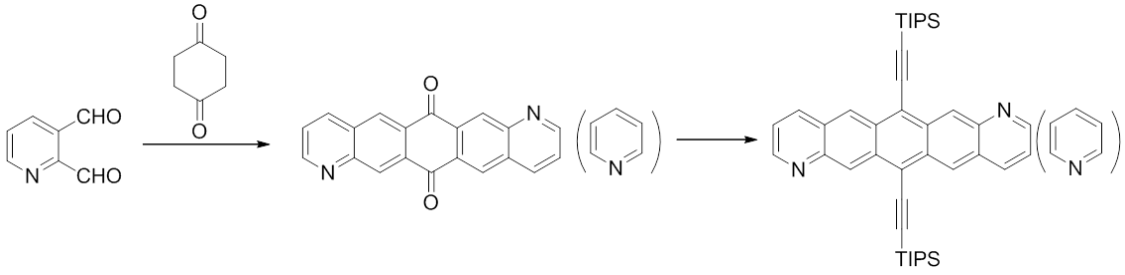

Fig 2.6 Synthesize N-heteroacenes through aldol condensation reaction

2.2.2.2. Palladium catalysis

Developing from Buchwald–Hartwig amination reaction, Bunz group reported a method to synthesize N-heteroacene through a double palladium catalyzed coupling reaction.[34] This method was initially tried to coupling *o*-diamines with active aryl-*o*-dihalides in a

mild reaction condition. The N-heteroacenes can be obtained in good yield, as shown in Fig 2.7 (top). However, when the reactants are changed to deactivated aryl-*o*-dihalides, the reaction condition must be modified, as shown in Fig 2.7 (bottom). By changing the ligand, employing strong bases and applying microwave to promote the reaction, the reaction works well for some deactivated aryl-*o*-dihalides. However, for some aryl-*o*-dihalides, this condition still cannot yield N-heteroacenes. The stronger base was also employed, however, the catalyst decomposed in such tough conditions. Presently, this is the limitation for this method. In conclusion, this palladium catalyst method is an effective way to synthesize N-heteroacene, and many new N-heteroacenes have been reported through this approach.

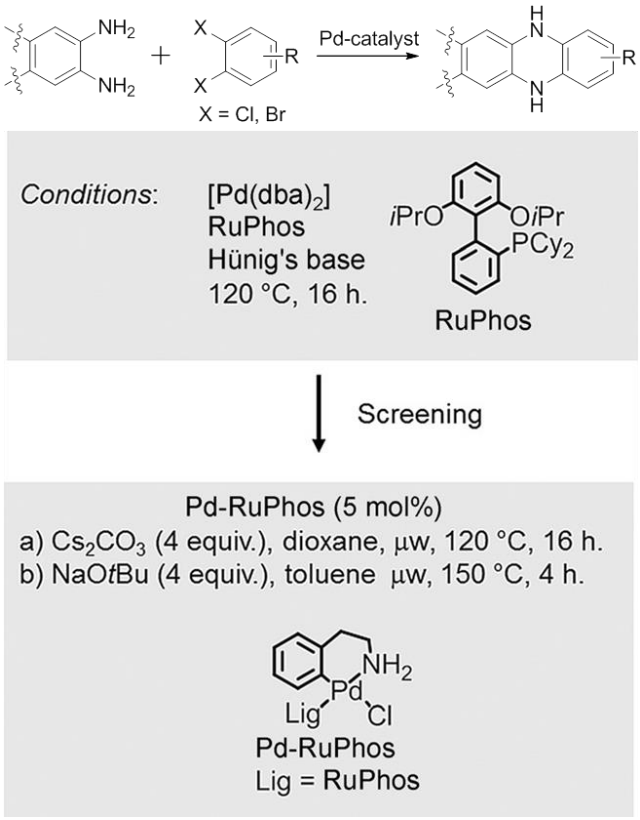

Fig 2.7 Synthesize N-heteroacene through Pd catalyst method. Reproduced with permission from ref. 34. Copyright 2014 Wiley-VCH Verlag GmbH & Co. KGaA.

2.2.2.3 Diels-Alder reaction

Diels-Alder reaction is a common and effective tool to synthesize acenes. However, few

N-heteroacenes are reported to be prepared by this reaction. The main reason is similar to the aldol condensation reaction: few building blocks that can be used in Diels-Alder reaction containing nitrogen atoms, and this reaction does not form chemical bonds that contain nitrogen atoms.

1,2,4,5-Tetrazines derivatives are building blocks containing nitrogen atoms and can be used in Diels-Alder reaction as dienes. A series of N-heteroacenes have been reported previously. These compounds are synthesized through using Diels-Alder reaction between 3,6-diphenyl-1,2,4,5-tetrazine and three *o*-aminoarylcarboxylic acids that can in situ generate arynes as dienophiles in good yield (above 40%), as shown in Fig 2.8. The structures are all confirmed by single crystal X-ray diffraction.

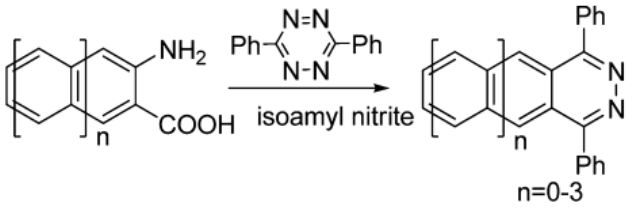

Fig 2.8 Synthesize N-heteroacene by using 1,2,4,5-tetrazine as diene

Zhang and coworkers reported two N-heteropentacenes by using Diels-Alder reaction and employing 2,3-bis(dibromomethyl)pyridine as diene precursor, as shown in Fig 2.9.[33] This Diels-Alder reaction goes in a good yield of 45% for both 1,4-anthraquinone compounds though the product diones are highly insoluble. The final tetrafluoride product is an ambipolar semiconductor.

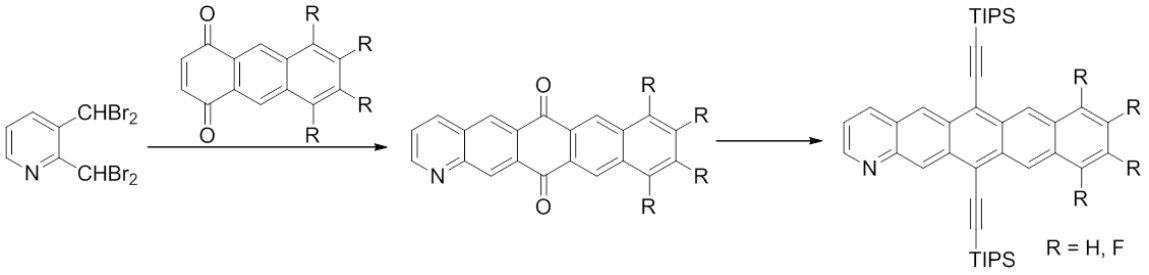

Fig 2.9 Synthesize N-heteroacene by using 2,3-bis(dibromomethyl)pyridine as dienes

Diels-Alder reaction is a powerful tool to synthesize N-heteroacenes, however, still

underdeveloped. Designing and synthesizing novel building blocks for synthesizing N-heteroacenes by Diels-Alder reaction should be a promising way to access more and new N-heteroacenes.

2.2.3 Building up large N-heteroacenes

Studying large N-heteroacenes has been a research hotspot in recent years. The large N-heteroacenes can be regarded as one-dimensional graphene or graphene nanoribbon. The synthesis of large N-heteroacenes can be regarded as a bottom-up approach to build up one-dimensional graphene. Comparing with the up-bottom approach, the biggest advantage of this bottom-up synthesis is that the structure of the target molecule is designable and precise, which is very meaningful to study the relationship between its characters and structure, especially when its single crystal structure is confirmed.

Normally, extending π-conjugated plane will cause stronger π-π stacking, which will benefit the performance in organic electronic, such as OFET. Hence N-hexacenes, N-heptacenes and even larger N-heteroacenes are quite desirable. However, with the conjugation increase, the stability and solubility of the N-heteroacenes will decrease seriously. So it is a challenge to synthesize larger N-heteroacenes.

Bunz's group leads in the area of research for large N-heteroacenes. In 2011, a class of stable N-hexacenes are reported.[35] The molecule structures are shown in Fig 2.10. These molecules show a better stability than hexacene, especially 2-10a and 2-10b, which can be stored in solution or solid state for a long time, proving that doping nitrogen atoms in the large acenes can help increase the stability. However, 2-10c, with six unsaturated nitrogen in the backbone, is not stable as 1a and 1b. It is likely to degrade into its N,N'-dihydrogenated precursors. The suitable quantity of nitrogen atoms in the backbones can help stabilize the molecules, however, too many doping nitrogen atoms will also make the N-heteroacenes unstable, probably because of deeper LUMO energy. The authors suggested that these N-hexacenes can be promising materials for OFET applications.

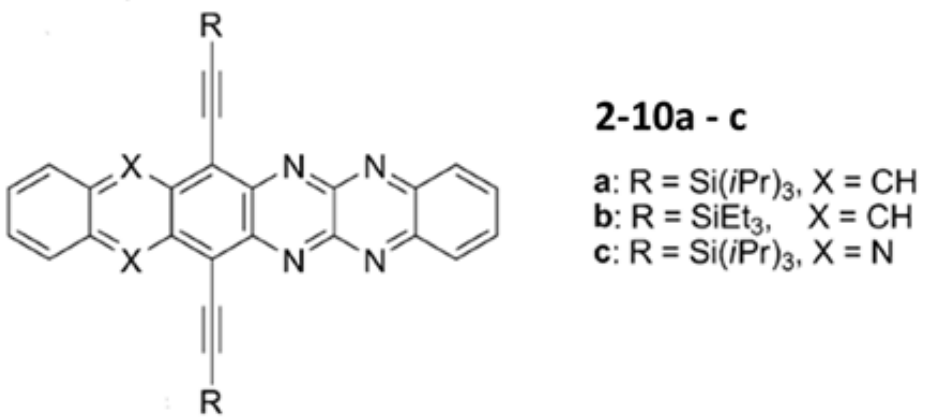

Fig 2.10 Molecular structures of N-hexacenes reported by Bunz group

In 2014, Bunz's group reported a class of diazaheptacene derivatives.[36] When the number of the rings comes to seven, it is more unstable and they behave more like polyenes, as shown in Fig 2.11. These N-heptacenes will fast change into dimer through Diels-Alder reaction once the N,N'-dihydrogenated precursors are oxidized to unsaturated form, the "true" acenes form with only one Clar's sextet. Seven rings fused in one row is the current record length of the "true" N-heteroacenes.

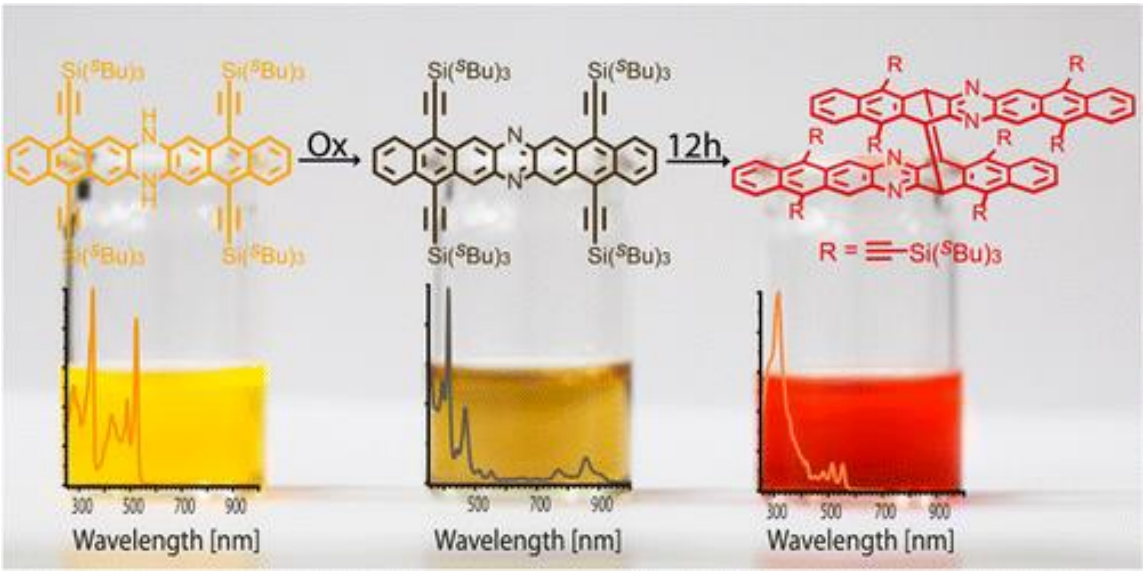

Fig 2.11 N-heptacene easily changing into a dimer. Reproduced with permission from ref. 36. Copyright 2009 American Chemical Society.

To achieve larger N-heteroacenes, more Clar's sextets must be introduced to ensure the stability.

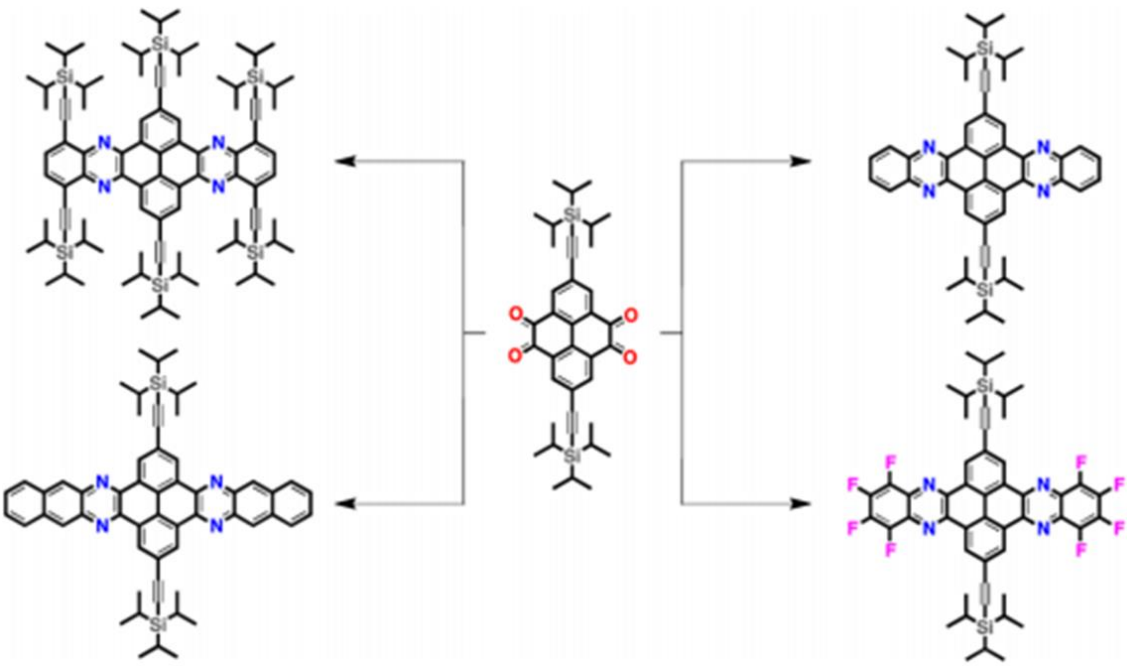

Fig 2.12 Example of pyrene bridged N-heteroacenes synthesized from pyrene-tetracene reported by Aurelio Mateo-Alonso and co-workers. Reproduced with permission from ref. 37. Copyright 2009 American Chemical Society.

It is a useful way to build up large N-heteroacenes by inserting pyrene units into the π-conjugated backbone. Mateo-Alonso and coworkers reported a series of pyrene bridged N-heteroacenes in 2012, as shown in Fig 2.12.[37] The pyrene-tetraketone is an effective precursor to synthesize large pyrene bridged N-heteroacenes. Unlike other large "true" N-heteroacenes, these pyrene-bridged N-heteroacenes are much more stable and not likely to be reduced to the corresponding NH compounds, because the aromaticity of N-heteroacenes is partially interrupted by the pyrene units, leading to segregated small the N-heteroacenes. In other words, one acene is separated into two "true" acenes by the pyrene unit and connected at the two sides of the pyrene. Though the aromaticity is interrupted, the conjugation still maintains. The pyrene units can increase the stability of the N-heteroacenes notably. As a proof, a pyrene bridged N-heteroacene polymer with 85 continuous aromatic rings in the backbone shows good air stability. The polymer shows a high TGA temperature of 545 ºC in the air.[38]

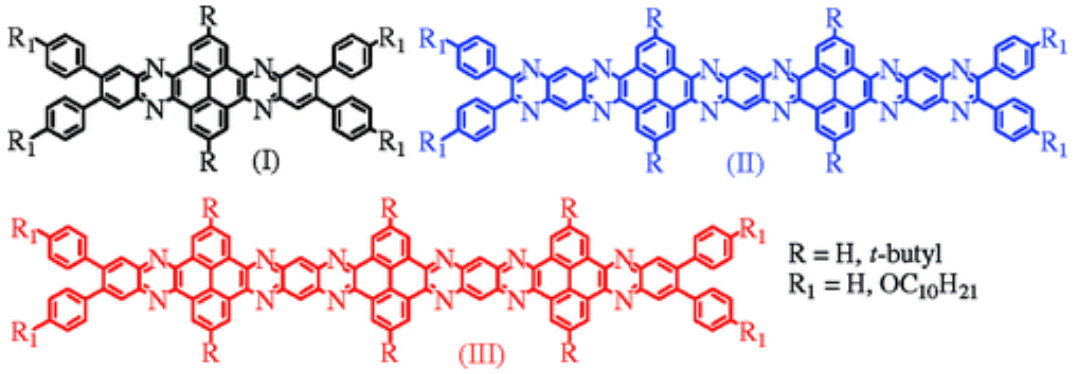

Fig 2.13 Pyrene bridged large N-heteroacenes reported by Wang and coworkers. Reproduced with permission from ref. 39. Copyright 2009 American Chemical Society.

Taking advantage of the cross-conjugation property of pyrene, Wang reported a series of pyrene-bridged large N-heteroacenes with up to sixteen aromatic rings fused in one row. However, only the six-linear-rings compound is confirmed by X-ray diffraction. All these compounds have high environmental stability. The authors suggested that these compounds can be good n-type semiconductors.[39]

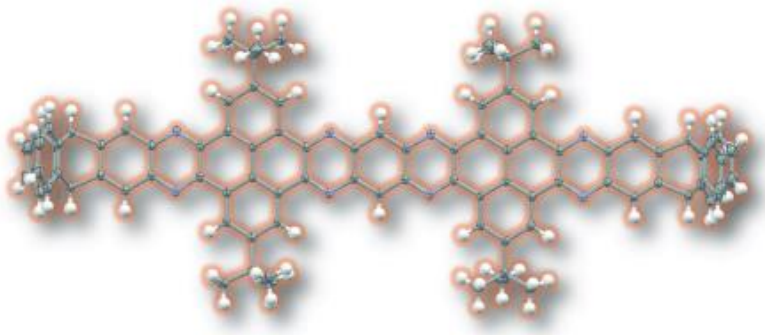

Fig 2.14 Pyrene bridged large N-heteroacenes reported by Mastalerz and coworkers. Reproduced with permission from ref. 40. Copyright 2014 Wiley-VCH Verlag GmbH & Co. KGaA.

In 2015, Mastalerz's group reported a large pyrene bridged N-heteroacenes with eleven six-membered rings fused in one row, by introducing two triptycenylene units at two terminals to increase its solubility. Two kinds of single crystal were obtained from two kinds of solvents, as shown in Fig 2.14. Eleven rings in a line is the record length of N-heteroacenes confirmed by SCXRD at that time.[40]

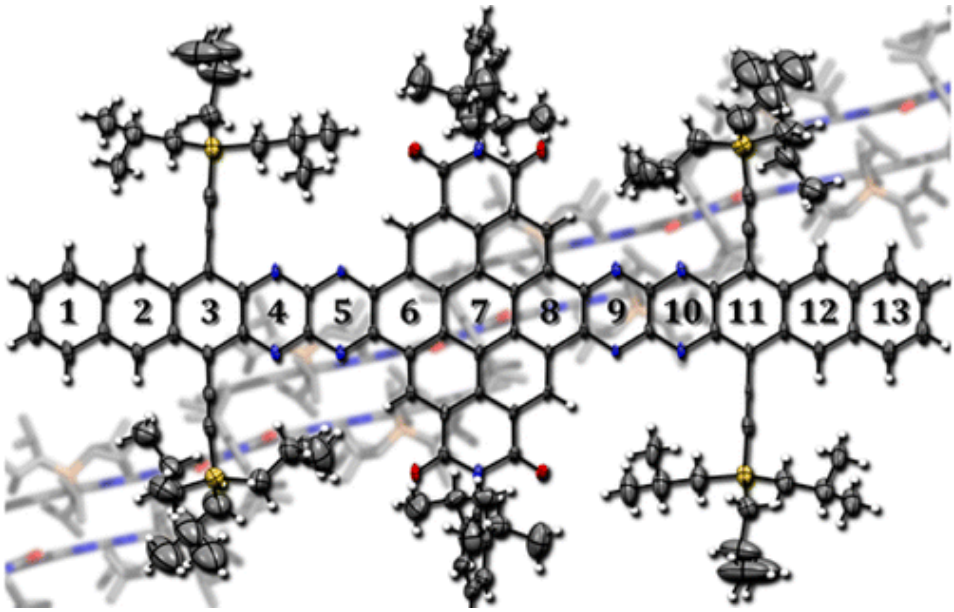

Fig 2.15 Large N-heteroacenes reported by Bunz's group. Reproduced with permission from ref. 41. Copyright 2009 American Chemical Society.

In 2016, Bunz's group reported a series of coronene bridged large N-heteroacenes with up to thirteen annulated six-membered rings fused in one row, as shown in Fig 2.15. It is the new record length of the large N-heteroacenes confirmed by SCXRD. Similar to the pyrene unit, coronene unit can also help stabilize the large N-heteroacene by adding more Clar's sextets into the conjugation framework. These series molecules all show deep low LUMO energy (from -4.25 to -4.45 eV). The 13-rings compound was applied in OFET and showed n-type semiconductor property with an electron mobility of up to 8×10^{-4} $cm^2V^{-1}S^{-1}$.[41]

Besides pyrene and coronene, quinone unit also can be used to build up large N-heteroacene by breaking the aromaticity. In 2015, a quinone bridged large N-heteroacene was reported, as shown in Fig 2.16. The quinone unit in the middle can not only break the aromaticity to stabilize the N-heteroacene, but also decrease the energy levels, which will benefit the environmental stability and the performance as N-type semiconductors. Hence this quinone bridged large N-heteroacene shows a low LUMO energy of -4.32 eV and a high electron mobility of up to 0.2 $cm^2 V^{-1} s^{-1}$ in single crystal OFET under ambient conditions.[25]

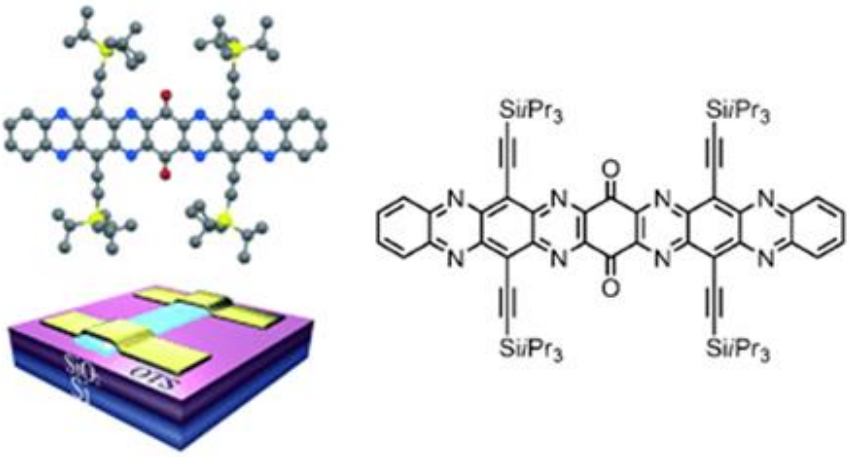

Fig 2.16 Quinone bridged large N-heteroacene. Reproduced with permission from ref. 25. Copyright 2014 Wiley-VCH Verlag GmbH & Co. KGaA.

2.2.4 Characteristic and application

The quantity and position of nitrogen atoms in N-heteroacenes backbones have a big influence on the properties. Miao's group did an excellent research on these.[42] By replacing two or four CH units with nitrogen atoms at different positions in the backbone of TIPS-PEN, molecule **2-11,12,13,14** were obtained, as shown in Fig 2.17. Molecules **2-11** and **2-12** have a higher solubility than that of **2-13** and **2-14** in acetic acid. The nitrogen atoms in the middle are shielded by the substituted TIPS groups. Hence they have lower or no interaction with the acid solvent molecules. In contrast, the nitrogen atoms at the terminals can have a strong interaction with the acid solvent, resulting in higher solubility. In the crystal structures: **2-11**, **2-13**, and **2-14** have similar packing structure of two-dimensional "bricklayer"; while **2-12** exhibits a different bilayer π-stacking structure of herringbone motif with C-H···N hydrogen bonds. By comparing **2-11** and **2-12**, it was found that only two nitrogen atoms at the terminal of N-heteropentacene are not enough to change the packing motif. The influence of nitrogen atoms on the molecular orbital energy levels was also studied, as shown in Fig 2.18 (top). As they expected, the nitrogen atoms make a contribution in lowering both HOMO and LUMO energy levels. Very interestingly, it was found that replacing CH units with nitrogen atoms in the middle is more effective in lowering the molecular orbital energy levels than that in the terminals. For example, the LUMO of **2-14** is -4.01 eV, which is

lower than that of molecule **2-12** (-3.68 eV). It was further confirmed by comparing with molecule **2-15**, which is constructed with two pyrazines at the third ring and fourth ring and two ethynyl groups substituting at the second ring. In this series of molecules, **2-15** has the lowest LUMO energy level of -4.28 eV[43] with the pyrazine rings in the center.

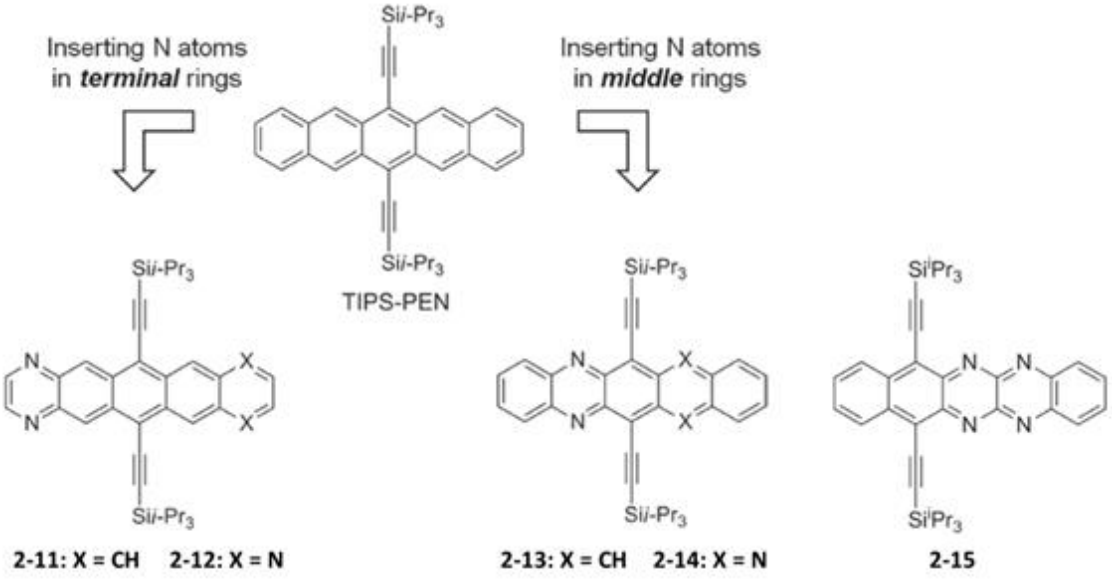

Fig 2.17 Structure of **2-11, 12, 13, 14**; TIPS-PEN and **2-15** are also shown for comparison. Reproduced with permission from ref. 42. Copyright 2014 Wiley-VCH Verlag GmbH & Co. KGaA.

At last the OFET performance of these molecules is investigated. The mobilities are shown in Fig 2.18 (bottom). By adjusting the quantity and position of the nitrogen atoms, N-heteropentacenes can serve as p-type, ambipolar, and n-type semiconductors. It coincides with the molecular orbital energy levels above. Molecule **2-11** can only serve as a p-type semiconductor with both higher HOMO and LUMO energy levels. Molecule **2-14** can only serve as an n-type semiconductor with both lower HOMO and LUMO energy levels. Molecules **2-12** and **2-13** are ambipolar semiconductors with the suitable HOMO and LUMO energy levels. In particular, molecule **2-14**, with an electron mobility of 3.3 $cm^2V^{-1}S^{-1}$, is one of the highest performances among n-type semiconductors.[7]

HOMO and LUMO energy levels of **2-11,12,13,14** and TIPS-PEN

	Experimental[a]		Calculated[b]	
	HOMO [eV]	LUMO [eV]	HOMO [eV]	LUMO [eV]
2-11	−5.25	−3.49	−5.19	−3.35
2-12	−5.49	−3.68	−5.44	−3.59
2-13	−5.34	−3.68	−5.28	−3.48
2-14	−5.75	−4.01	−5.64	−3.81
TIPS-PEN	−5.17	−3.32	−4.96	−3.08

[a]The experimental values of HOMO and LUMO energy levels were estimated from oxidation/reduction potentials and absorption edge as detailed in the supporting information and ref. , [b]The HOMO and LUMO energy levels of trimethylsilyl-substituted model molecules were calculated at the B3LYP level of DFT with 6-311^{++}G(d,p)//6-31G(d,p) basis sets.

Field-effect mobility of silylethynylated N-heteropentacenes measured from vacuum-deposited and solution-cast films.

	Field Effect Mobility [$cm^2 V^{-1} s^{-1}$][a]	
	Hole mobility	Electron mobility
[b] 2-11	0.3–1.2	–
[b] 2-12	0.05–0.22	0.3–1.1
[c] 2-13	0.02–0.05	$2–4 \times 10^{-4}$
[c] 2-14	–	1.0–3.3

[a]The hole mobility was measured in ambient air and the electron mobility was measured under vacuum; [b]The substrates were at room temperature during deposition of films; [c]Data from ref

Fig 2.18 Top: HOMO and LUMO energy of **2-11, 12, 13, 14** and TIPS-PEN; Bottom: Mobility of **2-11, 12, 13, 14**. Reproduced with permission from ref. 42. Copyright 2014 Wiley-VCH Verlag GmbH & Co. KGaA.

Involving more unsaturated nitrogen atom can help lower the molecular orbital energy levels, however, it has a limitation. Miao's group reported a class of N-heteropentacenes with three pyridine units in a row in the center and two ethynyl groups substituted at terminal rings, as shown in Fig 2.19. [32]

2-16a - c, with six unsaturated N atoms in the center, have extremely low LUMO energy levels. The LUMOs are -4.54 eV, -4.57 and -4.51 eV for **2-16a - c**, respectively. It was found that **2-16a - c** easily changed into the dihydro-precursors **2-17a - c** in the air at room temperature in several days under an unclear mechanism. The low LUMO energy

levels of **2-16a - c** make them potential n-type semiconductors. However, it is found that **2-16a - c** cannot be processed by thermal evaporation and the films from solution process are poor quality. Molecule **2-17a** exhibits a good π stacking in its crystal structure while **2-17b** exhibits NH···N hydrogen bonds in its crystal structure. The positions of the substituted groups have a big influence in the packing state. Though **2-17a** has a good π stacking, the high LUMO and low HOMO energy levels make it suitable for neither p-type nor n-type semiconductors. From the instability of **11a - c**, the authors conclude that the max number of unsaturated nitrogen atoms in ethynyl groups substituted N-heteropentacene system should be five.

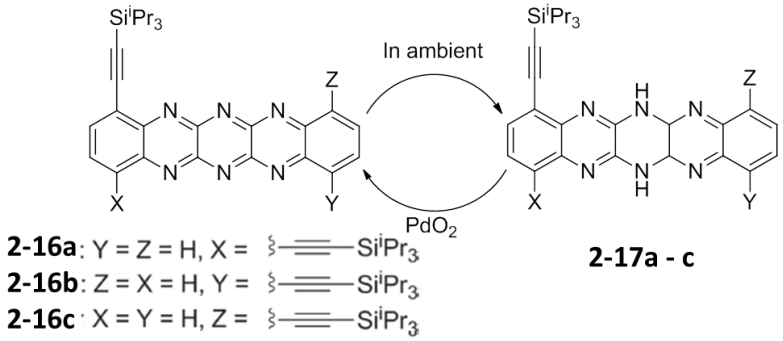

Fig 2.19 Molecule structures of **2-16a - c** and **2-17a - c**

Born from acenes but different from acenes, N-heteroacenes are likely to have strong intermolecular interactions caused by nitrogen atoms.

Zhang's group reported two ambipolar semiconductors **2-18** and **2-19**.[33] It is found that with the nitrogen atoms at the terminals, N-heteropentacenes can have a closer π stacking. Actually, the distances between two π plane backbones of the N-heteroacenes are 3.35 Å for **2-18** and 3.30 Å for **2-19** which are smaller than that of TIPS-PEN's 3.43 Å. The authors concluded that this is because of the interaction between the electronegative nitrogen atoms and the electropositive CH units caused by the overlapping. Both **2-18** and **2-19** are excellent ambipolar semiconductors with balanced electron and hole mobilities. The electron and hole mobilities for **2-18** are 0.15 and 0.11 $cm^2V^{-1}S^{-1}$, respectively. The electron and hole mobilities for **2-19** are 0.09 and 0.08 $cm^2V^{-1}S^{-1}$, respectively.

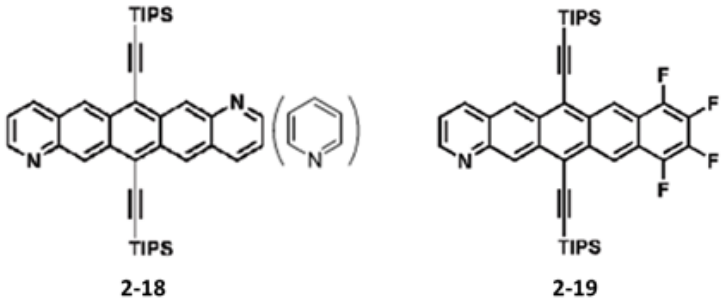

Fig 2.20 Molecule structures of **2-18** and **2-19** reported by Hao-Li Zhang's group

The hydrogen bond is a strong intermolecular interaction. The molecules should be carefully designed when taking advantage of it. It is an effective tool to increase the π-π stacking. However, sometimes it can also break the π-π stacking. Miao's group did a research about the hydrogen bond in N-heteropentacenes.[44] Molecule **2-20** and **2-21** (in Fig 2.21) exhibits NH···N hydrogen bonds in the crystal structure or NH···solvent hydrogen bonds. While the NH units of **2-22** are shielded by the silylethynylated substituted groups, hydrogen bonds are not found. In the crystal structure of **2-20**, the π planes are separated by the hydrogen bonds. In contrast, without the hydrogen bonds, **2-20** exhibits a good π-π stacking. Both **2-20** and **2-22** can serve as p-type semiconductors with the mobilities of 4 - 7 $\times 10^{-4}$ and 0.3 - 0.7 $cm^2V^{-1}S^{-1}$, respectively.

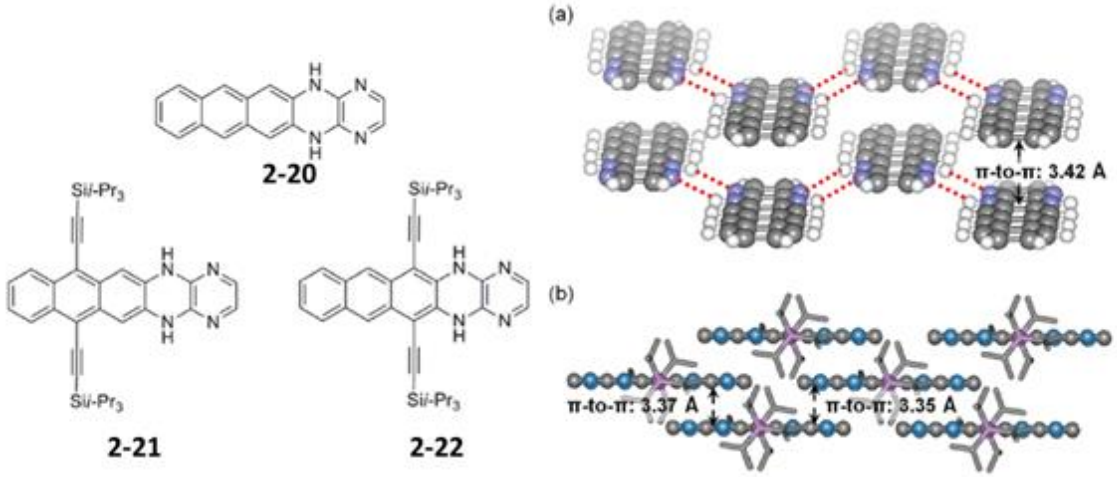

Fig 2.21 Molecule structures of **2-20, 21, 22** and the crystal structure of (a) **2-20** and (b) **2-22.** Reproduced with permission from ref. 44. Copyright 2009 American Chemical Society.

2.3 Other systems

2.3.1 Substituted Acenes

The substitute groups play an important role in the acenes based semiconductors. In N-heteroacenes, the knowledge of substitute groups is generally extended from pentacenes and other acenes. It will be a great help to design novel N-heteroacenes by being acquainted with the substitute groups of the acenes.

Aryl substituents. 2-23 and **2-29** are the first functionalized pentacenes, which were reported in the 1940s.[45] **2-23** has a better solubility and stability, because the benzenes substitute at the most reactive positions. Some other aryl group substituted pentacenes were also reported, as shown in Fig 2.22. Most of them exhibit an edge-to-face packing in the crystal structures hence only weak π-π stacking can be obtained. The crystal structure of **2-23** is shown as an example. While strong π-π stacking can be seen in the crystal structure of the thienyl substituted pentacene **2-25**[46], hence the OFET device of **2-25** shows a high mobility of 0.1 $cm^2V^{-1}S^{-1}$.

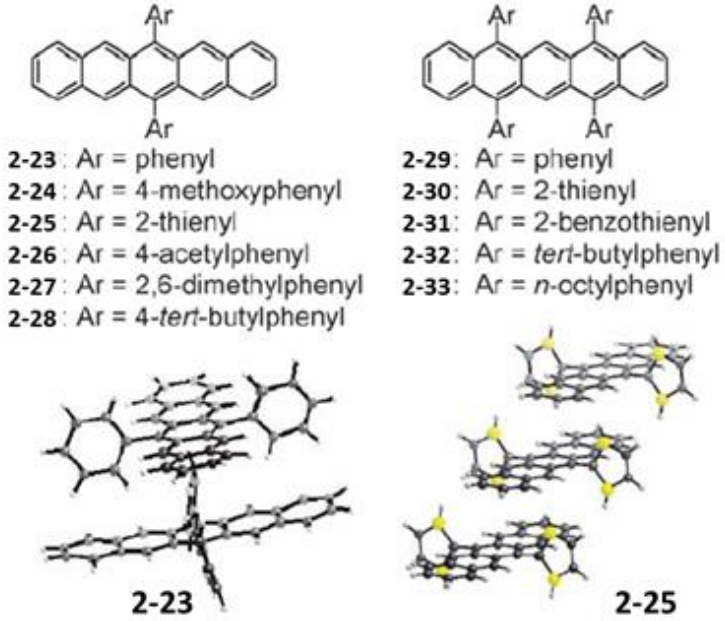

Fig 2.22 Structures of aryl group substituted pentacenes, and crystal structures of **2-23** and **2-25** Reproduced with permission from ref. 47. Copyright 2014 Wiley-VCH Verlag GmbH & Co. KGaA.

Alkyl substituents. The alkyl substituted acenes are quite limited. **2-34** exhibits a typical herringbone arrangement, and its OFET device has a mobility of 0.3 $cm^2V^{-1}S^{-1}$.[48] By replacing the methyl substituents of **2-34** with trimethyl-silyl substituents, **2-35** exhibits a very high solubility but low stability.[49]

Thio-substituents. Sulfur–sulfur interaction is often utilized to increase the intermolecular interaction. Taking advantage of sulfur-sulfur interaction, **2-36** exhibits a very strong π-π stacking. Its OFET device shows a mobility of 0.04 $cm^2V^{-1}S^{-1}$.[50]

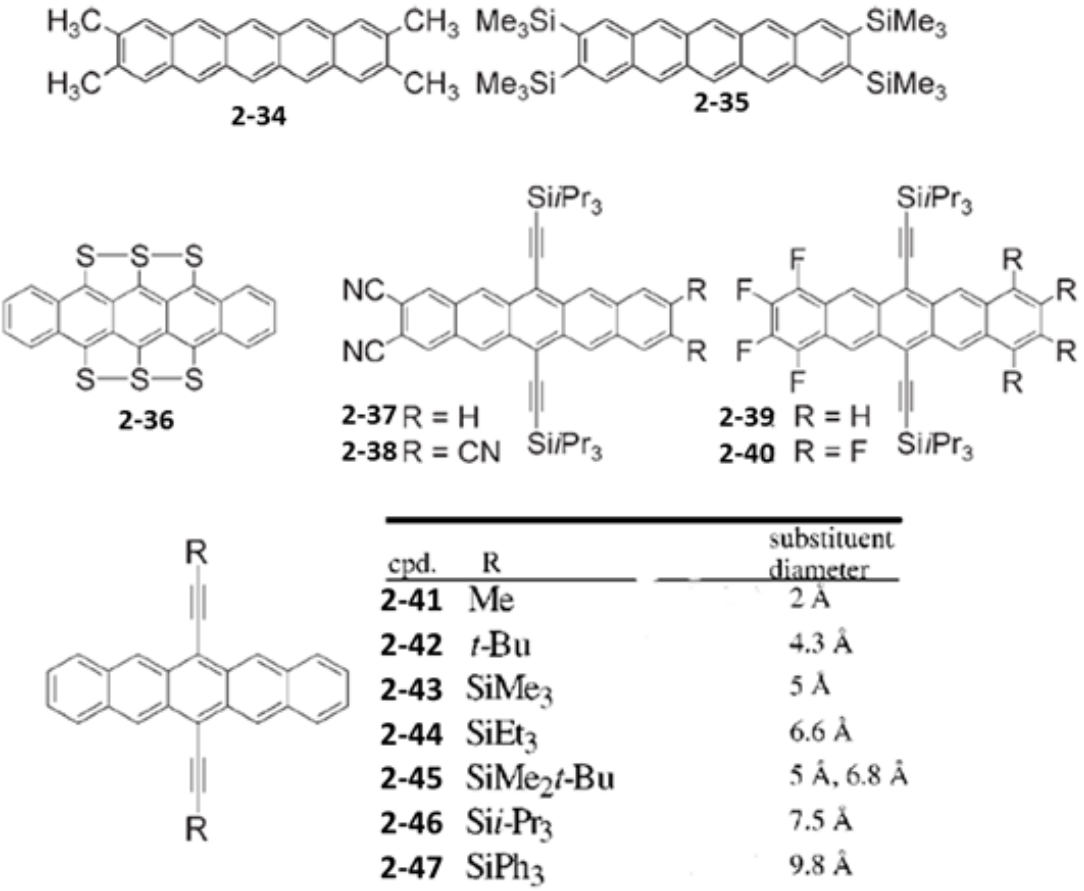

cpd.	R	substituent diameter
2-41	Me	2 Å
2-42	*t*-Bu	4.3 Å
2-43	$SiMe_3$	5 Å
2-44	$SiEt_3$	6.6 Å
2-45	$SiMe_2t$-Bu	5 Å, 6.8 Å
2-46	Si*i*-Pr_3	7.5 Å
2-47	$SiPh_3$	9.8 Å

Fig 2.23 Structures of substituted pentacenes. Reproduced with permission from ref. 52. Copyright 2009 American Chemical Society.

Electron-withdrawing substituents. In order to lower the molecular orbital energy levels, electron-withdrawing substituents are often utilized in the pentacenes. The nitrile substituents can lower the molecule energy effectively in **2-37** and **2-38**, however, they

also decrease the solubilities, which is not beneficial to form a uniform film in certain applications. The influence of fluorine atom is similar with nitrile group. For **2-39** and **2-40,** the mobility increases with the increased substituted fluorine atoms number, because of the close packing caused by fluorine atoms.[51]

Ethynyl substituents. Ethynyl groups are most utilized substituents in acenes, especially silylethynyl groups. The silyl-ethynyl groups show several advantages: Firstly, the electron-withdrawing ethynyl groups can lower molecule energy levels of acenes and increase the stability. Secondly, the alkylsilyl groups can increase the solubility in a large extent. Lastly and very interestingly, the silylethynyl groups are very effective in adjusting the arrangement of acenes in the crystal structures. The alkylsilyl groups are ball shape in general. When the diameter of the alkylsilyl groups roughly equals to the half-length of the acenes (length of pentacene ~ 14 Å), acenes will adopt a 2D brickwork arrangement with strong π-π stacking, just like the crystal structure of **2-43** shown in Fig 2.24. Molecules **2-42** - **2-46** all adopt the similar packing structures, with the π overlap range from 20% for **2-45** to 40% for **2-44**. If the substituted groups are too small or too large, the 2D brickwork arrangement can no longer be adopted. That is why **2-41** and **2-47** can only form powder.[52]

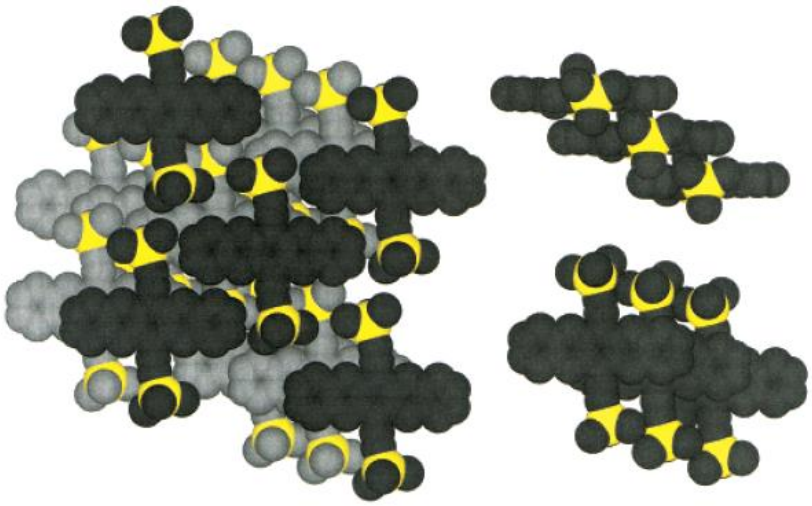

Fig 2.24 Crystal structure of **2-43.** Reproduced with permission from ref. 52. Copyright 2009 American Chemical Society.

2.3.2 Graphitic Carbon nitride

Graphitic carbon nitride (g-C_3N_4) is a kind of nitrogen-rich two-dimensional n-type semiconductor material. Its structure is shown in Fig 2.25. Recently, g-C_3N_4 has been a research hotspot in many applications, including photocatalytic reactions,[53] light emitting device,[54] sensors,[55] etc, because of its unique electron property and excellent stability. Especially in water splitting[56] and photoelectrochemical (PEC) cells,[57] g-C_3N_4 has been one of the most investigated materials since Wang and coworkers firstly utilized g-C_3N_4 to split water and produced H_2 in 2009.[58] With nearly ten years developing, the performance of g-C_3N_4 in water splitting and PEC cells have been greatly improved mainly through two approaches: 1. Reducing the energy gap of g-C_3N_4 (The band gap of monolayered g-C_3N_4 is about 2.65 eV.[56]) to harvest more light; 2. Reducing the recombination of the excitons and holes by optimizing the morphology or heterojunctions.[59]

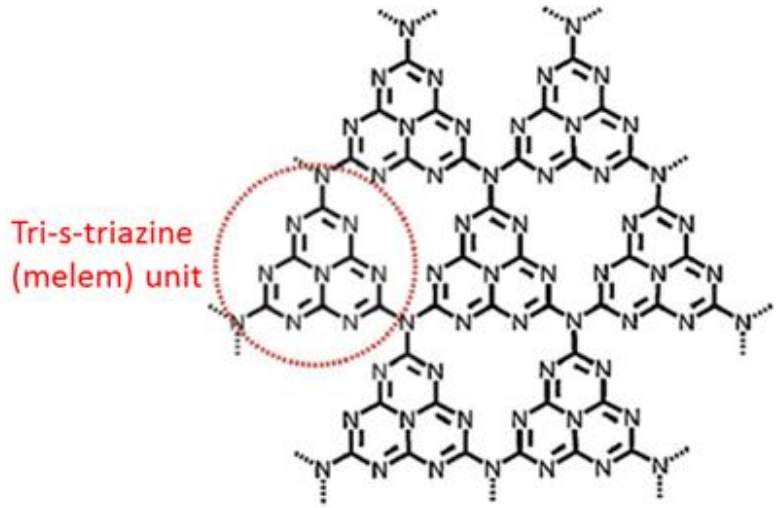

Fig 2.25 Molecular structure of g-C_3N_4

N-heteroacenes, as one-dimensional nitrogen doped graphitic material, is similar to g-C_3N_4 to a certain degree. Hence N-heteroacenes hold the possibility good prospect in the application of water splitting and PEC cells. Comparing with g-C_3N_4, N-heteroacenes have both advantages and disadvantages. The HOMO and LUMO energy levels of N-heteroacenes can easily meet the requirements of light harvesting and photocatalytic

reactions. The structures of N-heteroacenes can be conveniently designed to meet special conditions. While on the other hand, g-C_3N_4 has superior thermal, chemical and environmental stability.

2.4 Questions to be answered based on literature

N-heteroacenes have been developed rapidly in this century, and many achievements have been made in this field. However, there are still some scientific questions to be answered, some challenges to overcome and to achieve the real industry application.

Firstly, it is still hard to precisely predict the property and stacking structure from the molecular structure. Design more special N-heteroacenes and study the relationship between the molecular structures and properties is a pathway to develop a general theory to predict that.

Secondly, several SCXRD confirmed large N-heteroacenes have been reported and it has become a new hot research topic. What will happen if the N-heteroacenes become larger? What is the limit length of the large N-heteroacenes? Several interesting questions need to be answered in this new field.

Thirdly, N-heteroacenes have shown the potential as n-type semiconductors. The performances are still not good enough for industrial applications. It is urgent to develop new strategies to increase the performances.

2.5 Ph.D. in context of literature

In this literature review, a history of the N-heteroacenes is briefly introduced. The recent developments of N-heteroacenes are discussed in detail in four parts: theoretical calculations, the synthetic methods, the large N-heteroacenes, characteristic and applications. All these research is the most important foundations of this thesis. Some literature in other fields are also introduced. These literature also give inspiration and guidance to this thesis.

References

[1] a) E. Clar, F. John, *Berichte der deutschen chemischen Gesellschaft (A and B Series)* **1931**, *64*, 981-988; b) E. Clar, F. John, *Berichte der deutschen chemischen Gesellschaft (A and B Series)* **1930**, *63*, 2967-2977; c) E. Clar, F. John, *Berichte der deutschen chemischen Gesellschaft (A and B Series)* **1929**, *62*, 3021-3029.

[2] O. Hinsberg, *Justus Liebigs Annalen der Chemie* **1901**, *319*, 257-286.

[3] a) O. Fischer, E. Hepp, *Berichte der deutschen chemischen Gesellschaft* **1890**, *23*, 2789-2793; b) O. Fischer, E. Hepp, *Berichte der deutschen chemischen Gesellschaft* **1895**, *28*, 293-301.

[4] E. Leete, O. Ekechukwu, P. Delvigs, *The Journal of Organic Chemistry* **1966**, *31*, 3734-3739.

[5] F. Kummer, H. Zimmermann, *BERICHTE DER BUNSEN-GESELLSCHAFT FUR PHYSIKALISCHE CHEMIE* **1967**, *71*, 1119-+.

[6] Q. Miao, T.-Q. Nguyen, T. Someya, G. B. Blanchet, C. Nuckolls, *Journal of the American Chemical Society* **2003**, *125*, 10284-10287.

[7] Z. Liang, Q. Tang, J. Xu, Q. Miao, *Advanced Materials* **2011**, *23*, 1535-1539.

[8] X. Xu, Y. Yao, B. Shan, X. Gu, D. Liu, J. Liu, J. Xu, N. Zhao, W. Hu, Q. Miao, *Advanced Materials* **2016**, *28*, 5276-5283.

[9] Q. Miao, *Advanced Materials* **2014**, *26*, 5541-5549.

[10] J. Li, Q. Zhang, *ACS Applied Materials & Interfaces* **2015**, *7*, 28049-28062.

[11] a) M. B. Casu, P. Imperia, S. Schrader, B. Falk, M. Jandke, P. Strohriegl, *Synthetic Metals* **2001**, *124*, 79-81; b) G. Li, A. P. Abiyasa, J. Gao, Y. Divayana, W. Chen, Y. Zhao, X. W. Sun, Q. Zhang, *Asian Journal of Organic Chemistry* **2012**, *1*, 346-351; c) B. D. Lindner, Y. Zhang, S. Hofle, N. Berger, C. Teusch, M. Jesper, K. I. Hardcastle, X. Qian, U. Lemmer, A. Colsmann, U. H. F. Bunz, M. Hamburger, *Journal of Materials Chemistry C* **2013**, *1*, 5718-5724; d) M. Ganschow, S. Koser, S. Hahn, F. Rominger, J. Freudenberg, U. H. F. Bunz, *Chemistry – A European Journal* **2017**, *23*, 4415-4421.

[12] Q. Zhang, J. Xiao, Z. Yin, H. M. Duong, F. Qiao, F. Boey, X. Hu, H. Zhang, F. Wudl, *Chemistry – An Asian Journal* **2011**, *6*, 856-862.

[13] a) P.-Y. Gu, F. Zhou, J. Gao, G. Li, C. Wang, Q.-F. Xu, Q. Zhang, J.-M. Lu, *J. Am. Chem. Soc.* **2013**, *135*, 14086-14089; b) P.-Y. Gu, J. Gao, C.-J. Lu, W. Chen, C. Wang, G. Li, F. Zhou, Q.-F. Xu, J.-M. Lu, Q. Zhang, *Materials Horizons* **2014**, *1*, 446-451; c) C. Wang, J. Wang, P.-Z. Li, J. Gao, S. Y. Tan, W.-W. Xiong, B. Hu, P. S. Lee, Y. Zhao, Q. Zhang, *Chemistry – An Asian Journal* **2014**, *9*, 779-783; d) C. Wang, B. Hu, J. Wang, J. Gao, G. Li, W.-W. Xiong, B. Zou, M. Suzuki, N. Aratani, H. Yamada, F. Huo, P. S. Lee, Q. Zhang, *Chemistry – An Asian Journal* **2015**, *10*, 116-119.

[14] P.-Y. Gu, Z. Wang, Q. Zhang, *Journal of Materials Chemistry B* **2016**, *4*, 7060-7074.

[15] G. Li, J. Miao, J. Cao, J. Zhu, B. Liu, Q. Zhang, *Chemical Communications* **2014**, *50*, 7656-7658.

[16] Y. Wu, Z. Yin, J. Xiao, Y. Liu, F. Wei, K. J. Tan, C. Kloc, L. Huang, Q. Yan, F. Hu, H. Zhang, Q. Zhang, *ACS Applied Materials & Interfaces* **2012**, *4*, 1883-1886.

[17] M. Tadokoro, S. Yasuzuka, M. Nakamura, T. Shinoda, T. Tatenuma, M. Mitsumi, Y. Ozawa, K. Toriumi, H. Yoshino, D. Shiomi, K. Sato, T. Takui, T. Mori, K. Murata, *Angewandte Chemie International Edition* **2006**, *45*, 5144-5147.

[18] M. L. Tang, A. D. Reichardt, P. Wei, Z. Bao, *Journal of the American Chemical Society* **2009**, *131*, 5264-5273.

[19] X.-D. Tang, Y. Liao, H. Geng, Z.-G. Shuai, *Journal of Materials Chemistry* **2012**, *22*, 18181.

[20] M. Winkler, K. N. Houk, *Journal of the American Chemical Society* **2007**, *129*, 1805-1815.

[21] J. Hu, D. Zhang, F. W. Harris, *The Journal of Organic Chemistry* **2005**, *70*, 707-708.

[22] P.-Y. Gu, N. Wang, C. Wang, Y. Zhou, G. Long, M. Tian, W. Chen, X. W. Sun, M. G. Kanatzidis, Q. Zhang, *Journal of Materials Chemistry A* **2017**, *5*, 7339-7344.

[23] U. H. Bunz, S. Hahn, F. Rominger, S. Koser, o. tverskoy, A. Dreuw, M. Hodecker, *Chemistry – A European Journal* **2017**, 8148-8151.

[24] M. D. Clayton, Z. Marcinow, P. W. Rabideau, *Tetrahedron Lett.* **1998**, *39*, 9127-9130.

[25] C. Wang, J. Zhang, G. Long, N. Aratani, H. Yamada, Y. Zhao, Q. Zhang, *Angewandte Chemie International Edition* **2015**, *54*, 6292-6296.

[26] R. Ponce Ortiz , H. Herrera, M. J. Mancheño, C. Seoane, J. L. Segura, P. Mayorga Burrezo, J. Casado, J. T. López Navarrete, A. Facchetti, T. J. Marks, *Chemistry – A European Journal* **2013**, *19*, 12458-12467.

[27] B. D. Lindner, J. U. Engelhart, M. Märken, O. Tverskoy, A. L. Appleton, F. Rominger, K. I. Hardcastle, M. Enders, U. H. F. Bunz, *Chemistry – A European Journal* **2012**, *18*, 4627-4633.

[28] M. Porz, F. Rominger, U. H. F. Bunz, *Crystal Growth & Design* **2014**, *14*, 5962-5965.

[29] W. Chen, S. Y. Tan, Y. Zhao, Q. Zhang, *Organic Chemistry Frontiers* **2014**, *1*, 391-394.

[30] a) C. Seillan, H. Brisset, O. Siri, *Organic Letters* **2008**, *10*, 4013-4016; b) T. Itoh, S. Aomori, M. Oh-e, M. Koden, Y. Arakawa, *Synthetic Metals* **2012**, *162*, 1264-1270.

[31] a) K. Cai, Q. Yan, D. Zhao, *Chemical Science* **2012**, *3*, 3175-3182; b) J. U. Engelhart, B. D. Lindner, O. Tverskoy, F. Rominger, U. H. F. Bunz, *The Journal of Organic Chemistry* **2013**, *78*, 10832-10839.

[32] Z. He, R. Mao, D. Liu, Q. Miao, *Organic Letters* **2012**, *14*, 4190-4193.

[33] Y.-Y. Liu, C.-L. Song, W.-J. Zeng, K.-G. Zhou, Z.-F. Shi, C.-B. Ma, F. Yang, H.-L. Zhang, X. Gong, *J. Am. Chem. Soc.* **2010**, *132*, 16349-16351.

[34] U. H. F. Bunz, J. U. Engelhart, *Chemistry – A European Journal* **2016**, *22*, 4680-4689.

[35] B. D. Lindner, J. U. Engelhart, O. Tverskoy, A. L. Appleton, F. Rominger, A. Peters, H.-J. Himmel, U. H. F. Bunz, *Angewandte Chemie International Edition* **2011**, *50*, 8588-8591.

[36] J. U. Engelhart, O. Tverskoy, U. H. F. Bunz, *J. Am. Chem. Soc.* **2014**, *136*, 15166-15169.

[37] S. More, R. Bhosale, S. Choudhary, A. Mateo-Alonso, *Organic Letters* **2012**, *14*, 4170-4173.

[38] J. K. Stille, E. L. Mainen, *Macromolecules* **1968**, *1*, 36-42.

[39] B. Gao, M. Wang, Y. Cheng, L. Wang, X. Jing and F. Wang, *J. Am. Chem. Soc.*, **2008**, *130*, 8297-8306.

[40] B. Kohl, F. Rominger, M. Mastalerz, *Angewandte Chemie International Edition* **2015**, *54*, 6051-6056.

[41] A. H. Endres, M. Schaffroth, F. Paulus, H. Reiss, H. Wadepohl, F. Rominger, R. Krämer, U. H. F. Bunz, *Journal of the American Chemical Society* **2016**, *138*, 1792-1795.

[42] Z. Liang, Q. Tang, R. Mao, D. Liu, J. Xu, Q. Miao, *Advanced Materials* **2011**, *23*, 5514-5518.

[43] O. Tverskoy, F. Rominger, A. Peters, H.-J. Himmel, U. H. F. Bunz, *Angewandte Chemie International Edition* **2011**, *50*, 3557-3560.

[44] Z. He, D. Liu, R. Mao, Q. Tang, Q. Miao, *Organic Letters* **2012**, *14*, 1050-1053.

[45] C. F. H. Allen, A. Bell, *Journal of the American Chemical Society* **1942**, *64*, 1253-1260.

[46] Q. Miao, X. Chi, S. Xiao, R. Zeis, M. Lefenfeld, T. Siegrist, M. L. Steigerwald, C. Nuckolls, *Journal of the American Chemical Society* **2006**, *128*, 1340-1345.

[47] J. E. Anthony, *Angewandte Chemie International Edition* **2008**, *47*, 452 – 483.

[48] H. Meng, M. Bendikov, G. Mitchell, R. Helgeson, F. Wudl, Z. Bao, T. Siegrist, C. Kloc, C. H. Chen, *Advanced Materials* **2003**, *15*, 1090-1093.

[49] S. H. Chan, H. K. Lee, Y. M. Wang, N. Y. Fu, X. M. Chen, Z. W. Cai, H. N. C. Wong, *Chemical Communications* **2005**, 66-68.

[50] A. L. Briseno, Q. Miao, M.-M. Ling, C. Reese, H. Meng, Z. Bao, F. Wudl, *Journal of the American Chemical Society* **2006**, *128*, 15576-15577.

[51] C. R. Swartz, S. R. Parkin, J. E. Bullock, J. E. Anthony, A. C. Mayer, G. G. Malliaras, *Organic Letters* **2005**, *7*, 3163-3166.

[52] J. E. Anthony, D. L. Eaton, S. R. Parkin, *Organic Letters* **2002**, *4*, 15-18.

[53] a) F. Goettmann, A. Fischer, M. Antonietti, A. Thomas, *Angewandte Chemie International Edition* **2006**, *45*, 4467-4471; b) F. Su, S. C. Mathew, G. Lipner, X. Fu, M. Antonietti, S. Blechert, X. Wang, *Journal of the American Chemical Society* **2010**, *132*, 16299-16301.

[54] J. Gao, Y. Zhou, Z. Li, S. Yan, N. Wang, Z. Zou, *Nanoscale* **2012**, *4*, 3687-3692.

[55] E. Z. Lee, Y.-S. Jun, W. H. Hong, A. Thomas, M. M. Jin, *Angewandte Chemie International Edition* **2010**, *49*, 9706-9710.

[56] S. Yang, Y. Gong, J. Zhang, L. Zhan, L. Ma, Z. Fang, R. Vajtai, X. Wang, P. M. Ajayan, *Advanced materials* **2013**, *25*, 2452-2456.

[57] J. Bian, L. Xi, C. Huang, K. M. Lange, R.-Q. Zhang, M. Shalom, *Advanced Energy Materials* **2016**, *6*, 1600263-n/a.

[58] X. Wang, K. Maeda, A. Thomas, K. Takanabe, G. Xin, J. M. Carlsson, K. Domen, M. Antonietti, *Nature materials* **2009**, *8*, 76-80.

[59] G. Dong, Y. Zhang, Q. Pan, J. Qiu, *Journal of Photochemistry and Photobiology C: Photochemistry Reviews* **2014**, *20*, 33-50.

Chapter 3

Experimental Methodology

In this chapter, the details of the experiment method and principles are introduced. The synthetic details are described and it is mainly about the mechanisms of the employed reactions including Schiff base reaction, Buchwald-Hartwig reaction, $LiAlH_4$ reduction reaction and MnO_2 oxidization reaction. Subsequently, the material purification methods are described including column chromatography, extraction, recrystallization and filtration. In the third part, the characterization methods are introduced. Nuclear magnetic resonance (NMR), high-resolution mass spectrometry (HRMS) and single crystal X-ray diffraction are applied to confirm and study the molecular structure. Cyclic voltammetry (CV) and ultraviolet-visible spectroscopy (UV-Vis) are used to investigate the molecular orbital energy levels. Fluorescence spectroscopy is applied to study the photophysics property. In the final part, the experiments of material performance test for photoelectrochemical (PEC) and organic field effect transistor (OFET) are introduced.

3.1 Rationale for selection

All experiments and tests are designed for particular purposes. The specific reactions are selected to synthesize the target molecules. Schiff base reaction and Buchwald-Hartwig reaction are often reported for building up kinds of N-heteroacenes. $LiAlH_4$ and MnO_2 are common reduction and oxidization reagents, respectively. These reactions are reliable and can be easily operated in the common experiment conditions to obtain the target molecules.

The purification steps are as important as the synthesis. Successful synthesis but failed in purification is equal to failing to get the target compound. Only the pure compound can give the right information in the characterization test, and the purity will also seriously affect the performance in PEC and OFET test. Thus, effective purification methods are necessary. Generally, extraction and filtration can process separation roughly, while recrystallization and column chromatography can process purification thoroughly. Extraction can be selected to separate organic-solvent-soluble compounds from water-soluble salts. Filtration is selected to separate solids and solution. Column chromatography is selected to fine separate different organic compounds by the polarity difference. Recrystallization is usually selected to remove a small amount of impurities by the solubility difference. Several purification methods are often applied together to get the pure product.

Characterization tests can provide the basic properties and parameter of the as-obtained compounds. NMR and HRMS test are normally firstly processed, due to the results can basically confirm the molecular structure. Single crystal X-ray diffraction (SCXRD) is a more powerful method to study the molecular structure. Though it is often difficult to grow a crystal with good quality for the test, it is still worth trying it. Due to the SCXRD test result can produce large amounts of useful data including the molecule conformation, bond length, bond angle and packing structure. CV and UV-Vis test are selected to study the molecular orbital energy levels, and they are classic methods to investigate organic semiconductors. For some compounds, the fluorescence spectroscopy is processed to explore the photophysical property.

In the final part, the experiment details of PEC and OFET are introduced. PEC and OFET test are processed to evaluate the performance of new materials.

3.2 Synthesis

3.2.1 Schiff base reaction

Schiff base, which also can be called imine, can be synthesized through a condensation reaction between aldehydes (or ketones) and amines. The reaction mechanism is shown in Scheme 3.1. The lone pair electrons on the nitrogen atom of nucleophilic primary amine attack the electrophilic carbon atom of aldehydes or ketones. With the nucleophilic addition reaction completing, a α-hydroxy amine intermediate is generated. After dehydration, the starting C=O double bond changes into the C=N bond. Weak acid can act as a catalyst in this reaction.

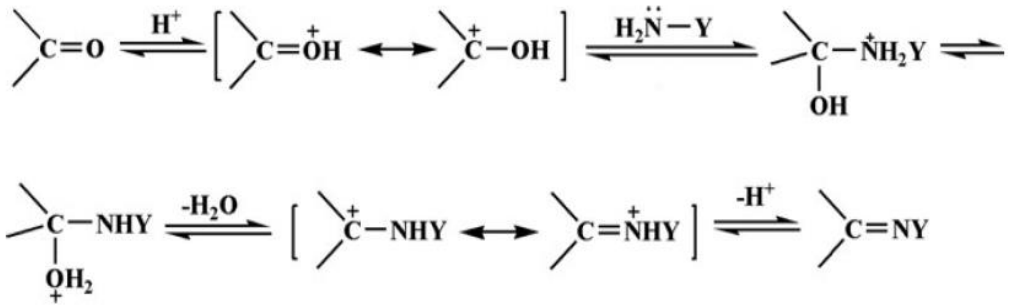

Scheme 3.1 The condensation reaction mechanism between aldehydes or ketones and amines

Double Schiff base reaction is the most common method to synthesize N-heteroacenes by condensing an *o*-quinone compound and an *o*-diamine compound, as shown in Scheme 3.2.

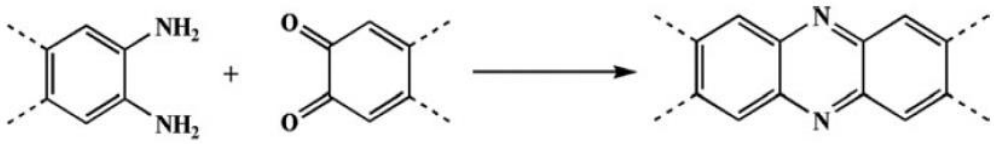

Scheme 3.2 Synthesize N-heteroacene through a double Schiff base reaction

2-Iodoxybenzoic acid (IBX) can act as a catalyst in this double Schiff base reaction and increase the yield. Though it is still not clear how IBX works in this reaction, a possible

mechanism has been reported [1] and shown in Scheme 3.3. The iodine cation in IBX can act as a Lewis acid and coordinate with one carbonyl group to active the carbon atom and make it more easy to be attacked by amine group subsequently. After one amine group is attacked by one IBX activated carbonyl group, a complex compound formed. The other amine group will attack the other carbonyl group. At last, IBX will leave the complex and N-heteroacene is produced as the result.

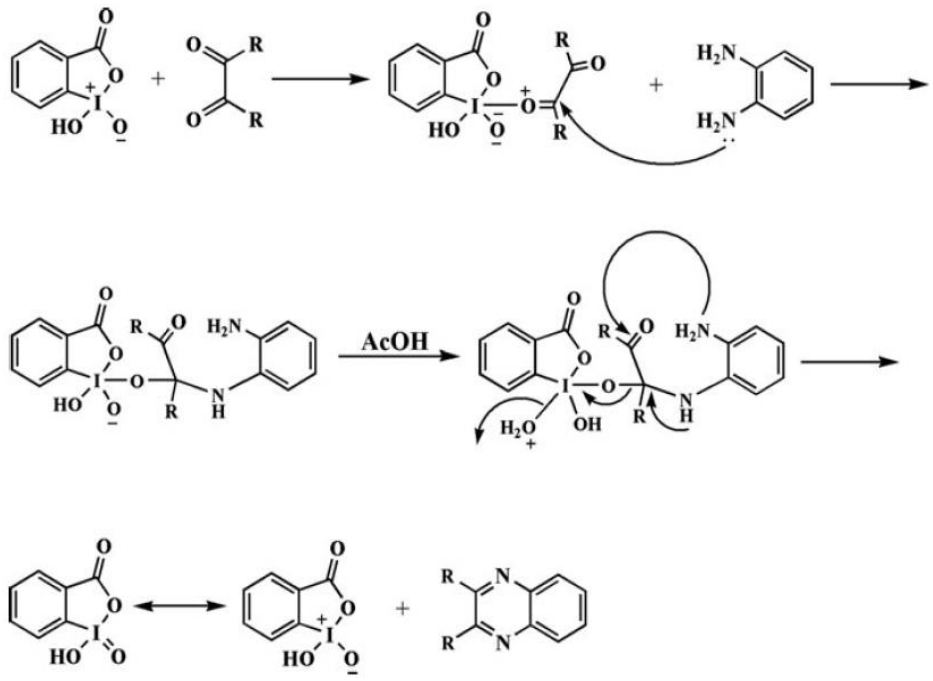

Scheme 3.3 A possible catalysis mechanism of IBX in the double Schiff base reaction

3.2.2 Buchwald-Hartwig reaction

Buchwald-Hartwig reaction is a palladium-catalyzed coupling reaction between amines and aryl halides in a base condition, forming a C-N bond as a result. The reaction equation is shown in scheme 3.4.

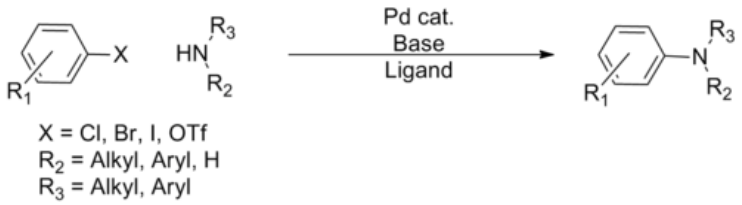

Scheme 3.4 Buchwald-Hartwig reaction equation

The reaction mechanism is shown in scheme 3.5.[2] Firstly, Pd^{II} catalyst (**1**) is reduced into Pd^{0} form (**2**), then one ligand leaves to form compound **3**, and re-enters into catalysis cycle. Subsequently, an oxidation addition reaction happens between aryl halides (**4**) and compound (**3**), producing intermediate compound **5**. Compound **5** can stay in a balance with its own dimer (**5b**). Afterwards, one halogen atom is replaced by one amine group, producing intermediate compound **7**, which will be further deprotonated by the strong base (**8**) and converts into compound **9**. Compound **9** can undergo two possible reactions: One is reductive elimination reaction, resulting in the desired aryl amines (**10**); the other one is β-hydrogen elimination reaction, resulting aromatics (**11**) and imines (**12**). In both reactions, Pd-L catalyst regenerates and enters into the next catalysis cycle.

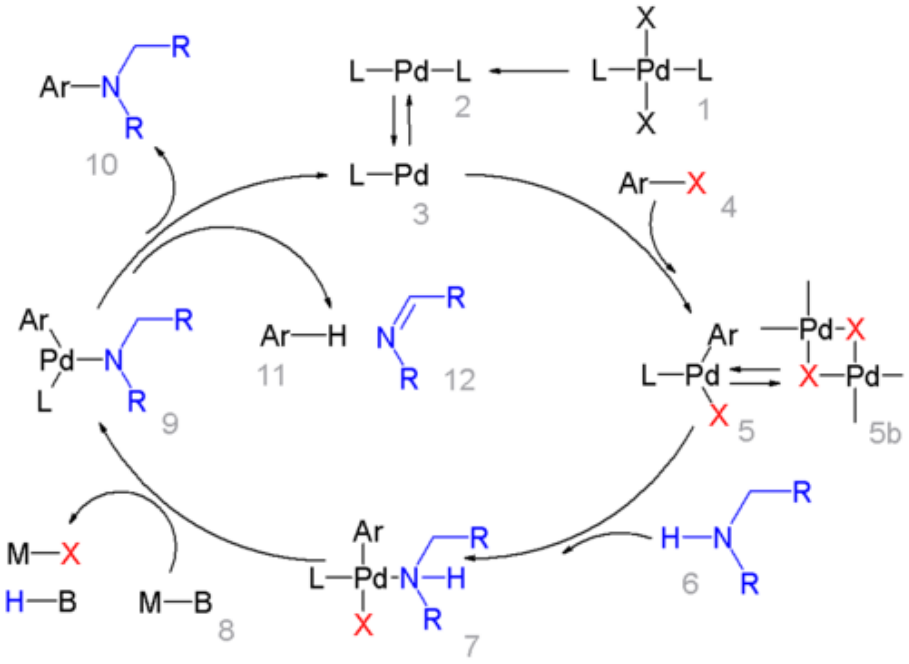

Scheme 3.5 Mechanism of Buchwald-Hartwig reaction

Based on Buchwald-Hartwig reaction, Bunz's group reported an effective method to synthesize N-heteroacene by using a double Buchwald-Hartwig reaction between *o*-diamine compounds and aryl-*o*-dihalides. The as-obtained N-heteroacene with NH units can be further oxidized into unsaturated form, the "true" N-heteroacene,[3] As shown in Scheme 3.6.

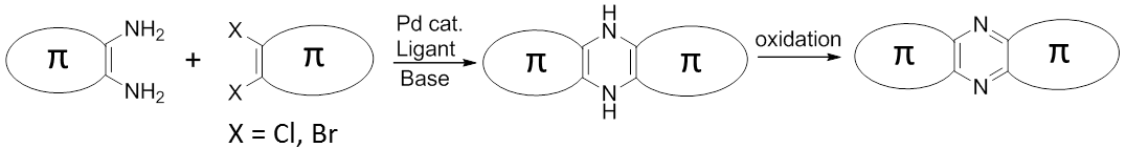

Scheme 3.6 Synthesis N-heteroacene through double Buchwald-Hartwig reaction

In this double Buchwald-Hartwig reaction, $Pd(dba)_2$ (Bis(dibenzylideneacetone)palladium(0)) is often used as the Pd catalyst, RuPhos (2-Dicyclohexylphosphino-2′,6′-diisopropoxybiphenyl) is often used as the ligand, and Hünig's base is used as the base. For some non-activated aryl-dihalides, RuPhos-Pd-G2 (Chloro(2-dicyclohexylphosphino-2′,6′-diisopropoxy-1,1′-biphenyl)[2-(2′-amino-1,1′-biphenyl)]palladium(II)) is used as Pd catalyst and ligand complex, and Cs_2CO_3 or NaO*t*Bu is used as the strong base. This improved double Buchwald-Hartwig reaction is an effective tool, and it has greatly enlarged the family of N-heteroacene.

3.2.3 LiAlH4 reduction reaction

$LiAlH_4$ (lithium aluminum hydride) is a composite hydride. It is an important strong reducing agent, because of the weak Al-H bond. It can reduce haloalkanes into alkanes, reduce silicon halides into silanes, reduce carbonyl compounds and epoxy compounds into alcohols, and reduce nitriles, oximes, nitro compounds, azides, amides and imides into amines.[4] $LiAlH_4$ explosively decomposes when meeting water, therefore it must be used in the dry condition. Diethyl ether and tetrahydrofuran (THF) are often used as the solvent in the $LiAlH_4$ reduction reaction, because of the high solubility of $LiAlH_4$ in these two solvents (25 ºC: diethyl ether: 5.92 mol/L; THF: 2.96 mol/L). $LiAlH_4$ is more stable in THF and that makes THF the better solvent for this reaction, [5] even though the solubility of THF is not as good as that of diethyl ether.

In this thesis, $LiAlH_4$ is mainly used to reduce benzothiadiazole compounds into *o*-diamine compounds, which is shown in scheme 3.7.

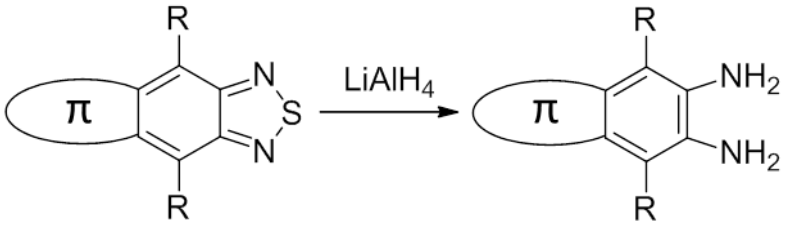

Scheme 3.7 Reducing benzothiadiazole compounds into *o*-diamine compounds by using $LiAlH_4$

3.2.4 MnO_2 oxidization reaction

MnO_2 (manganese dioxide) is a common oxidant in organic synthesis. It is stable black or brown solid depending on its different crystal forms. The brown one is more active. Water will affect the MnO_2 oxidization reaction. Hence, it is used in a dry solvent. In this thesis, MnO_2 is mainly used to oxidize NH units of N-heteroacenes into the unsaturated form, as shown in scheme 3.8.

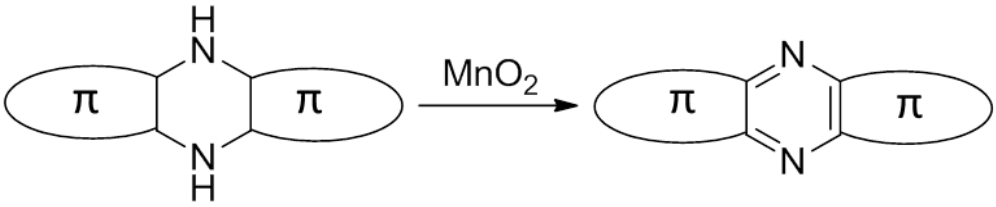

Scheme 3.8 Oxidizing NH units of N-heteroacene into unsaturated form by using MnO_2

3.3 Purification

3.3.1 Column chromatography

Column chromatography is a kind of low-cost preparative chromatography. It is the most common method to separate pure product from a mixture in organic chemistry. It can be used to separate products in varying scales from milligram to kilograms.

In a classic column chromatography experiment, as shown in Fig 3.1, an activated porous or powdered solid adsorbent with a large surface area is used as stationary phase and filled into the column. The column normally has a glass tube with a diameter of 5 mm to 50 mm, a height of 5 cm to 1 m, a faucet at the bottom to control the flow speed of eluent, degreasing cotton or glass fiber upon the faucet to prevent the stationary phase getting

through. Silica gel powder is the most common stationary phase used in the lab, and sometimes alumina powder is also used. The mixture which needs to be purified is placed on the top of the stationary phase. The mixture flows through the stationary phase with the eluent flowing down. The flowing down speeds of different compounds are different because of the different adsorption abilities. As a result, different compounds stay in the different area in the column. Due to the different flowing speeds, some compound will come out of the column first, and some will come out later. Subsequently, the solution of different compounds can be collected one after another. After removing the solvents, the pure compounds can be obtained.

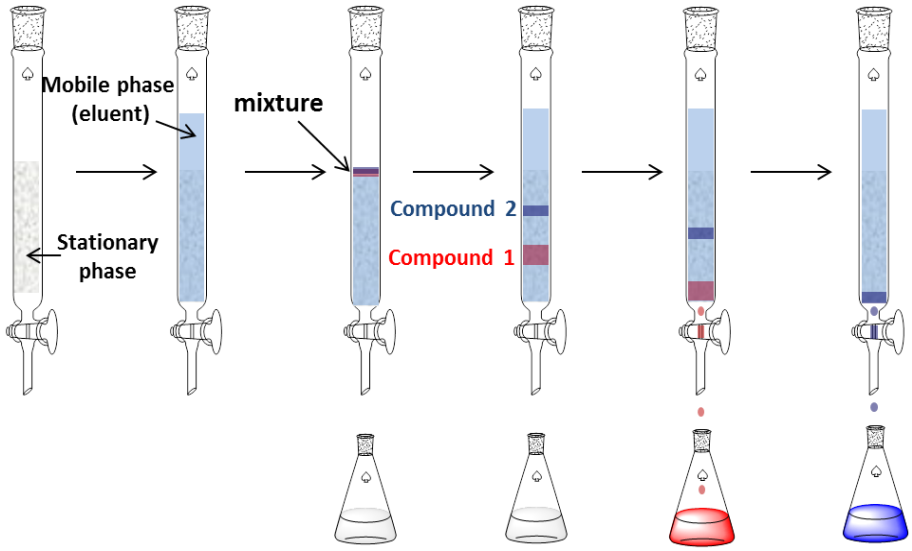

Fig 3.1 A classic column chromatography experiment

The adsorption ability is related to the activity of the stationary phase, the polarity of the eluent and the molecular polarity of the compound. The greater of the molecular polarity, the stronger of the adsorption ability is. The more of the polar groups contained, the bigger of the polar groups, the stronger of the adsorption ability is. Compounds containing the following groups, the adsorption ability of them are arranged: -Cl，-Br，-I < -C=C- < $-OCH_3$ < $-CO_2R$ < -CO- < -CHO < -SH < $-NH_2$ < -OH < -COOH.

The polarity of the eluent affects the flow speeds of compounds in the column. Choosing a suitable polarity of the eluent is the key of column chromatography. The eluent can be

one kind of solvent. However, in most conditions, it is a mixed solvent. The polar compounds are more easily to be washed down from the stationary phase by polar solvents, and the nonpolar compounds are more easily to be washed down by nonpolar solvents. To get the suitable ratio of the mix solvents, thin layer chromatography (TLC) is often used. Normally, the ratio of the solvents that offers the compound a retardation factor (R_f) of 0.2 to 0.3 is suitable for column chromatography.

3.3.2 Extraction

Extraction is a technique that separates the mixture by using different solubilities of the components in the solvent. Concretely, it is a method in which the solute substance is transferred from one solvent to another by taking advantage of the solubility or partition coefficient difference of the solute substance in these two immiscible or slightly soluble solvents. It is widely used in chemical, metallurgical, food and other industries. It is also commonly used in the oil refining industry. There are two kinds of extraction: liquid-liquid extraction liquid-solid extraction. In this thesis, extraction refers to liquid-liquid extraction.

The distribution law is the main theoretical basic of the extraction method. The substance has different solubility in different solvents. When a compound is added into two kinds of immiscible solvents, it can be dissolved in two solvents. At a certain temperature, the ratio of this compound in the two solvents or phase is a constant value, no matter how much of the compound added totally. Taking advantage of that, the vast majority of the compounds can are extracted, by repeating several times of the extraction operation.

Fig 3.2 shows the illustration of the extraction by using separating funnel. The two phases are firstly fully mixed by shaking the capped separating funnel, then stand for a moment till two phase totally separate. The organic phase can be judged staying on the top or in the bottom of the aqueous phase depending on its density. Subsequently, two phases are collected respectively. The organic compounds left in the aqueous phase can be washed out by repeating this extraction operation using additional organic solvent.

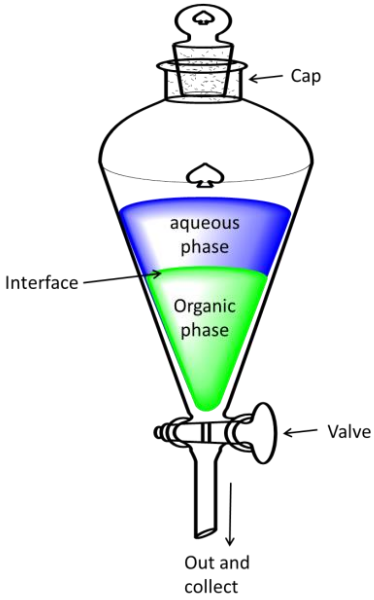

Fig 3.2 An extraction illustration by separating funnel

3.3.3 Recrystallization

Recrystallization is a process in which the compound is dissolved in the solvent or melted and then recrystallized from the solvent or melt. This process can purify or separate the samples.

Recrystallization can process in several ways including cooling the hot saturated solution, solvent diffusion and solvent evaporation.

The solubility of the solid compounds in the solvent is closely related to the temperature. The solubility is normally increased with the temperature. If a solution is saturated in high temperature, crystals will precipitate with the temperature slowly decreasing, because the solubility will decrease and then supersaturated solution forms. Different compounds have a different lattice structure. It has low possibility that two compounds with different lattice structures crystallize together. The compounds with the same lattice structure are more likely crystallize together. Taking advantage of the solubility difference, the substance needs to be purified can precipitate, meanwhile, the impurities stay in the solution. (The impurities also can be removed by filtrating from the saturated solution, if the solubility of the impurity is too low.) Hence the purification can be done.

Solvent diffusion is another common method for recrystallization. One substance has different solubility in different solvents. The solvent with high solubility is called good solvent; the solvent with low solubility is called poor solvent. Taking advantage of the solubility difference, crystals will precipitate leaving the impurities in the solution, when slowly adding (by dropping or diffusion) poor solvent into a saturated solution of good solvent, or adding a saturated solution of good solvent into a poor solvent, because of the decreasing solubility in the mixed solvent.

Solvent evaporation is a long time recrystallization method, and it is more often used to grow a high quality crystal. The compound needs to be purified is first dissolved in a volatile solvent in high concentration. With the solvent volatilizing, the solution will change into saturated, supersaturated, and then crystals precipitate. It is more likely to form a high quality big crystal, because of the low precipitating speed.

3.3.4 Filtration

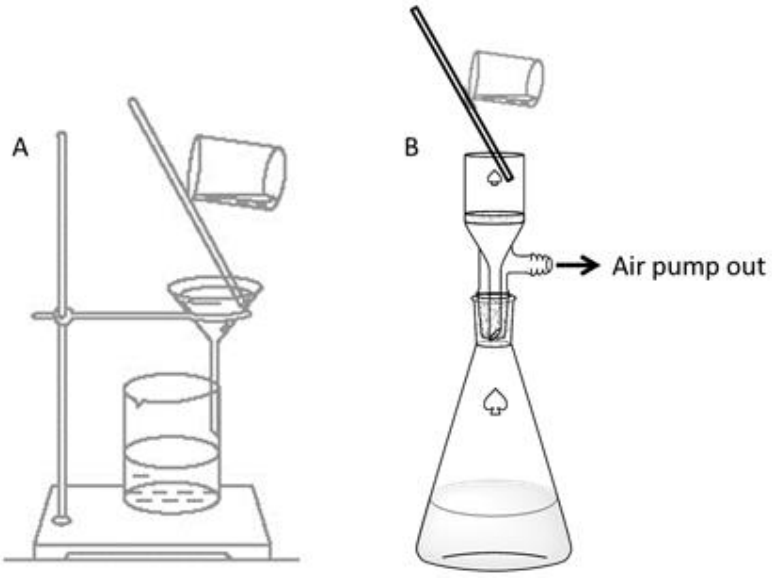

Fig 3.3 An illustration for filtration

In this thesis, filtration refers to a process in which the solid can be separated from the liquid. In this method, a porous media is necessary, to let the liquid pass through and block the solid. The filter paper is the most common porous media used in filtration, as

shown in Fig 3.3A. Sometimes a sand-core funnel is used for fast filtration by jointing with an air pump, as shown in Fig 3.3B.

3.4 Characterization

3.4.1 Nuclear Magnetic Resonance (NMR)

NMR is a technology applying nuclear magnetic resonance phenomena in analyzing molecular structure. It is one of the most important spectra in analyzing the structure of organic molecules. The study of NMR is mainly focused on studying nucleus of ^{1}H and^{13}C atoms.

When an isolated nucleus is in an external magnetic field with a certain intensity, the nucleus of the same atom is only sensitive to a radio-frequency field of a special frequency. When a nucleus is in a molecule structure, the real external magnetic field of the nucleus will change in a certain degree, caused by some factors like the distribution of electron clouds in the molecule. The influence of the nearby electron clouds and chemical bonds are different to the nuclei in different positions of the molecule structure. Hence intensities of the external magnetic fields are different. The special frequencies of the radio-frequency field, which the nuclei are sensitive with, are hence different. This will cause the difference in the signals of the NMR. These differences are the fundamental of analyzing molecular structure by using NMR. The situation of the nearby electron clouds and chemical bonds of the nucleus is called chemical environment. The shift in frequency position of NMR signals, caused by chemical environment, is called chemical shift. It is represented by the symbol "δ", and its unit is ppm. By analyzing the chemical shifts, the chemical environment information can be known; hence the molecular structure can be obtained.

J-coupling is another important factor offered from NMR besides chemical shift. J-coupling is caused by the interaction of the spin angular momentums between neighboring atoms, which will change the energy levels' distributions of the nuclei spins in the external magnetic field. That will cause the energy level splitting, resulting in a change in the signal peak shape in the NMR spectrum. The coupling between two

adjacent hydrogen nuclei follows a certain rule: n hydrogen nuclei split the signal peak of the adjacent nucleus into n + 1 multiple peaks, and the intensity relationship between the n + 1 multiple peaks follows Pascal's triangle rules. By analyzing the changing in the peak shape, the information of connection between the atoms in the molecular structure can be surmised.

The peak intensity is the third important information of the NMR spectrum. The nuclei with the same chemical environment show the same signal in the NMR spectrum. By analyzing the peak intensity, the quantity of the nucleus can be known, which is important to analyze the molecular structure. The signal peak intensity indicates the integration of the area under the curve of the peak. This information is particularly important for the ^{1}H NMR spectrum. The signal peak intensity is not so important for the ^{13}C NMR spectrum, because the correspondence between the peak intensity and the number of nuclei is not significant.

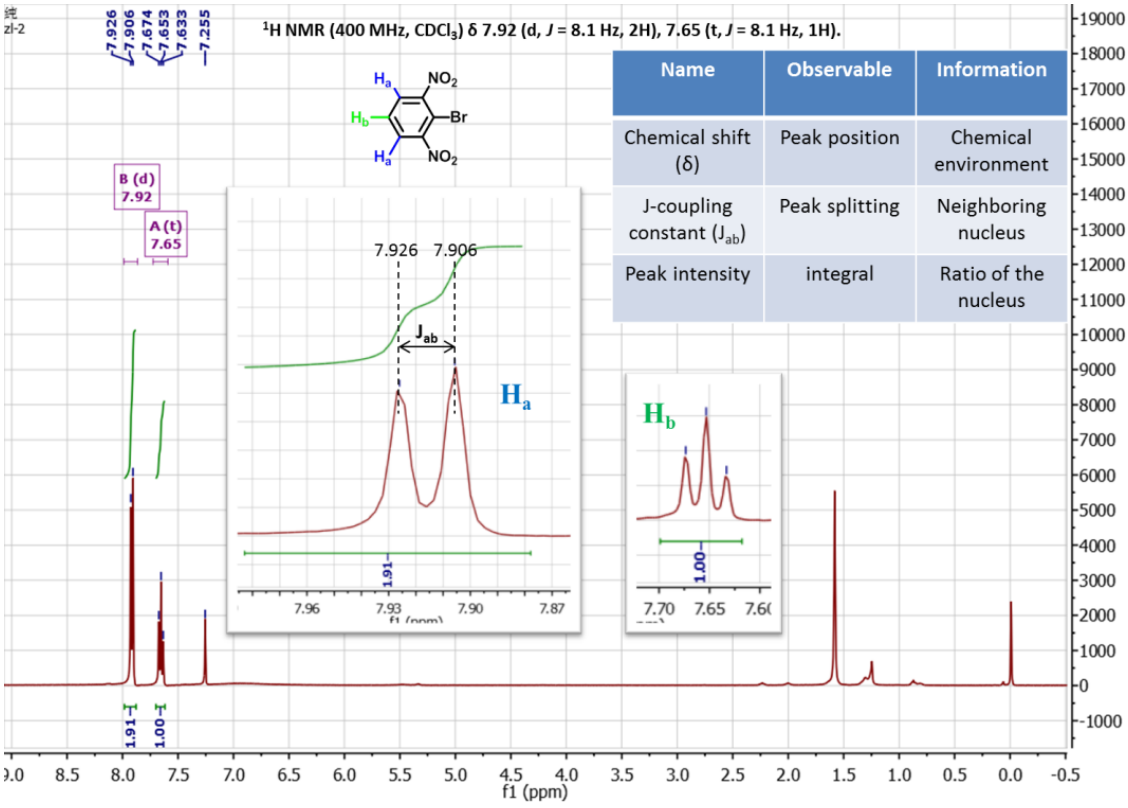

Fig 3.4 An example of ^{1}H NMR spectrum

Fig 3.4 shows a typical example of ^{1}H NMR spectrum. The chemical shift, J-coupling and peak intensity are marked in the Fig, and they are further introduced by analyzing this example. There are two kinds of hydrogen in this molecule: H_a and H_b. The chemical shifts are around 7.92 and 7.65, respectively. They have the same J-coupling constant of 8.1 Hz. The peak of H_a splits into double peaks, and the peak of H_b splits into triple peaks, according to the n + 1 rule. The ratio of the H_a : H_b is 2 : 1, according to the integration ratio of 1.91 : 1.00.

3.4.2 High-resolution mass spectrometry (HRMS)

Mass spectrometry is an analysis method of measuring the ratio of the molecule's mass to charge. It can be used to analyze the isotopic composition, organic molecular structure, elemental composition, etc.

The mass spectrometry is tested on a mass spectrometer. The components in the sample are ionized in the ionization device, and then positive charge ions with different charge/mass ratios generate. These positive charge ions are accelerated in the electric field, form ion beam, subsequently enter into the mass analyzer. Through filtering or the interaction of electric field and/or magnetic field, these ions with different charge/mass ratios separated in the mass analyzer in space or time. Finally, they are focused on the detectors respectively, resulting in the mass spectrum.

The HRMS is a special mass spectrometry with a high resolution of ppm or greater. It can be used to analyze the elemental composition of the compounds. It is especially useful to distinguish different compound with the similar molecular masses. For example: C_5H_4N and C_6H_6 have the same molecular mass of 78 in the normal mass spectrum and they cannot be distinguished. However, in HRMS, the calculated masses (M+1) are 79.0062 for C_5H_4N and 79.0470 for C_6H_6, which are very different. In the HRMS, if a mass of 79.0468 is found, it belongs to C_6H_6 (M+1) but not C_5H_4N.

3.4.3 Single crystal X-ray diffraction (SCXRD)

Single crystal X-ray diffraction is a technology to study the arrangement of the atoms in the single crystals by using X-ray. To be more accurate, the distribution of electron density in the crystal is firstly obtained by x-ray diffraction, and then the information of the atoms' locations and chemical bonds can be obtained by analyzing from that. Hence the crystal structure can be obtained. It can be regarded as a microscope of ultra-high resolution from which the atoms can be seen, as shown in Fig 3.5. Single crystal X-ray diffraction is the main method to study molecular structure at the atomic scale.

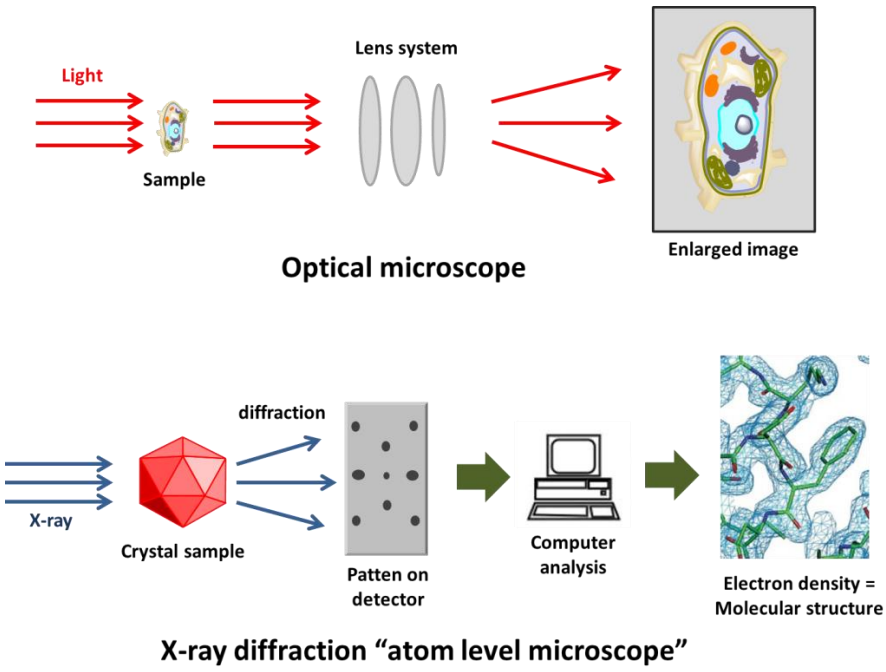

Fig 3.5 Single crystal X-ray diffraction compare with optical microscope

X-ray can be used to study the molecular structure of kinds of substances. It is because the wavelength of X-ray (0.001 to 10 nm) is comparable with the distance between the bonding atoms (around 0.1 to 0.2 nm), and all atoms have electronics. However, it is still impossible to image the molecules by using X-ray, because the lens that can focus X-ray is now not available, and the X-ray diffraction of a single molecule is rather weak and cannot be detected. In a single crystal, there are a huge number of atoms in the same direction; therefore the signal can be detected after piling up the X-ray diffraction of all

these atoms. In this sense, the single crystal is acting as an amplifier of the X-ray diffraction signal.

In a single-crystal X-ray diffraction measurement, when a beam of X-rays strikes a single crystal, the crystalline atoms cause a beam of incident X-rays to diffract into many specific directions. These beams make a diffraction pattern of spots on a piece of film or other detectors. Each spot is called a reflection, since it corresponds to the reflection of the X-rays from one set of evenly spaced planes within the crystal. As the crystal is gradually rotated, previous reflections disappear, and new ones appear; the intensity of every spot is recorded at every orientation of the crystal. Then these data are combined computationally with complementary chemical information. The two-dimensional images taken at different orientations are converted into a three-dimensional model of the density of electrons or the arrangement of atoms within the crystal. The refined model of the atomic arrangement is called the crystal structure.

3.4.4 Cyclic voltammetry (CV)

Cyclic voltammetry is a common electrochemistry study method. In CV test, a cycle potential is applied from a starting potential scanning to a terminal potential at a certain speed then scanning back to the starting point at the same speed as one cycle, and the current - potential curve is recorded. This CV curve can help determine at which potential the oxidation or reduction reaction will happen.

A three-electrode system is normally applied in CV, and they are the working electrode, the reference electrode and the counter electrode.

The working electrode normally employs gold or platinum disc electrode, glass carbon electrode, suspended mercury electrode, etc. The oxidation and reduction reactions happen at the surface of the working electrode.

The reference electrode has a stable potential regardless of the concentration of the solution to be tested. It is usually composed of a solid-phase pair, for example: Ag/AgCl electrode, and saturated calomel electrode. In CV measurement, the current through the

reference electrode is controlled to be zero, and the working electrode potential is measured by controlling the potential difference between the working electrode and the reference electrode.

The counter electrode is used to complete the current loop. The current flow through the working electrode and the counter electrode. The direction is determined by the reaction type of reduction or oxidation.

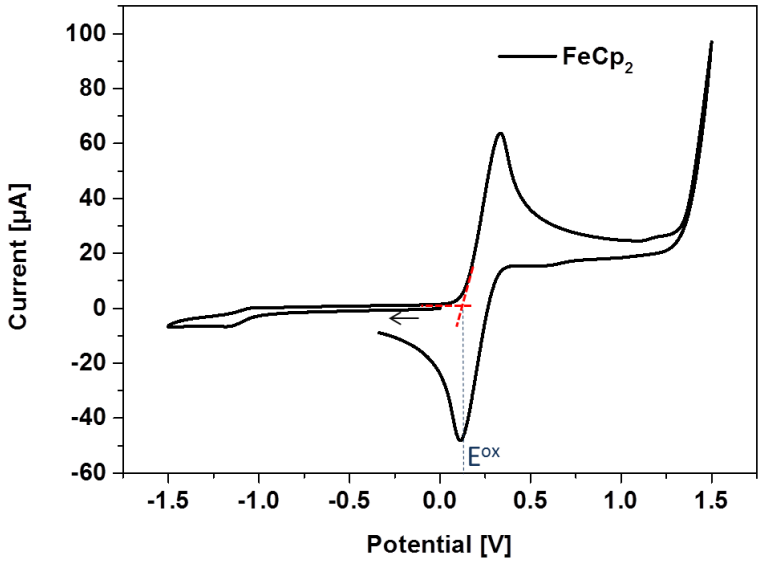

Fig 3.6 A typical CV curve

In this thesis, CV is applied to test the energy levels of the molecules. Fig 3.6 shows a typical CV curve as an example. When a positive potential is applied to the working electrode, the substance attached to the working electrode will lose its electron in the valence band, and the electrochemical oxidation reaction happens. When a higher positive potential is applied, the oxidation reaction will keep going on. The potential at which the oxidation reaction begins to happen is E^{ox}, and the HOMO energy level can be calculated from it. Similarly, when a negative potential is applied to the working electrode, the substance obtain electron on the conduction band, and the reduction reaction happens. The potential at which the reduction reaction begins to happen is E^{red}, and the LUMO energy level can be calculated from it.

3.4.5 Ultraviolet-Visible Spectroscopy (UV-Vis)

Ultraviolet-visible spectroscopy is a method to study the substance's absorption relative intensity of light, by irradiating the sample with the light source of continuous wavelength from ultraviolet to visible region (normally 200 – 800 nm). The absorption is caused by the valence electrons' transition. With different composition and molecular structure, every substance has its special characteristic energy levels, and the difference values between the energy levels are also different for different substances. The substance can only absorb the light with the similar energy as the difference values of substance's energy levels. Hence, the absorption is selective and the UV-Vis spectrum is characteristic.

In this thesis, UV-Vis is applied to measure the energy gap of the compounds. When a photon is absorbed, an electron will transfer from occupied orbital to unoccupied orbital. The energy of the photon must be similar with the energy gap between the orbitals of the electron transfer, as shown in Fig 3.7. The energy gap (E_g) between LUMO and HOMO can be calculated from the absorption edge, by using formula: $E_g = 1240/\lambda_{max}$, as shown in Fig 3.8.

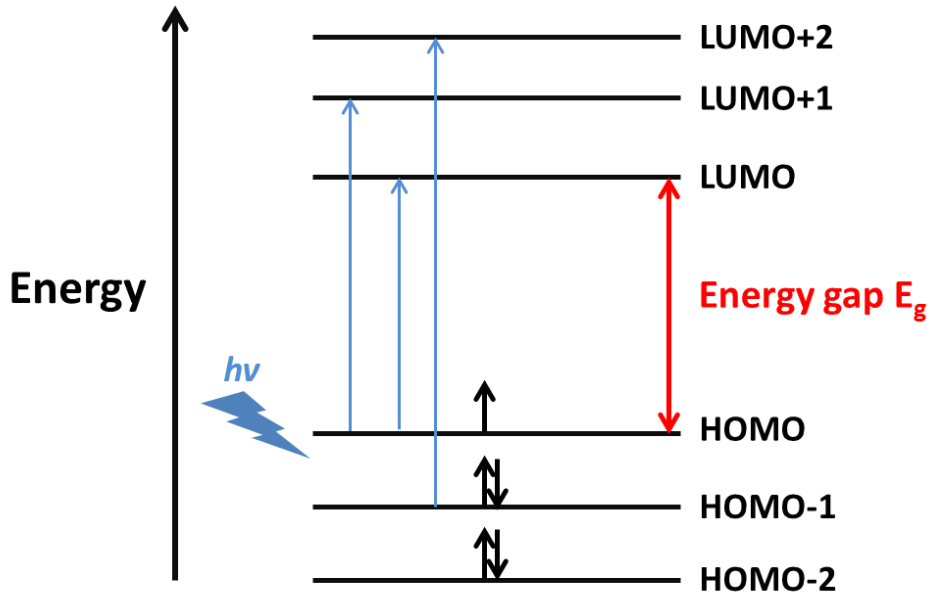

Fig 3.7 An energy levels diagram for UV-Vis spectroscopy

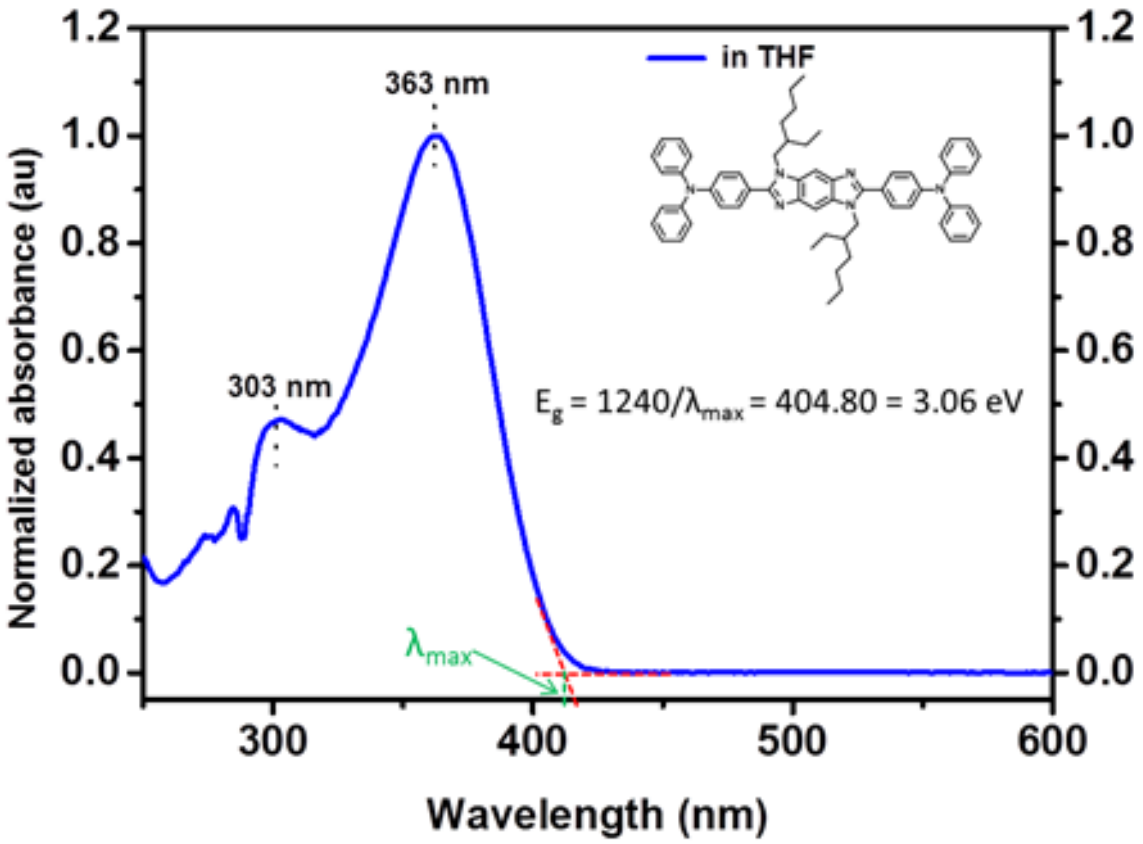

Fig 3.8 A typical UV-Vis spectrum

3.4.6 Fluorescence spectroscopy

What is fluorescence?

When a substance absorbs the energy of a short wavelength light, it transfers from ground state to excited state. When the substance transfers from excited state back to ground state, the energy of long wavelength light is emitted. The emitted long wavelength light is called fluorescence.

When substance transfers from excited state to ground state, the energy is lost in the form of heat or other forms. In some cases, the energy is lost by emitting photons. As shown in Fig 3.9.

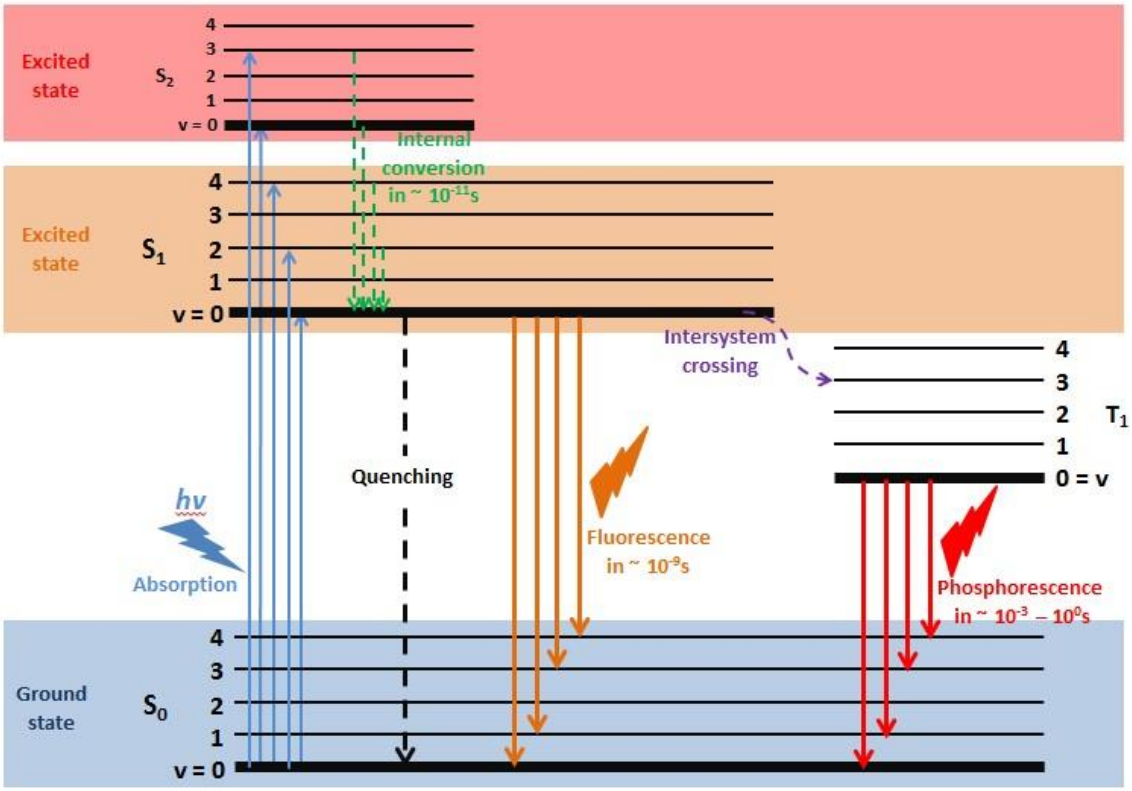

Fig 3.9 Energy levels and transitions in fluorescence spectroscopy

After absorbing energy, the excited molecule firstly transfers to the lowest vibration level (v_0) of S_1 by consuming energy through nonradiative processes. This process is called internal conversion, which happens in 10^{-11} second. Subsequently, the molecule transfers from v_0 of S_1 to ground state S_0 by emitting energy in the form of photons. This process is called fluorescence, which happens in 10^{-9} second. If the molecule transfers from v_0 of S_1 to S_0 by consuming energy through nonradiative processes, it is called quenching. If the molecule transfers from v_0 of S_1 to a metastable lower energy level – triplet along with the spin direction reversed of an electron, this process is called intersystem crossing. If the molecule transfers from v_0 of triplet to S_0 by emitting energy in the form of photons, it is called phosphorescence. Phosphorescence normally happens in 10^{-3} to several seconds, and its wavelength is longer than that of fluorescence.

Fluorescence is photoluminescence (PL). PL spectrum is a diagram shows the relationship between intensity and wavelength. There are two kinds of PL spectrum: excitation spectrum and emission spectrum.

In excitation spectrum, the substance is excited by the light with a changing wavelength, and the fluorescence intensity at a certain wavelength is recorded with that changing. The excitation spectrum shows the relative efficiency of the excitation light at different wavelengths.

In emission spectrum, the substance is excited by the light at a certain wavelength, and the fluorescence intensity at a different wavelength is recorded. The emission spectrum shows the relative intensity of the light at different wavelengths in the fluorescence.

In this thesis, PL spectrum refers to emission spectrum. Fig 3.10 shows a typical PL spectrum as an example.

Fluorescence quantum yield is one of the most basic parameters in the fluorescence measurement, which represents the fluorescence emitting ability of substance. Fluorescence quantum yields are usually expressed as φ, defined as the ratio of the photon number of substance emitted to the photon number of it absorbed, also known as fluorescence efficiency. φ = emitted photon number / absorbed photon number. The fluorescence efficiency is normally obtained by comparing with a standard reference substance.

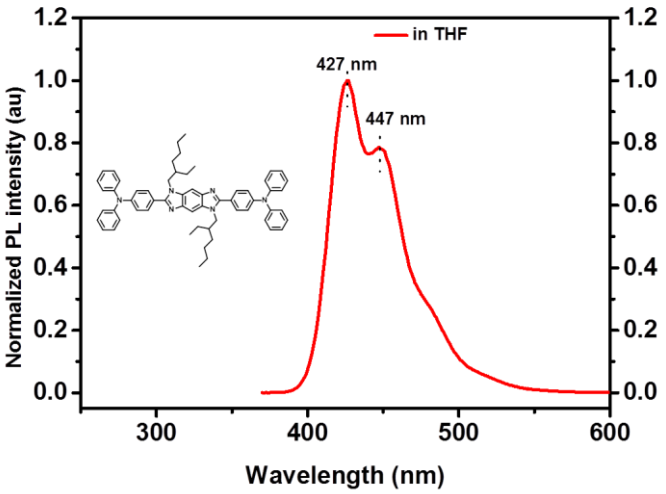

Fig 3.10 An example of PL spectrum

3.5 Material Test

3.5.1 Photoelectrochemical (PEC) cells and water splitting

Photocatalytic water splitting is a technology to directly decompose water into hydrogen fuel by using solar energy. It can convert light energy into chemical energy.

Semiconductors can serve as photocatalytic materials. To decompose water into hydrogen and oxygen, the semiconductors need to meet the thermodynamic requirements: the conduction band (LUMO for organic semiconductors) should be slightly positive than the hydrogen electrode potential (E_{H^+/H_2}), and the valence band (HOMO for organic semiconductors) should be slightly negative than oxygen electrode potential (E_{O_2/H_2O}). The principle of photocatalytic water splitting by PEC cell is shown in Fig 3.11[6]: If the energy of the light that radiating on the semiconductor is greater than or equivalent to the bandgap of the semiconductor, the electrons in the valence band in the semiconductor are excited and transfer to the conduction band leaving holes on the valence band. Subsequently, the electrons and holes separate and drift to different interfaces at where water is reduced into hydrogen gas and oxidized into oxygen, respectively.

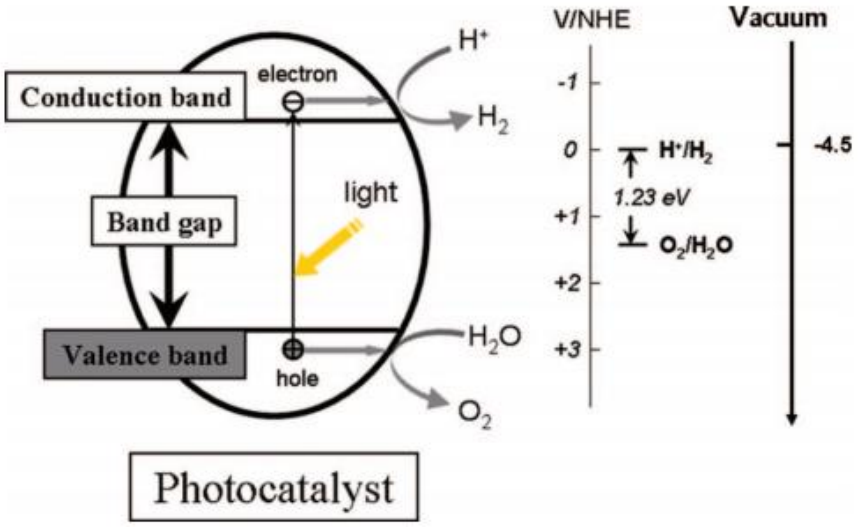

Fig 3.11. The principle of photocatalytic water splitting in PEC. Reproduced with permission from ref. 6. Copyright 2009 American Chemical Society.

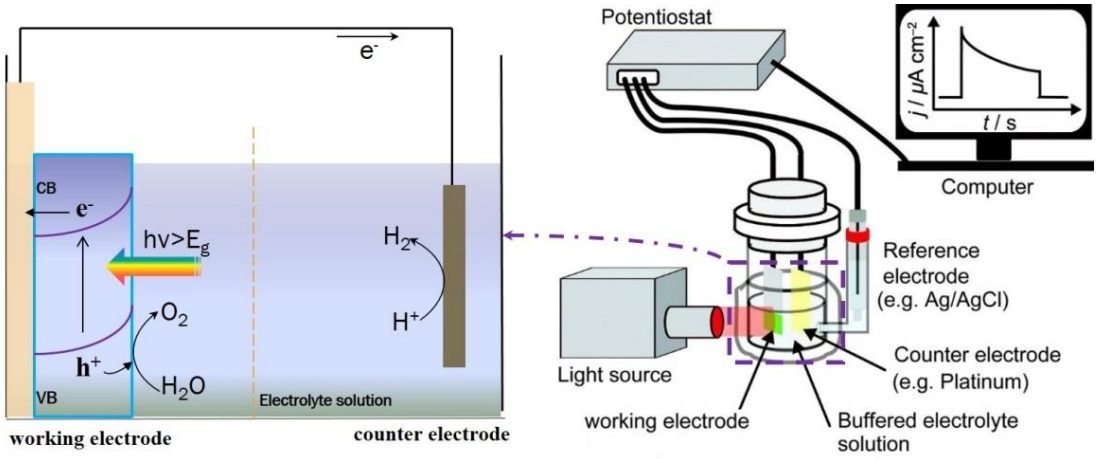

Fig 3.12 A diagram for typical PEC cell and the instruments. Reproduced with permission from ref. 7. Copyright 2014 Wiley-VCH Verlag GmbH & Co. KGaA.

In practical application, the material for water splitting in PEC should be with: high stability, no light corrosion, low cost; meeting the thermodynamic requirements and high sunlight absorption. There is one problem for organic semiconductors: the electrons and holes always recombined fast inside the semiconductor or at the interface. To reduce the recombination, a bias potential is normally applied. Fig 3.12 shows a typical PEC cell diagram and the instruments.[7]

Mott-Schottky plot. In this thesis, the Mott-Schottky plot measurement is used alone with the PEC cells test.

In semiconductor electrochemistry, a Mott-Schottky plot describes the reciprocal of the square of capacitance ($1/C^2$) versus the potential difference (V) between bulk semiconductor and bulk electrolyte. In many theories, and in many experimental measurements, the plot is linear. The use of Mott–Schottky plots to determine system properties (such as flatband potential, doping density or Helmholtz capacitance) is termed Mott–Schottky analysis. In this thesis, Mott-Schottky plot is used to estimate the type of the semiconductor and the flatband potential.

For p-type semiconductors, when the potential difference (V) between bulk semiconductor and bulk electrolyte goes positive, holes are induced in the semiconductors, the capacitance becomes higher, and the reciprocal of the square of capacitance ($1/C^2$) becomes smaller. So, the slope in Mott-Schottky plot for p-type semiconductor is negative.

For n-type semiconductors, when the potential difference (V) between bulk semiconductor and bulk electrolyte goes more negative, electrons are induced in the semiconductors, the capacitance becomes higher, and the reciprocal of the square of capacitance ($1/C^2$) becomes smaller. So, the slope in Mott-Schottky plot for n-type semiconductor is positive.

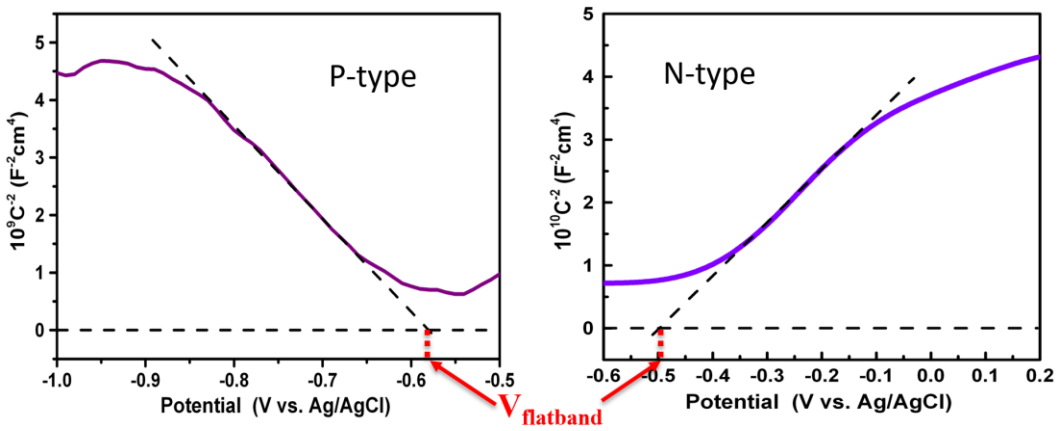

Fig 3.13 Examples of Mott-Schottky plot

The intercept of the slope of the linear region on the plot to the *x* axis provides the built-in potential, or the flatband potential (as here the surface barrier has been flattened) and allows establishing the semiconductor conduction band level with respect to the reference of potential.

3.5.2 Organic field effect transistor (OFET)

Organic field effect transistor is a kind of field effect transistor employing organic semiconductor as a signal channel. It is a kind of active device of which the current between source and drain can be regulated by adjusting the gate voltage. The OFET device is composed of three parts: an electrode (source, drain and gate), an organic semiconductor, and an insulator. There are several kinds of devices structure, and the most common one is shown in Fig 3.13. The gate electrode is placed at the bottom with source and drain electrodes on the top.

OFET can be regarded as a flat-plate capacitor formed by the gate and the semiconductor layer. For the n-type semiconductors, when a positive voltage is applied to the gate, negative carriers (electrons) will be induced and aggregate at the interface between insulator and semiconductor layer. With the gate voltage (V_g) increasing, the carriers can reach the source and drain electrodes, subsequently, electrons flow generating a current which means the OFET device is on "on" state. Similarly, for the p-type semiconductors, when a negative voltage is applied to the gate, positive carriers (holes) induced, subsequently, holes are transported. When V_g is zero, the current between source and drain electrode is very small, which means the device is on "off" state.

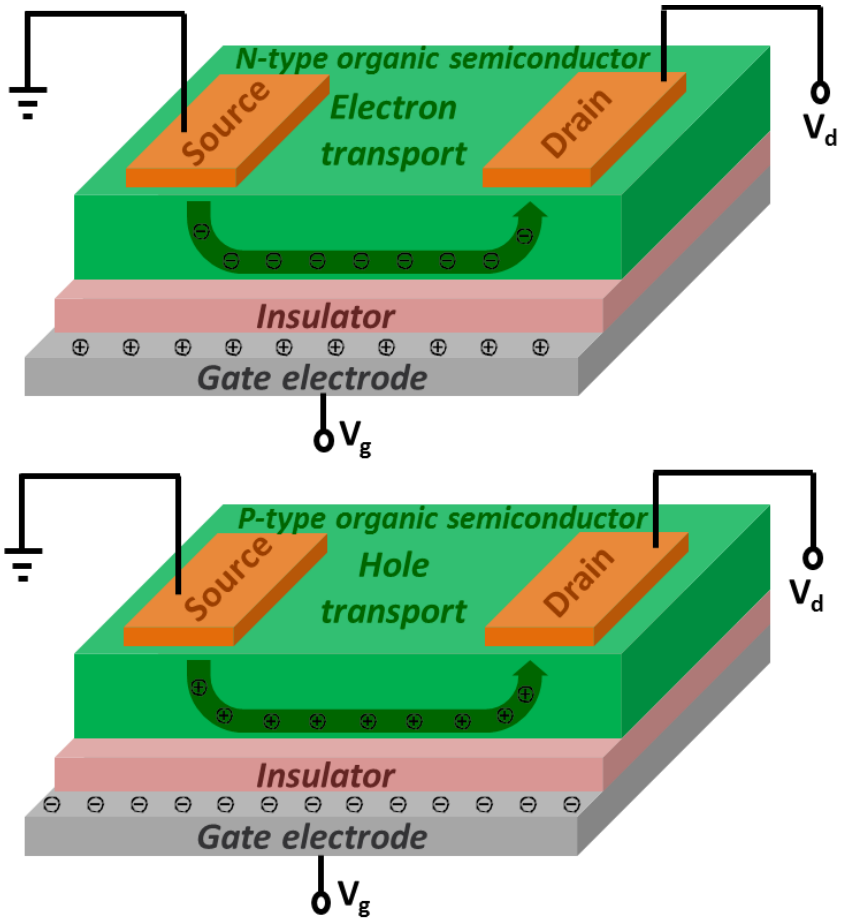

Fig 3.14 Device structure of OFET

The key parameters determining the performance of OFET are carrier mobility (μ) and switching ratio (on/off). Carrier mobility is: under the unit electric field, the distance of

the carriers drift in the unit time, and its unit is $cm^2 \cdot V^{-1} \cdot s^{-1}$. Switching (on/off) ratio refers to: in a certain gate voltage, the transistor's current ratio in the open state to off state. These two parameters determine the performance of the field effect transistor.

References

[1] Y. Wu, L. Lv, *Polycyclic Aromatic Compounds* **2016**, 1-8.

[2] J. Louie, J. F. Hartwig, *Tetrahedron Letters* **1995**, *36*, 3609-3612.

[3]U. H. F. Bunz, J. U. Engelhart, *Chemistry – A European Journal* **2016**, *22*, 4680-4689.

[4] G. Gerrans, P. Hartmann-Petersen, R. Hartmann-Petersen, *Sasol Encyclopaedia of Science and Technology*, New Africa Books, **2004**.

[5] V. I. Mikheeva, E. A. Troyanovskaya, *Bulletin of the Academy of Sciences of the USSR, Division of chemical science* **1971**, *20*, 2497-2500.

[6] X. Chen, S. Shen, L. Guo, S. S. Mao, *Chemical Reviews* **2010**, *110*, 6503-6570.

[7] X. Shi, L. Cai, M. Ma, X. Zheng, J. H. Park, *ChemSusChem* **2015**, *8*, 3192-3203.

Chapter 4*

Full Characterization and Photoelectrochemical Behaviors of Pyrene-fused Octaazadecacene and Tetraazaoctacene

Large azaacenes are very important because of the enormous potential in organic electronics. In this chapter, two stable pyrene-fused large azaacenes, octaazadecacene and tetraazaoctacene are successfully synthesized by employing relatively moderate aromatic unit pyrenes as embedded species in the backbone of azaacenes to ensure the large conjugation and stability. The photoelectrochemical (PEC) studies indicate that both azaacenes display n-type semiconductor behaviors.

*This section published substantially as reference: Z. Wang, J. Miao, G. Long, P. Gu, J. Li, N. Aratani, H. Yamada, B. Liu and Q. Zhang, *Chem. Asian. J.*, 2016, **11**, 482-485

4.1 Introduction

Developing novel n-type organic π-conjugated materials have attracted a lot of attentions in past decades. These compounds have shown several great advantages over inorganic semiconductors, including the low cost to process, flexibility, and variability of the properties.[1] Hence organic low-bandgap compounds have been considered to be next generation semiconductors.[2] Although great achievements in developing p-type organic semiconductors have been witnessed, the progress in searching high-performance n-type organic semiconductors has obviously fallen behind p-type ones.[3] Due to p-type and n-type materials have equal importance in organic electronic devices, developing well-performed n-type organic semiconductors is highly desirable.[4]

Azaacenes, derived from the well-known p-type semiconductors oligoacenes[5], have been proven to be a promising and efficient pathway to approach novel n-type organic materials.[6] Replacing CH moieties in the backbone of oligoacenes with N atoms can lower the LUMO level without changing the geometric structure, which benefits to the realization of air-stable electron transportation.[7] Clearly, large azaacenes are highly desirable, due to larger π-conjugated backbones in the longer azaacenes lead to a lower LUMO level and stronger π–π interactions. Hence, that is helpful to achieve air-stable and more efficient electron transport.[8] Although azapentacenes with no more than five nitrogen atoms are stable,[6c] larger azaacenes with more nitrogen atoms always show a poor stability owing to the sensitivity to moisture or oxygen, or the dimerization through Diels−Alder reaction (molecule I[9] in Scheme 4.1, for example).[10] Very recently, it was found that employing a moderate π-conjugated quinone bridge, which can offer additional Clar's sextets, could be an effective strategy to build up large π-conjugated backbones. Octaazanonacene-8,19-dione (**OANQ**) can be obtained through this strategy, as shown in scheme 4.1.[11] Inspired from this, it should be very interesting to prepare large azaacenes through employing a moderate aromatic pyrene bridge because: (1) pyrene can increase the conjugation length of as-designed molecules, which could benefit to the strong π-π interaction; (2) pyrene species might enhance the stability of as-prepared compounds because of the aromaticity nature of pyrene (cross-conjugation);[12] and (3) pyrene unit might provide more chances to modify the molecular structures and tune the

properties of as-prepared compounds.[13] Previously, some pyrene bridged large azaacene has been reported.[6e,13] These azaacenes were all built up by attaching small acene structures (three or less aromatic rings acenes structure) on the pyrene bridges. These molecules didn't show good charge transport property. So, larger acene structure is tried to be attached to the pyrene bridge in this chapter. The larger azaacene is supposed to show narrower band gap, lower molecular orbital energy levels, and better charge transfer property. In this chapter, two large pyrene-fused azaacenes (octaazadecacene (**OADA**) and tetraazaoctacene (**TAOA**)) are successfully synthesized and fully characterized. **OADA** has ten aromatic rings in a line and eight N atoms in the backbone. **TAOA** with eight aromatic rings in a line and four N atoms in the backbone. Both **OADA** and **TAOA** show very good stability, and they can be stored in air at least for months. This research suggests that employing a moderate aromatic building block could be an effective strategy to challenge large azaacene and develop n-type semiconductors.

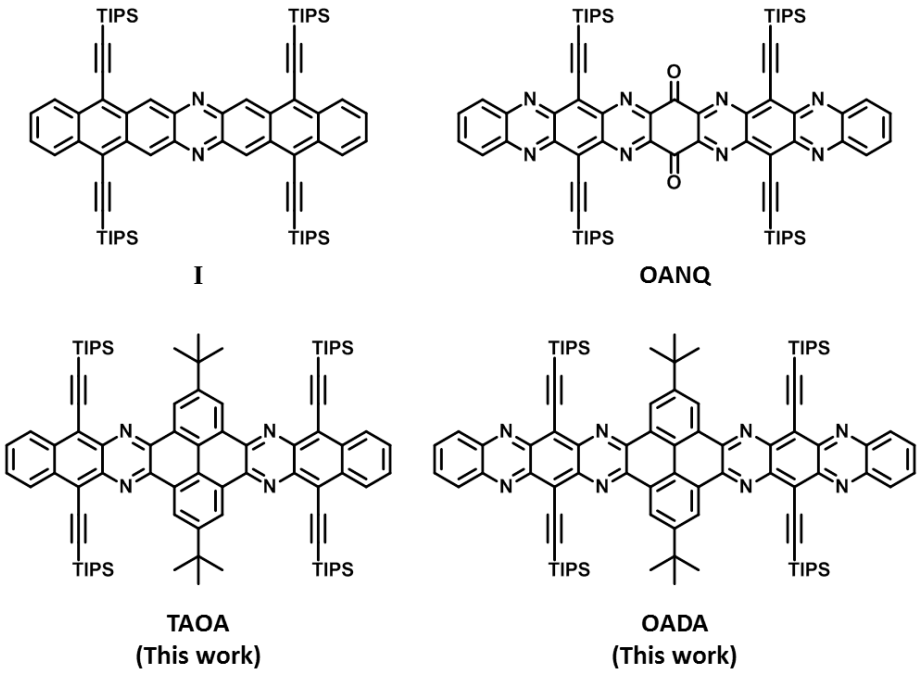

Scheme 4.1 Molecular structures of the large azaacene examples

4.2 Experimental Methods

4.2.1 Materials

All the chemicals and solvents are purchased and used without further treatment unless special note. Tetrahydrofuran (THF) was dried by refluxing with Na and indicated by benzophenones. Dichloromethane (DCM) was dried by refluxing with CaH_2 for 24 h.

4.2.2 Instruments and methods

Electrospray ionization high-resolution mass spectrum (HR-MS (ESI)) was recorded on a Waters Q-Tof premierTM mass spectrometer. ^{1}H-NMR and ^{13}C-NMR were tested on Bruker Advance 300 spectrometer and the chemical shift values were given in ppm. UV-vis absorbance was tested on a Shimadzu UV-2501 spectrophotometer. The geometry structures of the azaacenes were optimized by using DFT calculations (B3LYP/6-31G*),[14] The frequency analysis was followed to assure that the optimized structures were stable states. All calculations were carried out using *Gaussian 09*.[15]

Cyclic voltammetry was tested on a CHI 604E Electrochemical Analyzer. Glassy carbon (diameter: 1.6 mm; area 0.02 cm^2) was used as the working electrode, platinum wires were used as the counter electrode and the reference electrode, respectively. nBu_4NPF_6 (0.1M) was used as supporting electrolyte. Potential was recorded in an anhydrous DCM solution and the scanning rate was 50 mV/s. Fc^+ /Fc (HOMO = -4.80 eV) was used as an external standard.

4.2.3 Synthesis

Synthesis of 2,13-di-*tert*-butyl-5,10,16,21-tetrakis((triisopropylsilyl)ethynyl)dibenzo[*a*$_1$*b*$_1$,*jk*]-4,11,15,22-tetraazaoctacene (TAOA)

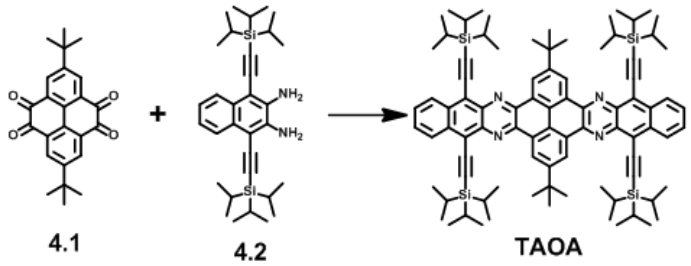

Compound **4.2** (114 mg, 0.22 mmol), compound **4.1** (37.4 mg, 0.1 mmol) and catalytic amount of 2-iodoxybenzoic acid (IBX) were dissolved in 20 mL AcOH in argon atmosphere. Subsequently, the mixture was stirred and refluxed for 24 h. After cooling to room temperature, the solvent was removed under reduced pressure. The residue was washed by MeOH (40 mL) and further purified by column chromatography on silica gel using mixture solvent eluent, Hexane/CH_2Cl_2 (4:1), to afford **TAOA** as orange solid (95 mg, yield 71%). ^{1}H-NMR (300 MHz, $CDCl_3$): 9.92 (s, 4H), 8.92 (dd, J = 6.7, 3.2 Hz, 4H), 7.73 (dd, J = 6.7, 3.2 Hz, 4H), 1.74 (s, 18H), 1.45 – 1.20 (m, 84H). ^{13}C-NMR (75 MHz, $CDCl_3$): δ = 151.17, 144.30, 139.83, 135.36, 129.63, 127.76, 126.91, 126.42, 120.71, 107.23, 103.10, 35.64, 31.76, 19.08, 11.77. HR-MS (ESI) *m/z* Calc. for $[M+H]^+$ $C_{88}H_{115}N_4Si_4$: 1339.8199, found : 1339.8198.

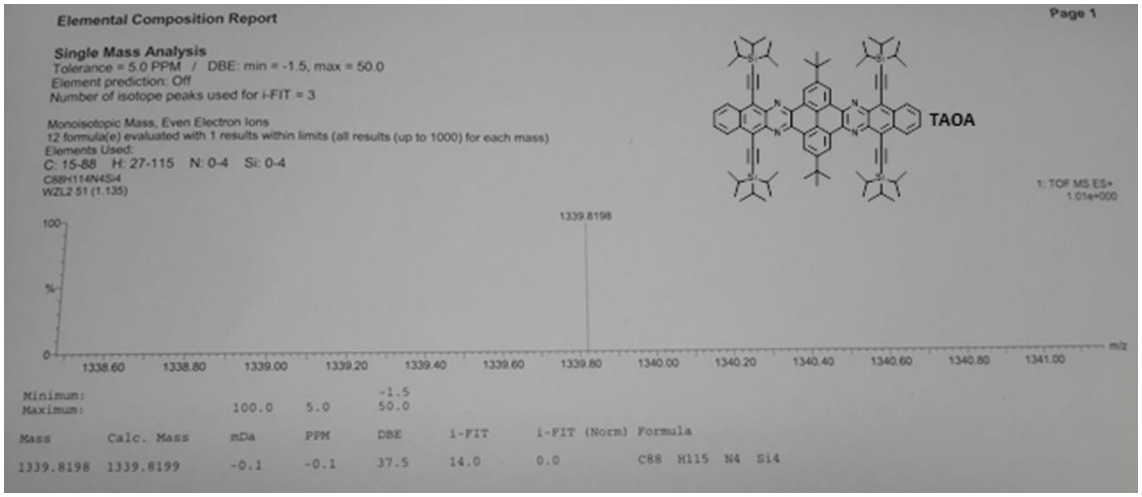

Fig 4.1 HR-MS(ESI) spectrum of **TAOA**

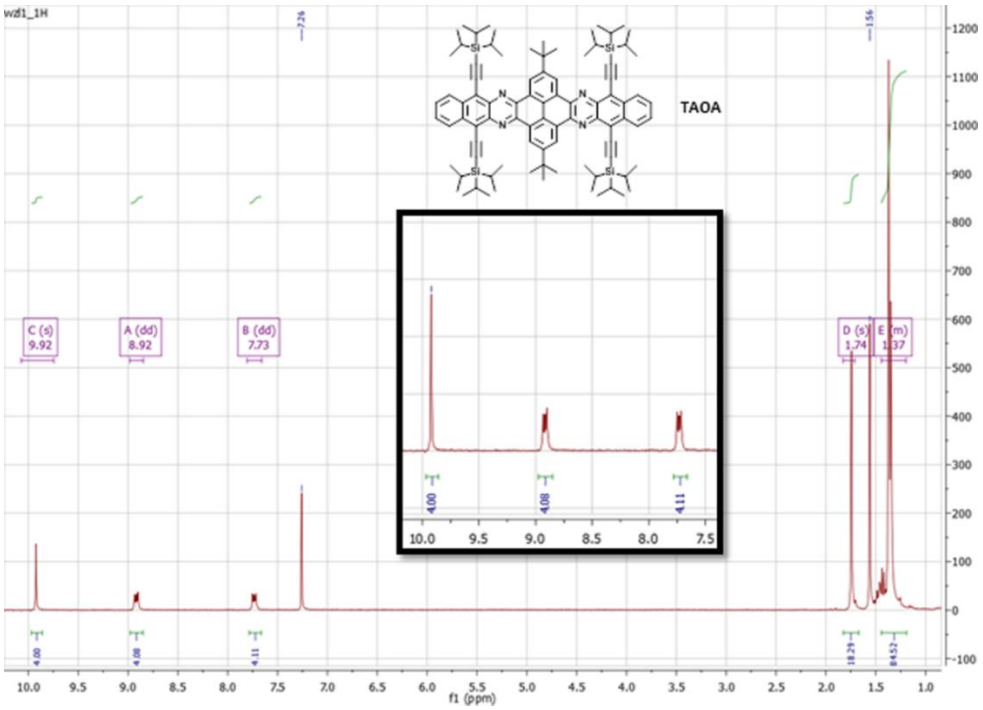

Fig 4.2 ^{1}H-NMR spectrum of **TAOA,** 300 MHz, $CDCl_3$, room temperature.

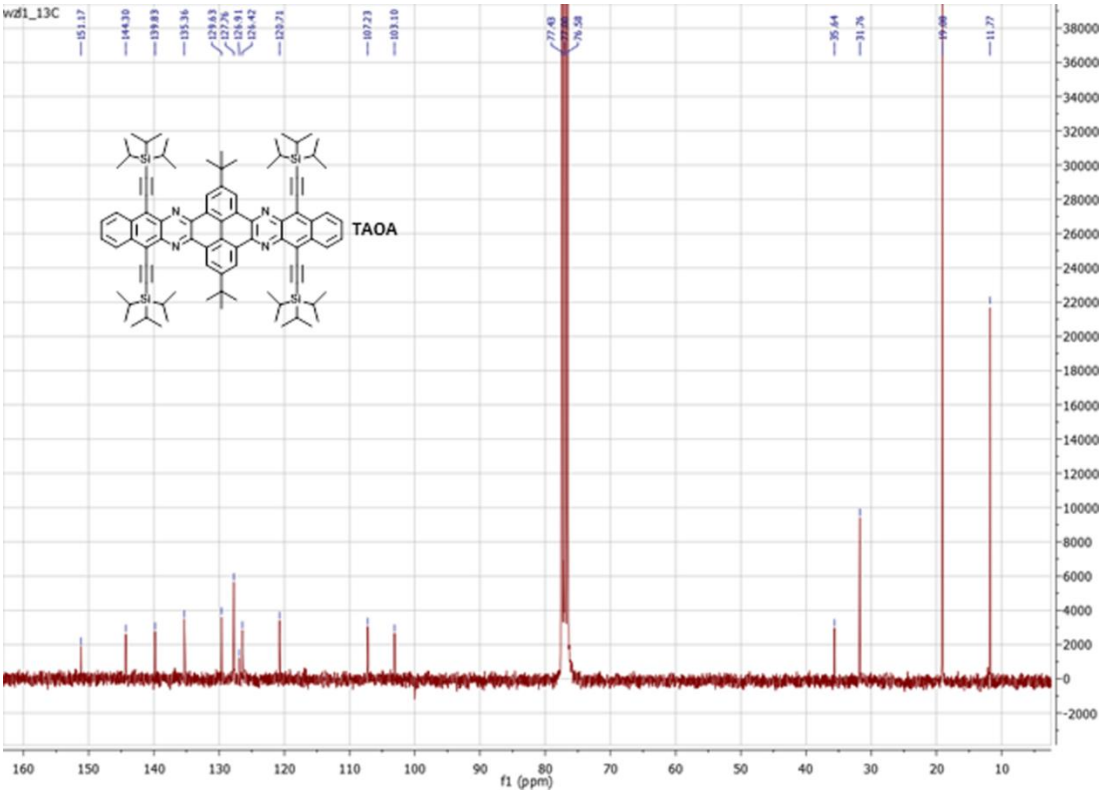

Fig 4.3 ^{13}C NMR spectrum of **TAOA**, 75 MHz, $CDCl_3$, room temperature.

Synthesis of 2,15-di-*tert*-butyl-5,12,18,25-tetrakis((triisopropylsilyl)ethynyl)dibenzo[*g*$_1$*h*$_1$,*lm*]-4,6,11,13,17,19,24,26-octaazadecacene (OADA)

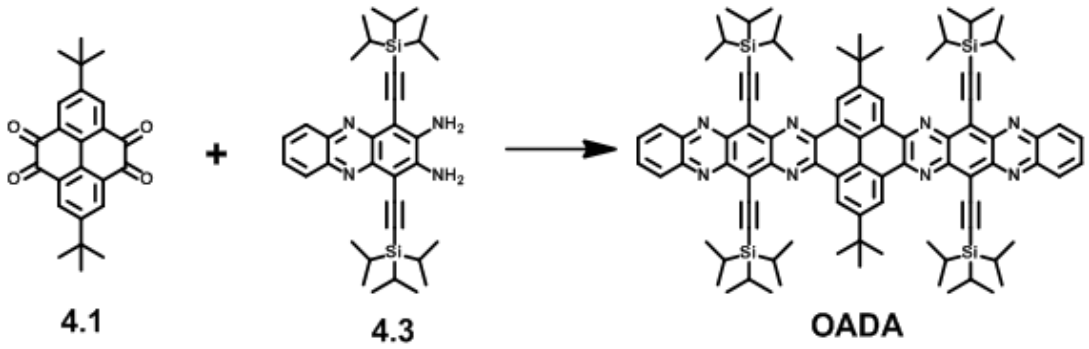

Similarly, compound **4.3** (126 mg, 0.22 mmol), compound **4.1** (37.4 mg, 0.1 mmol) and a catalytic amount of 2-iodoxybenzoic acid (IBX) were dissolved in 20 mL AcOH in argon atmosphere. Subsequently, the mixture was stirred and refluxed for 48 h. After cooling to room temperature, the solvent was removed under reduced pressure. The residue was washed with MeOH (40 mL) and further purified by column chromatography on silica gel using mixture solvent eluent, Hexane/CH_2Cl_2 (4:1).Then the crude product was dissolved in dry CH_2Cl_2 (10 mL) and stirred with an excess amount of activated MnO_2 (500 mg) at room temperature. Subsequently, MnO_2 and the solvent were removed by filtration and rotary evaporation. After recrystallizing from $CHCl_3$/Et_2O, **OADA** was obtained as dark purple solid with a blackish green luster (74 mg, yield 51%). ^{1}H-NMR (300 MHz, $CDCl_3$): δ = 9.97 (s, 4H), 8.32 (dd, J = 6.9, 3.4 Hz, 4H), 7.90 (dd, J = 6.9, 3.3 Hz, 4H), 1.76 (s, 18H), 1.45 (d, J = 3.9 Hz, 84H). ^{13}C NMR (75 MHz, $CDCl_3$) δ = 151.53, 145.16, 144.75, 143.27, 141.47, 131.48, 130.03, 129.26, 127.51, 127.30, 122.26, 111.06, 102.68, 35.44, 31.42, 18.92, 11.53. HR-MS (ESI) *m/z* Calc. for $[M+H]^+$ $C_{92}H_{115}N_8Si_4$: 1443.8322, found : 1443.8350.

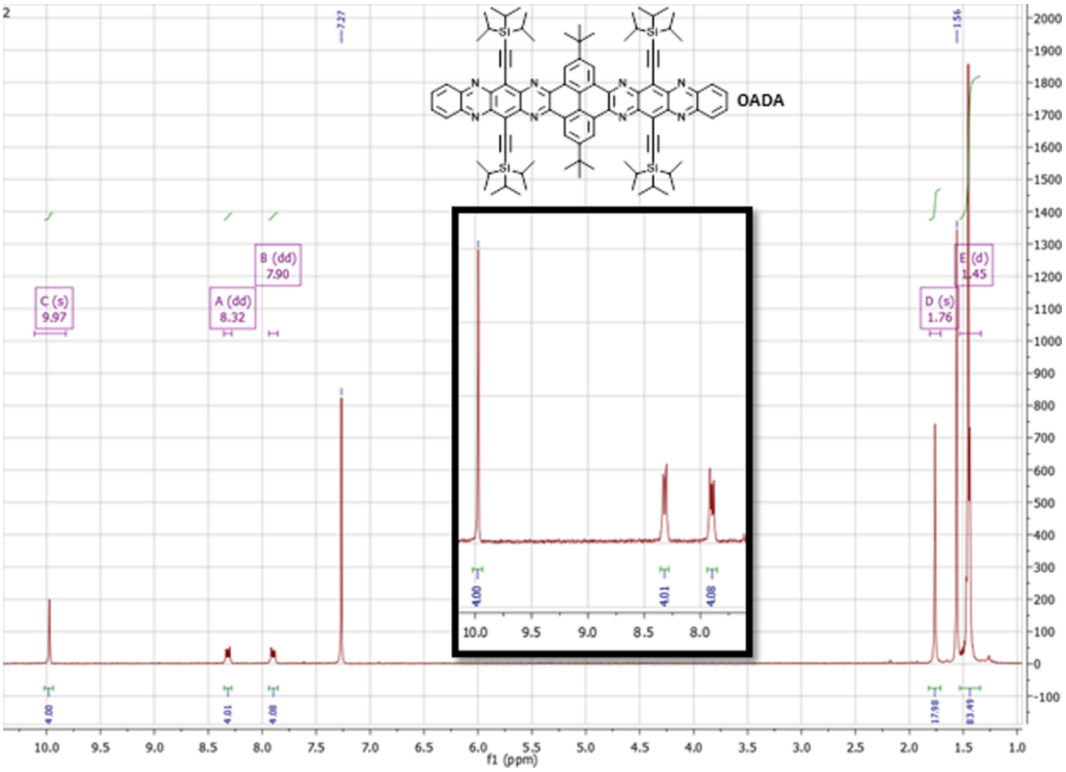

Fig 4.4 ^{1}H NMR spectrum of **OADA**, 300 MHz, $CDCl_3$, room temperature.

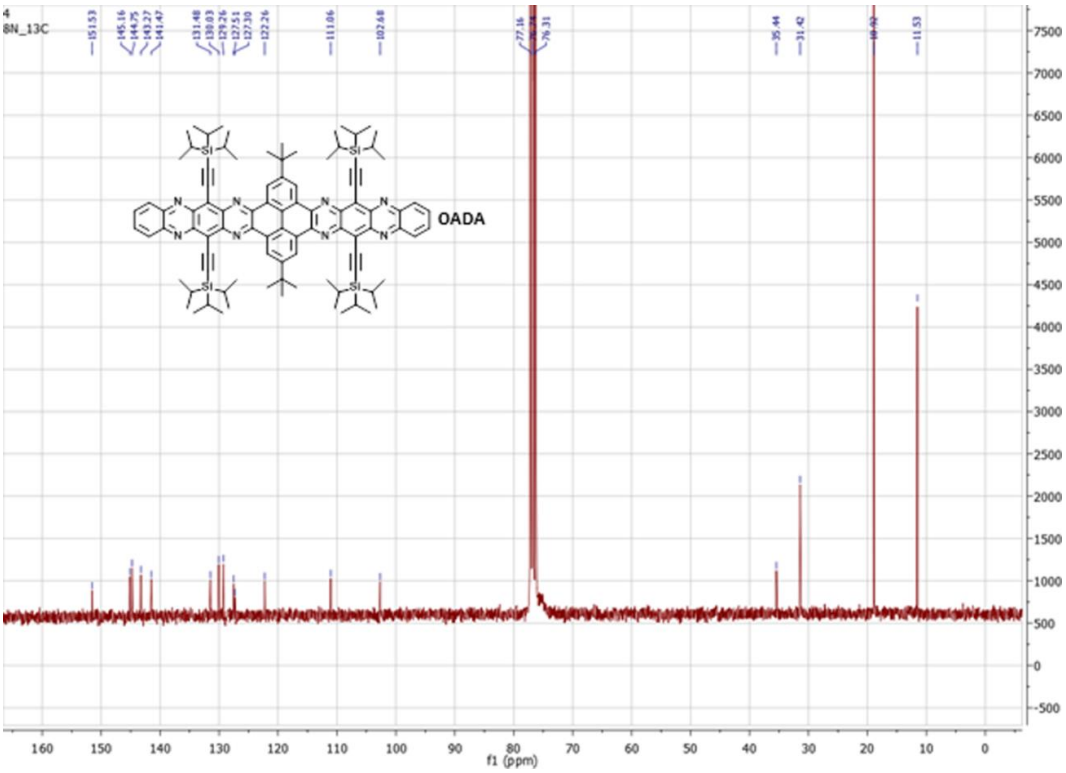

Fig 4.5 ^{13}C NMR spectrum of **OADA**, 75 MHz, $CDCl_3$, room temperature.

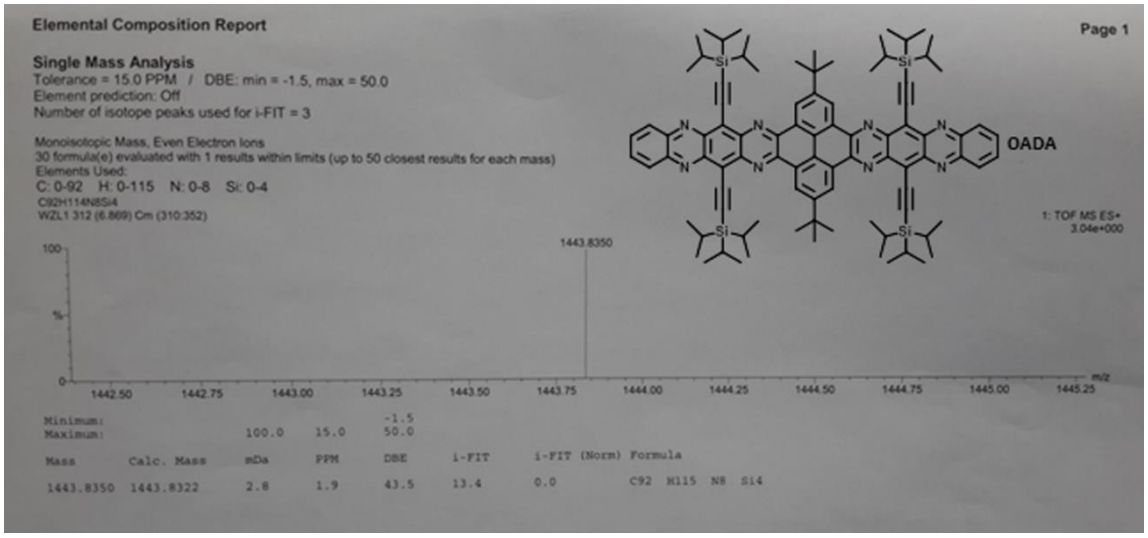

Fig 4.6 HR-MS(ESI) spectrum of **OADA**

4.2.4 Photoelectrochemical (PEC) measurements

4.2.4.1 Electrode Fabrication

To fabricate the electrodes, a well-dispersed 5 mg/mL suspension for each of the samples with pure ethanol as the solvent was prepared by brief sonication in a water bath. Fluorine-doped tin oxide (FTO) coated glasses (1.0 × 2.5 cm^2) were used as the substrate. The substrates were cleaned thoroughly by sonication in 5% detergent (Decon ® 90) for 30 minutes firstly and then rinsed with de-ionized water (DI water) for several times, which were followed by sonication in DI water for 15 minutes. The sonication in DI water process was repeated for three times. Before coating with samples, the FTO substrates were cleaned with UV-ozone plasma for 15 minutes to remove the organic residues. After that, 50 μL of different sample suspensions were dropped onto the surface of FTO substrates, which were masked using Ti foil with an effective area of 1.0 × 1.0 cm^2. The samples were first dried naturally in the dark to avoid the photochemical formation of phosgene, subsequently, placed in a 60˚C oven for 30 minutes.

4.2.4.2 PEC measurements

The PEC measurements were carried out in a 22.5 ml extrasil (ES) quartz cell filled with 0.5 M Na_2SO_4 aqueous solution (pH = 6.96), using an electrochemical workstation (CHI 760E). Prior to the measurement, the electrolyte was degassed by purging with argon continuously for 30 minutes. A 300 W xenon lamp (Newport) coupled to an AM 1.5 G filter was used as the standard light source. The surface illumination intensity of the photoelectrode was ~ 100 mW/cm^2, calibrated using a standard silicon photodiode. Three-electrode was set up with a platinum plate (1.0 × 2.0 cm^2) and a silver-silver chloride (Ag/AgCl, in 3 M KCl) as the counter and reference electrodes, respectively, to study the photovoltage response (illuminated open circuit potential) of the samples. Meanwhile, the photocurrent was carried out using a two-electrode set-up, in which the working electrode and the counter electrode were short-circuited.

4.2.4.3 Mott-Schottky measurement

The Mott-Schottky plots of different samples were generated using the impedance-potential technique. The capacitance of the semiconductor–electrolyte interface was collected at 1 kHz, with 10 mV AC voltage amplitude, in the same electrolyte (0.5 M Na_2SO_4, pH=7.2) and setup for PEC measurements. For estimating the flat-band potential of the samples, the measured voltage was converted into RHE scale by applying the following calculation:

$$V_{RHE}=V_{measured} + V^0_{Ag/AgCl} + 0.059 \times pH$$

Where V_{RHE} is the converted potential, $V_{measured}$ is the potential reading from potentiostat and $V^0_{Ag/AgCl}$ is the potential difference between Ag/AgCl reference electrode and a standard hydrogen electrode (SHE).

4.3 Principle outcomes

4.3.1 Synthetic route for TAOA and OADA

The synthetic route of **OADA** and **TAOA** is shown in Scheme 4.2. The pyrene-tetraone **1**[16] and the diamine building blocks **2**[17] and **3**[10a] can be prepared according to the literature. The tert-butyls and (triisopropylsilyl)-acetylene groups were employed to

ensure the reactions going well and to increase the solubility of the large azaacenes. Both **OADA** and **TAOA** can be obtained in good yields, (51% for **OADA** and 70% for **TAOA** respectively), through the double coupling reactions between the pyrene-tetraone compounds **4.1** and the diamine compounds **4.2** or **4.3**. **TAOA** can be obtained as orange powder directly after purified by chromatography on silica gel. while **OADA** needs further treatment by MnO_2 to afford dark purple powder. It indicates that **OADA** is more likely to pick proton and become into its N,N'-dihydrogenated analogue. This result suggests that **OADA** may have a lower LUMO energy level and it is more likely to be reduced. Both **OADA** and **TAOA** have been fully characterized by ^{1}H NMR, ^{13}C NMR, high-resolution mass spectroscopy (HRMS) and single-crystal X-ray diffraction analysis.

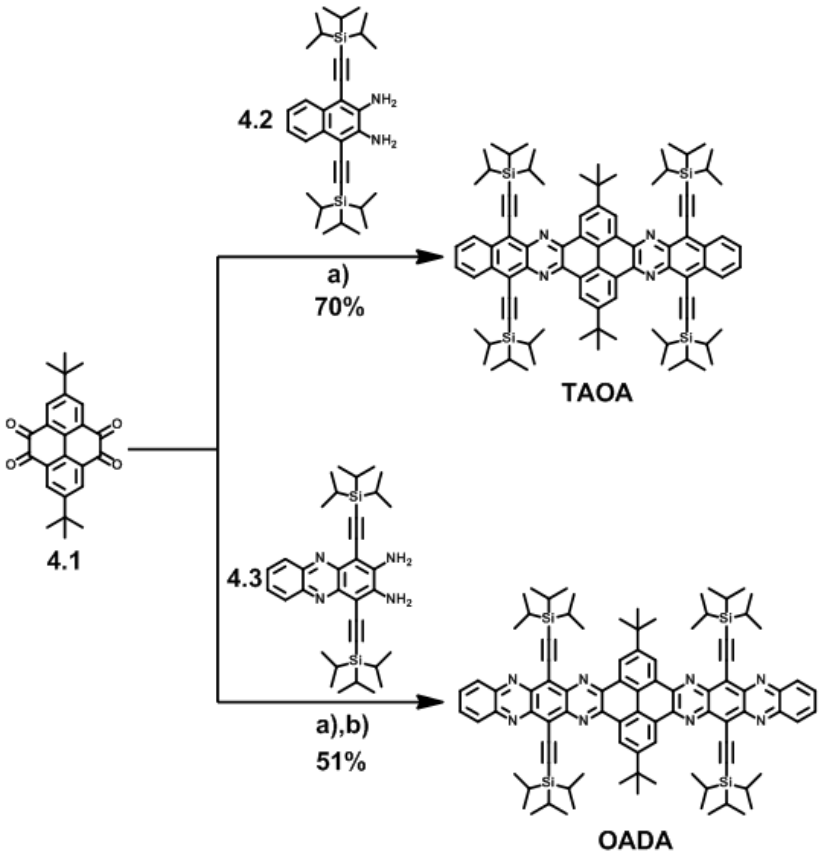

Scheme 4.2 Synthesis routes of **TAOA** and **OADA**. a) AcOH, IBX, reflux; b) MnO_2, CH_2Cl_2

4.3.2 Single-crystal X-ray diffraction analysis

The plate shaped single crystals of **TAOA** and **OADA** can be obtained through placing a toluene solution in a methanol atmosphere in about one week, and the as-obtained crystals are good enough for the single crystal X-ray diffraction analysis.

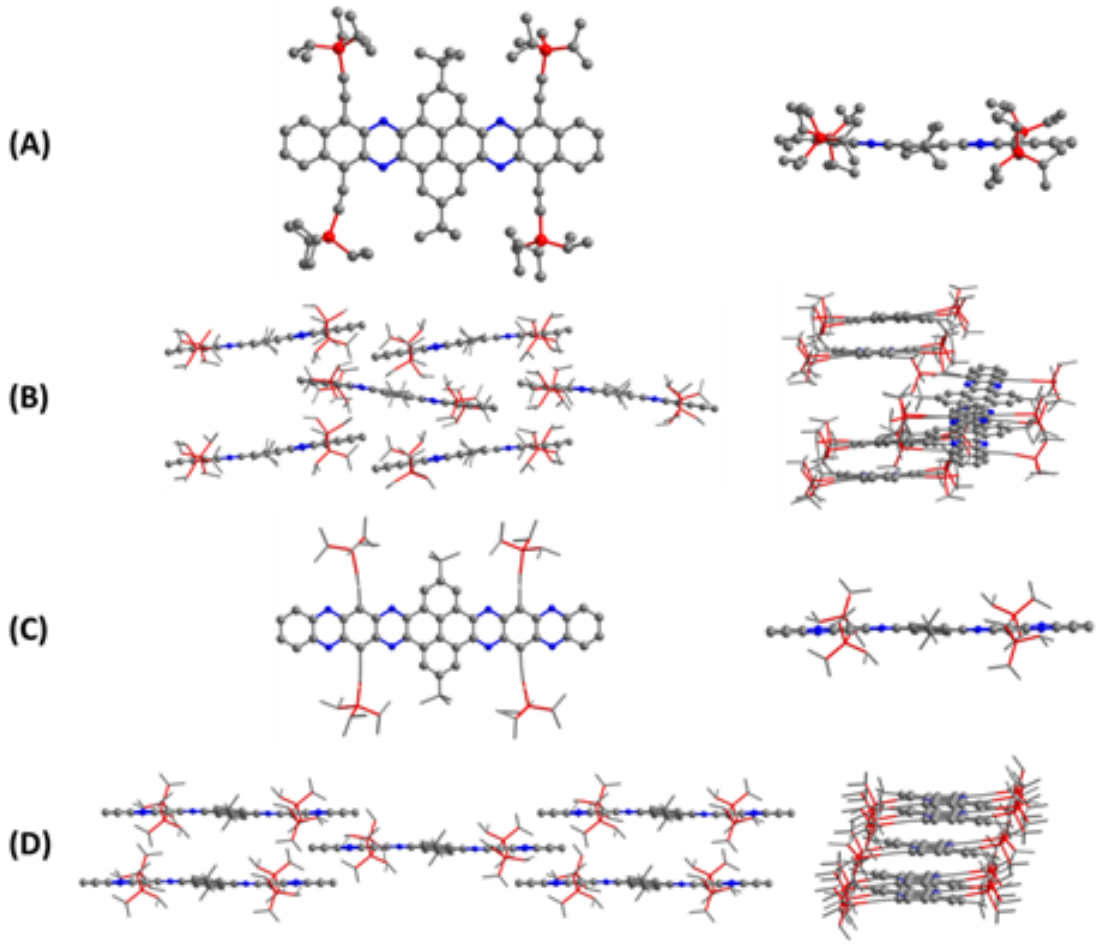

Fig 4.7 Single-crystal structures of A) **TAOA** and C) **OADA** (left: top view, right: side view). Molecular stacking structures of B) **TAOA** and D) **OADA** (left: side view perpendicular to long axis of the azaacene core; right: side view along the long axis of the azaacene core)

The single crystal of **TAOA** belongs to the monoclinic system (*P* 21/c space group) with a big unit cell (V = 11947(4) Å^3). The SCXRD analysis clearly confirmed that **TAOA** possesses eight aromatic rings linearly annulated in a row (Fig 4.7a).

The single crystal of **OADA** belongs to the triclinic system ($P\bar{1}$ space group) with a big unit cell (V = 2366.6(7) Å^3). The SCXRD analysis clearly confirmed that **OADA** possesses ten aromatic rings linearly annulated in a row (Fig 4.7c).

The molecular structures and stacking patterns are shown in Fig 4.7. All hydrogen atoms and solvent molecules are hidden for clarification. Both **TAOA** and **OADA** show planar backbones. However, the stacking patterns are very different. The π-π stacking of **TAOA** is totally destroyed by the steric hindrance of the four TIPS groups. The C-H···π

interaction between TIPS groups and the azaacene conjugation backbone is the main force to stabilize the packing structure of **TAOA**. The similar result has been reported in other azaacene systems.[18] With a longer π-conjugated backbone, **OADA** molecules adopt a face-to-face two-dimensional (2D) "bricklayer" arrangement. The short distances of the conjugation planes ranging from 3.27 Å to 3.23 Å suggest the existence of strong π-π interactions, which are the main force to stabilize the packing of **OADA**. In addition, the interactions between solvent molecules and **OADA** also make a contribution to stabilizing the packing. The packing patterns of **OADA** with solvent molecules (toluene or chloroform) are shown in Fig 4.8.

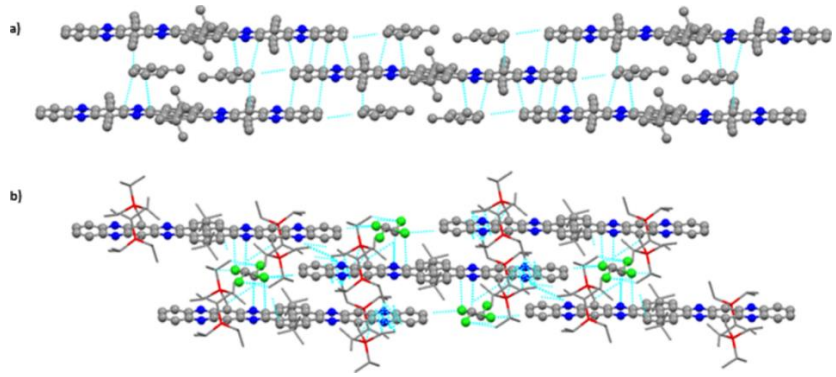

Fig 4.8 Molecular stacking patterns of **OADA** with solvent molecules: a) toluene, TIPS groups are hidden; and b) chloroform. The short contacts are shown as dashed lines. All hydrogen atoms are hidden

4.3.3 Photophysical and electrochemical properties and energy levels

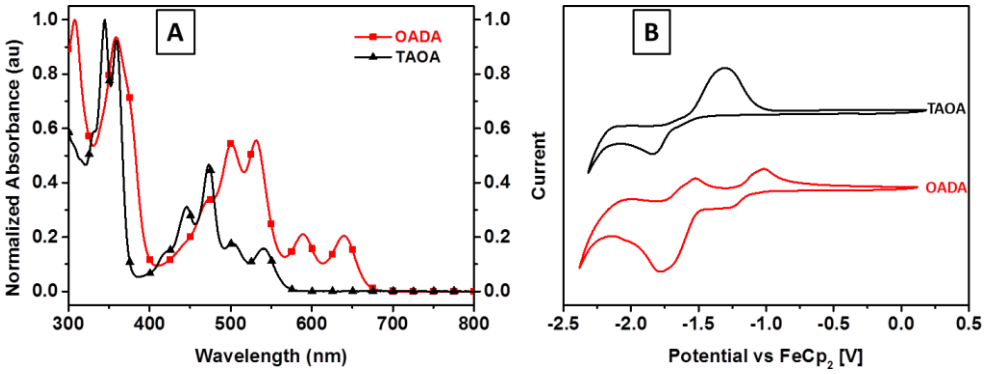

Fig 4.9 A) UV/Vis absorption spectra of OADA and TAOA in CH_2Cl_2. B) CV curves of OADA and TAOA in CH_2Cl_2/0.1M nBu_4NPF_6. (Externally referenced against ferrocene/ferrocenium)

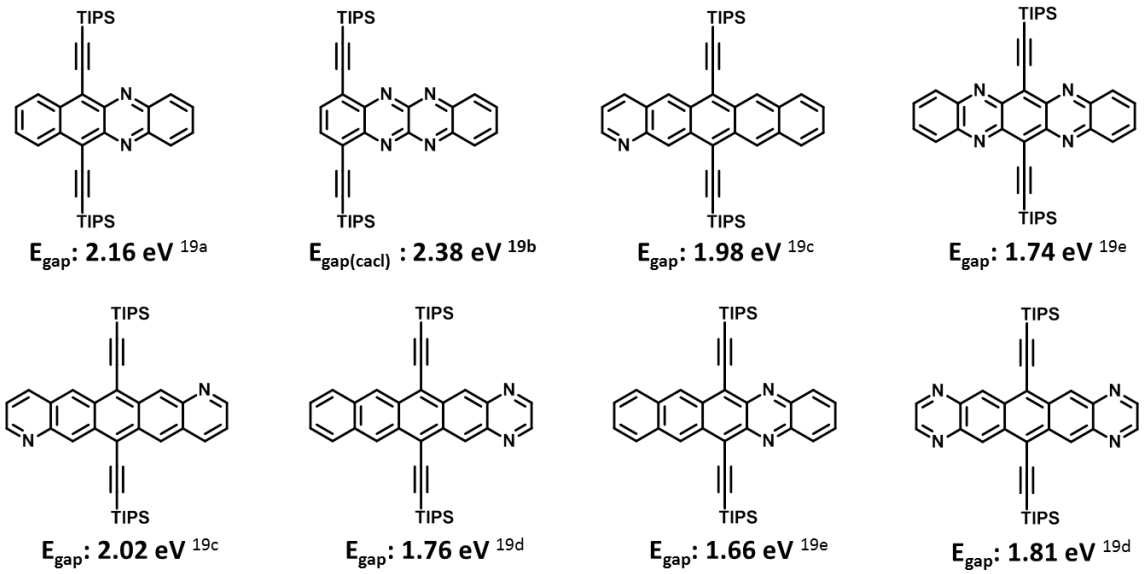

Fig 4.10 Reported TIPS-azatetracenes and TIPS-azapentacenes and the bandgap energies[19]

The normalized UV-vis absorption spectra of **OADA** and **TAOA** in CH_2Cl_2 are shown in Fig 4.9. **TAOA** shows four absorption peaks between 400 nm and 600 nm and the onset absorption (λ_{onset}) at 566 nm suggests that the optical band gap is 2.19 eV. Similarly, **OADA** shows four absorption peaks between 400 nm and 700 nm and the λ_{onset} at 667 nm suggests a narrow optical band gap of 1.86 eV. It is worth noting that, **TAOA** has a similar band gap with the reported TIPS-azatetracenes (2.16 eV ~ 2.38 eV, See Fig 4.10) and the band gap of **OADA** is similar with that of the reported TIPS-azapentacenes (1.66 eV ~ 2.02eV, See Fig 4.10). This suggests that the molecular orbital energy levels of **TAOA** and **OADA** are more like azatetracenes and azapentacenes, respectively, and the aromaticity of the whole conjugation backbones are interrupted by the relatively moderate aromatic unit pyrenes. To further confirm this, the nucleus-independent chemical shift (NICS) calculations were performed in the following part.

To gain more insight of the electronic and optical properties of these two pyrene-fused octaazadecacene and tetraazaoctacene derivatives, the geometry structure of **OADA** and **TAOA** were optimized by using DFT calculations (B3LYP/6-31G*)[20]. The frequency analysis was followed to ensure that the optimized structures were stable states. The electron density distributions of **OADA** and **TAOA** are illustrated in Fig 4.11. Both **OADA** and **TAOA** have similar HOMO and LUMO electron distributions due to the

same pyrene core. The HOMO and LUMO electron density mainly delocalized on the two azatetracenes parts for **TAOA** and azapentacenes parts for **OADA**, respectively.

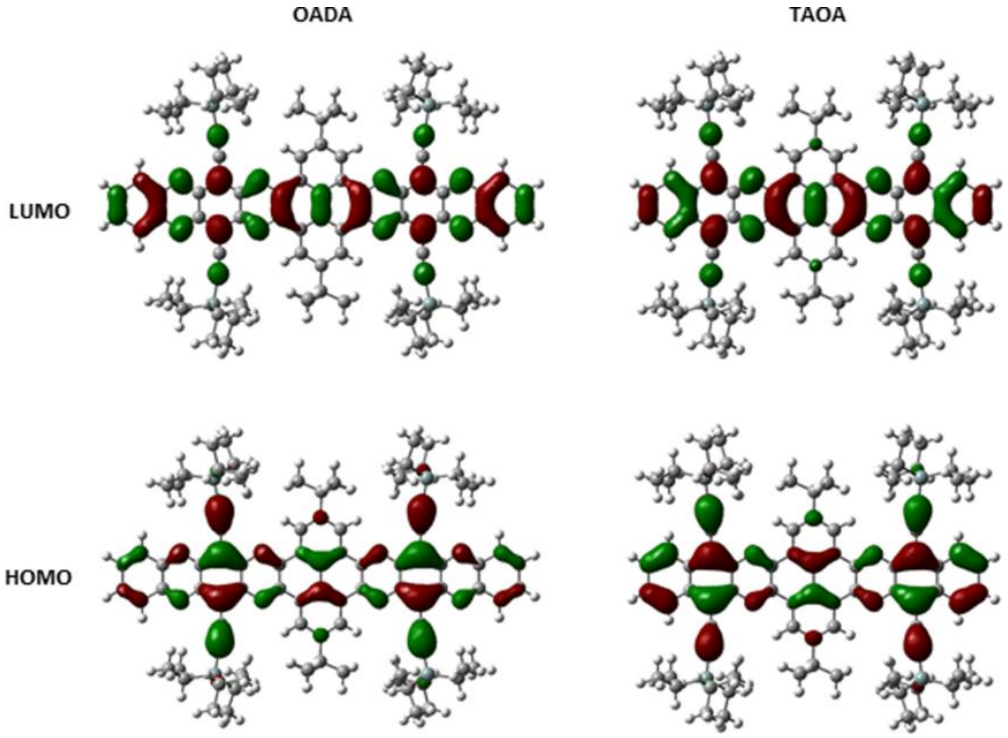

Fig 4.11 The electron density distribution of **OADA** and **TAOA**

Table 4.1 Summary of photophysical and electrochemical property and energy levels (eV) (experimental and calculated) of compounds **OADA** and **TAOA**

Compd.	λ_{max} (nm)	λ_{onset} (nm)	$E_{gap(opt)}$[a] (eV)	$E_{red(onset)}$ (eV)	$E_{LUMO(CV)}$[b] (eV)
TAOA	540	566	2.19	-1.72	-3.08
OADA	640	667	1.86	-1.12	-3.68
	E_{HOMO}[c] (eV)	$E_{LUMO(calc)}$[d] (eV)	$E_{HOMO(calc)}$[d] (eV)	$E_{gap(calc)}$[d] (eV)	
TAOA	-5.27	-2.81	-5.31	2.50	
OADA	-5.54	-3.38	-5.40	2.02	

[a] $E_{gap(opt)}$ was calculated from 1240nm/ λ_{onset}. [b] $E_{LUMO(CV)} = -(E_{red(onset)} + 4.8)$ (eV). [c] $E_{HOMO} = E_{LUMO(CV)} - E_{gap(opt)}$ (eV).[d] DFT calculations (B3LYP/6-31G*) using *Gaussian 09.*

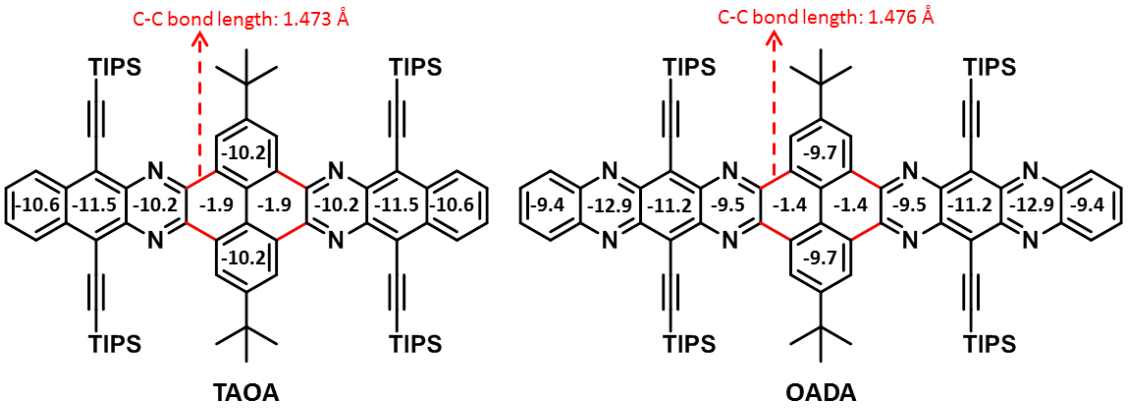

Fig 4.12 NICS(1) values of **TAOA** and **OADA** at the GIAO-B3LYP/6-31G(d) level

Then the NICS calculation was performed with the Gaussian 09 package using the gauge invariant atomic orbital (GIAO) approach at the B3LYP/6-31G(d) level. As shown in Fig 4.12, the central pyrene rings in **OADA** and **TAOA** show a large NICS(1) value of -1.9 and -1.4, respectively, which reveals a low aromaticity in the central pyrene rings. This could also be confirmed by the increased C-C bond length in the central pyrene units of **OADA** (1.476 Å in single crystal) and **TAOA** (1.473 Å in single crystal). This is also consistent with the above-mentioned bandgaps and max absorptions in UV-Vis spectra of **OADA** and **TAOA.** On the contrary, other benzene or pyrazine rings in **OADA** and **TAOA** exhibit smaller NICS(1) values (smaller than -9), which indicates that good aromatic feature exists in the two azatetracenes and azapentacenes fragments. Although the aromaticity is interrupted at the pyrene units, the large conjugations of the whole backbones are real.

4.3.4 PEC behaviors

In order to reveal the electronic properties of **OADA** and **TAOA**, the photoelectrochemical behaviors have been employed to investigate the semiconductor property. The repeatable anodic (positive) photocurrents (Fig 4.13A and C) of **TAOA** and **OADA** suggest that they are n-type semiconductors, which is corresponding with the negative photovoltage (illuminated open-circuit potential) responses (Fig 4.13B and D). To further understand the photoelectrochemical property, the Mott-Schottky (MS) measurements of both compounds were performed in 0.5 M Na_2SO_4 aqueous solution (Fig 4.14). The positive slopes further confirmed the n-type semiconductor behaviors of

OADA and **TAOA**. The flat-band potentials of **OADA** and **TAOA** can also be estimated from the plots which are about 0.11 V and 0.085 V vs. RHE, respectively.

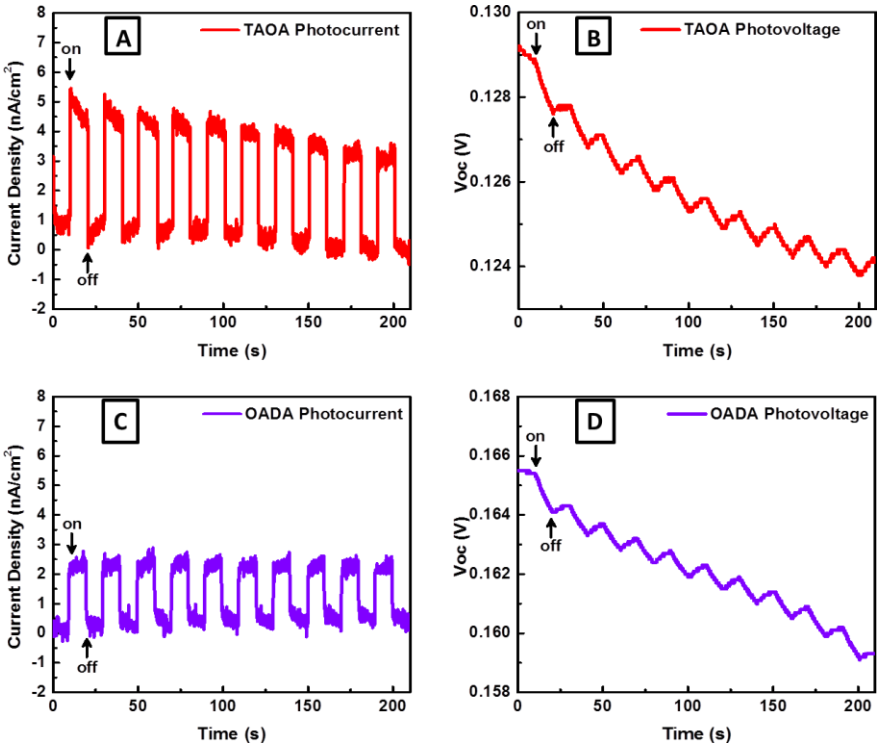

Fig 4.13 The photoelectrochemical measurements under chopped AM 1.5 G light illumination: Zero-biased photocurrent responses of A) **TAOA**/FTO electrode and C) **OADA**/FTO; Photovoltage responses of B) **TAOA** and D) **OADA**

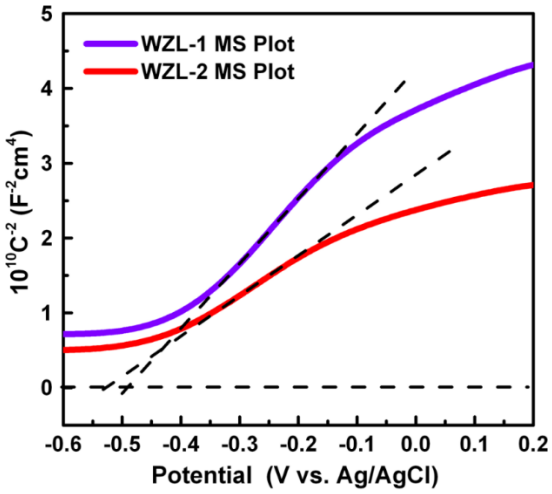

Fig 4.14 Mott-Schottky plots of **TAOA** /FTO and **OADA**/FTO measured at a frequency of 1000 Hz. The flat-band potentials are indicated by the intercept of the dashed lines

4.4 Conclusion

In conclusion, two new pyrene-fused large azaacenes **OADA** and **TAOA** has been successfully synthesized and fully characterized. **TAOA** shows no π-π stacking, while **OADA**, with a longer conjugation, shows strong π-π interactions in the molecular packing. The band gaps of **OADA** and **TAOA** are 1.86 eV and 2.19 eV, which are at the same level with TIPS-azapentacene and TIPS-azatetracene, respectively. This suggests that pyrene is a relatively moderate aromatic building block which is suitable to build up large azaacene. Due to **OADA** and **TAOA** contain more than one Clar's sextets and their aromaticity is interrupted, they are not real azaacenes. However, the large conjugations of the whole molecules are real. The large conjugations offer a great possibility for certain applications. These results suggest that employing a relatively moderate aromatic unit is a practical strategy to build up large azaacenes for novel stable n-type organic semiconductors.

References

[1]a) T. Sekitani, U. Zschieschang, H. Klauk, T. Someya, *Nat Mater* **2010**, *9*, 1015-1022; b) G. H. Gelinck, H. E. A. Huitema, E. van Veenendaal, E. Cantatore, L. Schrijnemakers, J. B. P. H. van der Putten, T. C. T. Geuns, M. Beenhakkers, J. B. Giesbers, B.-H. Huisman, E. J. Meijer, E. M. Benito, F. J. Touwslager, A. W. Marsman, B. J. E. van Rens, D. M. de Leeuw, *Nat Mater* **2004**, *3*, 106-110; c) H. Usta, A. Facchetti, T. J. Marks, *Acc. Chem. Res* **2011**, *44*, 501-510; d) I. McCulloch, R. S. Ashraf, L. Biniek, H. Bronstein, C. Combe, J. E. Donaghey, D. I. James, C. B. Nielsen, B. C. Schroeder, W. Zhang, *Acc. Chem. Res* **2012**, *45*, 714-722; e) X.-K. Chen, L.-Y. Zou, J.-F. Guo, A.-M. Ren, *J. Mater. Chem* **2012**, *22*, 6471-6484; f) S. C. B. Mannsfeld, B. C. K. Tee, R. M. Stoltenberg, C. V. H. H. Chen, S. Barman, B. V. O. Muir, A. N. Sokolov, C. Reese, Z. Bao, *Nat Mater* **2010**, *9*, 859-864. g) J. Xiao, B. Yang, J. I. Wong, Y. Liu, F. Wei, K. J. Tan, X. Teng, Y. Wu, L. Huang, C. Kloc, F. Boey, J. Ma, H. Zhang, H. Yang, Q. Zhang, *Org. Lett,* **2011**, 13, 3004-3007. h) J. Xiao, H. M. Duong, Y. Liu, W. X. Shi, L. Ji, G. Li, S. Li, X. Liu, J. Ma, F. Wudl, Q. Zhang, *Angew Chem. Int. Ed,* **2012**, 51, 6094-6098. i) J.Li, Q. Zhang, *Synlett,* **2013**, 24, 686-696.

[2] H. Sirringhaus, *Adv. Mater* **2014**, *26*, 1319-1335.

[3] C. Wang, H. Dong, W. Hu, Y. Liu, D. Zhu, *Chem. Rev* **2012**, *112*, 2208-2267.

[4] Y. Zhao, Y. Guo, Y. Liu, *Adv. Mater* **2013**, *25*, 5372-5391.

[5] O. D. Jurchescu, M. Popinciuc, B. J. van Wees, T. Palstra, *Adv. Mater* **2007**, *19*, 688.

[6] a) U. H. F. Bunz, J. U. Engelhart, B. D. Lindner, M. Schaffroth, *Angew. Chem. Int. Ed* **2013**, *52*, 3810-3821; b) Q. Miao, *Adv. Mater* **2014**, *26*, 5541-5549; c) U. H. F. Bunz, *Acc. Chem. Res* **2015**, *48*, 1676-1686; d) A. L. Appleton, S. M. Brombosz, S. Barlow, J. S. Sears, J.-L. Bredas, S. R. Marder, U. H. F. Bunz, *Nat Commun* **2010**, *1*, 91; e) S. More, R. Bhosale, S. Choudhary, A. Mateo-Alonso. *Org. Lett* **2012**, 14, 4170-4173; f) D.-C. Bernd Kohl, F. Frank Rominger, M. Mastalerz, *Angew Chem. Int. Ed* **2015**, 54, 6051-6056; g) C. Wang, P. Gu, B. Hu, Q. Zhang, Q, *J. Mater. Chem. C* **2015**, 3, 10055-10065; h) J. Li, Q. Zhang, *ACS Appl. Mater. Interfaces* **2015**, DOI: 10.1021/acsami.5b00113; i) J. Li, J. Miao, G. Long, J. Zhang, Y. Li, R. Ganguly, Y. Zhao, Y. Liu, B. Liu, Q. Zhang, *J. Mater. Chem. C* **2015**, 3, 9877-9884; j) G. Li, J. Miao, J. Cao, J. Zhu, B. Liu, Q. Zhang, *Chem Comm*, **2014**, 50, 7656-7658; k) J. Li, P. Li, J. Wu, J. Gao, W. Xiong, G. Zhang, Y. Zhao, Q. Zhang, *J. Org. Chem.* **2014**, 79, 4438-4445; l) P. Gu, F. Zhou, J. Gao, G. Li, C. Wang, Q. Xu, Q. Zhang, J.-M Lu, *J. Am. Chem. Soc* **2013**, 135, 14086-14089; m) G. Li, Y. Wu, J. Gao, J. Li, Y. Zhao, Q. Zhang, *Chem. Asian J* **2013**, 8, 1574-1578; n) G. Li, K. Zheng, C. Wang, K. S. Leck, F. Hu, X. Sun, Q. Zhang, *ACS Appl. Mater. & interface* **2013**, 5, 6458-6462.

[7] a) M. Winkler, K. Houk, *J. Am. Chem. Soc* **2007**, *129*, 1805-1815; b) X.-D. Tang, Y. Liao, H. Geng, Z.-G. Shuai, *J. Mater. Chem* **2012**, *22*, 18181-18191.

[8] J. E. Anthony, *Angew. Chem. Int. Ed* **2008**, *47*, 452-483.

[9] J. U. Engelhart, O. Tverskoy, U. H. F. Bunz, *J. Am. Chem. Soc* **2014**, *136*, 15166-15169.

[10] a) B. D. Lindner, J. U. Engelhart, O. Tverskoy, A. L. Appleton, F. Rominger, A. Peters, H.-J. Himmel, U. H. F. Bunz, *Angew. Chem. Int. Ed* **2011**, *50*, 8588-8591; b) J. U. Engelhart, B. D. Lindner, O. Tverskoy, F. Rominger, U. H. F. Bunz, *Org. Lett* **2012**, *14*, 1008-1011; c) Z. He, R. Mao, D. Liu, Q. Miao, *Org. Lett* **2012**, *14*, 4190-4193.

[11] C. Wang, J. Zhang, G. Long, N. Aratani, H. Yamada, Y. Zhao, Q. Zhang, *Angew. Chem. Int. Ed* **2015**, *54*, 6292-6296.

[12] A. Mateo-Alonso, N. Kulisic, G. Valenti, M. Marcaccio, F. Paolucci, M. Prato, *Chemistry – Chem. Asian J* **2010**, *5*, 482-485.

[13] A. Mateo-Alonso, *Chem. Soc. Rev* **2014**, *43*, 6311-6324.

[14] a) A. D. Becke, *The Journal of Chemical Physics* **1993**, *98*, 5648-5652; b) C. Lee, W. Yang, R. G. Parr, *Physical review B* **1988**, *37*, 785.

[15] a) M. Frisch, G. Trucks, H. Schlegel, G. Scuseria, M. Robb, J. Cheeseman, G. Scalmani, V. Barone, B. Mennucci, G. Petersson, *There is no corresponding record for this reference*; b) G. W. T. M. J. Frisch, H. B. Schlegel, G. E. Scuseria, M. A. Robb, J. R. Cheeseman, G. Scalmani, V. Barone, B. Mennucci, G. A. Petersson, H. Nakatsuji, M. Caricato, X. Li, H. P. Hratchian, A. F. Izmaylov, J. Bloino, G. Zheng, J. L. Sonnenberg, M. Hada, M. Ehara, K. Toyota, R. Fukuda, J. Hasegawa, M. Ishida, T. Nakajima, Y. Honda, O. Kitao, H. Nakai, T. Vreven, J. A. Montgomery, Jr., J. E. Peralta, F. Ogliaro, M. Bearpark, J. J. Heyd, E. Brothers, K. N. Kudin, V. N. Staroverov, T. Keith, R. Kobayashi, J. Normand, K. Raghavachari, A. Rendell, J. C. Burant, S. S. Iyengar, J. Tomasi, M. Cossi, N. Rega, J. M. Millam, M. Klene, J. E. Knox, J. B. Cross, V. Bakken, C. Adamo, J. Jaramillo, R. Gomperts, R. E. Stratmann, O. Yazyev, A. J. Austin, R. Cammi, C. Pomelli, J. W. Ochterski, R. L. Martin, K. Morokuma, V. G. Zakrzewski, G. A. Voth, P. Salvador, J. J. Dannenberg, S. Dapprich, A. D. Daniels, O. Farkas, J. B. Foresman, J. V. Ortiz, J. Cioslowski, and D. J. Fox, Gaussian, Inc., Wallingford CT, 2009.

[16] J. Hu, D. Zhang, F. W. Harris, *J. Org. Chem* **2005**, *70*, 707-708.

[17] S. Miao, S. M. Brombosz, P. v. R. Schleyer, J. I. Wu, S. Barlow, S. R. Marder, K. I. Hardcastle, U. H. F. Bunz, *J. Am. Chem. Soc* **2008**, *130*, 7339-7344.

[18] A. L. Appleton, S. Barlow, S. R. Marder, K. I. Hardcastle, U. H. Bunz, *Synlett* **2011**, 1983-1986.

[19] a) S. Miao, S. M. Brombosz, P. v. R. Schleyer, J. I. Wu, S. Barlow, S. R. Marder, K. I. Hardcastle, U. H. F. Bunz, *Journal of the American Chemical Society* **2008**, *130*, 7339-7344; b) B. D. Lindner, J. U. Engelhart, M. Märken, O. Tverskoy, A. L. Appleton, F. Rominger, K. I. Hardcastle, M. Enders, U. H. F. Bunz, *Chemistry – A*

European Journal **2012**, *18*, 4627-4633; c) Y.-Y. Liu, C.-L. Song, W.-J. Zeng, K.-G. Zhou, Z.-F. Shi, C.-B. Ma, F. Yang, H.-L. Zhang, X. Gong, *Journal of the American Chemical Society* **2010**, *132*, 16349-16351; d) Z. Liang, Q. Tang, R. Mao, D. Liu, J. Xu, Q. Miao, *Advanced Materials* **2011**, *23*, 5514-5518; e) Z. Liang, Q. Tang, J. Xu, Q. Miao, *Advanced Materials* **2011**, *23*, 1535-1539.

[20] a) A. D. Becke, *J. Chem. Phys* **1993**, *98*, 5648-5652; b) C. Lee, W. Yang, R. G. Parr, *Phys. Rev. B* **1988**, *37*, 785-789.

Chapter 5*

An Ambipolar Azaacene as a Stable Photocathode for Metal-Free Light-Driven Water Reduction

Present photoelectrochemical (PEC) cells for water splitting are based on inorganic electrodes. For future large-scale applications, semiconductors with tunable and designable properties, large-scale solution-processed ability and relatively low-cost as well as sustainable production are crucial. Compared to the inorganic counterparts, organic π-conjugated materials should be a desirable choice. This chapter introduces a larger azaacene **DQNDN** *with ambipolar properties, which can be used as both photoanode and photocathode in PEC cells. Although the performance of* **DQNDN** *nanofibers as a photoanode is poor and unstable with 0.81 μA cm^{-2} at 0.87V versus RHE, the performance of* **DQNDN** *nanofibers as a photocathode is efficient and stable with 0.13 mA cm^{-2} at -0.13V versus RHE. It is the first time the organic material is used as a single active element for stable light-driven photoelectrichemical water reduction.*

*This section published substantially as reference: P.-Y. Gu†, Z. Wang†, F.-X. Xiao, Z. Lin, R. Song, Q.-F. Xu, J.-M. Lu, B. Liu, Q. Zhang, *Materials Chemistry Frontiers* **2017**, *1*, 495-498.

(† Dr P.-Y. Gu and Z. Wang contributed equally to this work.)

5.1 Introduction

Light-driven water splitting to produce renewable hydrogen fuel has been considered as an attractive technology to address energy issues.[1] Among various strategies to convert solar energy into chemical energy,[2] photoelectrochemical (PEC) cells are believed to be one of the most promising approaches because these inexpensive and simple devices only require semiconductor-based photoelectrodes, water, and sunlight.[3] As the heart of PEC cells, semiconductor-based photoelectrodes should possess strong absorption ability at the visible area, efficient charge separation and transport capability, excellent stability against corrosion, and suitable reduction and oxidation potentials for water splitting.[4] Up to now, the semiconductors for photoelectrodes are dominated by inorganic materials.[5] Although the efficiency and stability are pretty high, the ability for large-scale processing as well as the cost has posed a limitation for the practical applications. Thus, searching new photoelectrode materials with suitable energy level and inexpensive large-scale fabrication is highly desirable.

As the counterpart of inorganic semiconductors, organic π-conjugated materials have been widely employed as active elements in optoelectronic devices such as solar cells,[6] light-emitting diodes,[7] field-effect transistors,[8] and memory devices.[9] However, the applications as photoelectrodes in metal-free PEC cells are rare.[10] Till now, only a few polymers (BBL (poly(benzimidazobenzophenanthr-oline)[11] and carbon nitride[12]) and some small molecules (porphyrins, perylenediimides or the hybrids[13]) have been demonstrated as promising photoelectrodes in PEC cells. Employing ambipolar π-conjugated molecules as single active elements in photocathodes for light-driven metal-free water reduction is unprecedented. More importantly, comparing with polymer-based photoelectrodes, small molecules could offer several advantages including monodispersity, reliable synthetic reproducibility, and adjustable structure packing features.

It has been demonstrated that azaacenes can be served as promising organic semiconductors for many applications,[7f, 14] and the charge transport properties can range from p-, ambipolar, to n-type.[15] Considering the balance of dynamic charge transports

during PEC processing, ambipolar azaacenes could be good candidates as photoelectrodes. In this chapter, a new azaacene 6,11,18,23-tetrakis((triisopropylsilyl)ethynyl) diquinoxalino[*g*,*g*']naphtha[1",8":3,4,5;4",5":3',4',5']-dicyclopenta[1,2-*b*:1',2'-*b*']diquinoxaline (**DQNDN**, Scheme 5.1) were successfully synthesized. It has been confirmed to show the ambipolar transport property through Mott–Schottky measurement. It is supposed that the as-prepared azaacene may possess the following advantages: (1) **DQNDN** may display strong absorption in visible area due to the large planarity and longer conjugation length; (2) **DQNDN** may exhibit efficient charge separation and transport properties because large azaacenes usually possess good electron mobility; (3) **DQNDN** may possess suitable reduction and oxidation potentials for water splitting. These favorable facts strongly encouraged us to investigate **DQNDN** as a potential photocathode in PEC cells.

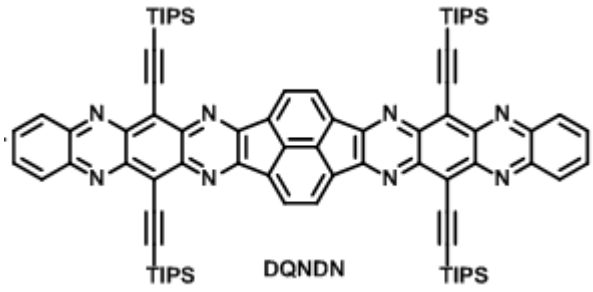

Scheme 5.1 molecular structure of **DANDN**

5.2 Experimental Methods

5.2.1 Materials

All chemicals and solvents were used directly without further purification.

5.2.2 Instruments and methods

Using $CDCl_3$ and CF_3COOD (TFA) as solvents and tetramethylsilane (TMS) as the internal standard, ^1H NMR and ^{13}C NMR spectra were measured on a Bruker Advance 300 NMR spectrometer at ambient temperature. High-resolution mass spectrum (HRMS) was performed on a Waters Q-Tof premier mass spectrometer. Thermogravimetric analysis (TGA) was carried out on a TA Instrument Q500 Thermogravimetric Analyzer

at a heating rate of 10 °C/min. The solid-state UV-Vis diffuse-reflectance spectrum was recorded at room temperature on powder samples with a Model UV-2501 PC. A $BaSO_4$ plate was used as a standard (100% reflectance). The absorption data was calculated from the reflectance spectrum using the Kubelka–Munkfunction: $\alpha/S = (1 - R)^2/2R$, where α is the absorption coefficient, S is the scattering coefficient and R is the reflectance.

5.2.3 Synthesis of DQNDN

A mixture of 1,4-bis((triisopropylsilyl)ethynyl)phenazine-2,3-diamine (285 mg, 0.5 mmol) and cyclopenta[*fg*]acenaphthylene-1,2,5,6-tetraone (47 mg, 0.2 mmol) in acetic acid/chloroform (150 mL, v:v = 1:1) was stirred and refluxed under nitrogen for 72 h. After cooling to room temperature, the mixture was poured into methanol and the obtained precipitate was isolated by filtration and washed with methanol. The crude product was dispersed into chloroform and stirred for 1 h. The obtained precipitate (177, 0.136 mmol, 68%) was isolated by filtration and washed with chloroform, THF, DMF, methanol. ^{1}H NMR (300 MHz, TFA) δ 8.98 (s, 4H), 8.68 (s, 4H), 8.55 (s, 4H), 1.66 – 1.35 (m, 84H). ^{13}C NMR (75 MHz, TFA) δ 155.32, 139.09, 134.82, 134.52, 133.79, 132.30, 129.08, 123.00, 121.30, 117.49, 92.64, 13.19, 7.03. HR-MS (ESI) m/z Calc. for $[M+H]^+$ $C_{82}H_{96}N_8Si_4$: 1305.6913, found: 1305.6953.

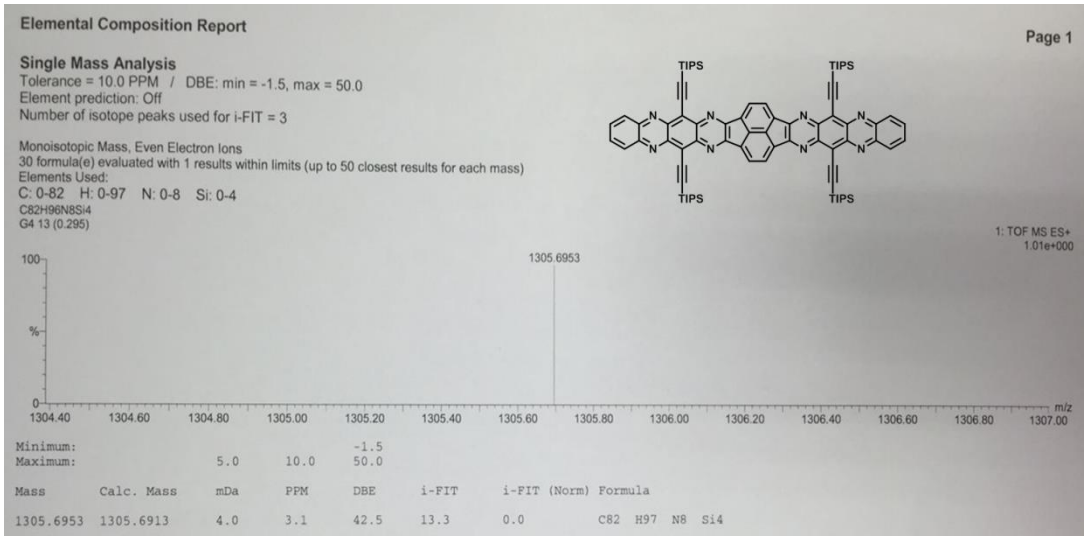

Fig 5.1 HR-MS (ESI) of **DQNDN**

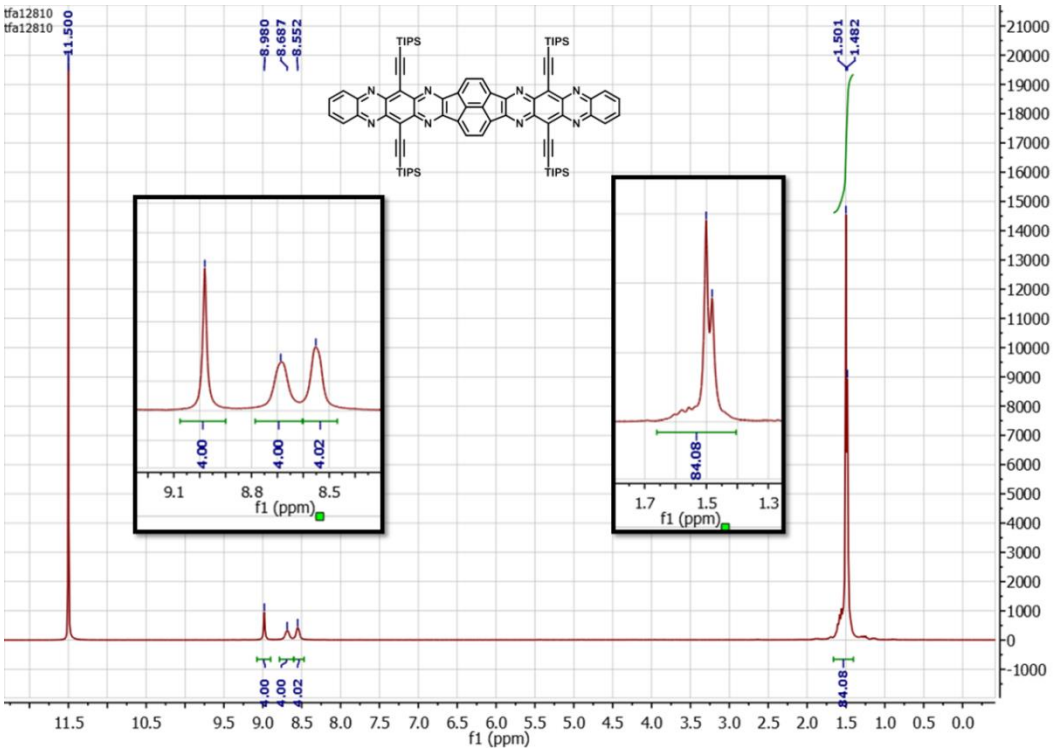

Fig 5.2 ^{1}H NMR spectrum of **DQNDN** in CF_3COOD (TFA), 300 MHz, room temperature.

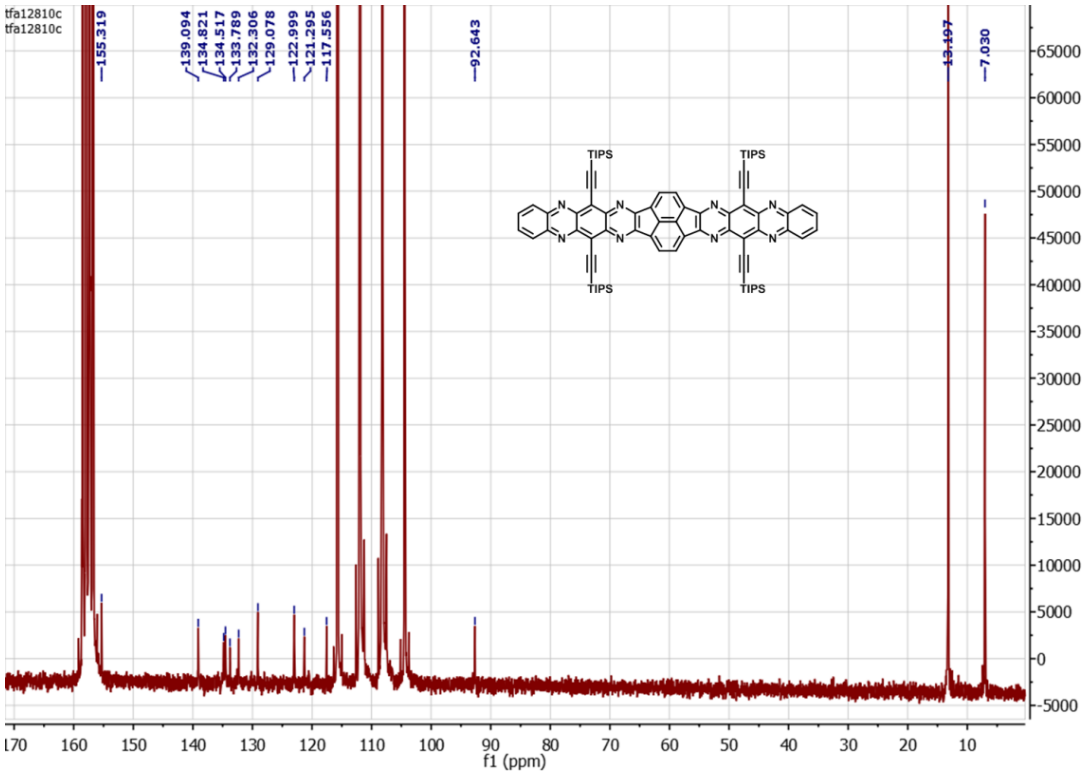

Fig 5.3 ^{13}C NMR spectrum of **DQNDN** in TFA, 75 MHz, $CDCl_3$, room temperature.

5.2.4 Photoelectrochemical (PEC) measurements

Generally, it is the same as that described in Chapter 4. A well-dispersed 5 mg/mL suspension for DQNDN with pure ethanol as the solvent was prepared by brief sonication in a water bath. The Fluorine-doped tin oxide (FTO) coated glasses (1.0 × 2.0 cm^2) were used as the substrate. The substrates were cleaned thoroughly by sonication in 5% detergent (Decon ® 90) for 30 minutes first and then rinsed with de-ionized water (DI water) for several times, which were followed by sonication in DI water, acetone, 2-propanol for each 15 minutes. After that, 25 μL of different sample suspensions were dropped onto the surface of FTO substrates, which were masked using Ti foil with an effective area of 0.283 cm^2.

5.3 Principle outcomes

5.3.1 Synthetic route and characterization

The synthetic route to prepare DQNDN is shown in Scheme 5.2. The intermediate compounds **5.1** and **5.2** were prepared according to literature procedures.[16] DQNDN was obtained as a brown-black powder in 68% yield through a one-step condensation reaction between **5.1** and **5.2** using acetic acid/chloroform as a mixed solvent. Although four triisopropylsilyl (TIPS) groups have been introduced to be attached onto the backbone, the solubility of DQNDN is still poor and it is insoluble in the common solvents. This suggests that strong π-π stacking may exist in its solid state. It can only dissolve in trifluoroacetic acid (TFA) owing to the protonation of nitrogen atoms.

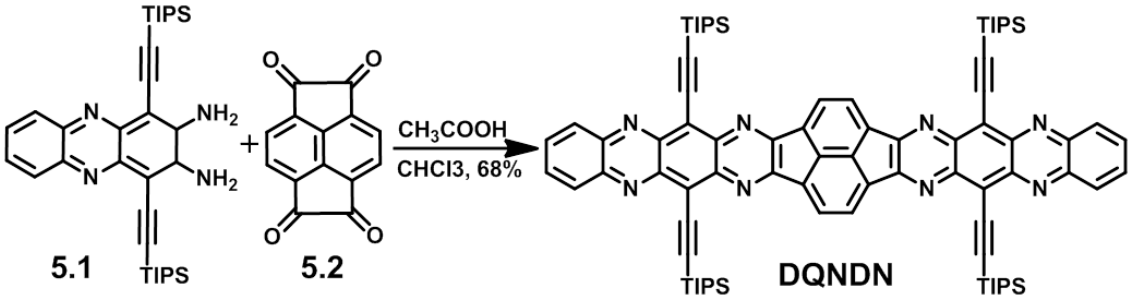

Scheme 5.2 Synthetic route to **DQNDN**

The thermal stability of **DQNDN** was evaluated by thermogravimetric analysis under a nitrogen atmosphere. As shown in Fig 5.4., **DQNDN** displays very good thermal stability with an onset decomposition temperature of ~405 ºC (considering the 5% weight-loss temperature).

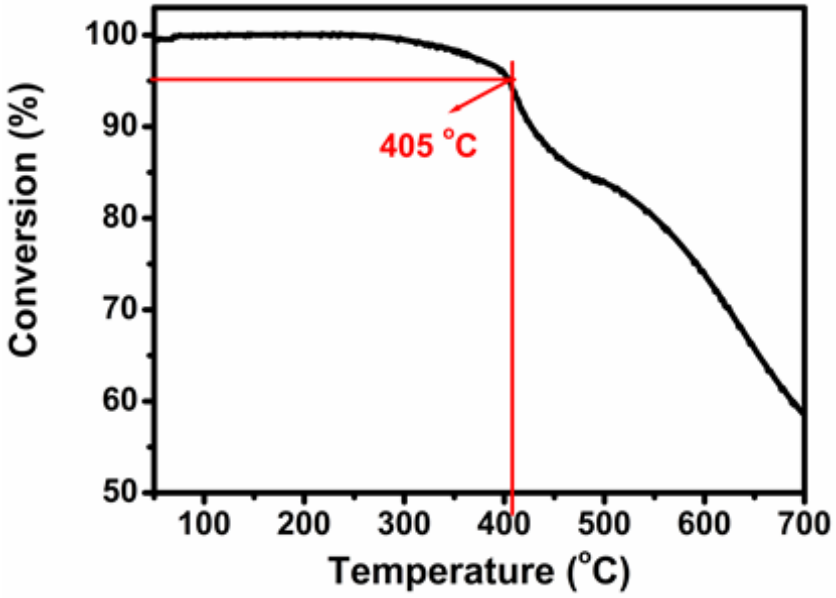

Fig 5.4 TGA curve of **DQNDN**

5.3.2 PEC cell for water splitting

The nanostructured **DQNDN** was fabricated by slowly dropping ethanol into **DQNDN**/TFA solution with rapid stirring. The as-prepared precipitation was centrifuged and washed with ethanol, deionized water, and ethanol, respectively. Scanning electron microscopy analysis (SEM, Fig 5.5) reveals that nanofibers (diameter: 100–200 nm) can evenly coat the surface of fluorine-doped tin oxide (FTO) glass. The normalized solid-state absorption spectrum of the nanostructured DQNDN film is shown in Fig 5.6, which possesses typical azaacene finger peaks (280, 360, 585 nm). The peak at 850 nm might come from its aggregation. Overall, the solid-state absorption spectrum of the nanostructured **DQNDN** film covers the whole visible spectrum region, suggesting that it should be a good light-absorbing material, which might be a good candidate for photoelectrodes in PEC cells.

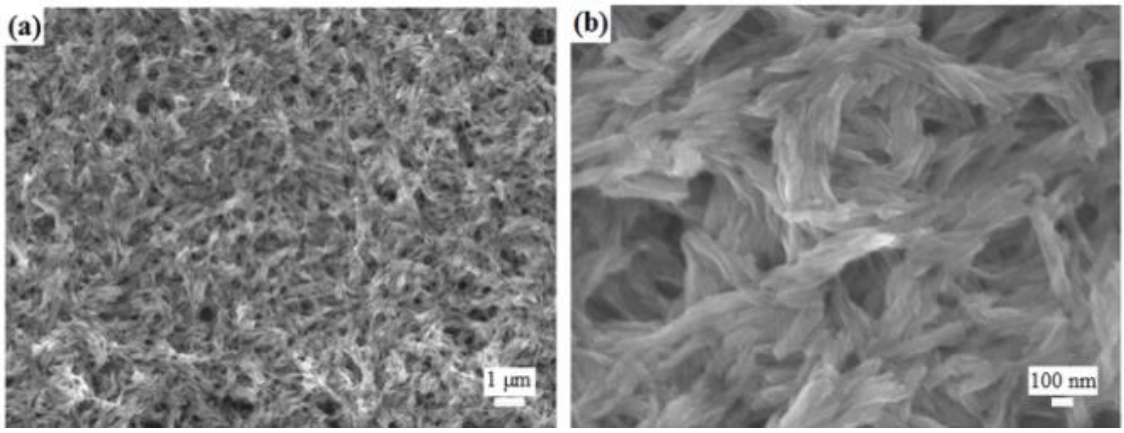

Fig 5.5 SEM images of nanostructured **DQNDN** nanofibers: (a) Low resolution and (b) high resolution

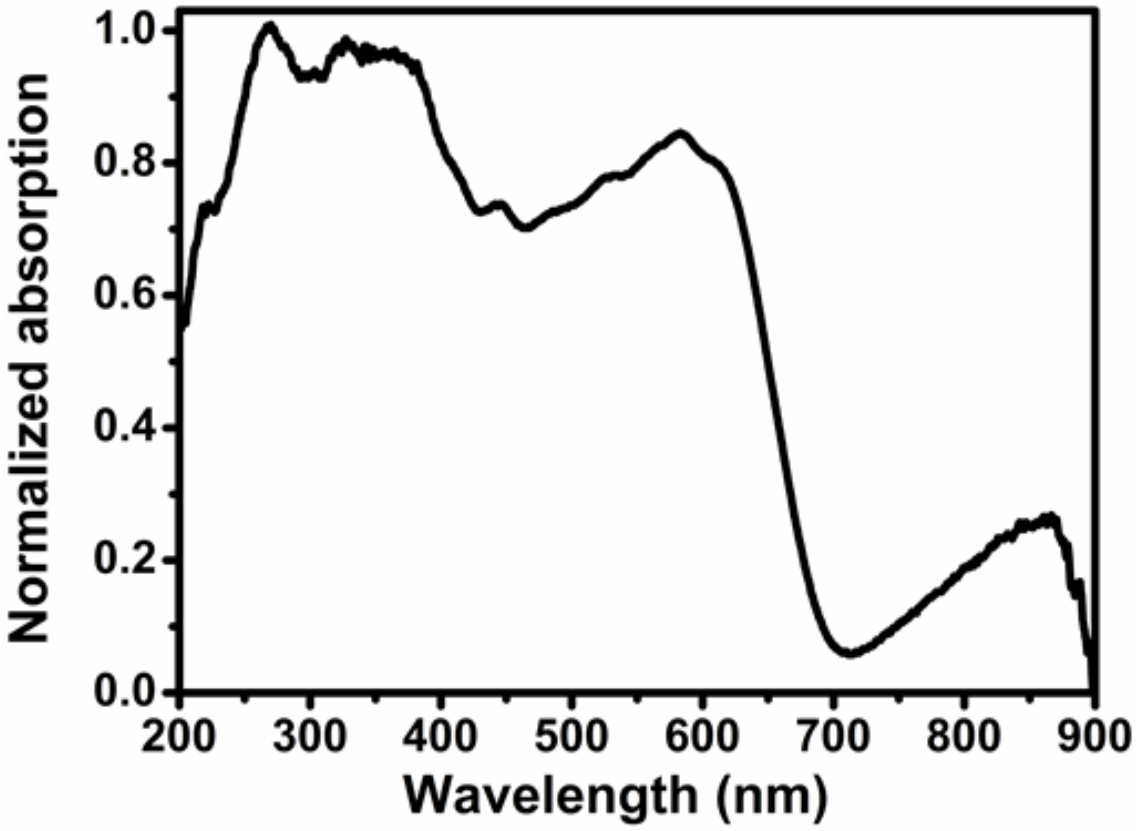

Fig 5.6 Solid-state absorption spectrum of DQNDN nanofibers

As shown in Fig 5.7a, the PEC behavior of **DQNDN** was measured under a 300 W Xenon lamp (Newport) coupled to an AM 1.5 G filter in a three-electrode

electrochemical system with Ag/AgCl electrode as a reference, Pt plate as a counter electrode, and nanostructured **DQNDN** film as a working electrode. A 0.5 M Na_2SO_4 aqueous solution was used as the electrolyte. In the previous research [17], azaacenes have already been demonstrated as photoanodes in PEC cells. As a new member of azaacene family, **DQNDN** were also tested as a photoanode in PEC cell. The linear scan voltammetry (LSV, Fig 5.7b) and corresponding current density-potential curves (Fig 5.7c) in dark and under light irradiation display the largest current density of 0.81 μA cm^{-2} at 0.87 V versus reversible hydrogen electrode (RHE), supporting the occurrence of PEC reactions. To confirm the real performance of PEC cells based on nanostructured **DQNDN** film, the time course of photocurrent density was measured at a potential of 1.23 V versus RHE in Fig 5.7d. At the beginning, a fast current density decay was found, followed by a slight current density decrease, suggesting that the charge transfer and extraction are not optimal (the adjustment of PEC cell components may further improve the performance). The time course of the photocurrent density (～30 nA cm^{-2}) has also been measured at a potential of 0.61 V versus RHE (Fig 5.7e) for the comparison with the previous works, [17-18] and these results are similar. To further reveal the charge transport behavior of nanostructured **DQNDN** film, the Mott–Schottky measurement was performed in 0.5 M Na_2SO_4 aqueous solution. As shown in Fig 5.7f, the positive slope displays n-type behavior of nanostructured **DQNDN** film, which is consistent with the previous PEC analysis.[17-18] Besides the n-type behavior, the Mott–Schottky measurement also provides us a negative slope (p-type behavior), suggesting that nanostructured **DQNDN** film could also be utilized as a photocathode in PEC cells.

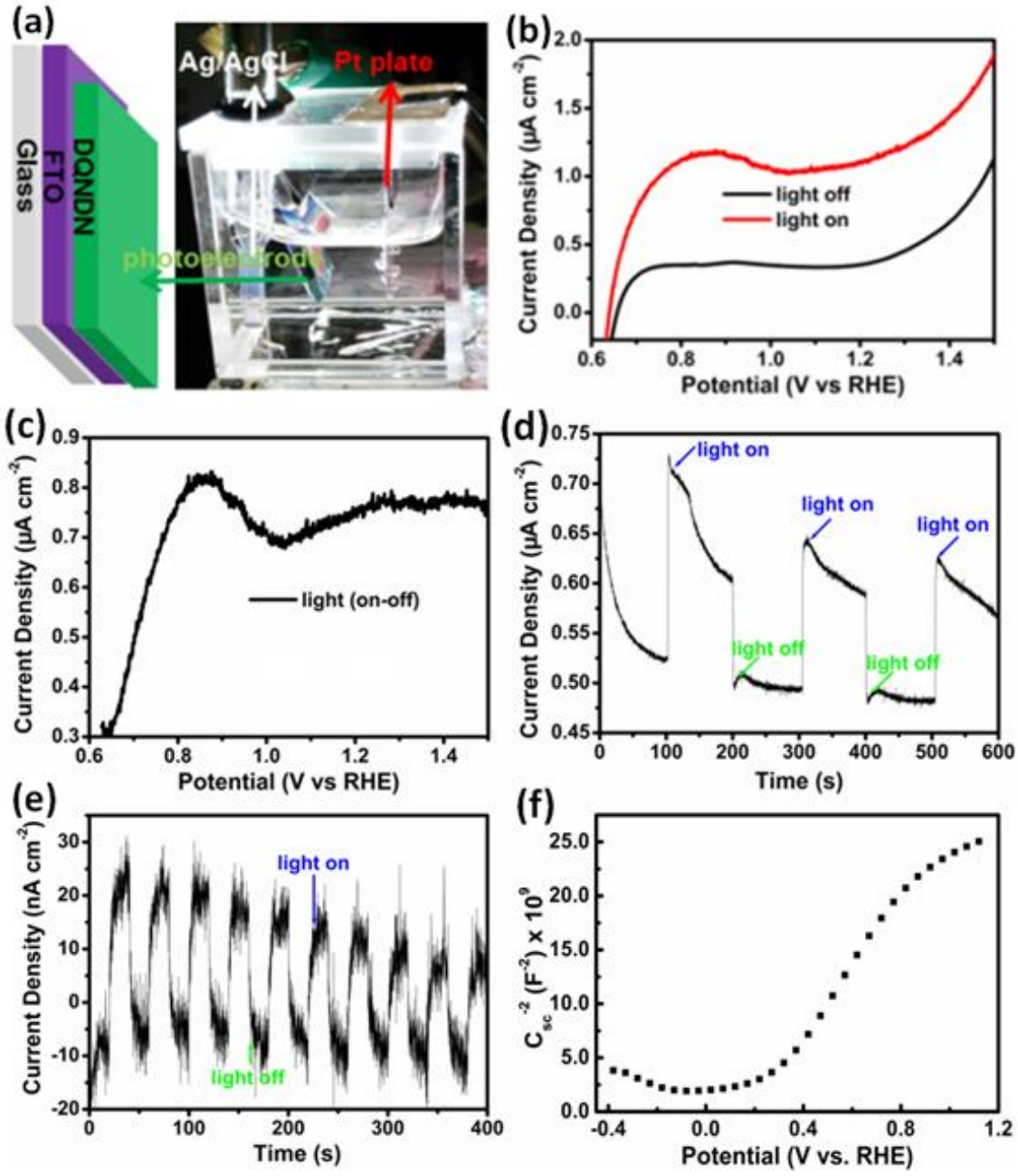

Fig 5.7 (a) Device architecture and the PEC cell; (b) LSV of nanostructured **DQNDN** film under dark (black line) and under simulated solar light irradiation (AM 1.5, 100 mW/cm^2) (red line) in 0.5 M Na_2SO_4 aqueous solution; (c) The current density-potential curve of **DQNDN** nanofibers; (d) the transient photocurrent density of **DQNDN** nanofibers under 1.23 V versus RHE; (e) The transient photocurrent density of **DQNDN** nanofibers under 0.61 V versus RHE; (f) Mott-Schottky plot of **DQNDN** nanofibers

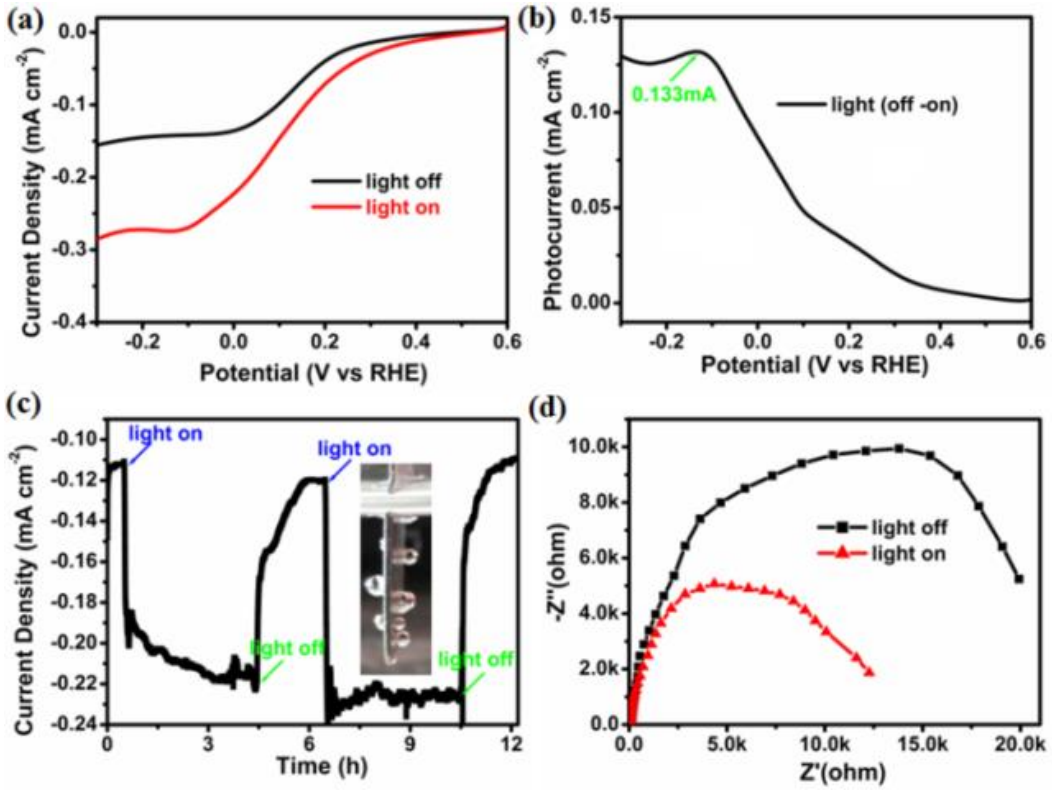

Fig 5.8 (a) LSV of nanostructured **DQNDN** films under dark (black line) and under simulated solar light irradiation (AM 1.5, 100 mW/cm^2) (red line) in 0.5 M Na_2SO_4; (b) Corresponding current density-potential curve; (c) The transient photocurrent density of nanostructured **DQNDN** film under -0.20 V versus RHE. Inset: the picture showing the bubbles formed on the Pt plate; (d) The electrochemical impedance spectroscopy of **DQNDN** at -0.20 V versus RHE in the dark and under light irradiation

As shown in Fig 5.8a, the LSV and corresponding current density-potential curve exhibit the largest current density with 0.13 mA cm^{-2} at -0.13 V versus RHE, indicating that nanostructured **DQNDN** film can be used as a good photocathode in PEC cells. To further understand the photocathode behaviors of nanostructured **DQNDN** film, the time course of the photocurrent density was measured at a potential of -0.20 V versus RHE in Fig 5.8c. The photocurrent density closely matches that of the LSV curve, and exhibits almost no change over repeated cycles with the stability for at least 12 h, which clearly suggests that nanostructured **DQNDN** film is stable as a photocathode and unstable as a photoanode. When **DQNDN** was used as a photoanode in PEC cells, the following reactions were presented:

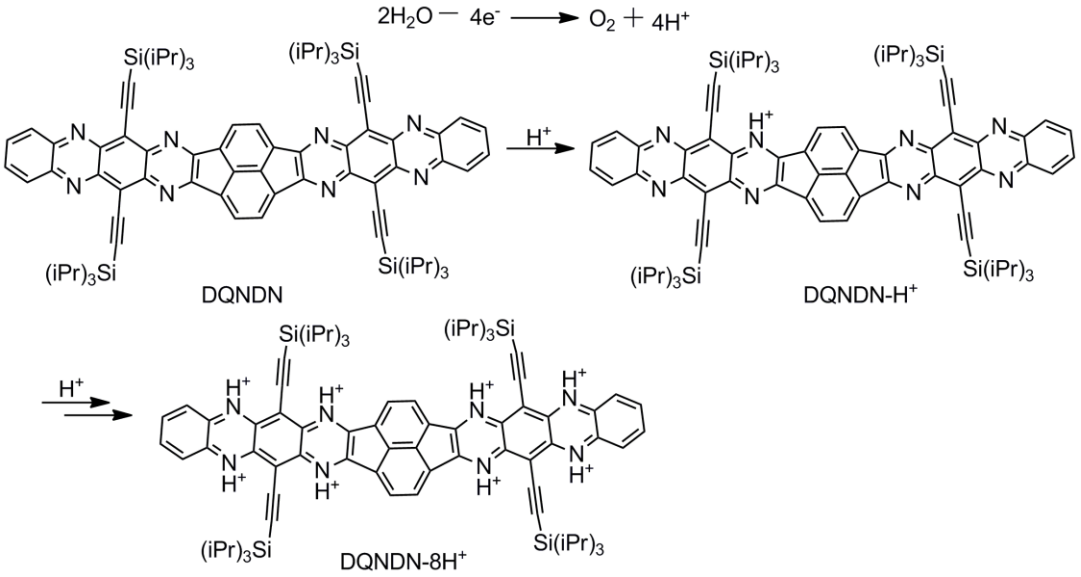

As a result, the performance and stability decrease. However, when **DQNDN** is used as a photocathode, the only following reaction was presented:

$$2H_2O + 4e^- \longrightarrow H_2 + 4OH^-$$

This reaction does not affect the performance and stability of PEC cells.

The electrochemical impedance spectroscopy (EIS) measurement of **DQNDN** at -0.20 V versus RHE (this condition is similar to the photocurrent measurements) are also conducted to characterize charge transport properties between the photoelectrode and the electrolyte. The as-obtained results are presented as Nyquist plots in Fig 5.3.2.4d, where x- and y-axes are the real part (Z') and the negative of imaginary part (-Z") of impedance. Comparing with the result attained under dark condition, the diameter of the semicircle in the Nyquist plots decreases under light irradiation, indicating that charge transport resistance of nanostructured **DQNDN** film at the interface domain of electrode is remarkably decreased under light irradiation than that in dark, which is in agreement with the increase of photocurrent upon light irradiation.

5.4 Conclusions

In summary, it is demonstrated that a large azaacene **DQNDN** can be employed as both photoanode and photocathode in PEC cells due to its ambipolar properties. Although the performance of **DQNDN** nanofibers as a photoanode is poor and unstable with the

current density of 0.81 μA cm^{-2} at 0.87 V versus RHE, the performance of nanostructured DQNDN film as a photocathode is very efficient and stable with the current density of 0.13 mA cm^{-2} at -0.13 V versus RHE. These results clearly suggest that ambipolar organic small molecules could be promising candidates as high efficient photocathodes in metal-free PEC cells for water reduction.

References

[1] a) L.-Z. Wu, B. Chen, Z.-J. Li, C.-H. Tung, *Accounts of Chemical Research* **2014**, *47*, 2177-2185; b) X. Wang, K. Maeda, A. Thomas, K. Takanabe, G. Xin, J. M. Carlsson, K. Domen, M. Antonietti, *Nature materials* **2009**, *8*, 76-80; c) N. Guijarro, M. S. Prévot, X. Yu, X. A. Jeanbourquin, P. Bornoz, W. Bourée, M. Johnson, F. Le Formal, K. Sivula, *Advanced Energy Materials* **2016**, *6*, 1501949-n/a; d) M. G. Walter, E. L. Warren, J. R. McKone, S. W. Boettcher, Q. Mi, E. A. Santori, N. S. Lewis, *Chemical reviews* **2010**, *110*, 6446-6473; e). D. Blakemore, R. H. Crabtree, G. W. Brudvig, *Chemical reviews* **2015**, *115*, 12974-13005; f) X. Yu, A. Shavel, X. An, Z. Luo, M. Ibáñez, A. Cabot, *Journal of the American Chemical Society* **2014**, *136*, 9236-9239; g) W. Li, D. He, S. W. Sheehan, Y. He, J. E. Thorne, X. Yao, G. W. Brudvig, D. Wang, *Energy & Environmental Science* **2016**, *9*, 1794-1802.

[2] a) T. Yu, Y. Zeng, J. Chen, Y.-Y. Li, G. Yang, Y. Li, *Angewandte Chemie International Edition* **2013**, *52*, 5631-5635; b) D. Kang, T. W. Kim, S. R. Kubota, A. C. Cardiel, H. G. Cha, K.-S. Choi, *Chemical reviews* **2015**, *115*, 12839-12887; c) J. R. Swierk, T. E. Mallouk, *Chemical Society reviews* **2013**, *42*, 2357-2387; d) Z. Ji, M. He, Z. Huang, U. Ozkan, Y. Wu, *Journal of the American Chemical Society* **2013**, *135*, 11696-11699; e) E. S. Kim, N. Nishimura, G. Magesh, J. Y. Kim, J.-W. Jang, H. Jun, J. Kubota, K. Domen, J. S. Lee, *Journal of the American Chemical Society* **2013**, *135*, 5375-5383; f) M. Gratzel, *Nature* **2001**, *414*, 338-344; gJ. R. Swierk, D. D. Méndez-Hernández, N. S. McCool, P. Liddell, Y. Terazono, I. Pahk, J. J. Tomlin, N. V. Oster, T. A. Moore, A. L. Moore, *Proceedings of the National Academy of Sciences* **2015**, *112*, 1681-1686.

[3] a) Z. Li, W. Luo, M. Zhang, J. Feng, Z. Zou, *Energy & Environmental Science* **2013**, *6*, 347-370; b) T. Hisatomi, J. Kubota, K. Domen, *Chemical Society reviews* **2014**, *43*,

7520-7535; c) J. Li, J. Miao, G. Long, J. Zhang, Y. Li, R. Ganguly, Y. Zhao, Y. Liu, B. Liu, Q. Zhang, *Journal of Materials Chemistry C* **2015**, *3*, 9877-9884; d) W. W. Xiong, J. Miao, K. Ye, Y. Wang, B. Liu, Q. Zhang, *Angewandte Chemie* **2015**, *127*, 556-560.

[4] a) J. Liu, T. Hisatomi, M. Katayama, T. Minegishi, J. Kubota, K. Domen, *Journal of Materials Chemistry A* **2016**, *4*, 4848-4854; b) K. Sivula, R. van de Krol, **2016**, *1*, 15010; c) J. Li, X. Gao, B. Liu, Q. Feng, X.-B. Li, M.-Y. Huang, Z. Liu, J. Zhang, C.-H. Tung, L.-Z. Wu, *Journal of the American Chemical Society* **2016**, *138*, 3954-3957.

[5] a) F. E. Osterloh, *Chemical Society reviews* **2013**, *42*, 2294-2320; b) Y. Li, L. Zhang, A. Torres-Pardo, J. M. González-Calbet, Y. Ma, P. Oleynikov, O. Terasaki, S. Asahina, M. Shima, D. Cha, L. Zhao, K. Takanabe, J. Kubota, K. Domen, **2013**, *4*, 2566; c) L. Wu, S.-Y. Chen, F.-J. Fan, T.-T. Zhuang, C.-M. Dai, S.-H. Yu, *Journal of the American Chemical Society* **2016**, *138*, 5576-5584.

[6] a) Y.-J. Cheng, S.-H. Yang, C.-S. Hsu, *Chemical reviews* **2009**, *109*, 5868-5923; b) T. M. Clarke, J. R. Durrant, *Chemical reviews* **2010**, *110*, 6736-6767; c) W. Chen, X. Yang, G. Long, X. Wan, Y. Chen, Q. Zhang, *Journal of Materials Chemistry C* **2015**, *3*, 4698-4705; d) Q. Zhang, J. Xiao, Z. Yin, H. M. Duong, F. Qiao, F. Boey, X. Hu, H. Zhang, F. Wudl, *Chemistry – An Asian Journal* **2011**, *6*, 856-862.

[7] a) A. C. Grimsdale, K. Leok Chan, R. E. Martin, P. G. Jokisz, A. B. Holmes, *Chemical reviews* **2009**, *109*, 897-1091; b) S. Scholz, D. Kondakov, B. Lüssem, K. Leo, *Chemical reviews* **2015**, *115*, 8449-8503; c) P.-Y. Gu, Y. Zhao, J.-H. He, J. Zhang, C. Wang, Q.-F. Xu, J.-M. Lu, X. W. Sun, Q. Zhang, *The Journal of organic chemistry* **2015**, *80*, 3030-3035; d) G. Li, Y. Zhao, J. Li, J. Cao, J. Zhu, X. W. Sun, Q. Zhang, *The Journal of organic chemistry* **2015**, *80*, 196-203; e) L. Xu, Y. Zhao, G. Long, Y. Wang, J. Zhao, D. Li, J. Li, R. Ganguly, Y. Li, H. Sun, X. W. Sun, Q. Zhang, *RSC Advances* **2015**, *5*, 63080-63086; f) J. Li, Q. Zhang, *ACS applied materials & interfaces* **2015**, *7*, 28049-28062; g) J. Li, Y. Zhao, J. Lu, G. Li, J. Zhang, Y. Zhao, X. Sun, Q. Zhang, *The Journal of organic chemistry* **2014**, *80*, 109-113.

[8] a) J. Zaumseil, H. Sirringhaus, *Chemical reviews* **2007**, *107*, 1296-1323; b) M. Mas-Torrent, C. Rovira, *Chemical reviews* **2011**, *111*, 4833-4856; c) J. Zhang, C. Wang, G. Long, N. Aratani, H. Yamada, Q. Zhang, *Chemical Science* **2016**, *7*, 1309-1313; d) J.

Zhang, P. Gu, G. Long, R. Ganguly, Y. Li, N. Aratani, H. Yamada, Q. Zhang, *Chemical Science* **2016**, *7*, 3851-3856; e) C. Wang, J. Zhang, G. Long, N. Aratani, H. Yamada, Y. Zhao, Q. Zhang, *Angewandte Chemie International Edition* **2015**, *54*, 6292-6296; f) W. Chen, J. Zhang, G. Long, Y. Liu, Q. Zhang, *Journal of Materials Chemistry C* **2015**, *3*, 8219-8224.

[9] a) N.-G. Kang, B. Cho, B.-G. Kang, S. Song, T. Lee, J.-S. Lee, *Advanced materials* **2012**, *24*, 385-390; b) J. Y. Seok, S. J. Song, J. H. Yoon, K. J. Yoon, T. H. Park, D. E. Kwon, H. Lim, G. H. Kim, D. S. Jeong, C. S. Hwang, *Advanced Functional Materials* **2014**, *24*, 5316-5339; c) C. Wang, P. Gu, B. Hu, Q. Zhang, *Journal of Materials Chemistry C* **2015**, *3*, 10055-10065; d) C. Wang, B. Hu, J. Wang, J. Gao, G. Li, W.-W. Xiong, B. Zou, M. Suzuki, N. Aratani, H. Yamada, F. Huo, P. S. Lee, Q. Zhang, *Chemistry – An Asian Journal* **2015**, *10*, 116-119; e) C. Wang, J. Wang, P.-Z. Li, J. Gao, S. Y. Tan, W.-W. Xiong, B. Hu, P. S. Lee, Y. Zhao, Q. Zhang, *Chemistry – An Asian Journal* **2014**, *9*, 779-783.

[10] a) A. Guerrero, M. Haro, S. Bellani, M. R. Antognazza, L. Meda, S. Gimenez, J. Bisquert, *Energy & Environmental Science* **2014**, *7*, 3666-3673; b) F. Fumagalli, S. Bellani, M. Schreier, S. Leonardi, H. C. Rojas, A. Ghadirzadeh, G. Tullii, A. Savoini, G. Marra, L. Meda, *Journal of Materials Chemistry A* **2016**, *4*, 2178-2187.

[11] P. Bornoz, M. S. Prévot, X. Yu, N. Guijarro, K. Sivula, *Journal of the American Chemical Society* **2015**, *137*, 15338-15341.

[12] a) J. Bian, L. Xi, C. Huang, K. M. Lange, R.-Q. Zhang, M. Shalom, *Advanced Energy Materials* **2016**, *6*, 1600263-n/a; b) S. Yang, Y. Gong, J. Zhang, L. Zhan, L. Ma, Z. Fang, R. Vajtai, X. Wang, P. M. Ajayan, *Advanced materials* **2013**, *25*, 2452-2456.

[13] T. Abe, K. Nagai, S. Kabutomori, M. Kaneko, A. Tajiri, T. Norimatsu, *Angewandte Chemie International Edition* **2006**, *45*, 2778-2781.

[14] U. H. F. Bunz, *Accounts of Chemical Research* **2015**, *48*, 1676-1686.

[15] a) Q. Miao, *Advanced materials* **2014**, *26*, 5541-5549; b) G. J. Richards, J. P. Hill, T. Mori, K. Ariga, *Organic & biomolecular chemistry* **2011**, *9*, 5005-5017; c) A. Mateo-Alonso, *Chemical Society reviews* **2014**, *43*, 6311-6324.

[16] a) B. D. Lindner, J. U. Engelhart, O. Tverskoy, A. L. Appleton, F. Rominger, A. Peters, H.-J. Himmel, U. H. F. Bunz, *Angewandte Chemie International Edition* **2011**, *50*, 8588-8591; b) L. Zhu, Z.-S. Fu, H.-J. Pan, W. Feng, C. Chen, Z.-Q. Fan, *Dalton transactions* **2014**, *43*, 2900-2906.

[17] G. Li, J. Miao, J. Cao, J. Zhu, B. Liu, Q. Zhang, *Chemical communications* **2014**, *50*, 7656-7658.

[18] Z. Wang, J. Miao, G. Long, P. Gu, J. Li, N. Aratani, H. Yamada, B. Liu, Q. Zhang, *Chemistry – An Asian Journal* **2016**, *11*, 482-485.

Chapter 6*

Large Pyrene-Fused N-Heteroacenes: Fifteen and Twenty Aromatic Six-Membered Rings Annulated in One Row

*The synthesis of two novel nitrogen-rich nanoribbons (**15RINGS** and **20RINGS**) with 15 and 20 linearly-fused aromatic six-membered rings are presented in this chapter. The as-prepared nanoribbons possess two and three moderately π-conjugated pyrene units, which make the as-prepared target compounds more stable. The single crystal of **15RINGS** has been obtained. The SCXRD analysis reveals that it belongs to the triclinic system ($P\bar{1}$) with a big unit cell (V = 8698.67 (4) $Å^3$). The long π-conjugated backbone (more than 35 Å) of **15RINGS** possesses a dual-bending feature (the bending angle is about 13.2°), which might be an important factor to stabilize such a large π-conjugated system. The optical bandgap of **15RINGS** is 1.85 eV, which is close to the calculated result obtained from DFT calculation. Moreover, the efficient intersystem crossing has been observed in **15RINGS** system, which is consistent with its low fluorescence quantum yield (3%). Further study on singlet fission in **15RINGS** did not show a positive result.*

*This section published substantially as reference: Z. Wang†, P.-Y. Gu, G. Liu, H. Yao, Y. Wu, Y. Li, G. Rakesh, J. Zhu, H. Fu, Q. Zhang, *Chem Commun*. **2017,** 10.1039/C7CC03898D.

6.1 Introduction

The large acene derivatives including N-heteroacenes has been becoming a hot research topic due to the unusual optical and electronic properties as well as the good prospects in organic electronic applications.[1] It is well known that the property and performance of acene derivatives vary a lot with the different conjugation lengths.[2] Hence, in the past few decades, scientists have put a lot of efforts to experimentally approach large acene derivatives, although the synthetic work is tedious and challenging.[3] Due to the solubility and stability of large acenes and the derivatives dramatically decrease with the increasing π-conjugated length, it becomes extremely difficult to well characterize large acene derivatives, especially through single-crystal X-ray diffraction (SCXRD) analysis. Obviously, SCXRD analysis is the most powerful method to directly obtain the information of the structures and the structure-property relationship. Such studies provide more guidance the designing novel molecules as well as theoretical investigation.[4] Unfortunately, large acene derivatives (n>10) with precise structures (through single-crystal X-ray analysis) are rarely reported. In 2008, Wang group reported a series of pyrene-embedded N-heteroacenes with 16 linearly-fused rings for most, however, only one compound with six linearly-annulated aromatic rings was confirmed by SCXRD analysis.[5] In 2015, Mastalerz group reported a novel N-heteroacene confirmed by SCXRD analysis containing 11 linearly-fused aromatic rings by introducing two terminal triptycenylene units into the backbone to increase its solubility.[6] Up to now, the record length with a precise structure was reported by Bunz group,[7] where a novel coronene-containing N-heteroacene with 13 annulated rings was fused in a row. In the previous work, it is already demonstrated that medium-conjugated pyrene units could make the prepared large acenes or acene derivatives (including N-heteroacenes) more stable.[8] Continuing on this strategy, it should be possible to challenge the current record set by Bunz.[7]

In this chapter, the synthesis of two novel large N-heteroacenes (named as **15RINGS** and **20RINGS**) with 15 and 20 annulated rings linearly fused in a row by embedding two and three pyrene units in the backbone is introduced. Note that the introduced cross-conjugated pyrene units can highly stabilize the obtained compounds.[2a,9] Moreover, ten

and fourteen spherical (triisopropylsilyl)-acetylene groups have been attached onto the backbone of **15RINGS** and **20RINGS**, which ensure the prepared heteroacenes' stability and solubility in organic solvents through decreasing π-π interaction by steric hindrance.[1b,10] **15RINGS** shows good stability and solubility which make it successfully fully characterized by ^{1}H NMR, ^{13}C NMR and HR-MS. Moreover, its optical and electronic properties are also studied by CV, UV, DFT calculation and femtosecond transient absorption spectra. Single crystals of **15RINGS** were obtained through an evaporation method and these obtained crystals are good enough for SCXRD analysis. **15RINGS** is the longest acene derivative confirmed by SCXRD so far. Though **20RINGS** is also soluble, it can be only characterized by ^{1}H NMR. Its single crystals still cannot be obtained.

6.2 Experimental Methods

6.2.1 Materials

All the chemicals and solvents are purchased and used without further treatment unless special note. Tetrahydrofuran (THF) was dried by refluxing with Na and indicated by benzophenones. Dichloromethane (DCM) was dried by refluxing with CaH_2 for 24 h.

6.2.2 Instruments and methods:

Electrospray ionization high-resolution mass spectrum (HR-MS (ESI)) was recorded on a Waters Q-Tof premierTM mass spectrometer. ^{1}H-NMR and ^{13}C-NMR were tested on Bruker Advance 300 spectrometer and the chemical shift values were given in ppm. UV-vis absorbance was tested on a Shimadzu UV-2501 spectrophotometer. Cyclic voltammetry was tested on a CHI 604E Electrochemical Analyzer. A glassy carbon (diameter: 1.6 mm; area 0.02 cm^2) was used as the working electrode, platinum wires were used as the counter electrode and the reference electrode, respectively. $^{n}Bu_4NPF_6$ (0.1M) was used as supporting electrolyte. The potential was recorded in an anhydrous DCM solution and the scanning rate was 50 mV/s. Fc+ /Fc (HOMO = -4.80 eV) was used as an external standard.

6.2.3 Synthesis

2,7,10,17-tetra((triisopropylsilyl)ethynyl)phenanthro[4,5-abc]quinoxalino[2,3-i]phenazine-4,5-dione (6.5).

1,4-bis((triisopropylsilyl)ethynyl)phenazine-2,3-diamine **6.3** (114 mg, 0.2 mmol) and 2,7-bis((triisopropylsilyl)ethynyl)pyrene-4,5,9,10-tetraone **6.4** (623 mg, 1mmol) were dissolved in a mix solvent of $CHCl_3$ (100 mL) and AcOH (50 mL). Subsequently, the orange solution was refluxed under argon at 80 ˚C for 36 h. After that, the solvent was removed by rotary evaporation, and the residue solid was purified by silica column chromatography (CH_2Cl_2: hexane = 1:3). The excess compound **6.4** was collected to be reused. The crude product **6.5** (blackish green in solution) and its reduced form compound (red color in solution, almost the same R_f on TLC with compound **6.5**) were collected together, and then dried under reduced pressure at 60 ºC and treated with excess amount of active MnO_2 (1g) in dry methylene chloride (20 mL) at room temperature for 2 h. Subsequently, MnO_2 was removed by filtrated through celite and washed with methylene chloride until the filtrate was colorless. After removing the solvent, the solid was dissolved in small amount of $CHCl_3$ and reprecipitated by adding methanol (50 mL). The solid was collected by filtration and washed with methanol (20 mL × 2) to afford pure compound **6.5** (160 mg, 0.14 mmol, 70%) as black solid. ^{1}H NMR (300 MHz, CDCl3): δ = 9.63 (s, 2H), 8.58 (s, 2H), 8.28 (m, 2H), 7.91 (m, 2H), 1.43 (br, 42H) 1.25 (br, 42H). ^{13}C NMR (75 MHz, $CDCl_3$): δ = 178.65, 145.41, 143.40, 142.74, 141.62, 137.81, 135.62, 132.29, 131.06, 130.48, 130.29, 130.12, 125.85, 123.04, 112.63, 104.67, 102.40, 96.67, 19.11, 18.78, 11.67, 11.48. HR-MS (ESI) m/z Calc. for $[M+H]^+$ $C_{72}H_{93}N_4O_2Si_4$: 1157.6376, found : 1157.6349.

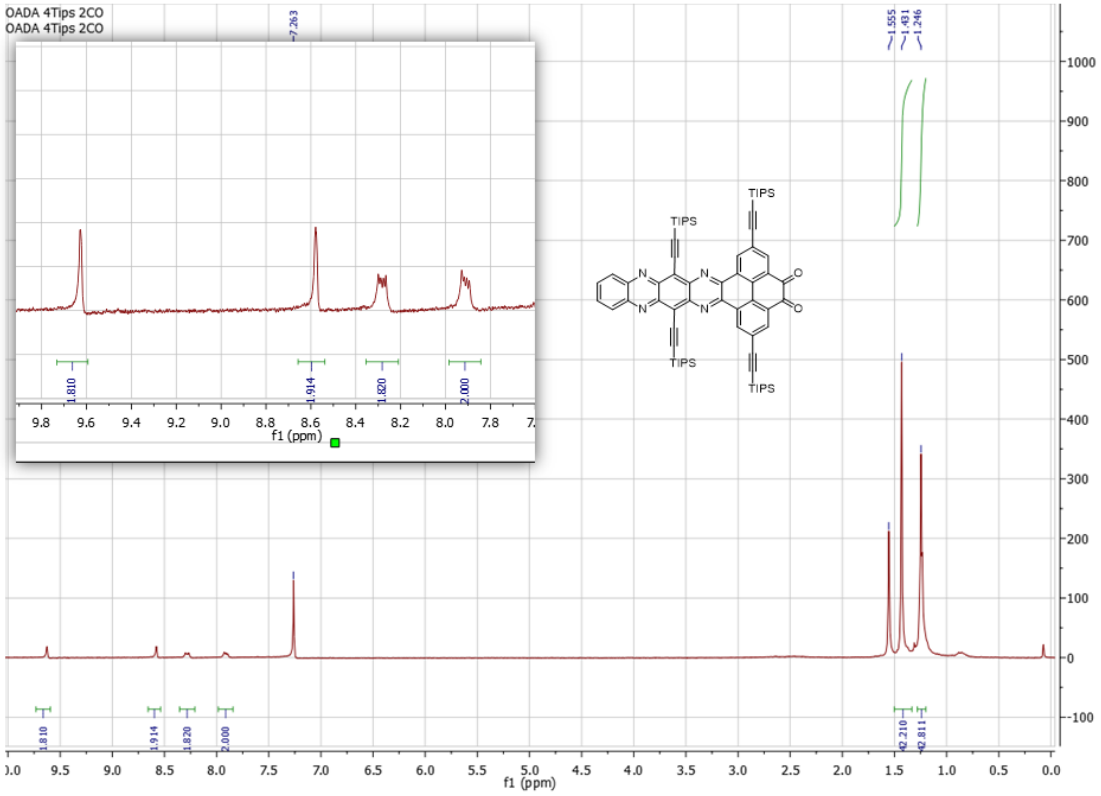

Fig 6.1 ^{1}H NMR spectrum of compound **6.5**, 300 MHz, $CDCl_3$, room temperature.

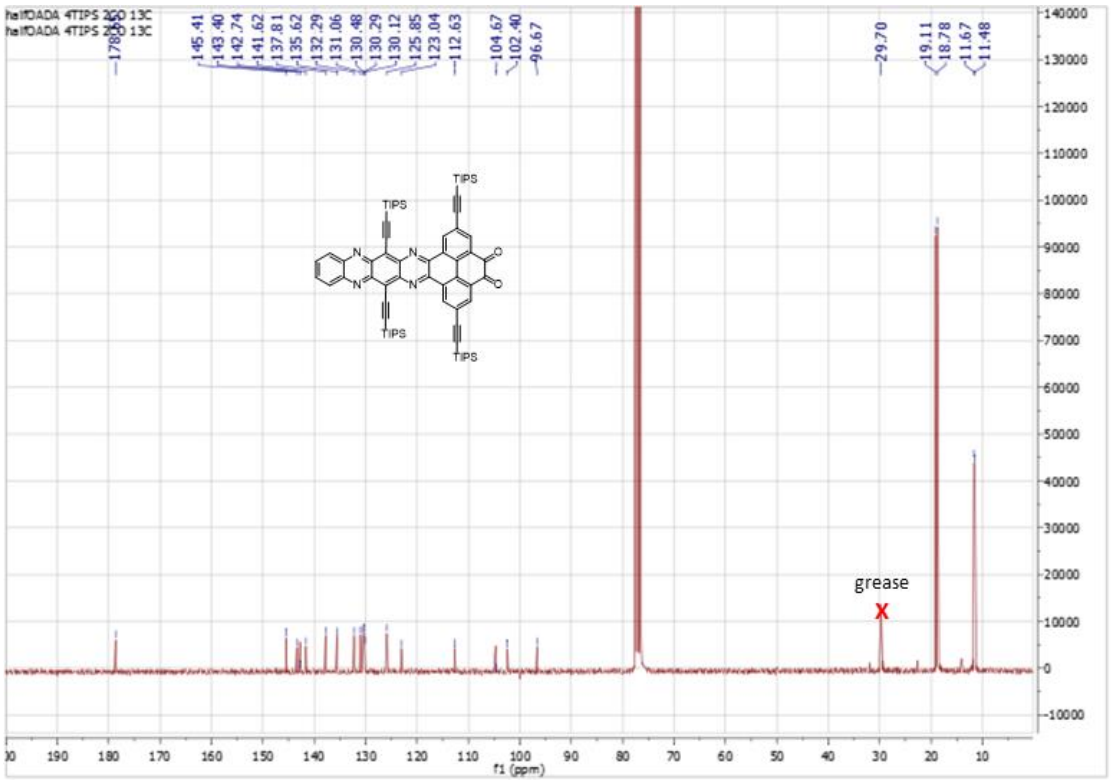

Fig 6.2 ^{13}C NMR spectrum of compound **6.5**, 75 MHz, $CDCl_3$, room temperature.

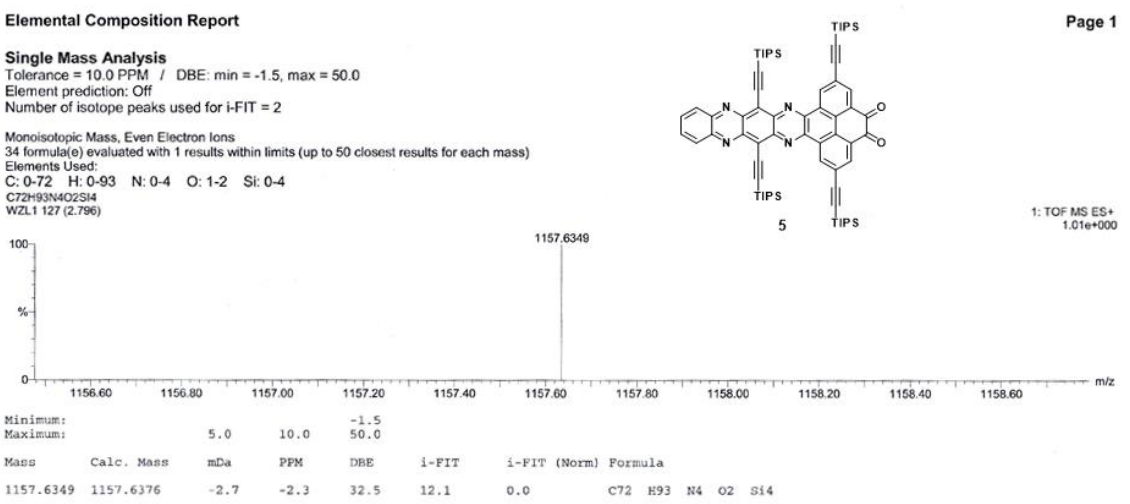

Fig 6.3 HR-MS(ESI) spectrum of compound **6.5**

Compound 6.8

Compound **6.5** (231 mg, 0.2 mmol) and Compound **6.7** (116 mg, 0.22 mmol) were dissolved in a mixed solvent of $CHCl_3$ (30 mL) and AcOH (15 mL) and refluxed under argon at 80 ºC for 30 h. Subsequently, the solvent was removed by rotary evaporation, and the residue was purified by silica column chromatography (CH_2Cl_2: hexane = 1:3). The crude product **6.8** was dissolved in small amount of $CHCl_3$ and reprecipitated by adding methanol (60 mL). The solid was collected by filtration and washed with methanol (20 mL × 2) to afford pure compound **6.8** (180 mg, 0.12 mmol, 60%) as black solid. H NMR (300 MHz, CDCl3): δ = 9.82 (s, 2H), 9.74 (s, 2H), 8.32 (m, 2H), 7.92 (m, 2H), 1.49 – 1.22 (m, 126H). ^{13}C NMR (75 MHz, $CDCl_3$): δ = 155.29, 145.22, 144.18, 144.17, 143.41, 141.84, 141.61, 133.39, 133.27, 131.97, 130.45, 130.23, 130.03, 128.40, 124.73, 122.72, 114.52, 112.14, 111.24, 105.90, 102.66, 101.71, 94.34, 19.15, 19.03, 18.88, 12.08, 11.69, 11.53. HR-MS (ESI) m/z Calc. for $[M+H]^+$ $C_{100}H_{135}N_8Si_6S$: 1647.9146, found : 1647.9116.

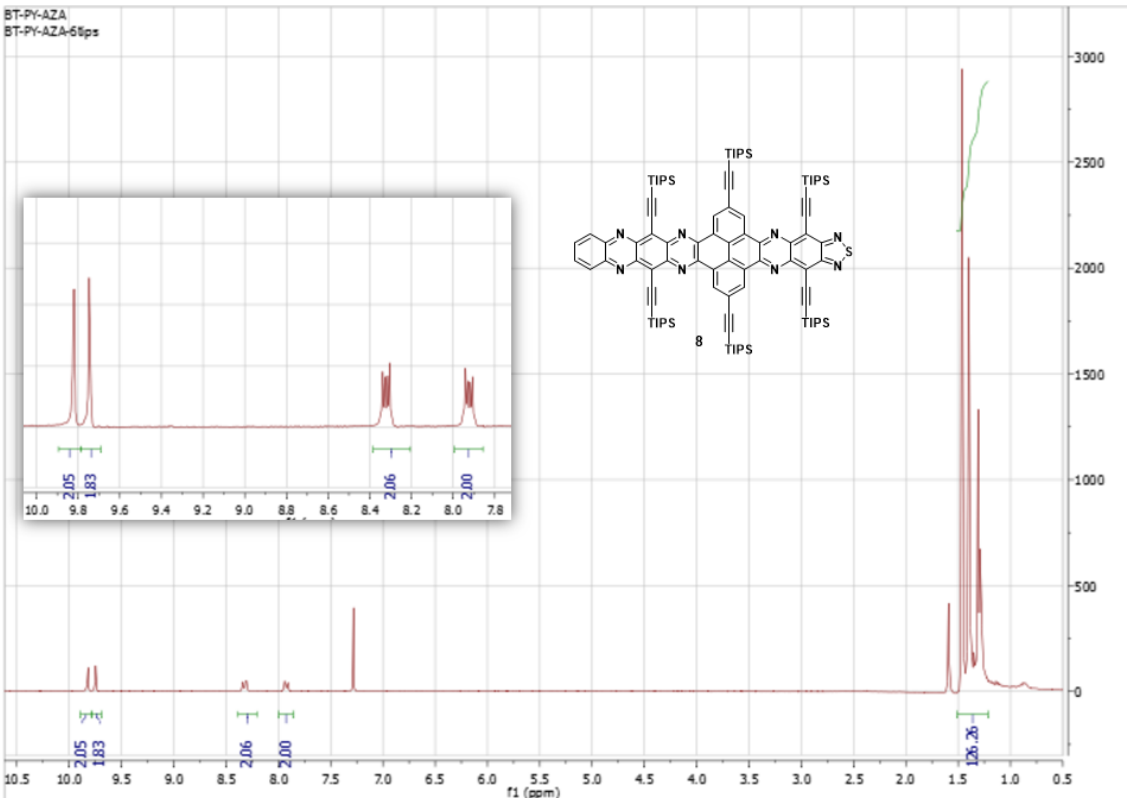

Fig 6.4 ^{1}H NMR spectrum of compound **6.8**, 300 MHz, $CDCl_3$, room temperature

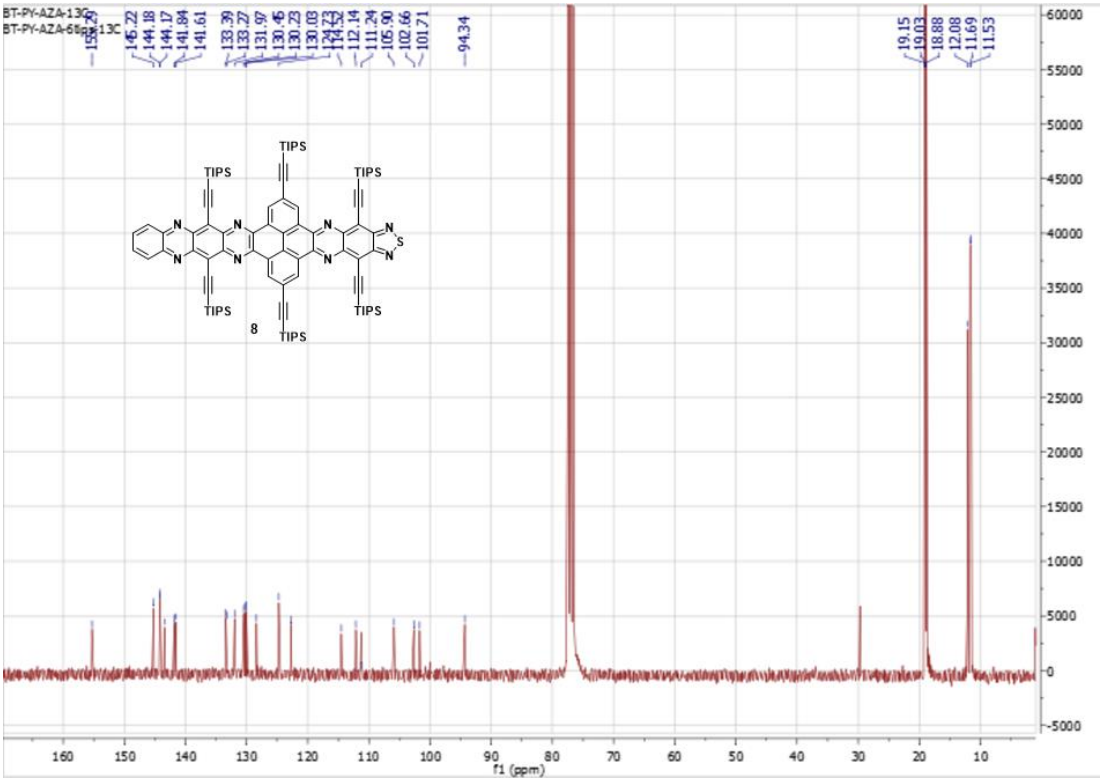

Fig 6.5 ^{13}C NMR spectrum of compound **6.8**, 75 MHz, $CDCl_3$, room temperature

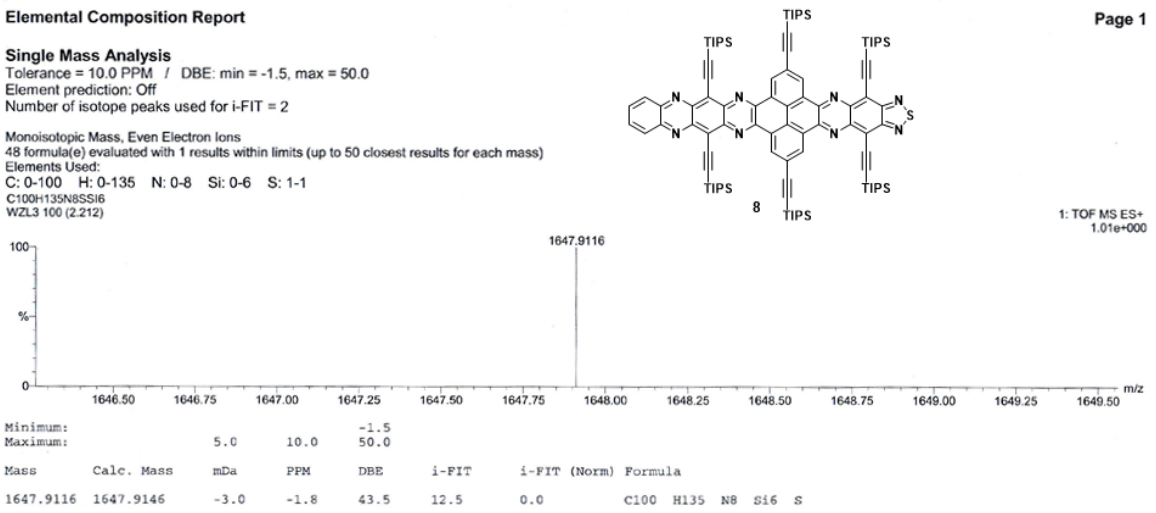

Fig 6.6 HR-MS(ESI) spectrum of compound **6.8**

Compound 6.9

Compound **6.8** (165 mg, 0.1 mmol) was dissolved in dry THF (15 mL) under argon and stirred at 0 ºC. Subsequently, $LiAlH_4$ (38 mg, 1mmol) was slowly added. After that, the reaction mixture was allowed to warm to room temperature and stirred for 14 h. The completion of the reaction was confirmed by TLC, and then the reaction was quenched with a saturated aqueous NH_4Cl solution. The mixture was extracted with diethyl ether (30 mL × 3). The combined organic layers were dried over Na_2SO_4 and concentrated under reduced pressure to afford compound **6.9** as brownish black solid (155 mg, 95%). ^{1}H NMR (300 MHz, CDCl3): δ = 9.78 (s, 4H), 8.31 (m, 2H), 7.91 (m, 2H), 4.96 (br, 4H) 1.49-1.20 (m, 126H). ^{13}C NMR (75 MHz, $CDCl_3$): δ = 145.08, 145.01, 143.44, 143.35, 141.98, 139.65, 138.92, 131.87, 131.74, 131.17, 130.91, 130.44, 129.79, 127.14, 123.83, 122.47, 111.68, 106.68, 104.31, 103.47, 102.75, 100.98, 93.01, 19.15, 19.04, 18.89, 12.10, 11.69, 11.37. HR-MS (ESI) m/z Calc. for $[M+H]^+$ $C_{100}H_{139}N_8Si_6$: 1619.9738, found : 1619.9731.

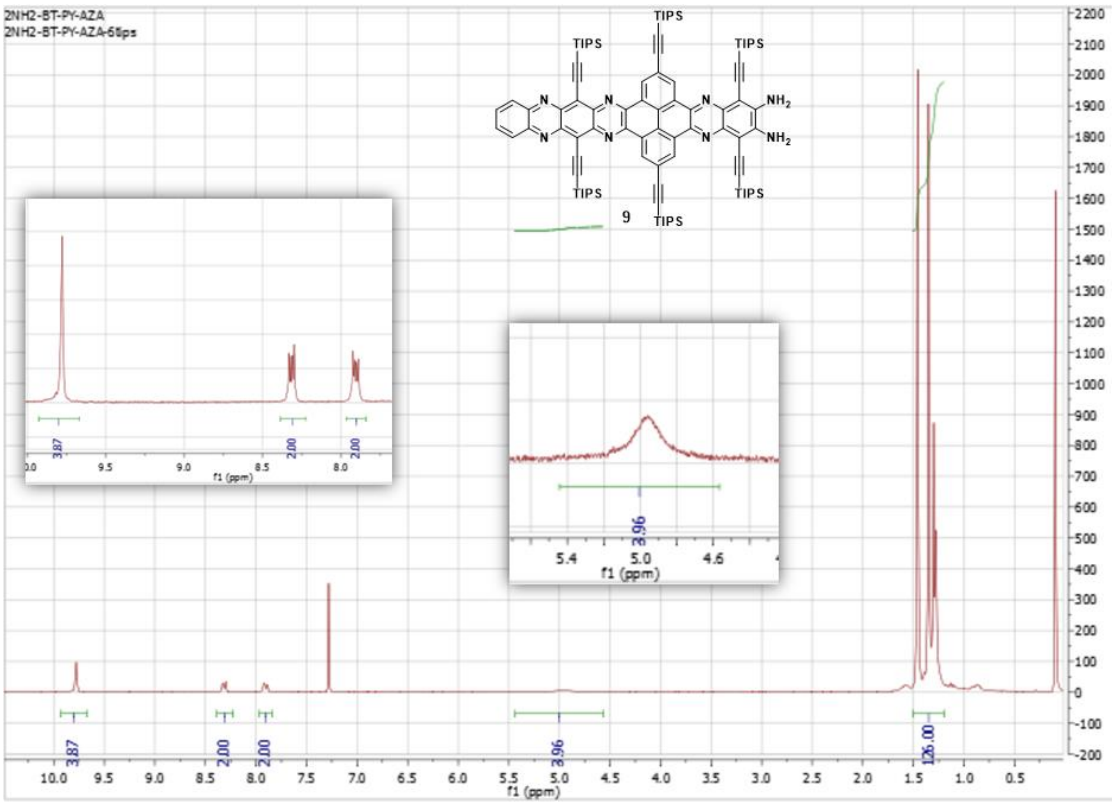

Fig 6.7 ^{1}H NMR spectrum of compound **6.9**, 300 MHz, $CDCl_3$, room temperature

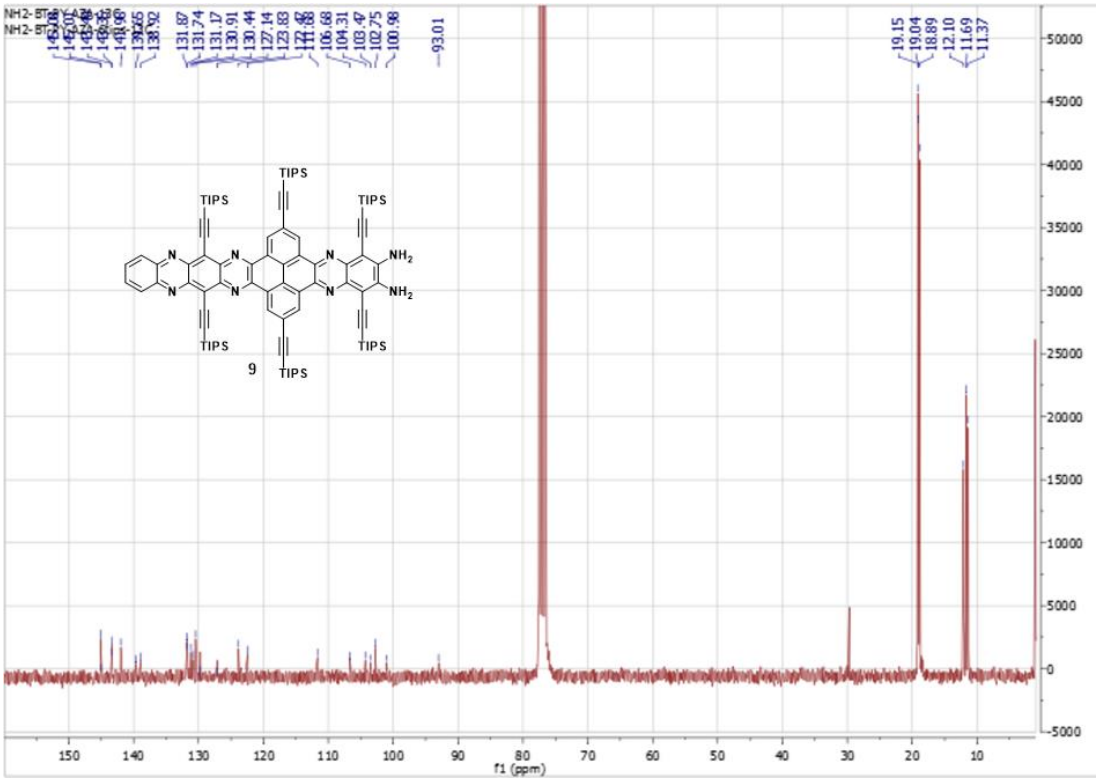

Fig 6.8 ^{13}C NMR spectrum of compound **6.9**, 75 MHz, $CDCl_3$, room temperature

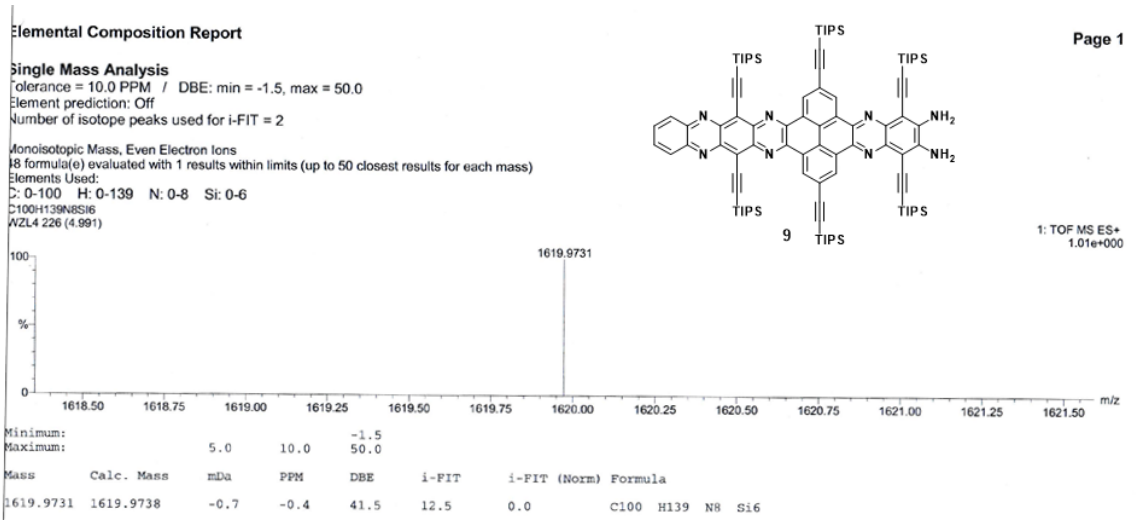

Fig 6.9 HR-MS(ESI) spectrum of compound **6.9**

Compound 15RINGS.

Compound **6.9** (32 mg, 0.02 mmol) and compound **6.5** (23 mg, 0.02 mmol) were dissolved in a mixed solvent of $CHCl_3$ (20 mL) and AcOH (5 mL) and refluxed under argon at 80 ºC for 48 h. Subsequently, the solvent was removed by rotary evaporation, and the residue was purified by silica column chromatography (CH_2Cl_2: hexane = 1:3). The crude product **15RINGS** was dissolved in small amount of $CHCl_3$ and reprecipitated by adding methanol (30 mL). The solid was collected by filtration and washed with methanol (10 mL × 2) to afford pure compound **15RINGS** (25 mg, 0.009 mmol, 46%) as black solid. ^{1}H NMR (300 MHz, CDCl3): δ = 9.89 (d, 8H), 8.33 (m, 4H), 7.93 (m, 4H), 1.60-1.22 (m, 240H (This number is larger than the theoretical number of 210, due to the peak of H_2O was merged in these peaks.)). ^{13}C NMR (75 MHz, $CDCl_3$): δ = 145.26, 144.37, 144.03, 143.51, 142.62, 141.95, 133.51, 133.40, 132.02, 130.52, 130.32, 130.24, 128.48, 124.74, 122.77, 122.28, 112.12, 111.79, 106.06, 102.75, 102.46, 94.50, 19.29, 19.16, 18.92, 12.13, 11.71, 11.58. HR-MS (ESI) m/z Calc. for $[M+Na]^+$ $C_{172}H_{228}N_{12}Na^{28}Si_8{}^{29}Si_2$: 2766.5792, $C_{172}H_{228}N_{12}Na^{29}Si_9{}^{30}Si$: 2766.5769, found : 2766.5842.

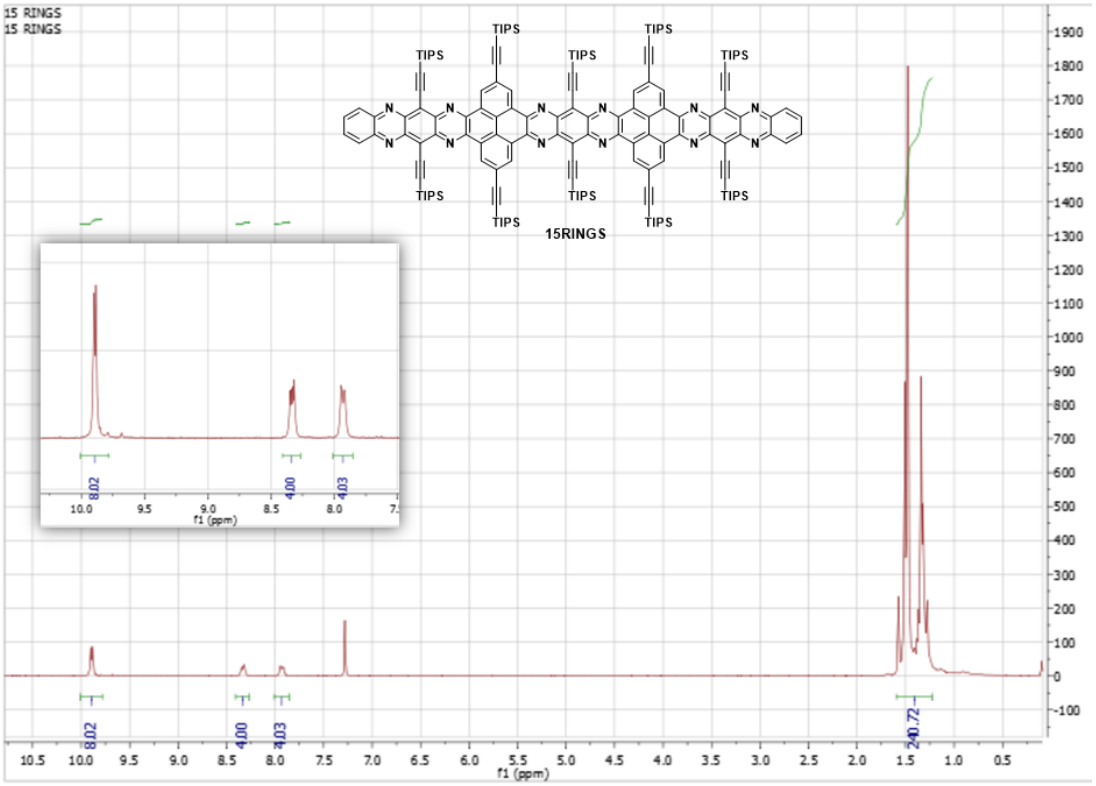

Fig 6.10 ^{1}H NMR spectrum of compound **15RINGS**, 300 MHz, $CDCl_3$, room temperature

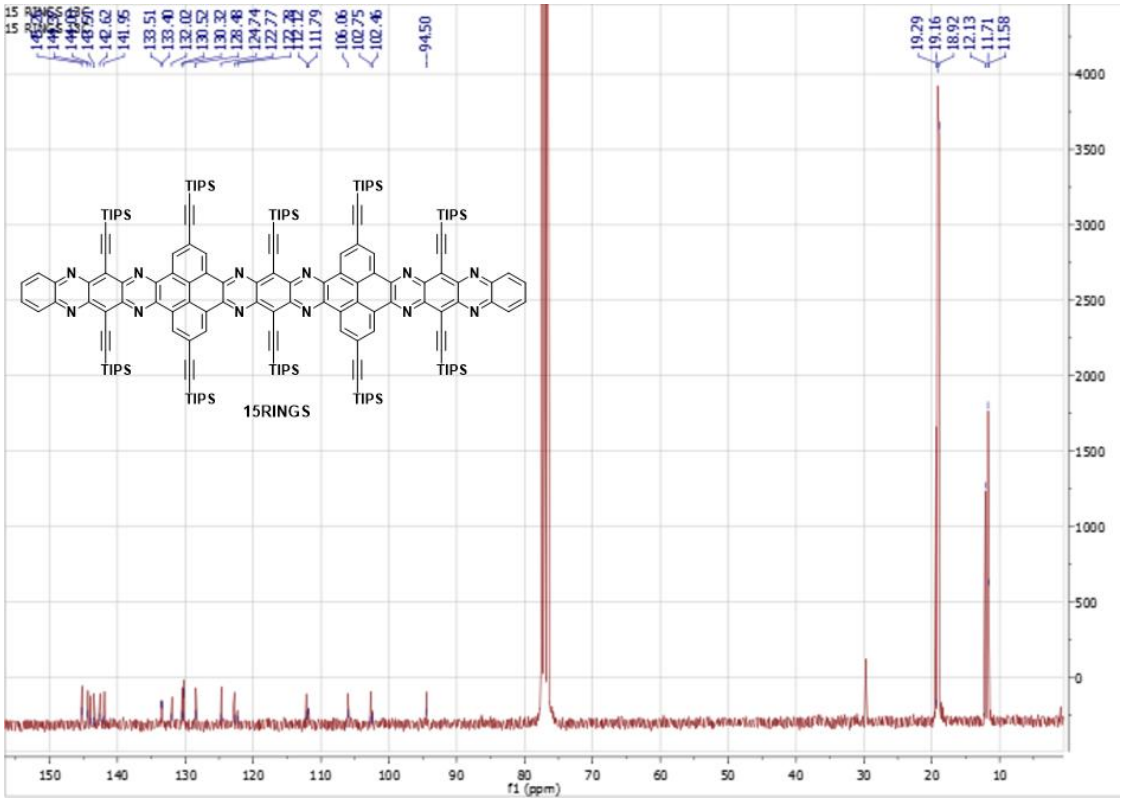

Fig 6.11 ^{13}C NMR spectrum of compound **15RINGS**, 75 MHz, $CDCl_3$, room temperature

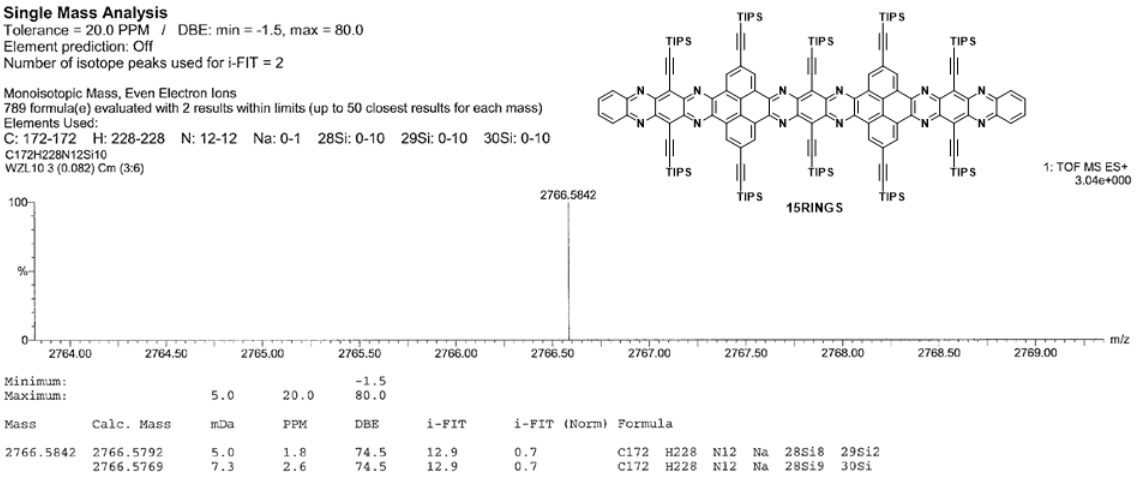

Fig 6.12 HR-MS(ESI) spectrum of compound **15RINGS**

Compound 6.10

Compound **6.4** (62 mg, 0.1 mmol) and Compound **6.7** (116 mg, 0.22 mmol) were dissolved in a mix solvent of $CHCl_3$ (20 mL) and AcOH (10 mL) and refluxed under argon at 80 ºC for 24 h. Subsequently, the solvent was removed by rotary evaporation, and the residue was purified by silica column chromatography (CH_2Cl_2: hexane = 1:3). The crude product **6.8** was dissolved in small amount of $CHCl_3$ and reprecipitated by adding methanol (60 mL). The solid was collected by filtration and washed with methanol (20 mL × 2) to afford pure compound **6.8** (140 mg, 0.12 mmol, 87%) as brownish red solid. ^{1}H NMR (300 MHz, CDCl3): δ = 9.72 (s, 4H), 1.47-1.22 (m, 126H). ^{13}C NMR (75 MHz, $CDCl_3$): δ = 155.31, 144.14, 141.61, 133.29, 130.06, 128.39, 124.75, 114.55, 111.33, 105.84, 101.69, 94.47, 19.02, 18.86, 12.03, 11.53. HR-MS (ESI) m/z Calc. for $[M+H]^+$ $C_{94}H_{131}N_8Si_6S_2$: 1603.8554, found : 1603.8593.

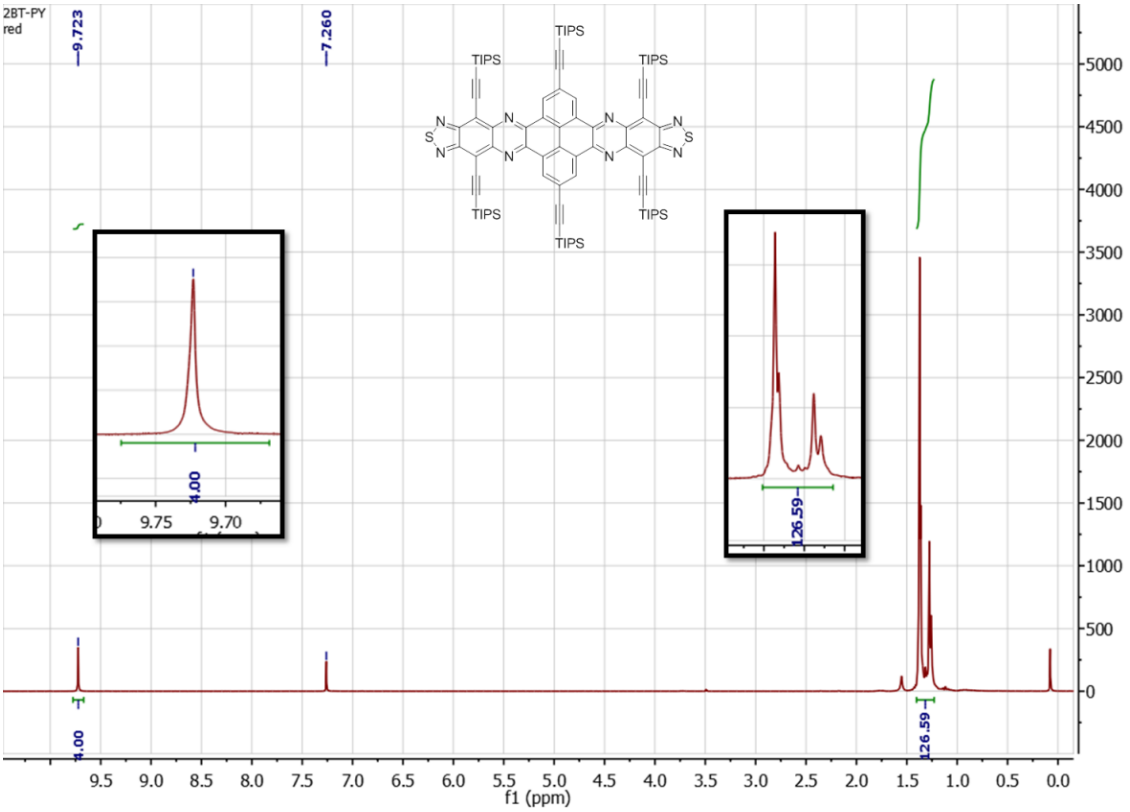

Fig 6.13 ^{1}H NMR spectrum of compound **6.10**, 300 MHz, $CDCl_3$, room temperature

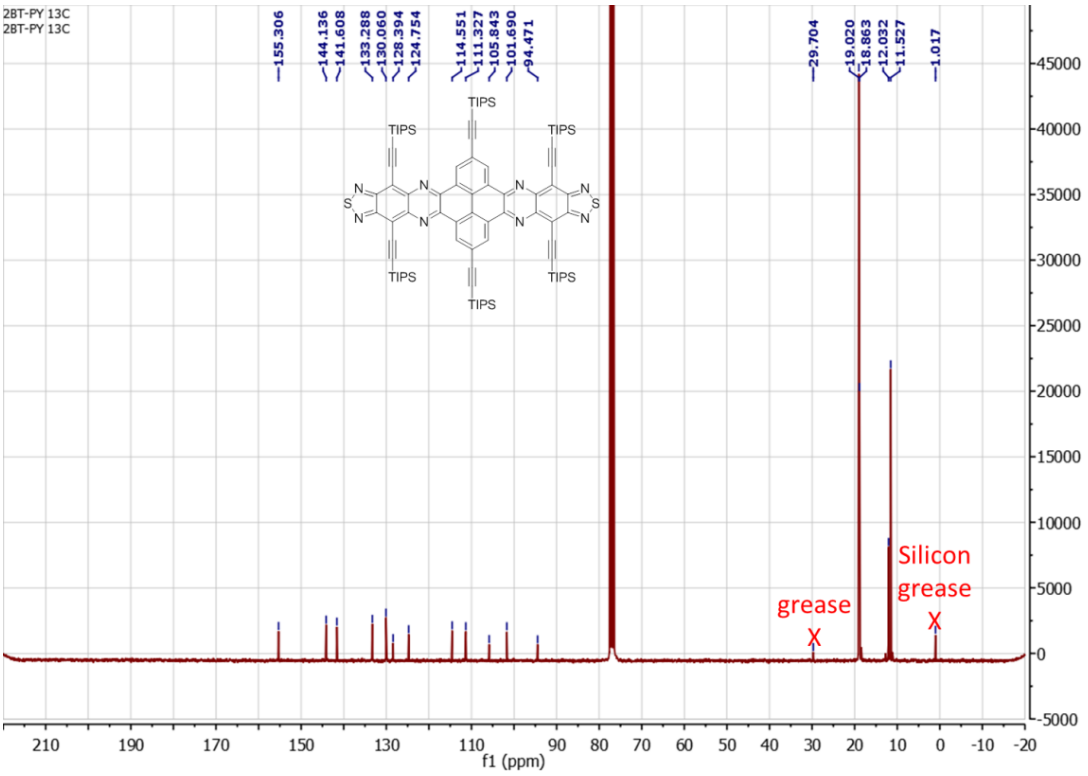

Fig 6.14 ^{13}C NMR spectrum of compound **6.10**, 75 MHz, $CDCl_3$, room temperature

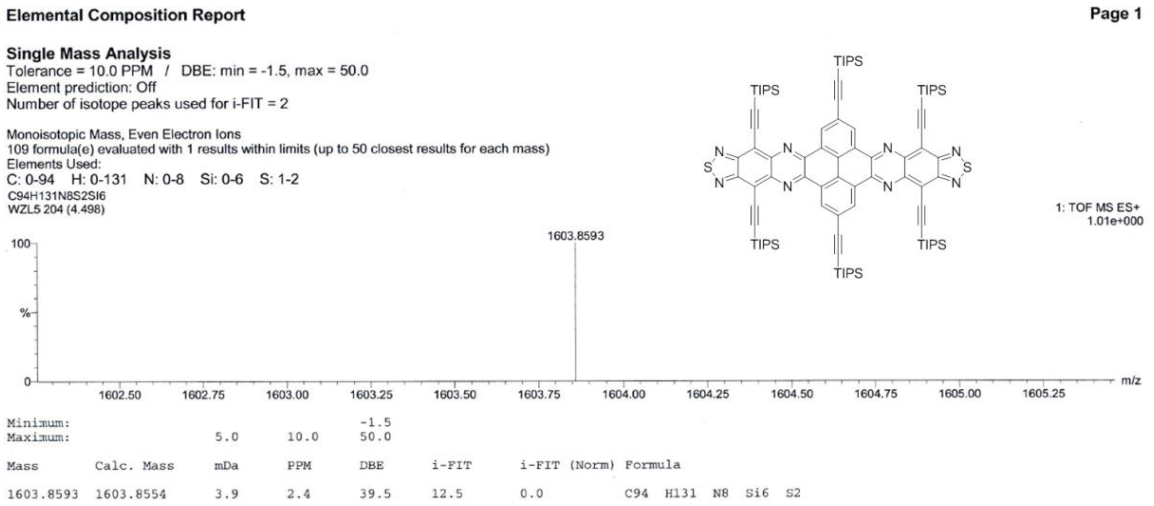

Fig 6.15 HR-MS(ESI) spectrum of compound **6.10**

Compound 6.11

Compound **6.10** (160 mg, 0.1 mmol) was dissolved in dry THF (15 mL) under argon and stirred at 0 ºC. Subsequently, $LiAlH_4$ (76 mg, 2mmol) was slowly added. After that, the reaction mixture was allowed to warm to room temperature and stirred for 14 h. The reaction was confirmed to complete by TLC and quenched with a saturated aqueous NH_4Cl solution. The mixture was extracted with diethyl ether (30 mL × 3). The combined organic layers were dried over Na_2SO_4 and concentrated under reduced pressure to afford compound **6.9** as brownish yellow solid (150 mg, 97%). ^{1}H NMR (300 MHz, CDCl3): δ = 9.70 (s, 4H), 4.89 (s, 8H), 1.37-1.22 (m, 126H). ^{13}C NMR (75 MHz, $CDCl_3$): δ = 143.15, 139.50, 130.42, 129.44, 129.35, 129.29, 125.93, 122.98, 104.09, 103.64, 101.16, 19.04, 18.89, 12.08, 11.38 (One carbon peak missing). HR-MS (ESI) m/z Calc. for $[M+H]^+$ $C_{94}H_{139}N_8Si_6$: 1547.9738, found : 1547.9773.

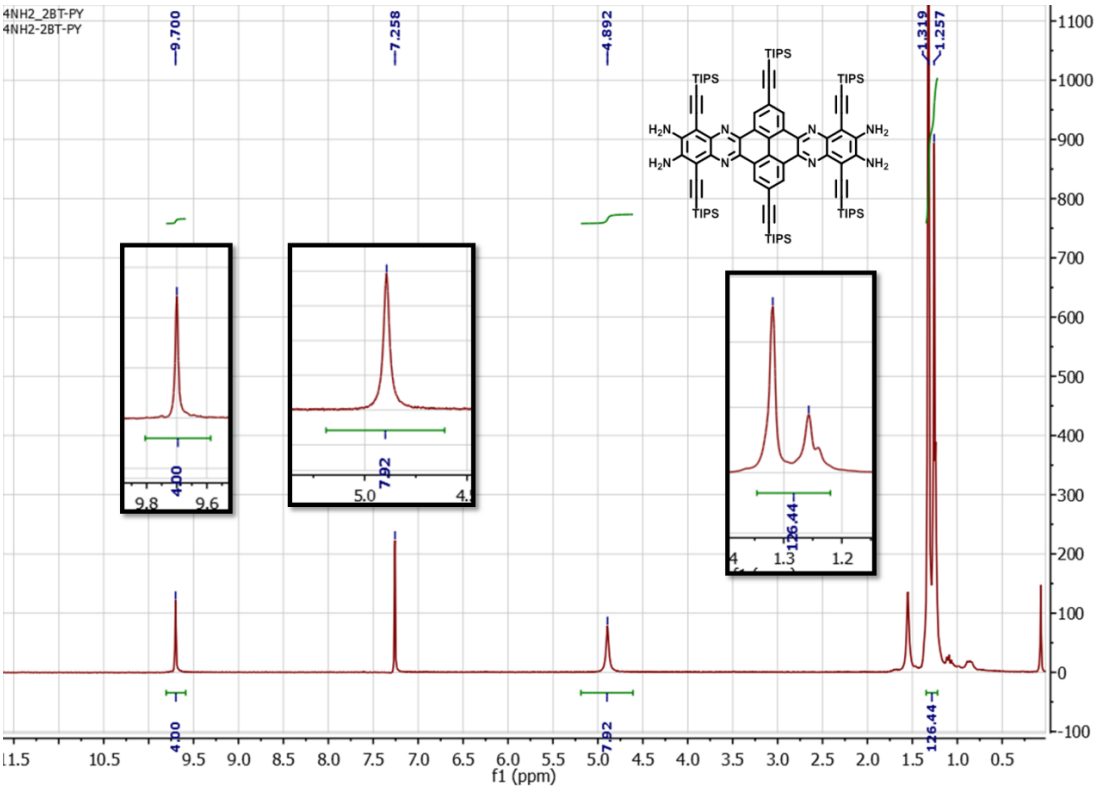

Fig 6.16 ^{1}H NMR spectrum of compound **6.11**, 300 MHz, $CDCl_3$, room temperature

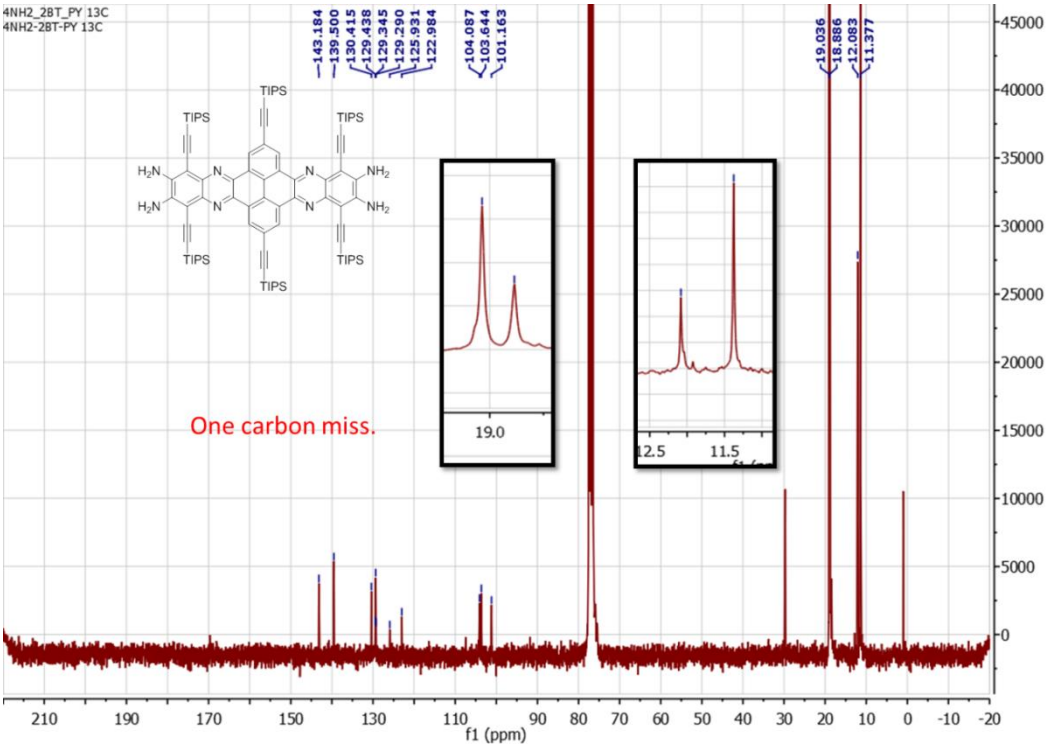

Fig 6.17 ^{13}C NMR spectrum of compound **6.11**, 75 MHz, $CDCl_3$, room temperature

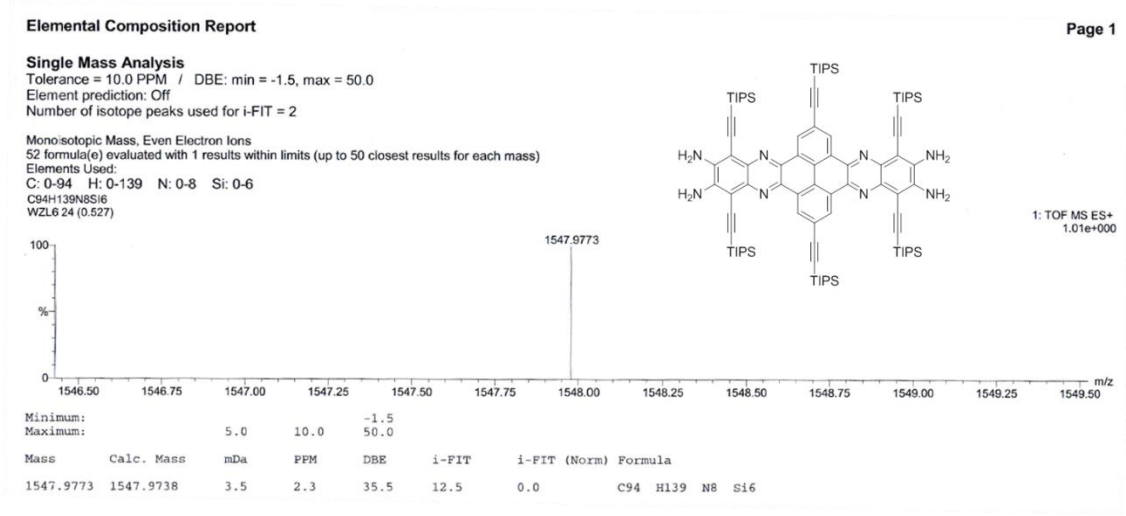

Fig 6.18 HR-MS(ESI) spectrum of compound **6.11**

20RINGS

Compound **6.11** (31 mg, 0.02 mmol) and compound **6.5** (51 mg, 0.044 mmol) were dissolved in a mixed solvent of $CHCl_3$ (20 mL) and AcOH (5 mL) refluxed under argon at 80 ºC for 48 h. Subsequently, the solvent was removed by rotary evaporation, and the residue was purified by silica column chromatography (CH_2Cl_2: hexane = 1:3). The crude product **20RINGS** was dissolved in a small amount of $CHCl_3$ and reprecipitated by adding methanol (30 mL). The solid was collected by filtration and washed with methanol (10 mL × 2) to afford pure compound **20RINGS** (20 mg, 0.005 mmol, 26%) as black solid. ^{1}H NMR (300 MHz, CDCl3): δ = 9.86 (m, 12H), 8.33 (m, 4H), 7.94 (m, 4H), 1.60-1.20 (m, 330H (This number is larger than the theoretical number of 294, due to the peak of H_2O was merged in these peaks.)). ^{13}C NMR (75 MHz, $CDCl_3$) (low quality): δ = 145.31, 145.21, 144.41, 144.34, 143.49, 143.44, 142.68, 142.63, 142.47, 142.43, 141.91, 130.36, 130.28, 130.13, 128.37, 122.17, 112.10, 110.18, 106.17, 103.55, 102.67, 94.41, 19.36, 19.16, 19.06, 18.92, 12.12, 11.71, 11.59, 11.39.

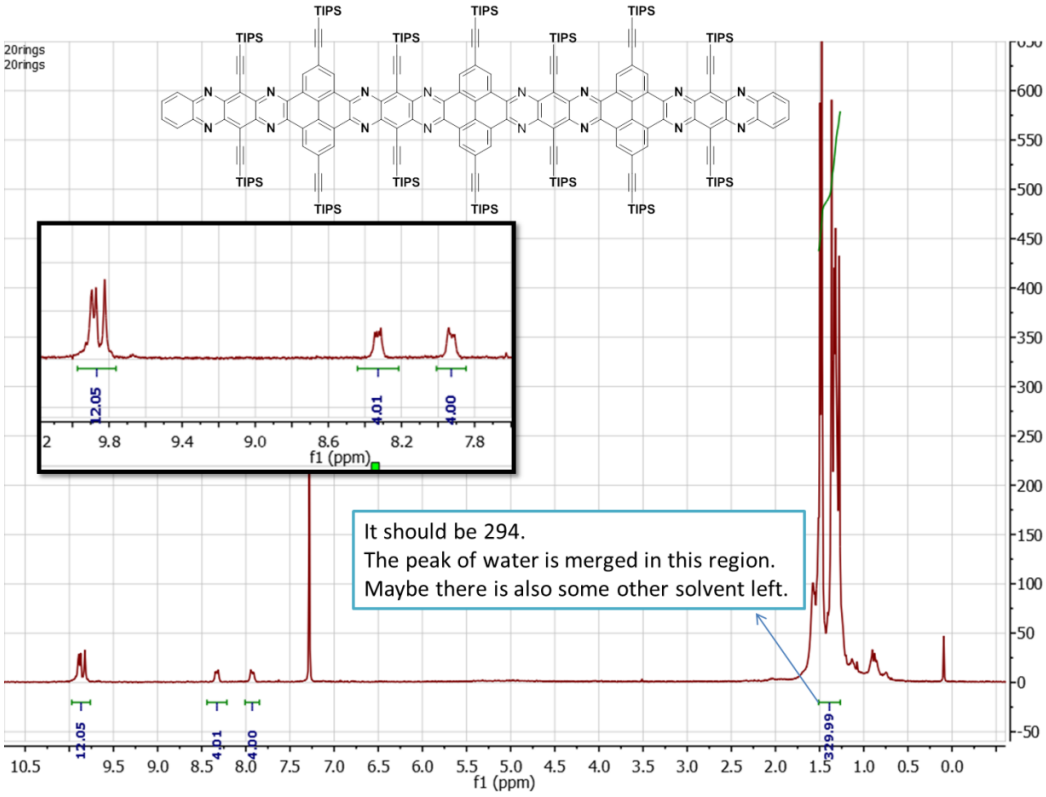

Fig 6.19 ^{1}H NMR spectrum of compound **20RINGS**, 300 MHz, $CDCl_3$, room temperature

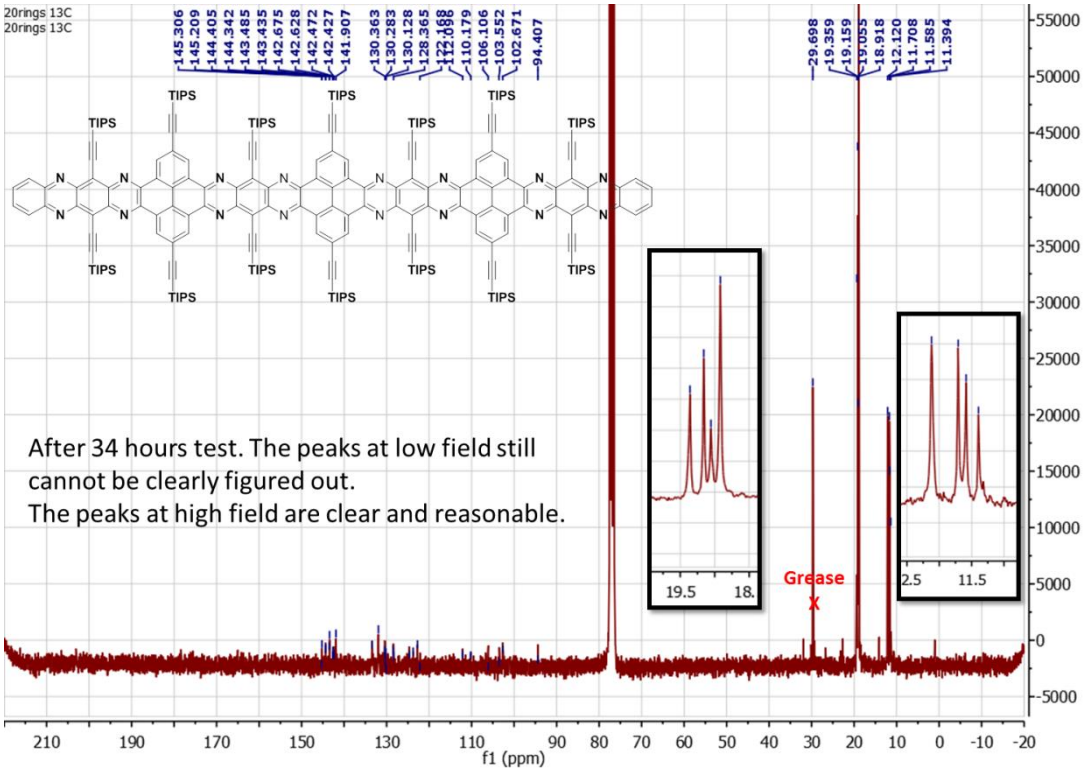

Fig 6.20 ^{13}C NMR spectrum of compound **20RINGS**, 75 MHz, $CDCl_3$, room temperature

6.2.4 Femtosecond Transient Absorption Spectroscopy

A Ti:sapphire femtosecond laser system was used to provided laser pulses for the femtosecond transient absorption measurements. A regenerative amplifier (Spectra Physics, Spitifire) seeded with a mode-locked Ti:sapphire laser (Spectra Physics, Tsunami) was used to delivered laser pulses at 800 nm (120 fs, 1 kHz), which was subsequently divided into two components by using a 9:1 beam splitter. The major component was sent to an optical parametric amplifier (Spectra Physics, OPA-800CF) to generate the pump pulses (480 nm, 130 fs, 1 kHz). The minor component was further attenuated and focused into a 3-mm sapphire plate to generate the probe pulses. A band-pass filter (SPF-750, CVI) was inserted into the probe beam to select visible probe (420–750 nm). The time delay between the pump and probe beams were regulated through a computer-controlled motorized translation stage in the pump beam. A magic scheme was adopted in the pump-probe measurement when necessary. The temporal resolution between the pump and the probe pulses was determined to be ~150 fs (FWHM). The transmitted light was detected by a CMOS linear image sensor (S8377-512Q, Hamamatsu). The excitation pulsed energy was ~ 50 nJ/pulse as measured at the sample site. The stability of the samples was spectrophotometrically checked before and after each experiment. Analysis of the kinetic traces derived from time-resolved spectra was performed using a nonlinear least-square fitting to a general sum-of-exponentials function after deconvolution of instrument response function (IRF).

6.2.5 Single-crystal X-ray diffraction

The suitable single-crystal (0.02 × 0.06 × 0.08 mm) was selected for single-crystal X-ray data collection with a Bruker SMART APEX-II CCD area detector on a D8 goniometer. The data were collected by using graphite-monochromated and Cu Kα radiation (λ = 1.54178 Å) with the ω scan method at 153 K. The data were processed with the SAINT program of the APEX3 software for reduction and cell refinement. Multi-scan absorption corrections were applied by using the SADABS program for area detector. All structures were solved by the direct method and refined by the full-matrix least-squares method on F2 (SHELX-97).[11] All non-H atoms were refined anisotropically. Hydrogen atoms were

placed in idealized positions and included as riding with Uiso (H) = 1.2 Ueq (C). Crystallographic data and structural refinements are summarized in table 6.1.

CCDC 1537461 contains the supplementary crystallographic data for this crystal The data can be obtained free of charge from The Cambridge Crystallographic Data Centre via www.ccdc.cam.ac.uk/data_request/cif.

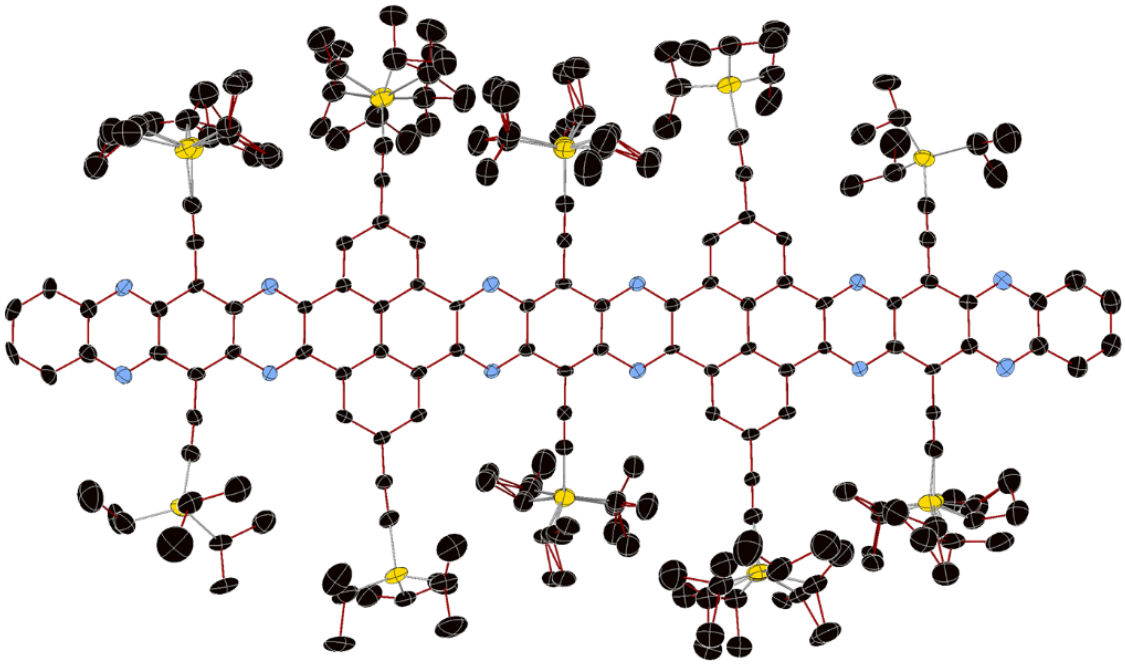

Fig 6.21 The ellipsoid plot of the **15RINGS** shows that the atomic thermal ellipsoids of carbon and nitrogen atoms in the skeleton are acceptable although the TIPS chains are disorder in some degree (50% probability ellipsoid, color scheme: C, black; N, blue; Si, yellow. H atoms are omitted for clarity)

Table 6.1 Crystallographic data and structure refinement parameters of the compound **15RINGS**

	15RINGS
T (K)	153 (2)
Formula	C_{364} H_{450} N_{24} O_{10} Si_{20}
Formula weight	5883.25
Crystal system	triclinic
Space group	$P\bar{1}$
Z	1
a (Å)	20.1652 (5)
b (Å)	21.0142 (5)
c (Å)	21.8327 (6)
α (deg)	70.114 (2)
β (deg)	89.128 (2)
γ (deg)	89.198 (2)
V (Å^3)	8698.7 (4)
ρ calcd (g/cm^3)	1.123
λ (Cu Kα) (Å)	1.54178
Collected reflns	63252
Unique reflns	29982
Parameters	2447
R (int)	0.2658
R_1 [$I > 2\sigma(I)$]	0.1019
wR_2 [$I > 2\sigma(I)$]	0.2314
GOF	0.931

6.3 Principle outcomes

6.3.1 Synthetic route

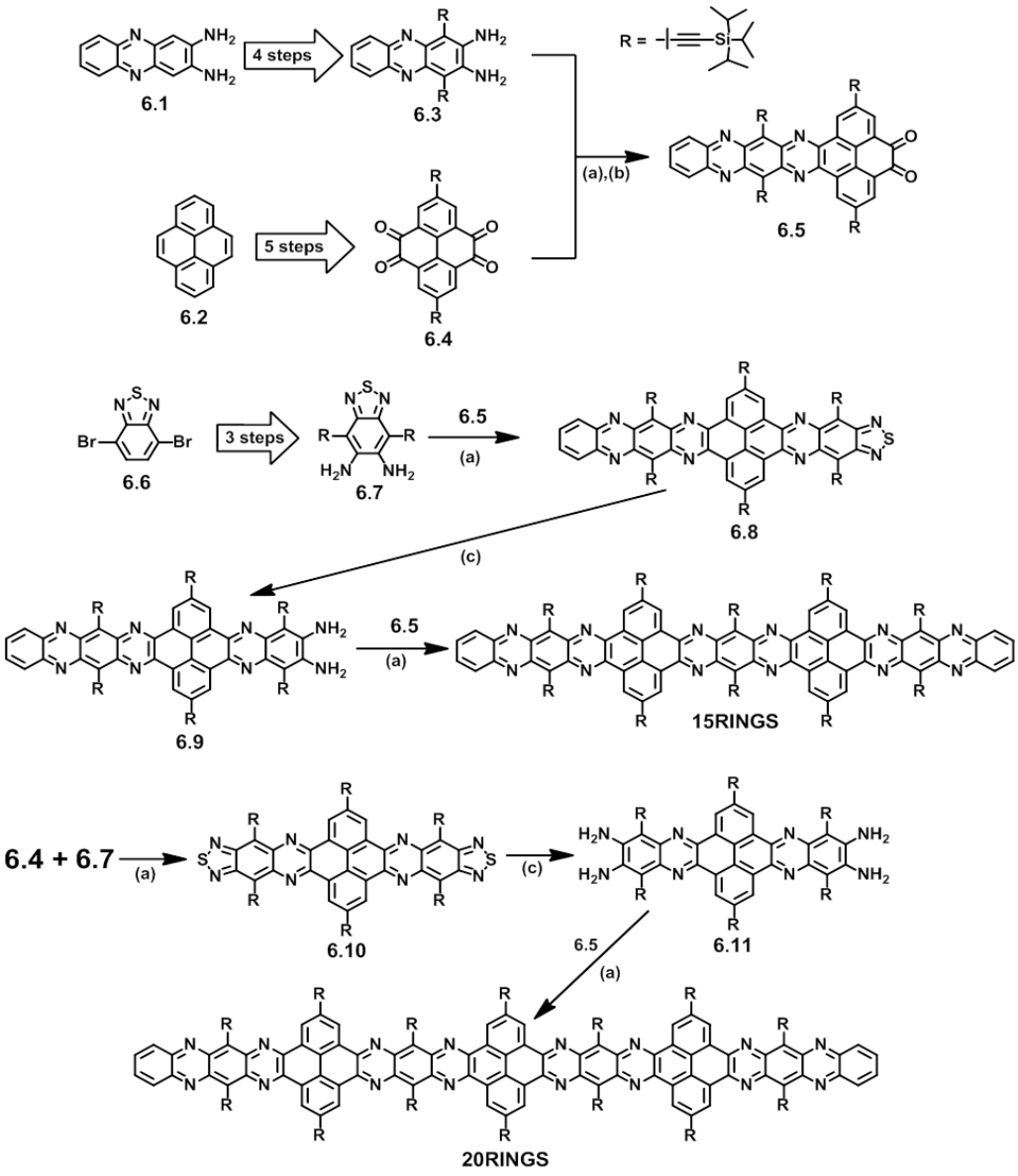

Scheme 6.1 Synthetic route of 1**5RINGS** and **20RINGS**: (a) $CHCl_3$, AcOH, reflux; (b) MnO_2, CH_2Cl_2; (c) $LiAlH_4$, THF, 0ºC to RT

The synthetic route is shown in Scheme 6.1. Compounds **6.3**[12], **6.4**[13] and **6.7**[14] were synthesized according to the reported procedures. Following Anthony's strategy, TIPS groups were employed to increase the solubility crystallinity.[1a,1b,9] Compound **6.5** were synthesized in a good yield (~ 70%) through the condensation reaction between diamine

6.3 and an excess amount of tetraketone **6.4**. The unreacted tetraketone can be reused after silica gel column chromatography separation. Compound **6.8** was obtained through the condensation reaction between **6.5** and **6.7**. After reducing compound **6.8** with lithium aluminum hydride, diamine **6.9** was obtained in 95% yield. Subsequently, the target compound **15RINGS** was prepared by condensing diketone **6.5** with diamine **6.9** in a mixed solvent of $CHCl_3$/AcOH under reflux condition. **20RINGS** was synthesized in the similar strategy. Compound **6.10** was synthesized by condensing **6.5** with **6.7**. Subsequently, the key tetraamine compound **6.11** can be obtained by reducing compound **6.10**. **20RINGS** was synthesized through the condensation reaction between **6.5** and **6.11**. Except for **20RINGS**, All new compounds were confirmed by ^{1}H NMR, ^{13}C NMR, and HR-MS. **20RINGS** can only be confirmed by ^{1}H NMR. Its solubility is not good enough to give a clear ^{13}C NMR spectrum, and its single crystal still cannot be obtained. Due to the structure of **20RINGS** cannot be confirmed by SCXRD, yet; its characterization will not be discussed here. This chapter focuses on the **15RINGS** compound.

6.3.2 Single-crystal X-ray diffraction analysis

Black needle-like single-crystals of N-heteroacene **15RINGS** were obtained through slowly evaporating the solution of mixed solvents (chloroform: 1,4-dioxane = 1:1) under ambient conditions. Although the attachment of ten TIPS groups onto the backbone of **15RINGS** could significantly improve the solubility and benefit to grow high-quality single crystals, the disorder of these TIPS groups has already shown negative effects on the X-ray diffraction of these crystals. Luckily, this negative effect does not affect too much on the crystal structure analysis of **15RINGS.** The atomic thermal ellipsoids of carbon and nitrogen atoms in the skeleton are reasonable (Fig 6.21). The single crystal of **15RINGS** belongs to the triclinic system ($P\bar{1}$ space group) with a big unit cell (V = 8698.67 (4) Å^3). The SCXRD analysis clearly confirmed that this prepared pyrene-bridged N-heteroacene possesses 15 aromatic rings linearly annulated in a row (Fig 6.22a). **15RINGS** is the longest N-heteroacene structure (more than 35 Å) confirmed by SCXRD so far. The configuration of the π-conjugated backbone is not as planar as the calculated result (in Fig 6.22a and b), however, slightly twisted at two pyrene units (Fig 6.22c). This is similar to the previously reported pyrene/acene hybrids.[8b] This twisted

conformation might help stabilize this large azaacene by releasing the strain resulted from the structure packing. The packing motif of **15RINGS** is shown in Fig 6.22b. It clearly indicated that two adjacent **15RINGS** molecules formed a dimer first. Subsequently, the as-formed dimers further adopted a face-to-edge herringbone packing mode with the short distance of about 3.38 Å between the adjacent π-planes. It suggests that there is some π-π interaction between the dimer. Fig 6.22c shows the side view of the dimer with a dual-bending feature (the bending angle is about 13.2°). The top view of the dimer indicates that the overlapped degree of the adjacent π-plane is very small (Fig 6.22d). Finally, solvent molecules (1,4-dioxane) are caged in the crystal voids formed by four dimers.

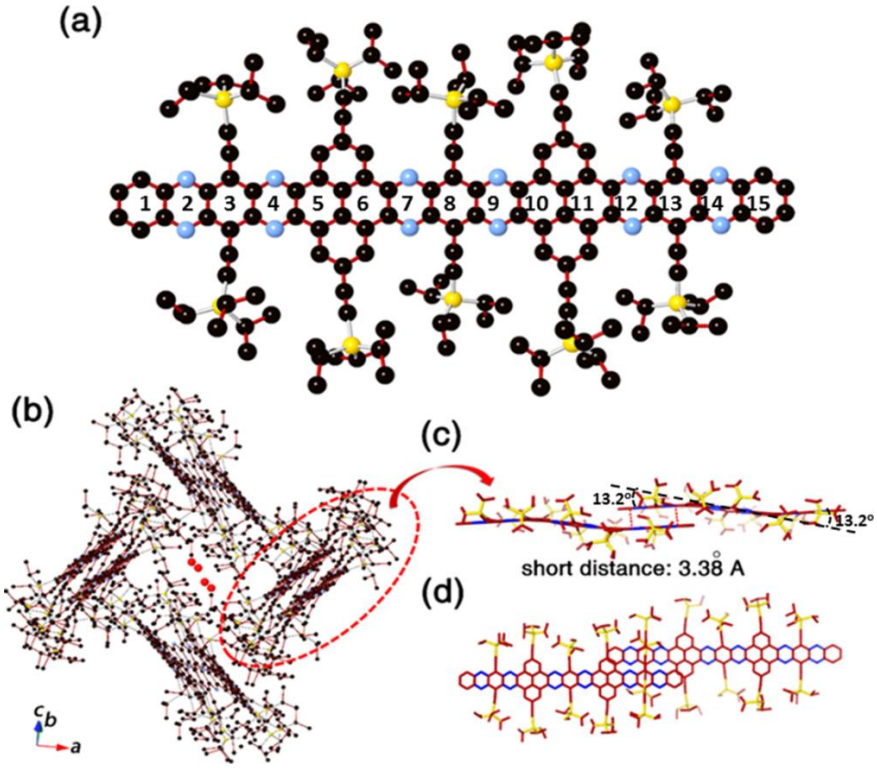

Fig 6.22 Single-crystal X-ray structure of **15RINGS**: (a) Molecular structure (color scheme: C, black; N, blue; Si, yellow. H atoms are omitted for clarity); (b) Crystal packing mode of **15RINGS** shows that two adjacent molecules form a dimer first, and then 1,4-dioxane molecules are encaged (just show the O atoms in here) in the crystal voids formed by four dimers; (c) Side view of the dimer shows a dual-bending feature with a short distance of about 3.38 Å between the adjacent π-planes; (d) Top view of the dimer indicates that the overlapped degree of the adjacent π-planes is very small

6.3.3 Photophysical and electrochemical properties and energy levels

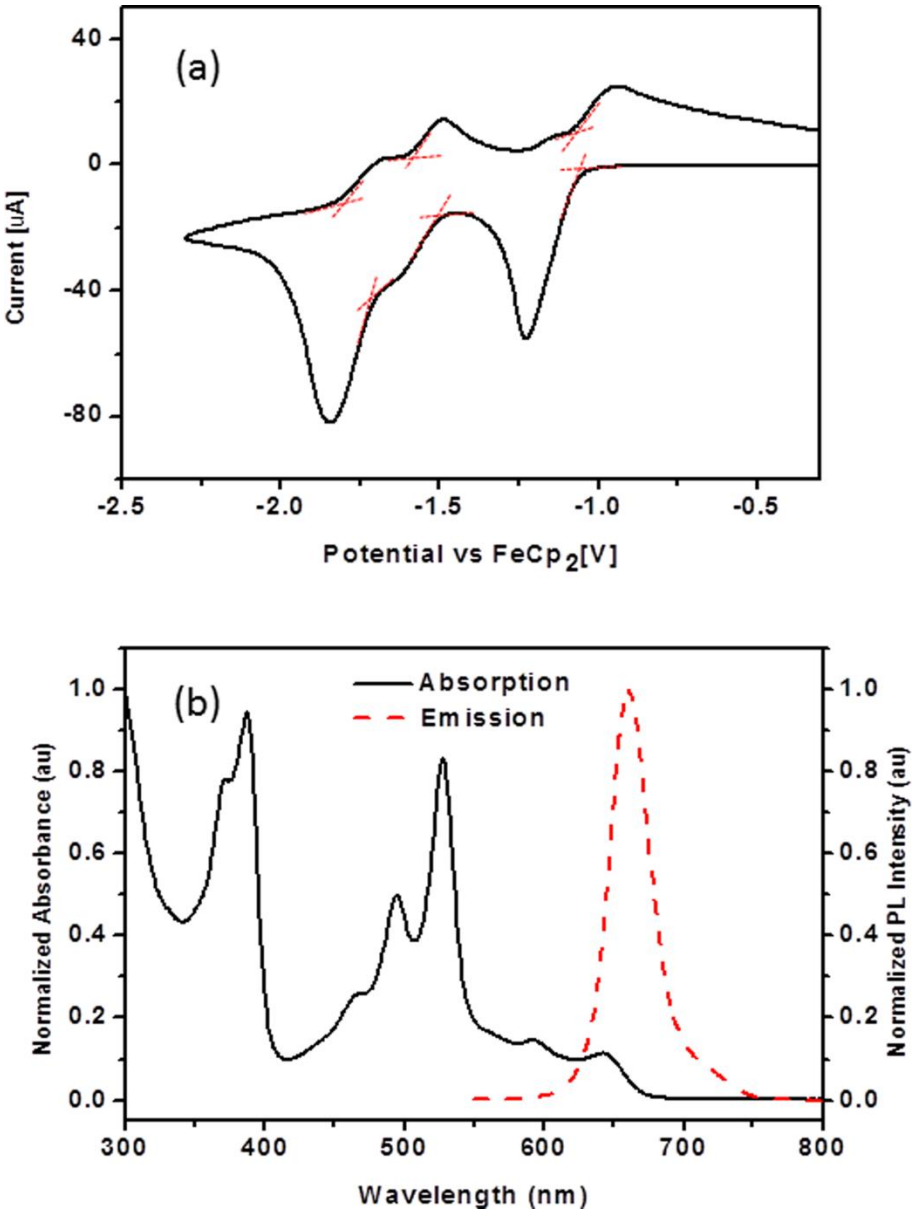

Fig 6.23 (a) Cyclic voltammetry curve of **15RINGS** (Electrolyte: 0.1M nBu_4NPF_6, Scanning speed: 50 mV/s); (b) UV-vis absorption spectrum and fluorescence emission spectrum of **15RINGS** in CH_2Cl_2 (λ_{ex} = 530 nm)

The molecular energy levels of **15RINGS** were studied by cyclic voltammetry (CV) and UV-vis absorption (UV) test. As shown in Fig 6.23a, **15RINGS** shows three reversible reduction peaks at E_{onset} = -1.06V, -1.50V, and -1.70V in CV curve, from where the levels of LUMO, LUMO+1 and LUMO+2 can be calculated to be -3.74 eV, -3.30 eV and -3.10

eV, respectively. In UV-vis absorption spectrum (Fig 6.23b), **15RINGS** shows four peaks between 400 nm and 700 nm. The onset absorption at 670 nm suggests that the optical band gap is 1.85 eV, which is quite similar to that of azapentacenes.[10] This phenomenon corroborates with the cross-conjugation property of the pyrene units: although the backbone of **15RINGS** is conjugated, the aromaticity is interrupted at pyrene units. According to Clar's rule, one pyrene can add two aromatic π-sextets in the π-conjugated backbone,[15] which can effectively increase the stability of the large acenes. The photoluminescence (PL) spectrum of **15RINGS** is also investigated (Fig 6.23b). **15RINGS** has a maximum emission at 661 nm upon excitation at 530nm. Ten TIPS groups compacted along the whole π-conjugated backbone can prevent the formation of π-π interaction by steric hindrance, consequently increase the solubility and reduce the fluorescence quenching from the intermolecular interaction. However, due to the self-absorption effect caused by the broad overlap between PL and UV spectra, along with other nonradiative transition processes, **15RINGS** only exhibits a low fluorescence quantum yield (Φ) of 3%.

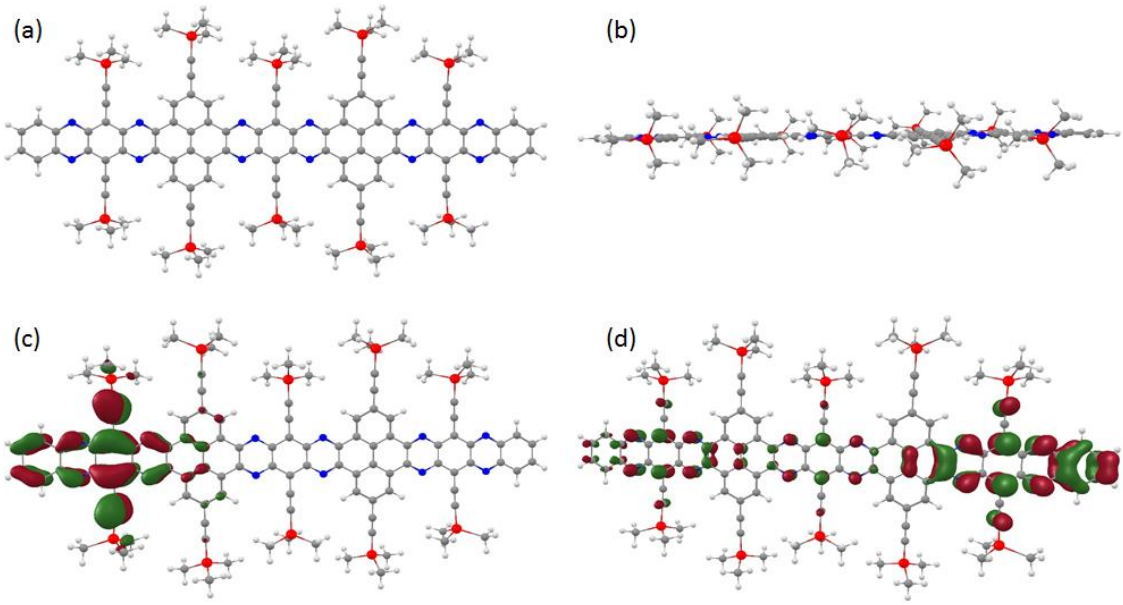

Fig 6.24 Optimal molecular structure of **15RINGS** using density functional theory (DFT) calculation (Red: Si atom, Blue: N atom, Gray: C atom and Light gray: H atom) (a) top view; (b) side view; Simulated orbits of HOMO (c) and LUMO (d) of **15RINGS** by DFT calculation

Electronic structure of **15RINGS** has been theoretically investigated by quantum chemistry calculations performed with Gaussian09 package[16]. The molecular geometry of **15RINGS** in the ground state (Fig 6.24a and b) was optimized and verified by no imaginary frequency analysis using density functional theory (DFT) calculation at the B3PW91/6-31G(d) level.[16] The groups on Si are substituted with methyl groups in the DFT calculation. The corresponding frontier molecular orbitals are illustrated in Fig 6.24c and d. As shown in Fig 6.24d, the electron distribution of LUMO orbital is more delocalized throughout the backbone of **15RINGS**, while mainly centralizing in the end of the molecule. The HOMO localizes over the rings on the other end of this molecular backbone. The calculated energies of HOMO, LUMO, and band gap are -5.54 eV, -3.52 eV and 2.02 eV, respectively. The energy of band gap was calculated by the equation of $E_{gap} = E_{LUMO} - E_{HOMO}$. The calculated results are close to experimental energy levels of **15RINGS**. It is noticeable that the isolated molecule considered in DFT calculations was different from the packing motif of **15RINGS** in the crystal shown in Fig 6.22, which caused the difference between calculated energies and experimental results. All photophysical and electrochemical data are summarized in Table 6.2.

Table 6.2 Photophysical and electrochemical data and energy levels (eV) of **15RINGS**

$E_{onset,red}$[1] (V)	$E_{onset,red}$[2] (V)	$E_{onset,red}$[3] (V)	$E_{LUMO,DFT}$ (eV)	$E_{HOMO,DFT}$ (eV)
-1.06	-1.50	-1.70	-3.52	-5.54
$E_{LUMO,CV}$ (eV)	$E_{LUMO+1,CV}$ (eV)	$E_{LUMO+2,CV}$ (eV)	Gap_{DFT} (eV)	$E_{HOMO,opt}$ (eV)
-3.74	-3.30	-3.10	2.02	-5.59
$\lambda_{max,pl}$ (nm)	ϕ_{pl}	$\lambda_{onset,abs}$ (nm)	Gap_{opt} (eV)	
661	3%	670	1.85	

6.3.4 Femtosecond transient absorption spectra

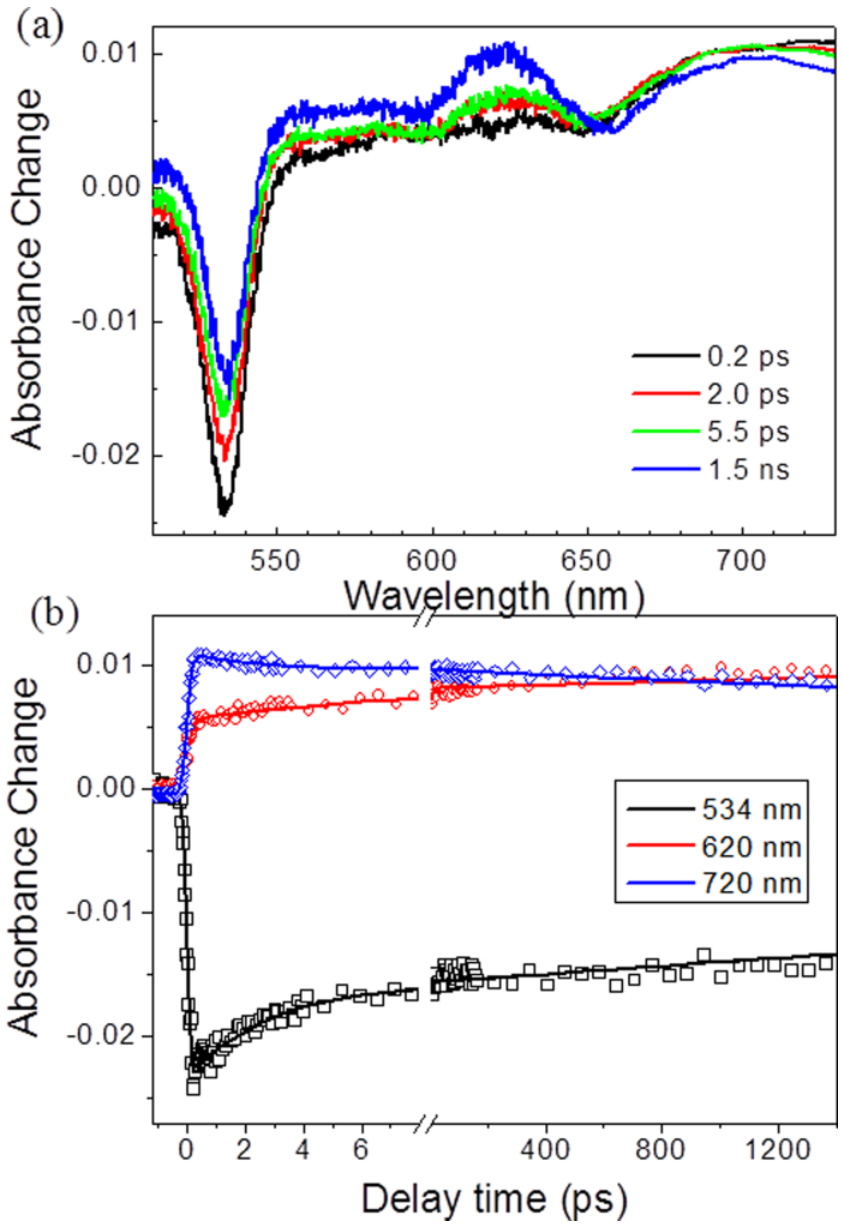

Fig 6.25 Femtosecond transient absorption spectra (a) and the representative kinetic curves (open symbols) as well as the correspond fits (solid lines) (b) of **15RINGS** in dichloromethane solution

Fig 6.25 shows the femtosecond transient absorption spectra of **15RINGS** solution (dichloromethane) upon excitation at 480 nm, which triggers the S2←S0 transition. Photoexcitation of **15RINGS** immediately produces a strong negative band at 534 nm

owing to ground state bleaching (GSB) along with a broad positive excited state absorption band peaked at 730 nm. As time proceeds, the band at 730 nm decays and slightly blue-shifts. Simultaneously, a new spectral feature at 620 nm gradually appears and dominates at ~1.5 ns. The long-lived absorption band is assigned to be the triplet state via intersystem crossing (ISC). The GSB signal decays bi-exponentially with two components of 3.0±0.8 ps and 28±8 ns. Analysis of the 620-nm curve results in one rising lifetime of 1.0±0.2 ns (red line in Fig 6.25b), suggesting the rate constant of 1.0×10^{9} s^{-1} for ISC process.

6.4 Conclusion

In conclusion, two novel pyrene-contained nitrogen-rich nanoribbon **15RINGS** and **20RINGS** are synthesized with 15 and 20 six-membered rings linearly annulated in one row, respectively. The structure of **15RINGS** was confirmed by ^{1}H NMR, ^{13}C NMR, HR-MS, and single crystal X-ray diffraction analysis (SCXRD). This is the longest acene derivative confirmed by single-crystal X-ray diffraction so far. The single-crystal structure analysis indicates that **15RINGS** possesses a dual-bending backbone (the bending angle is about 13.2^{o}), which might be an important factor to stabilize such a large π-conjugated system. The photophysical and electronic properties were studied by CV, UV, PL and DFT calculation. **15RINGS** shows a low LUMO energy of -3.74 eV, a narrow band gap of 1.85 eV, a maximum fluorescence emission at 661 nm with a fluorescence quantum yield of 3%. The low fluorescence quantum yield is due to the self-absorption effect and intersystem crossing. The efficient intersystem crossing in **15RINGS** system has been studied and the result is consistent with its low fluorescence quantum yield (3%). Further study on singlet fission in **15RINGS** did not show positive results.

References

[1]. a) J. E. Anthony, *Angew. Chem. Int. Ed.*, 2008, **47**, 452-483. b) Q. Miao, *Adv. Mater.*, 2014, **26**, 5541-5549. c) U. H. F. Bunz, *Acc. Chem. Res.*, 2015, **48**, 1676-1686. d) J. Li, S. Chen, Z. Wang and Q. Zhang, *Chem. Rec.*, 2016, **16**, 1518-1530. e) T. J. Sisto, Y. Zhong, B. Zhang, M. T. Trinh, K. Miyata, X. Zhong, X. Y. Zhu, M. L. Steigerwald,

F. Ng and C. Nuckolls, *J. Am. Chem. Soc.*, 2017, **139**, 5648-5651. f) C. Wang, J. Zhang, G. Long, N. Aratani, H. Yamada, Y. Zhao and Q. Zhang, *Angew. Chem. Int. Ed.*, 2015, **54**, 6292-6296.f) R. M. Metzger, *Chem. Rev.*, 2015, **115**, 5056-5115.

[2]. a) A. Mateo-Alonso, *Chem. Soc. Rev.*, 2014, **43**, 6311-6324. b) T. Zheng, Z. Cai, R. Ho-Wu, S. H. Yau, V. Shaparov, T. Goodson and L. Yu, *J. Am. Chem. Soc.*, 2016, **138**, 868-875. c) Z. Cai, W.-Y. Lo, T. Zheng, L. Li, N. Zhang, Y. Hu and L. Yu, *J. Am. Chem. Soc.*, 2016, **138**, 10630-10635.

[3].a) U. H. F. Bunz and J. U. Engelhart, *Chem. Eur. J.*, 2016, **22**, 4680-4689. b) C. Wang, P. Gu, B. Hu and Q. Zhang, *J. Mater. Chem. C.*, 2015, **3**, 10055-10065. c) B. Purushothaman, M. Bruzek, S. R. Parkin, A.-F. Miller and J. E. Anthony, *Angew. Chem. Int. Ed.*, 2011, **123**, 7151-7155. d) M. M. Payne, S. R. Parkin and J. E. Anthony, *J. Am. Chem. Soc.*, 2005, **127**, 8028-8029. e) J. U. Engelhart, O. Tverskoy and U. H. F. Bunz, *J. Am. Chem. Soc.*, 2014, **136**, 15166-15169. f) U. H. Bunz, J. U. Engelhart, B. D. Lindner and M. Schaffroth, *Angew. Chem. Int. Ed.*, 2013, **52**, 3810-3821.

[4] H. F. Bettinger, C. Tönshoff, M. Doerr, E. Sanchez-Garcia, *J. Chem. Theory Comput.* **2016**, *12*, 305-312.

[5] B. Gao, M. Wang, Y. Cheng, L. Wang, X. Jing, F. Wang, *J. Am. Chem. Soc.* **2008**, *130*, 8297-8306.

[6] B. Kohl, F. Rominger, M. Mastalerz, *Angew. Chem. Int. Ed.* **2015**, *54*, 6051-6056.

[7] A. H. Endres, M. Schaffroth, F. Paulus, H. Reiss, H. Wadepohl, F. Rominger, R. Krämer, U. H. F. Bunz, *J. Am. Chem. Soc.* **2016**, *138*, 1792-1795.

[8].a) J. Li and Q. Zhang, *ACS Appl. Mater. Interfaces.*, 2015, **7**, 28049-28062. b) J. Xiao, H. M. Duong, Y. Liu, W. Shi, L. Ji, G. Li, S. Li, X.-W. Liu, J. Ma, F. Wudl and Q. Zhang, *Angew. Chem. Int. Ed.*, 2012, **51**, 6094-6098. c) J. Li and Q. Zhang, *Synlett*, 2013, **24**, 686-696. d) P.-Y. Gu, Z. Wang, G. Liu, H. Yao, Z. Wang, Y. Li, J. Zhu, S. Li and Q. Zhang, *Chem. Mater.*, 2017, **29**, 4172–4175.

[9].P.-Y. Gu, Z. Wang and Q. Zhang, *J. Mater. Chem. B.*, 2016, **4**, 7060-7074.

[10]. Z. Wang, J. Miao, G. Long, P. Gu, J. Li, N. Aratani, H. Yamada, B. Liu and Q. Zhang, *Chem. Asian. J.*, 2016, **11**, 482-485.

[11]. G. M. Sheldrick, *Acta Crystallographica Section A: Foundations of Crystallography*, **2008**, *64*, 112-122.

[12]. B. D. Lindner, J. U. Engelhart, O. Tverskoy, A. L. Appleton, F. Rominger, A. Peters, H.-J. Himmel and U. H. F. Bunz, *Angew. Chem. Int. Ed.*, 2011, **50**, 8588-8591.

[13]. S. More, R. Bhosale, S. Choudhary and A. Mateo-Alonso, *Org. Lett.*, 2012, **14**, 4170-4173.

[14]. A. B. Marco, C. Gozalvez, M. Olano, X. Sun, A. Atxabal, M. Melle-Franco, L. E. Hueso and A. Mateo-Alonso, *Phys. Chem. Chem. Phys.*, 2016, **18**, 11616-11619.

[15]. M. Solà, *Front. Chem.*, 2013, **1**.

[16]. Gaussian 09, Revision **A.1**, M. J. Frisch, G. W. Trucks, H. B. Schlegel, G. E. Scuseria, M. A. Robb, J. R. Cheeseman, G. Scalmani, V. Barone, B. Mennucci, G. A. Petersson, H. Nakatsuji, M. Caricato, X. Li, H. P. Hratchian, A. F. Izmaylov, J.Bloino, G. Zheng, J. L. Sonnenberg, M. Hada, M. Ehara, K. Toyota, R. Fukuda, J. Hasegawa, M. Ishida, T. Nakajima, Y. Honda, O. Kitao, H. Nakai, T. Vreven, J. A. Montgomery, Jr., J. E. Peralta, F. Ogliaro, M. Bearpark, J. J. Heyd, E. Brothers,K. N. Kudin, V. N. Staroverov, R. Kobayashi, J. Normand, K. Raghavachari, A. Rendell, J. C. Burant, S. S. Iyengar, J.Tomasi, M. Cossi, N. Rega, J. M. Millam, M. Klene, J. E. Knox, J. B. Cross, V. Bakken, C. Adamo, J. Jaramillo, R.Gomperts, R. E. Stratmann, O. Yazyev, A. J. Austin, R. Cammi, C. Pomelli, J. W. Ochterski, R. L. Martin, K. Morokuma, V.G. Zakrzewski, G. A. Voth, P. Salvador, J. J. Dannenberg, S. Dapprich, A. D. Daniels, Ö. Farkas, J. B. Foresman, J. V. Ortiz,J. Cioslowski, and D. J. Fox, Gaussian, Inc., Wallingford CT, 2009.

Chapter 7*

Quinone Embedded Large Azaacenes and the OFET Behavior

*In this chapter, two large azaacene derivatives **Hex-CO** and **Hept-CO** were synthesized through palladium-catalyzed coupling reactions. These two molecules have been fully characterized including single crystal X-ray diffraction. The extended conjugation on one side of the quinone bridge can induce strong π-π interactions, and the length of the extended conjugation shows a great impact on the stacking modes and almost no influence on the molecular orbital energy levels. **Hex-CO** and **Hept-CO** have the same optical band gap (1.86eV), and the quinone units offer these two molecules deep low LUMO levels (~ -4.27). The OFET performance was investigated. **Hex-CO** and **Hept-CO** show very large transfer integrals for electron transport, and the films of **Hex-CO** and **Hept-CO** show the best electron mobilities of 3.8 × 10^{-3} cm^2 V^{-1} s^{-1} and 9.3 × 10^{-3} cm^2 V^{-1} s^{-1}, respectively.*

Manuscript in preparation. Z. Wang, Z. Wang, Y. Zhou, P. Gu, G. Liu, K. Zhao, L. Nie, Q. Zeng, J. Zhang, Y. Li, R. Ganguly, L. Huang, Z. Liu, Q. Zhang

7.1 Introduction

The azaacene derivatives are an important class of polycyclic aromatic hydrocarbons, which can serve as n-type and ambipolar semiconductors in kinds of applications including sensors[1], organic light-emitting diodes[2], organic memory devices[3], photoelectrochemical cell[4], solar cells[5] and especially in organic field effect transistors (OFETs).[6] The electron mobility of the classic azaacene, 5,7,12,14-tetraazapentacene (TIPS-TAP), can even exceed 10 cm^2 V^{-1} s^{-1} through an improved interface engineering.[7] To achieve better performance, extending the conjugation of the azaacenes is a good choice to adjust the properties, because it can shift the molecular orbital energy levels, increase the π-π interaction and change the molecules stacking structures in the solid state. Scientists have made a lot of effort in this field[8] and several methods have been developed to synthesize large azaacene derivatives.[9] The palladium-catalyzed method recently developed by Bunz's group makes a big step forward to access more azaacene derivatives, especially.[10] However, the dihalide reactants with suitable reactivity for this reaction are still limited and need to be more excavated.

Quinone is a useful unit in the azaacene derivatives. It can extend conjugation and reduce the LUMO energy levels of the molecules to afford n-type semiconductors with better performance.[11] Additionally, it provides the bonding sites for nucleophilic substitution reactions resulting in the real acenes (with only one Clar's π-sextet). This is a common method to introduce substituents into the acenes[12], such as TIPS-alkynyl[13] and phenyl[14]. Moreover, it can also be reduced into benzene unit to form real acenes.[15] The quinone units are normally introduced into the azaacene derivatives through Diels–Alder reactions,[16] condensation reactions between cyclohexanehexone and diamine compounds,[17] and directly oxidizing the azaacenes.[18] All these methods have limitations: either limited choice of reactants or extreme oxidation conditions.

In this chapter, a new method to synthesize quinone-embedded large azaacene derivatives through the palladium-catalyzed reaction is introduced. The large azaacene derivatives **Hex-CO** and **Hept-CO** with six and seven six-membered rings annulated in one row were easily synthesized in good yield and fully characterized by ^{1}H NMR, ^{13}C NMR,

HR-MS and single crystal X-ray diffraction. The quinone bridges can be effectively used to extend the conjugation length, increase the π-π interactions and change the molecules stacking mode in the solid state. The optical and electronic properties are also studied by CV, UV, and DFT calculation. These experiments reveal that the quinone units can effectively decrease the LUMO levels, and the extend conjugation on the other side of the quinone bridge has little influence on the molecular orbital energy levels of the azacenes. Finally, the OFET behaviors were investigated. **Hex-CO** and **Hept-CO** show very large transfer integrals for electron transport. The films of **Hex-CO** and **Hept-CO** show the best electron mobilities of 3.8×10^{-3} cm^2 V^{-1} s^{-1} and 9.3×10^{-3} cm^2 V^{-1} s^{-1}, respectively.

7.2 Experimental Methods

7.2.1 Materials

All the chemicals and solvents are purchased and used without further treatment unless special noted. Chloroform and *N*,*N*-Diisopropylethylamine (Hünig's base) were dried by refluxing with CaH_2 for 24 h.

7.2.2 Instruments and methods

Electrospray ionization high-resolution mass spectrum (HR-MS (ESI)) was recorded on a Waters Q-Tof premierTM mass spectrometer. ^{1}H-NMR and ^{13}C-NMR were tested on Bruker Advance 300 spectrometer and the chemical shift values were given in ppm. UV-vis absorbance was tested on a Shimadzu UV-2501 spectrophotometer. Cyclic voltammetry was tested on a CHI 604E Electrochemical Analyzer. Glassy carbon (diameter: 1.6 mm; area 0.02 cm^2) was used as working electrode, platinum wires were used as the counter electrode and the reference electrode, respectively. $^nBu_4NPF_6$ (0.1M) was used as supporting electrolyte. The potential was recorded in an anhydrous DCM solution and the scanning rate was 50 mV/s. Fc^+/Fc (HOMO = -4.80 eV) was used as an external standard.

7.2.3 Synthesis

Synthesis of 6,17-bis((triisopropylsilyl)ethynyl)naphtho[2,3-b]quinoxalino[2,3-i]phenazine-8,15(7H,16H)-dione (Compound 7.5)

The diamine compound **7.1** (114 mg, 0.2 mmol), dichloride compound **7.2** (125 mg, 0.45 mmol), 2-dicyclohexylphosphino-2',6'-diisopropoxybiphenyl (RuPhos) (7 mg, 0.015 mmol), tris(dibenzylideneacetone)dipalladium(0) ($Pd_2(dba)_3$) (14 mg, 0.015 mmol), dry Hünig's base (5 mL) and dry chloroform (20 mL) were added into the Schlenk flask in the argon. Subsequently, the mixture was further bubbled with argon for 5 min to remove the oxygen. Subsequently, the mixture was stirred at 70 ºC for 48 h. After the mixture was cooled to room temperature, it was filtered on celite and washed with methylene chloride until the filtrate is colorless. The filtrate was washed with saturated ammonium chloride solution and extracted with methylene chloride. The organic layer was collected and dried with Na_2SO_4, Subsequently, Na_2SO_4 was removed by filtration. Subsequently, the solvent was removed. The residue was purified by silica gel column chromatography (Eluent: CH_2Cl_2 : Hex = 1 : 3). Subsequently, the crude product was dissolved in small amount of $CHCl_3$ and reprecipitated by adding methanol. The solid was collected by filtration and washed with methanol to afford pure compound **7.5** (115 mg, 0.15 mmol, 74%) as brown solid. ^{1}H NMR (300 MHz, CDCl3): δ = 8.56 (s, 2H), 8.04 – 7.83 (m, 4H), 7.73 – 7.41 (m, 6H), 1.45 – 1.14 (m, 42H). ^{13}C NMR (75 MHz, $CDCl_3$) δ = 174.88, 144.10, 142.41, 138.02, 134.70, 130.13, 129.57, 129.16, 129.08, 128.61, 126.98, 126.26, 106.27, 101.19, 97.96, 18.88, 11.42. HR-MS (ESI) m/z Calc. for $[M+H]^+$ $C_{48}H_{55}N_4O_2Si_2$: 775.3864, found : 775.3848.

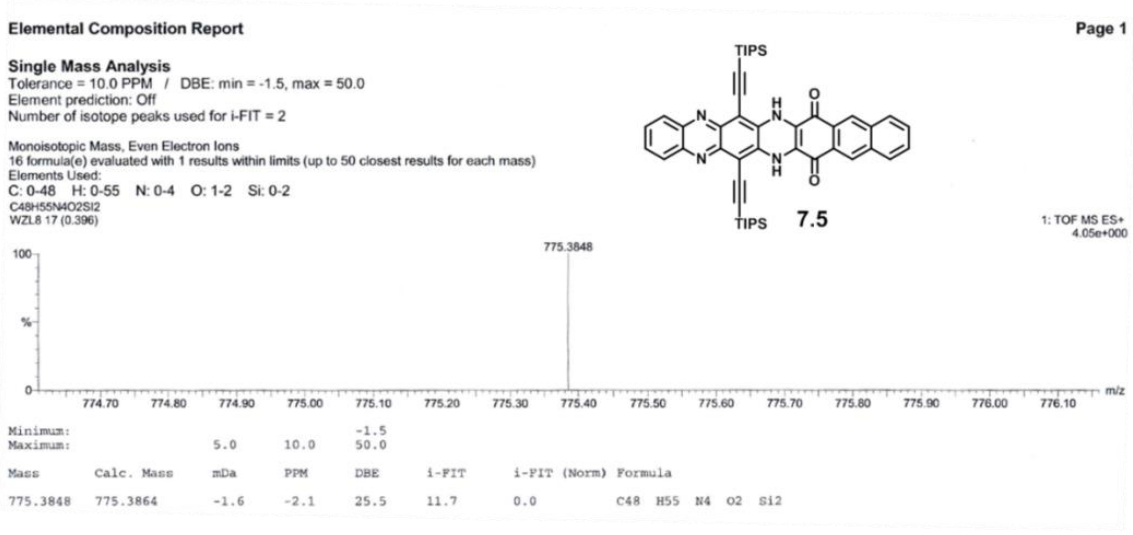

Fig 7.1 HR-MS(ESI) spectrum of compound **7.5**

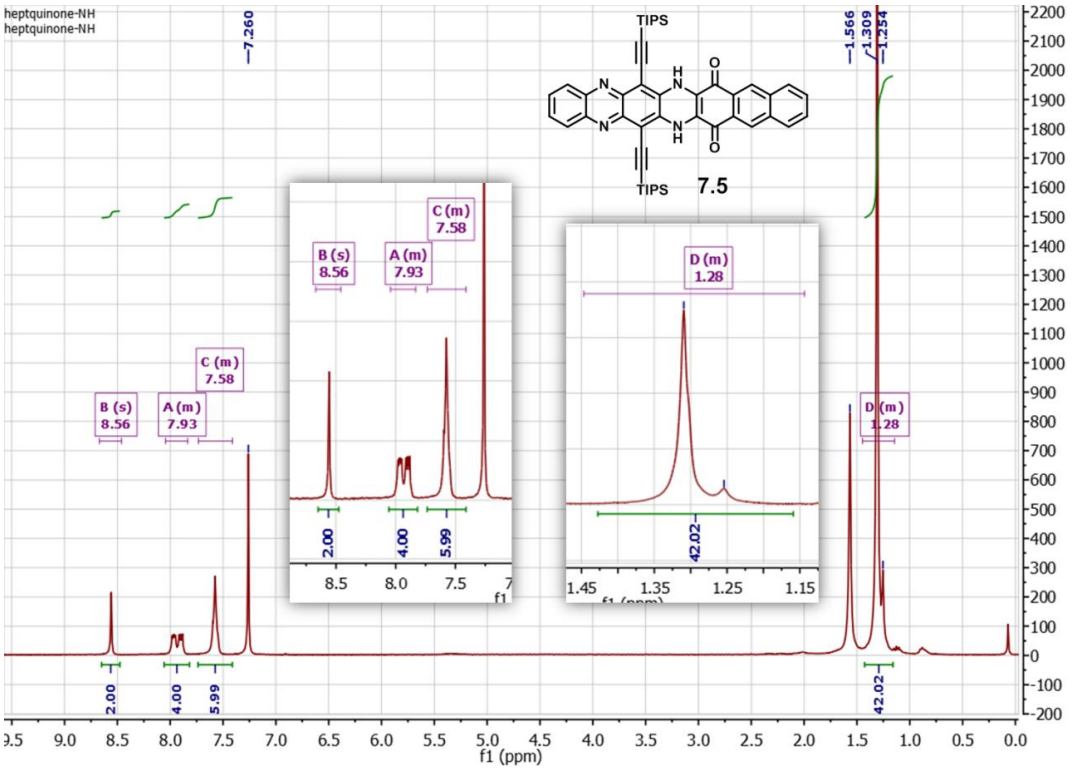

Fig 7.2 ^{1}H NMR spectrum of compound **7.5**, 300 MHz, $CDCl_3$, room temperature

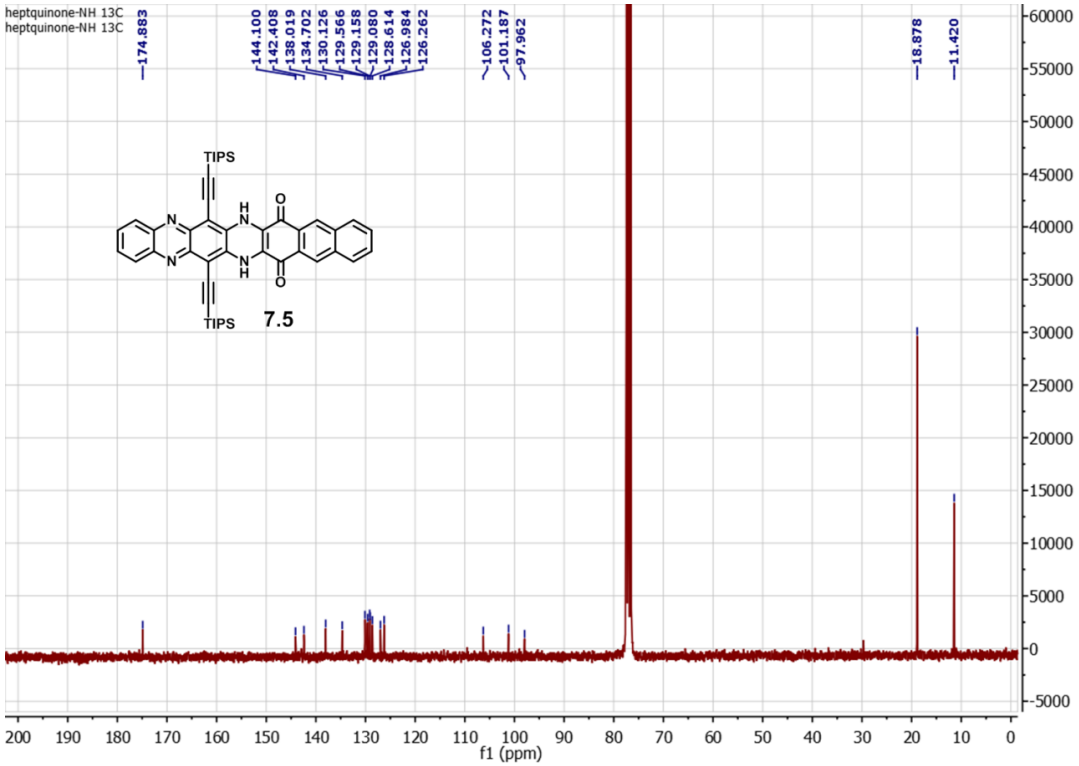

Fig 7.3 ^{13}C NMR spectrum of compound **7.5** , 75 MHz, $CDCl_3$, room temperature

6,15-bis((triisopropylsilyl)ethynyl)benzo[b]quinoxalino[2,3-i]phenazine-8,13(7H,14H)-dione (Compound 7.6)

Compound **7.6** was synthesized through the same procedure as that of compound **7.5**, by using compound **7.1** (114 mg, 0.2 mmol), dichloride compound **7.3** (103 mg, 0.45 mmol), RuPhos (7 mg, 0.015 mmol), $Pd_2(dba)_3$ (14 mg, 0.015mmol), dry Hünig's base (5 mL) and dry chloroform (15 mL). Compound **7.6** (120 mg, 0.17 mmol, 85%) was obtained as brown solid. ^{1}H NMR (300 MHz, $CDCl_3$) δ = 8.12 – 8.01 (m, 2H), 7.94 – 7.84 (m, 2H), 7.73 – 7.64 (m, 2H), 7.63 – 7.52 (m, 2H), 7.49 (s, 2H), 1.31 – 1.20 (m, 42H). ^{13}C NMR (75 MHz, $CDCl_3$) δ = 175.68, 144.18, 142.40, 138.23, 133.79, 130.37, 129.15, 129.08, 126.18, 124.78, 106.28, 101.13, 97.99, 18.85, 11.39. HR-MS (ESI) m/z Calc. for $[M+H]^+$ $C_{44}H_{53}N_4O_2Si_2$: 725.3707, found : 725.3674.

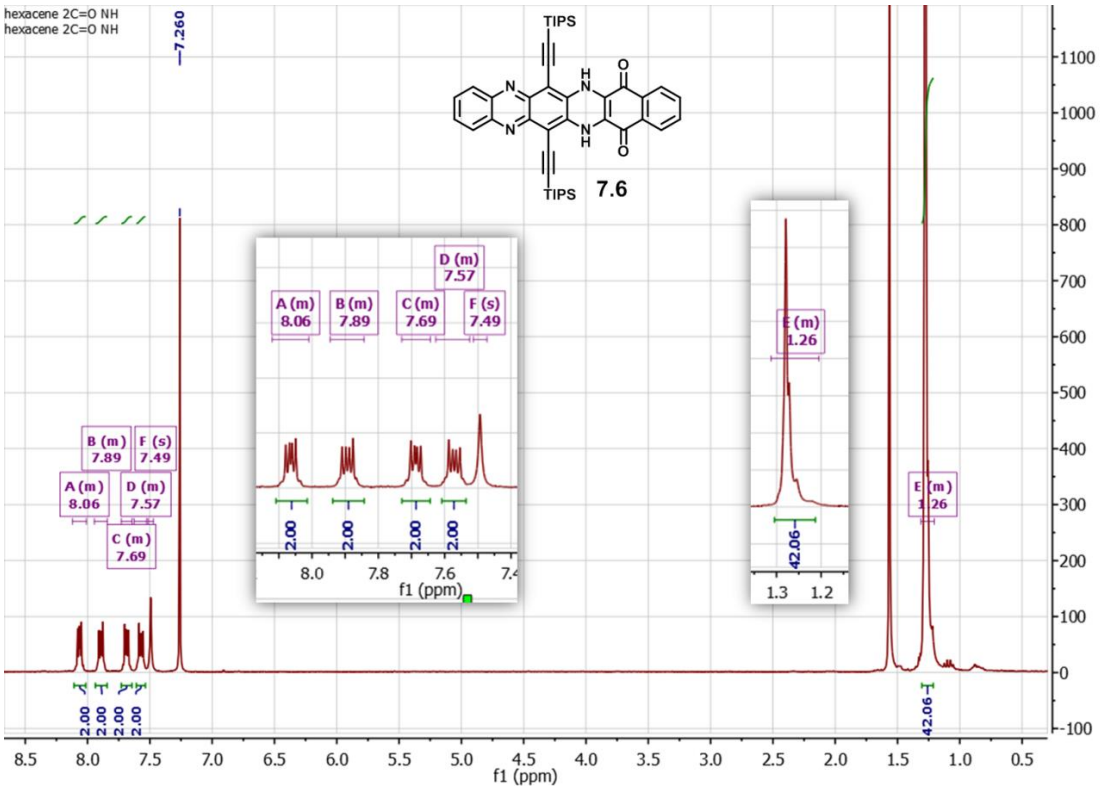

Fig 7.4 ^{1}H NMR spectrum of compound **7.6**, 300 MHz, $CDCl_3$, room temperature

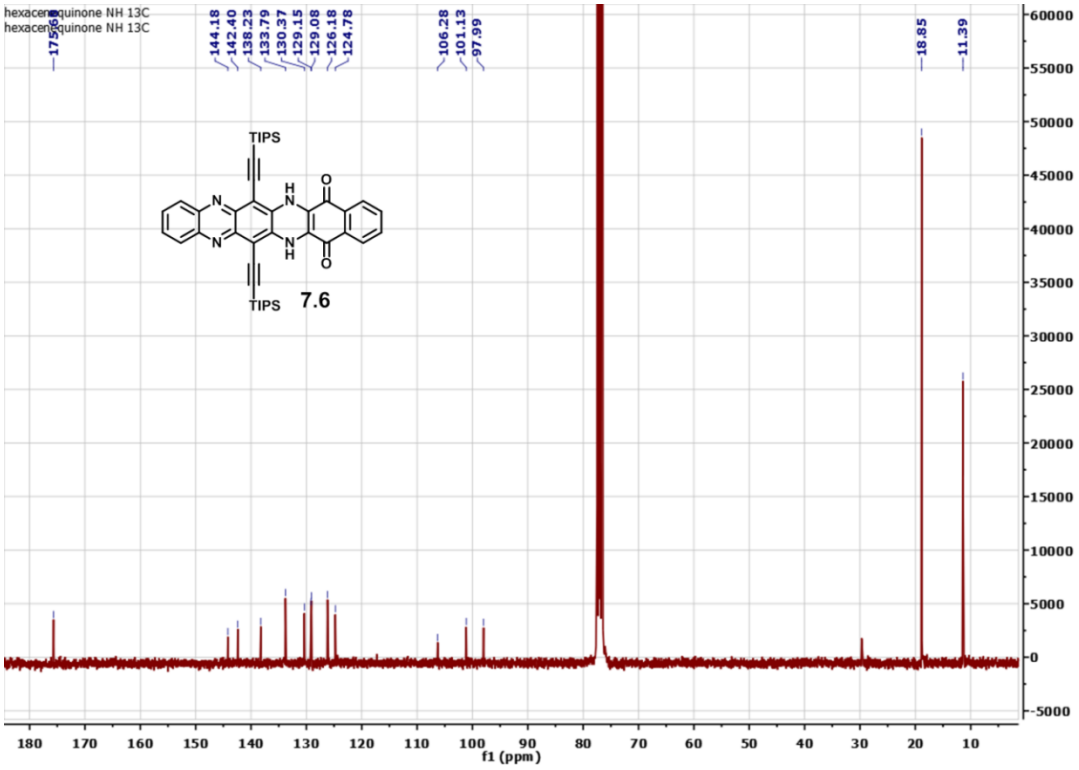

Fig 7.5 ^{13}C NMR spectrum of compound **7.6**, 75 MHz, $CDCl_3$, room temperature

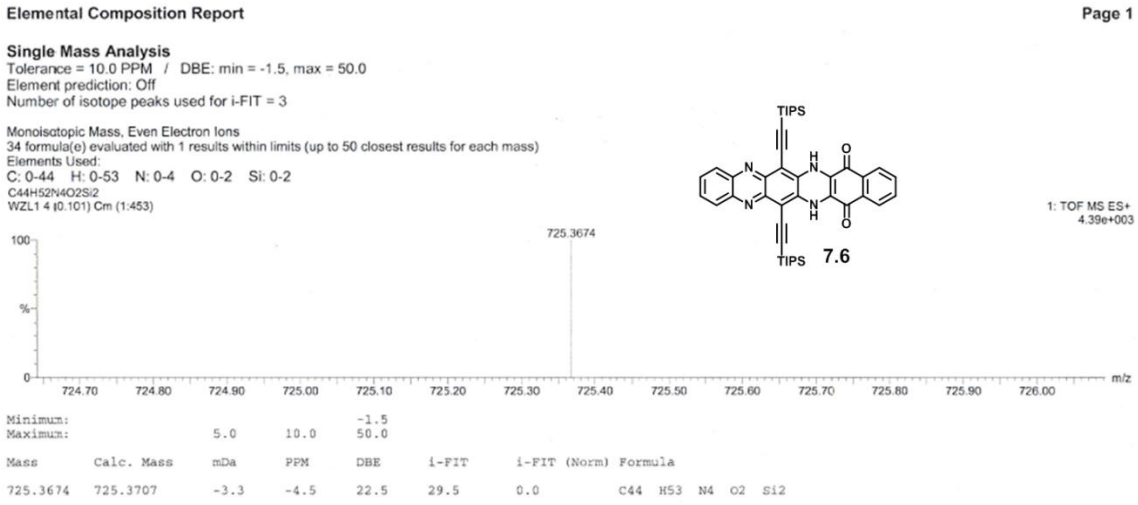

Fig 7.6 HR-MS(ESI) spectrum of compound **7.6**

1-chloro-6,13-bis((triisopropylsilyl)ethynyl)-6a,7,12,12a-tetrahydroquinoxalino[2,3-b]phenazin-2(14H)-one (Compound 7.8)

Compound **7.8** was synthesized through the same procedure as that of compound **7.5**, by using compound **7.1** (114 mg, 0.2 mmol), dichloride compound **7.4** (80 mg, 0.45 mmol), RuPhos (7 mg, 0.015 mmol), $Pd_2(dba)_3$ (14 mg, 0.015mmol), dry Hünig's base (5 mL)

and dry chloroform (10 mL). Compound **7.8** (43 mg, 0.06 mmol, 31%) was obtained as orange solid. ^{1}H NMR (300 MHz, $CDCl_3$) δ = 7.76 (d, *J*=9.0, 1H), 7.32 (d, *J*=9.0, 1H), 7.14 (s, 1H), 7.02 (s, 1H), 6.88 – 6.64 (m, 2H), 6.59 – 6.33 (m, 2H), 6.07 (s, 1H), 1.34 – 1.17 (m, 42H). ^{13}C NMR (75 MHz, $CDCl_3$) δ = 151.68, 143.61, 142.12, 140.38, 139.25, 138.99, 138.37, 128.69, 128.36, 128.06, 123.54, 123.31, 119.54, 113.93, 113.81, 112.91, 104.66, 104.51, 99.40, 99.25, 96.91, 96.76, 18.93, 18.89, 11.43, 11.42.

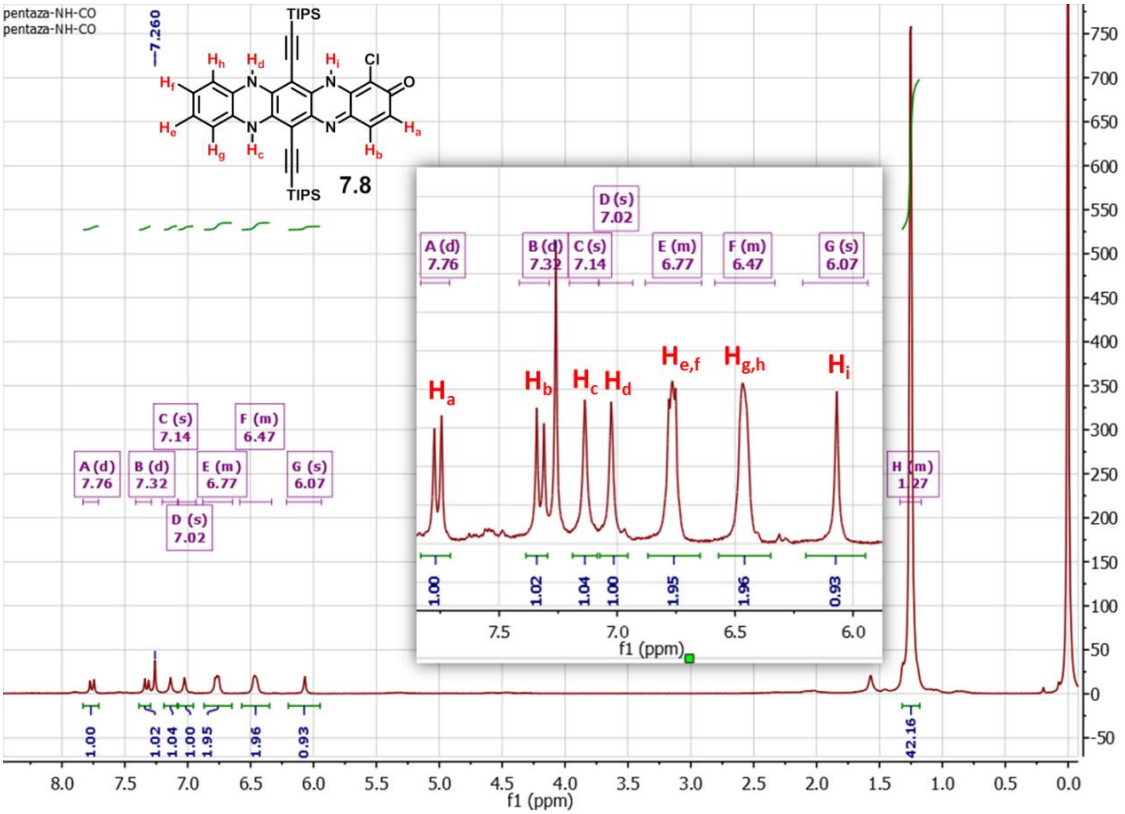

Fig 7.7 ^{1}H NMR spectrum of compound **7.8**, 300 MHz, $CDCl_3$, room temperature

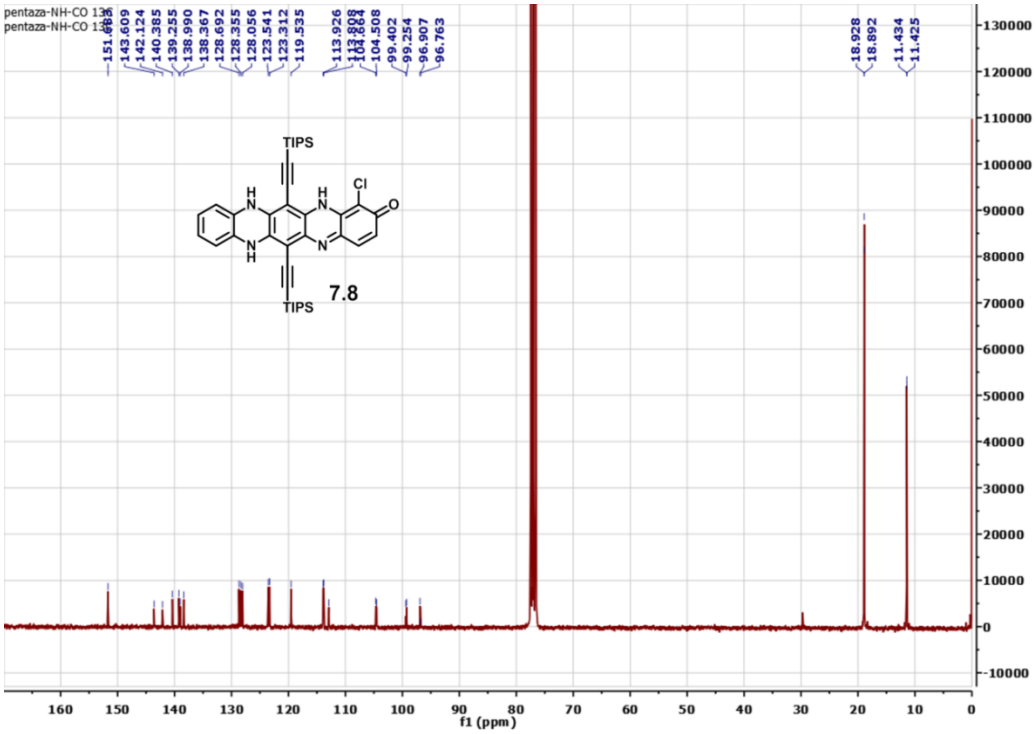

Fig 7.8 ^{13}C NMR spectrum of compound **7.8**, 75 MHz, $CDCl_3$, room temperature

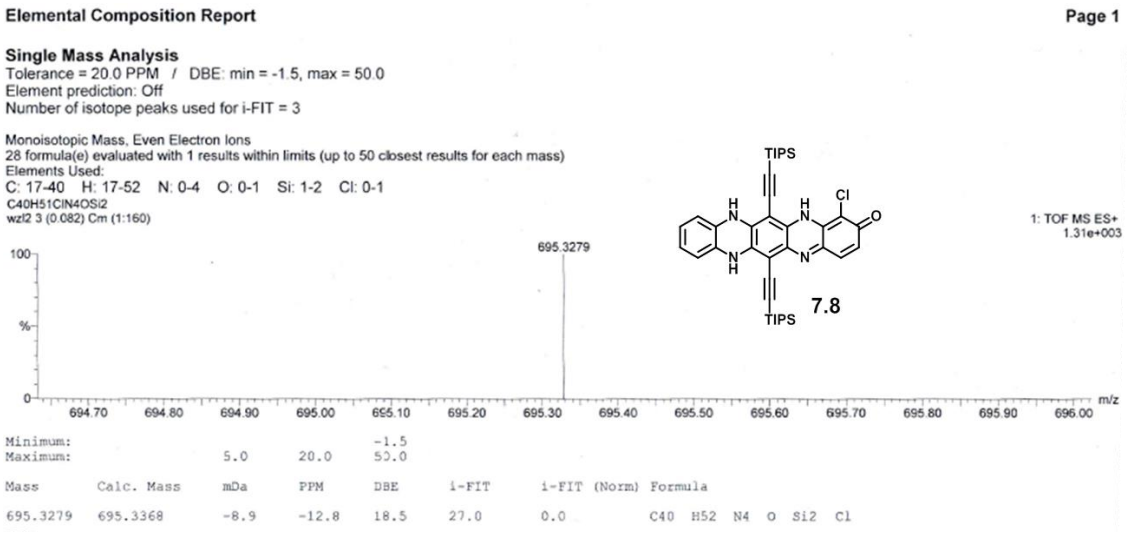

Fig 7.9 HR-MS(ESI) spectrum of compound **7.8**

6,17-bis((triisopropylsilyl)ethynyl)naphtho[2,3-b]quinoxalino[2,3-i]phenazine-8,15-dione (Hept-CO)

Compound **7.5** (50 mg, 0.06 mmol) was treated with excess amount of active MnO_2 in dry methylene chloride (20 mL) at room temperature for about 2 h. The solution turned to dark green, immediately. The completion of the reaction was confirmed by thin layer

chromatography (TLC). Subsequently, MnO_2 was removed by filtrated through celite and washed with methylene chloride until the filtrate was colorless. After removing the solvent, the solid was dissolved in small amount of diethyl ether and fastly reprecipitated by adding methanol. The solid was collected by filtration and washed with methanol to afford pure **Hept-CO** (32 mg, 0.04 mmol, 65%) as black solid. ^{1}H NMR (300 MHz, $CDCl_3$) δ = 9.13 (s, 2H), 8.33 – 8.23 (m, 2H), 8.23 – 8.14 (m, 2H), 7.97 – 7.87 (m, 2H), 7.86 – 7.72 (m, 2H), 1.49 – 1.26 (m, 42H). ^{13}C NMR (75 MHz, $CDCl_3$) δ = 180.21, 145.93, 145.71, 144.14, 142.36, 135.67, 132.94, 131.17, 130.64, 130.40, 130.37, 130.32, 125.75, 115.45, 101.65, 18.94, 11.71. HR-MS (ESI) m/z Calc. for $[M+H]^+$ $C_{48}H_{53}N_4O_2Si_2$: 773.3707, found : 773.3686.

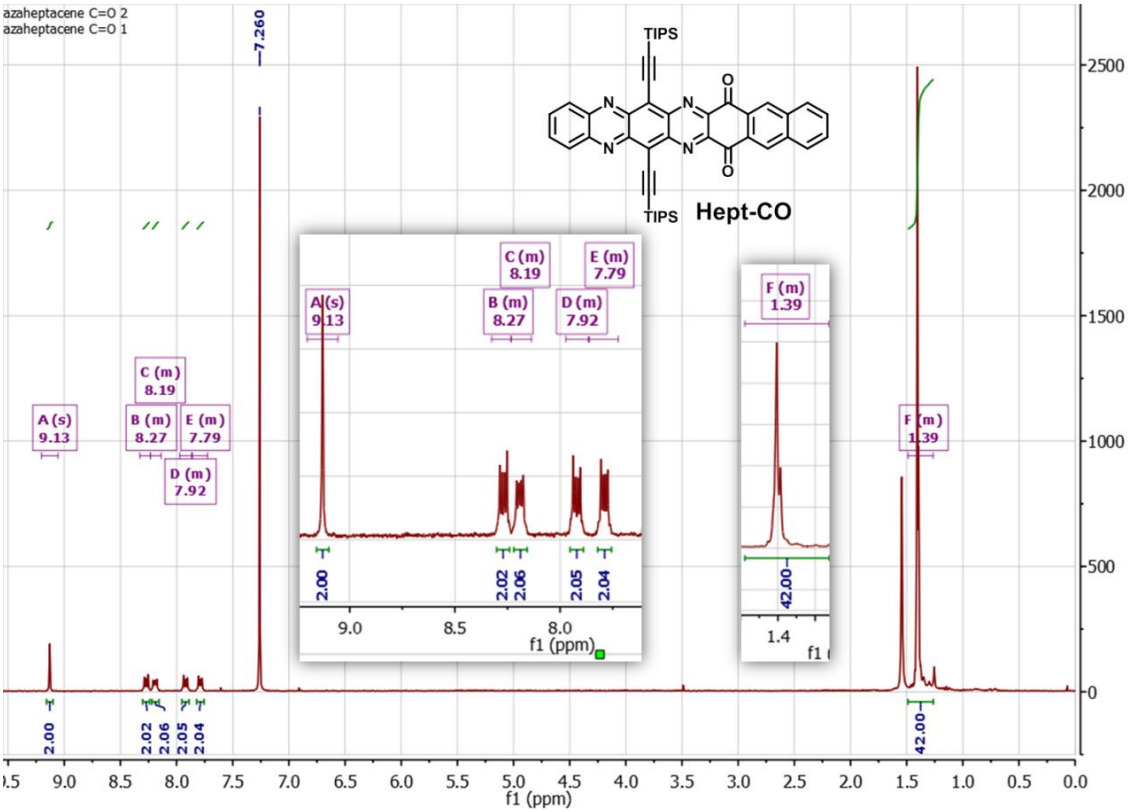

Fig 7.10 ^{1}H NMR spectrum of compound **Hept-CO**, 300 MHz, $CDCl_3$, room temperature

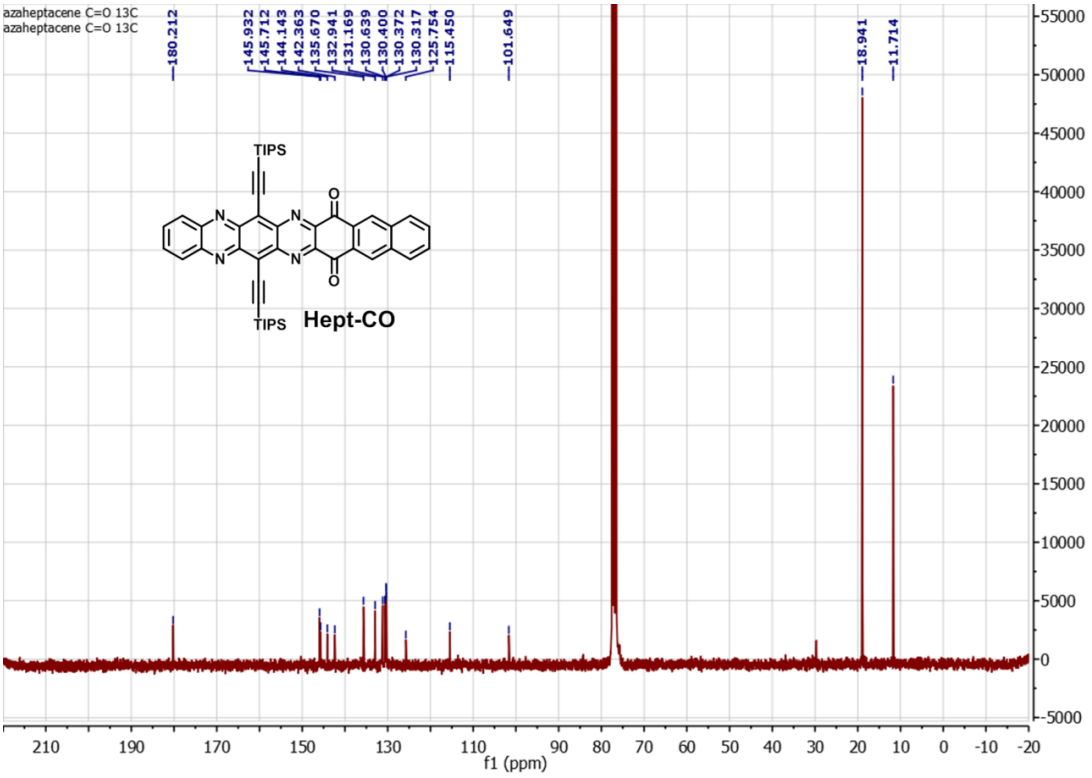

Fig 7.11 ^{13}C NMR spectrum of compound **Hept-CO**, 75 MHz, $CDCl_3$, room temperature

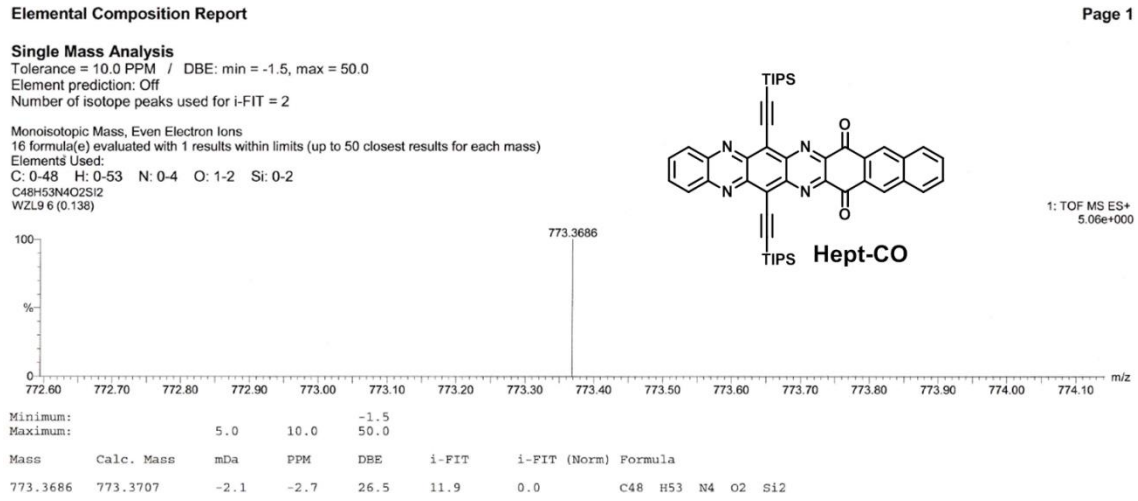

Fig 7.12 HR-MS(ESI) spectrum of compound **Hept-CO**

6,15-bis((triisopropylsilyl)ethynyl)benzo[b]quinoxalino[2,3-i]phenazine-8,13-dione (Hex-CO)

Hex-CO was synthesized through the same procedure as that of **Hept-CO**, by using compound **7.6** (50 mg, 0.07 mmol). Pure **Hex-CO** (28 mg, 0.04 mmol, 56%) was obtained as black solid. ^{1}H NMR (300 MHz, $CDCl_3$) δ = 8.60 – 8.50 (m, 2H), 8.31 – 8.22

(m, 2H), 8.00 – 7.88 (m, 4H), 1.46 – 1.27 (m, 42H). ^{13}C NMR (75 MHz, $CDCl_3$) δ = 180.04, 145.87, 145.04, 144.07, 142.27, 135.23, 134.63, 132.96, 130.57, 128.47, 125.78, 115.44, 101.52, 18.92, 11.69.

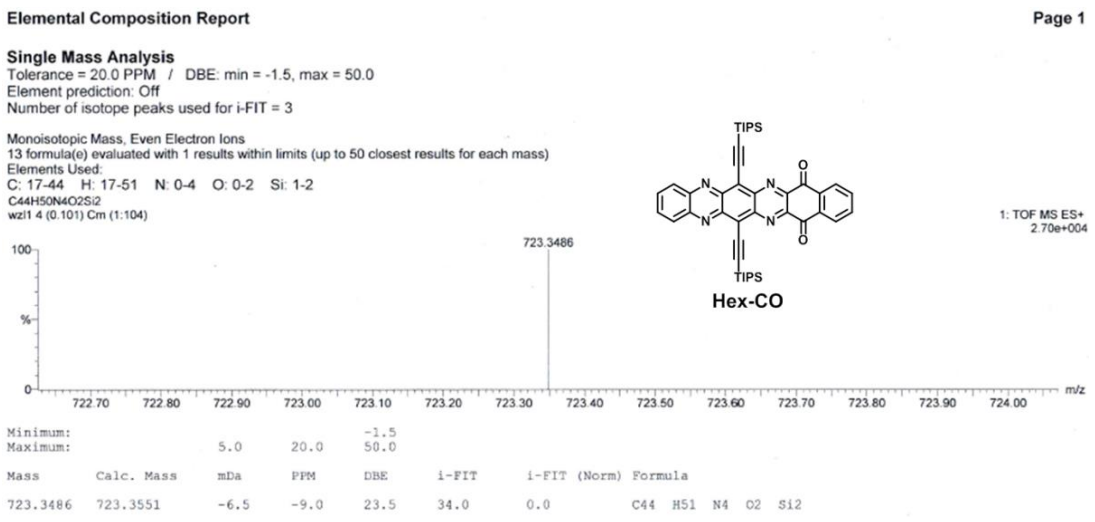

Fig 7.13 HR-MS(ESI) spectrum of compound **Hex-CO**

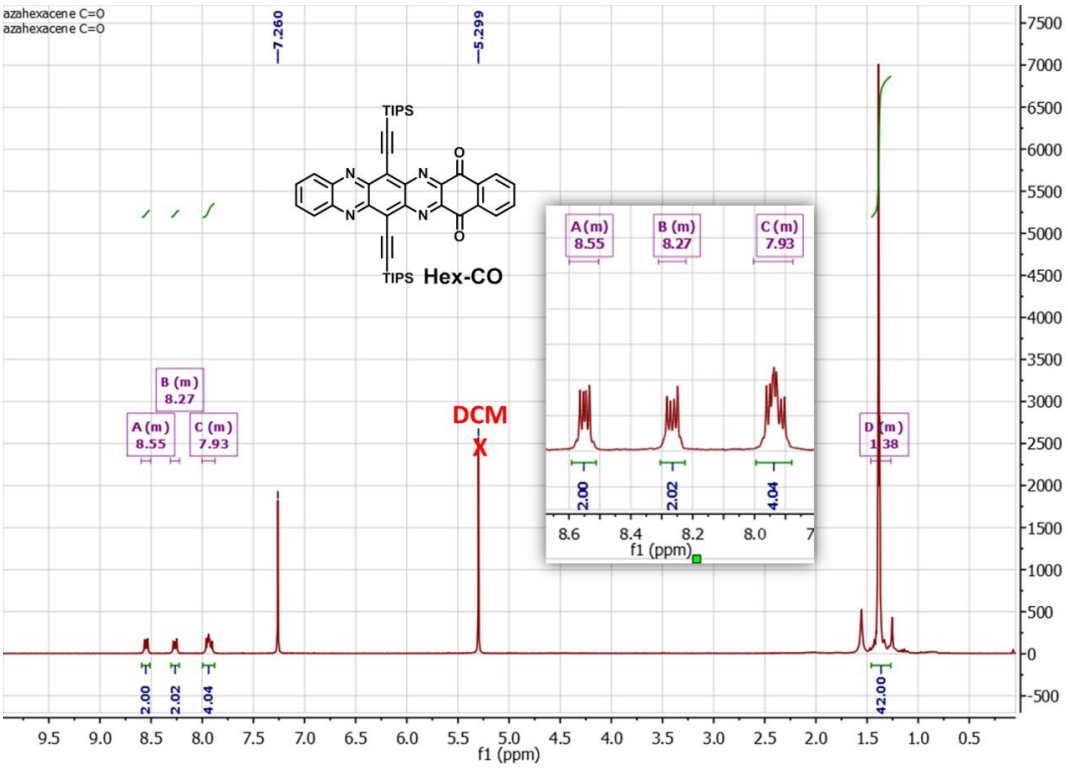

Fig 7.14 ^{1}H NMR spectrum of compound **Hex-CO**, 300 MHz, $CDCl_3$, room temperature

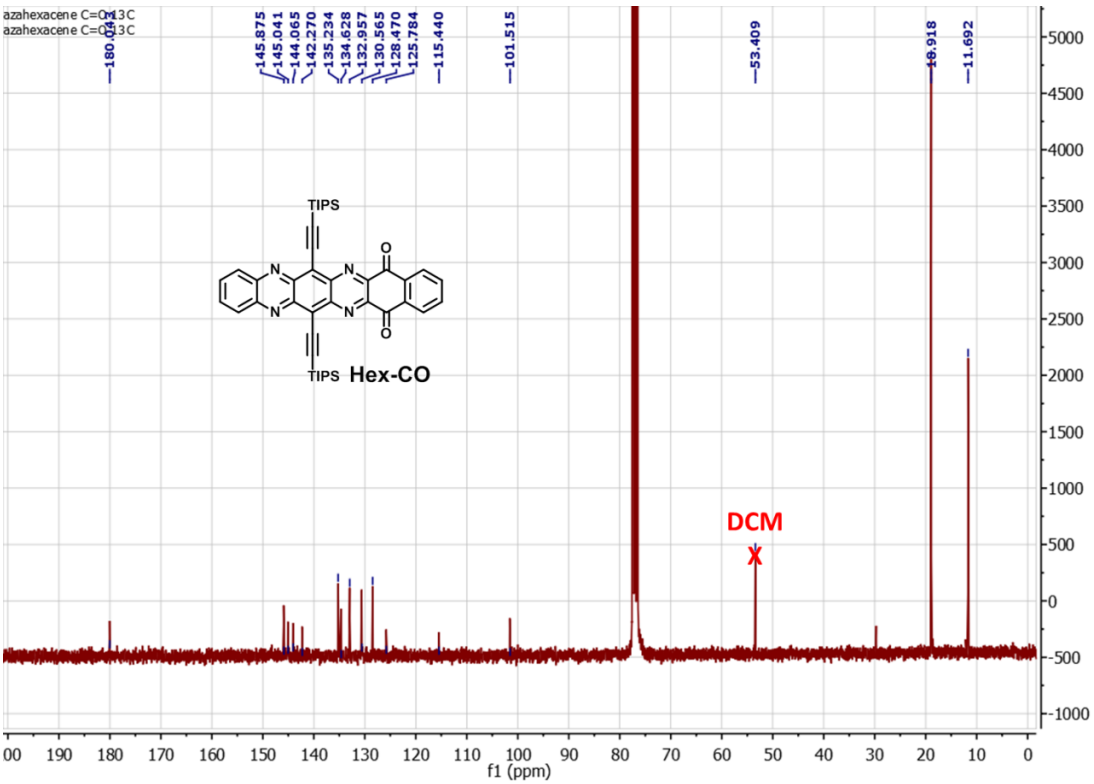

Fig 7.15 ^{13}C NMR spectrum of compound **Hex-CO**, 75 MHz, $CDCl_3$, room temperature

7.3 Principle outcomes

7.3.1 Synthetic route

The synthetic route is shown in Scheme 7.1. Compounds **7.1**[19], **7.2**[20] and **7.4**[20] were synthesized according to the reported procedures. The active dichloride quinone compounds **7.2** and **7.3** can react with the diamine compound **7.1** through double Buchwald–Hartwig reactions giving compound **7.5** (74%) and **7.6** (85%) in good yields, respectively. Compound **7.5** and **7.6** can be easily oxidized even on the TLC plate (color changing from brown to green). After treatment of compounds **7.5** and **7.6** by active MnO_2, the target compounds **Hept-CO** and **Hex-CO** can be obtained. The reaction between compounds **7.1** and **7.4** under the same condition cannot yield compound **7.7**; however, compound **7.8** was obtained. The increasing reactivity of ketones in compound **7.8** is probably the main reason causing the difference. All new compounds were confirmed by ^{1}H NMR, ^{13}C NMR, and HR-MS.

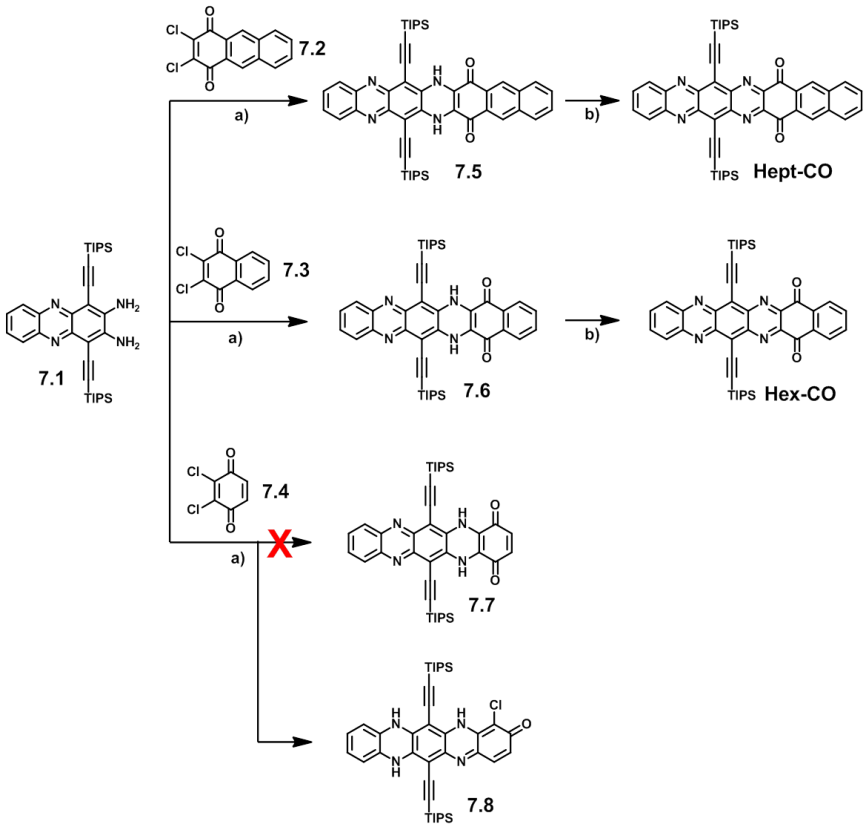

Scheme 7.1 Synthetic route of **Hept-CO** and **Hex-CO**. (a) $CHCl_3$, Hünig's base, $Pd_2(dba)_3$, AcOH, RuPhos, 70 ºC, 48 h; (b) MnO_2, CH_2Cl_2, RT

7.3.2 Single-crystal X-ray diffraction analysis

The rod-like crystal of **Hex-CO** was obtained by placing a chloroform solution in a methanol atmosphere in about one week. The crystal is good enough for the single crystal X-ray diffraction analysis. Fig 7.16 shows the single crystal structure of **Hex-CO**. The conjugation backbone of **Hex-CO** shows a plane configuration as shown in Fig 7.16a and b. The molecular stacking structure is shown in Fig 7.16d and e. Firstly, **Hex-CO** form a dimer (one dimer is highlighted in green color as an example in Fig 7.16d and e) through strong π-π interaction with a mean short distance of 3.310Å. Subsequently the dimers adopt a lamellar 2-D π-stacking motif, which is the ideal stacking mode for OFET application.[21] The mean short distances between the dimers are 3.342Å and 3.371 Å as shown in Fig 7.16d, suggesting existence of the strong π-π interactions. This molecular packing structure suggests **Hex-CO** may have a good performance in OFET application.

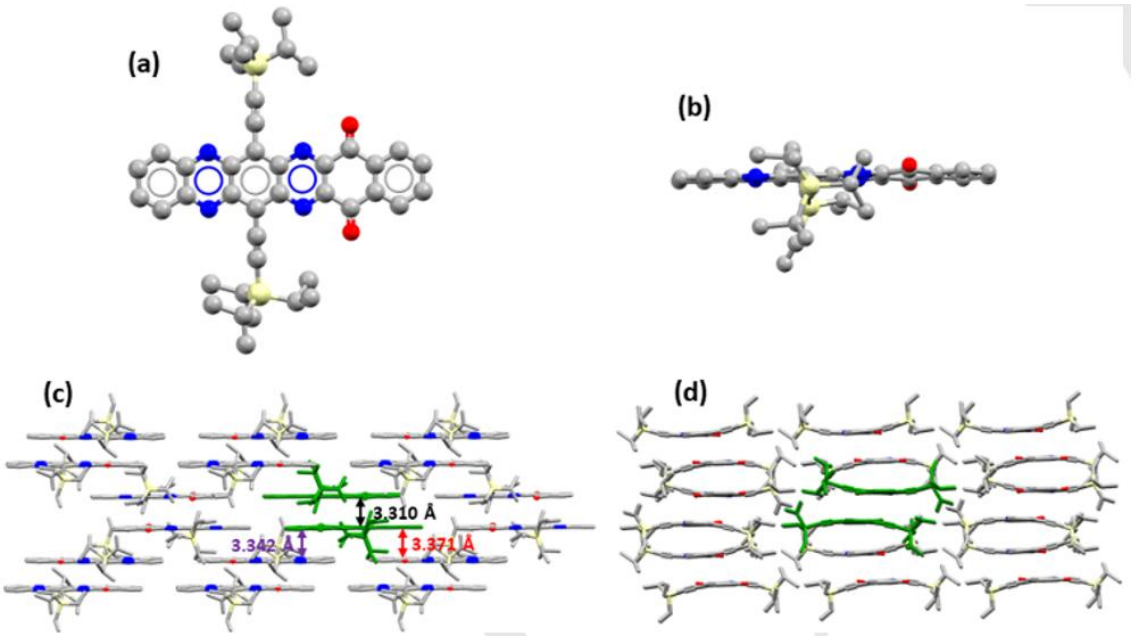

Fig 7.16 Single-crystal X-ray structure of **Hex-CO**: (a) Top view and (b) side view of the molecule configuration (color scheme: C, gray; N, blue; Si, yellow; O, red. H atoms are omitted for clarity); (c) A photograph of the as-obtain crystal; Molecular stacking structures (one dimer is shown in green color); (d) side view perpendicular to long axis of the conjugation backbone and (e) side view along the long axis of the conjugation backbone

The flake shape black crystal of **Hept-CO** was obtained by placing a chlorobenzene solution in a methanol atmosphere in about one week. A photograph of the as-obtain crystal is shown in Fig 7.17c. The single crystal structure of **Hept-CO** is shown in Fig 7.17. **Hept-CO** has a plane conjugation backbone as shown in Fig 7.17a and b. The molecular stacking structure is shown in Fig 7.17d – g. **Hept-CO** also form a dimer (green colour in Fig 7.17d and e) firstly through a stronger π-π interaction with a mean short distance of 3.275Å which is smaller than that of **Hex-CO**. It suggests that the asymmetry of molecules favors the formation of the dimers, and the strong π-π interaction caused by the extended conjugation further promotes the formation of the dimers. The dimers form a 1-D π-stacking structure (Fig 7.17d) through strong π-π interaction with a mean short distance of 3.396Å. The 1-D stacking structure subsequently aggregate together through C-H···π interaction forming a 2-D layer structure (Fig 7.17e): lamellar 1-D π-stacking motif, which is a classic stacking mode for OFET application.[21]. The 2-D layer structure further aggregate together forming a 3-D

structure (Fig 7.17f and g). The orientations of the molecules in adjacent layers have an angle of 90º.

With only one benzene rings difference in the conjugation length, the molecular packing mode of **Hex-CO** and **Hept-CO** differ very much, which suggest that the conjugation length of the acenes derivatives greatly affect the molecule packing in the solid state.

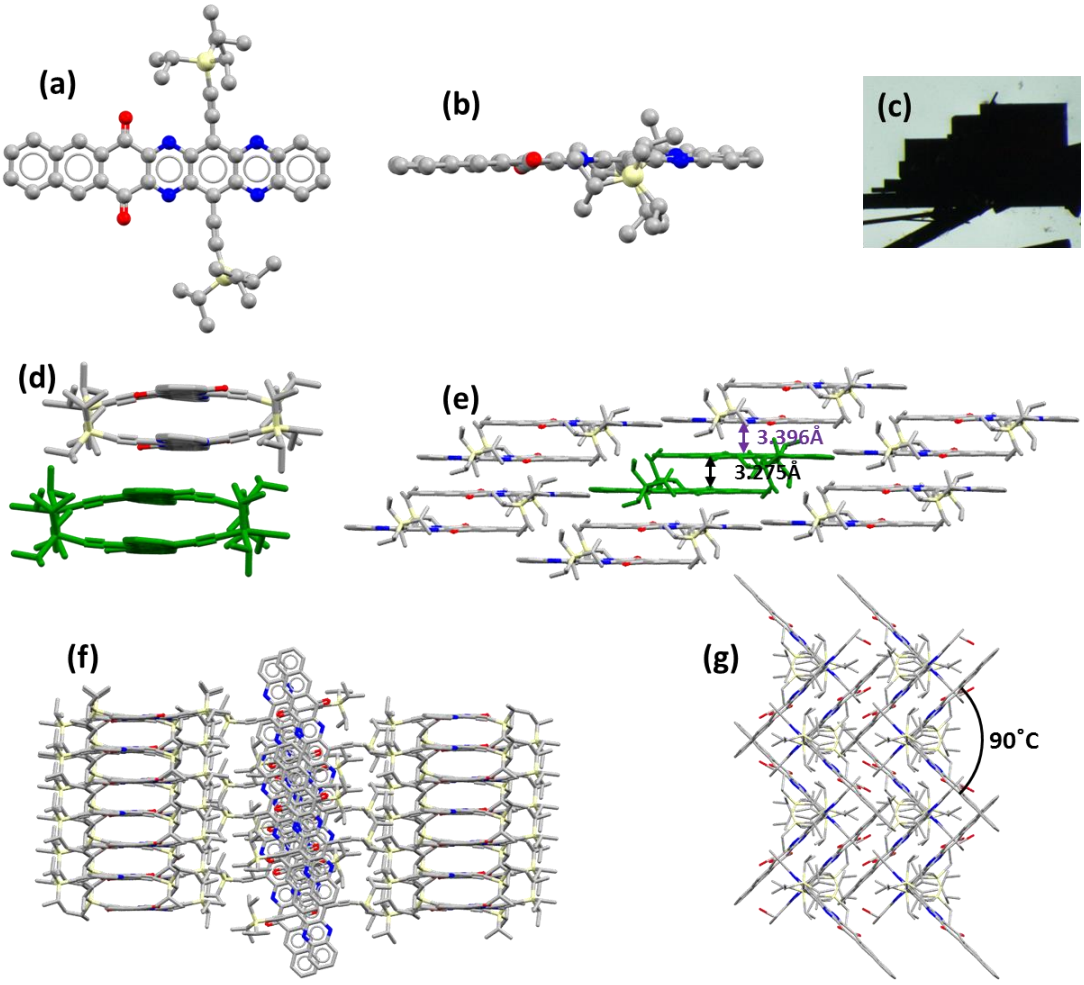

Fig 7.17 Single-crystal X-ray structure of **Hept-CO (**Hydrogen and solvent molecules (MeOH) are removed for clarification): (a) Top view and (b) side view of the molecule configuration (color scheme: C, gray; N, blue; Si, yellow; O, red. H atoms are omitted for clarity); (c) A photograph of the as-obtain crystal; (d) Molecular 1-D stacking structure: side view along the long axis of the conjugation backbone; (e) Molecular 2-D stacking structure: side view perpendicular to long axis of the conjugation backbone; (one dimer is shown in green color); (f) and (g): Molecular 3-D stacking structure

7.3.3 Photophysical and electrochemical properties and energy levels

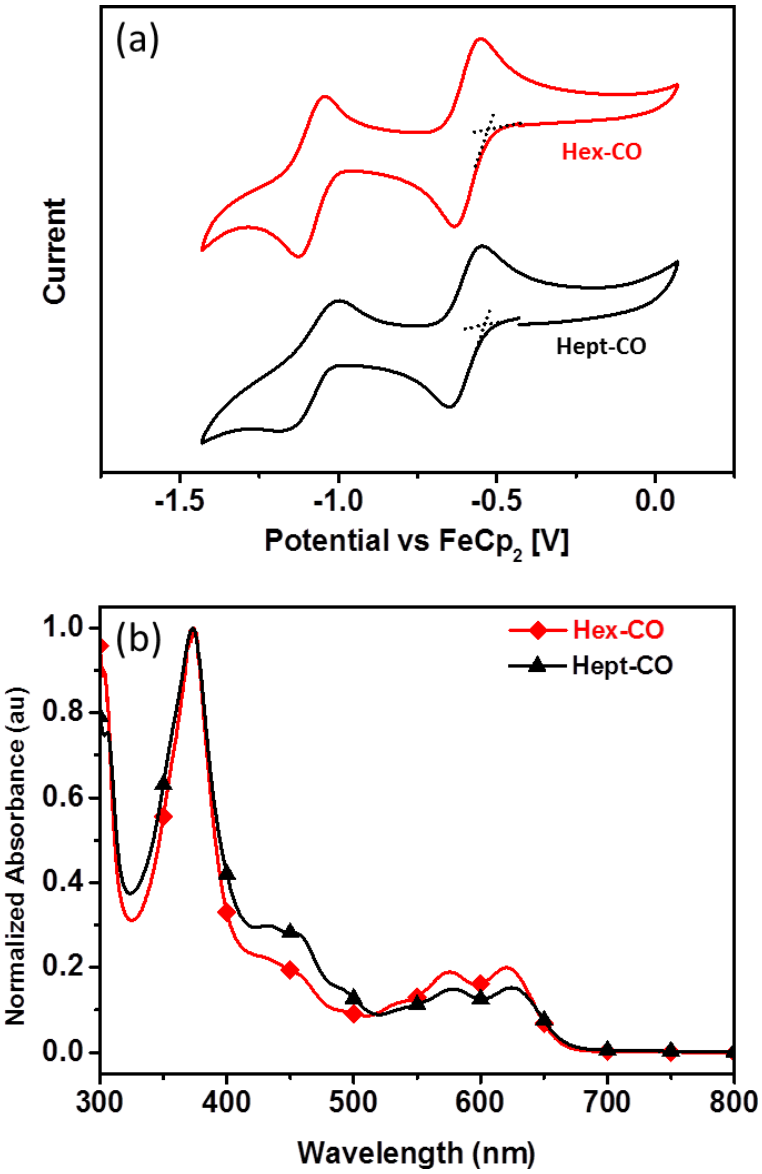

Fig 7.18 (a) Cyclic voltammetry curves of **Hex-CO** and **Hept-CO** (Electrolyte: 0.1M nBu_4NPF_6, Scanning speed: 50 mV/s); (b) UV-vis absorption spectrum spectra of **Hex-CO** and **Hept-CO** in CH_2Cl_2

The molecular energy levels of **Hex-CO** and **Hept-CO** were studied by cyclic voltammetry (CV) and UV-vis absorption (UV) test. As shown in Fig 7.18a, the CV curves of **Hex-CO** and **Hept-CO** are almost the same. Both of them show two reversible reduction peaks: the onset potentials are -0.53V and -1.03V for **Hex-CO**; and -0.54V and -1.04V for **Hept-CO**. The LUMO and LUMO+1 energy levels calculated from them are:

-4.27 eV and -3.96 eV for **Hex-CO**; -4.26 eV and -3.97 eV for **Hept-CO**. The oxidative peaks cannot be observed in the CV curves. The deep low LUMO levels suggest that they are candidate n-type semiconductors.

The UV-vis absorption spectra of **Hex-CO** and **Hept-CO** are also quite similar as shown in Fig 7.18b. Both of them show three absorption peaks between 400 nm and 700 nm. The onset absorptions at 666 nm for **Hex-CO** and 668 nm for **Hept-CO** suggest that their optical band gaps are both about 1.86 eV. This band gap value is similar with that of the reported TIPS-azapentacenes (as summarized in chapter 4, Fig 4.19.). This suggested that though the plane molecular backbones of **Hex-CO** and **Hept-CO** are π-conjugated, the aromaticity is interrupted at quinone units. In other words, there is one Clar's π-sextet existing on each side of the quinone bridge. The additional Clar's π-sextets can effectively increase the stability of the long π-conjugated azaacenes derivatives **Hex-CO** and **Hept-CO**. According to the optical band gaps and LUMO levels, the HOMO levels can be determined to be -6.13 eV for **Hex-CO** and -6.12 eV for **Hept-CO**.

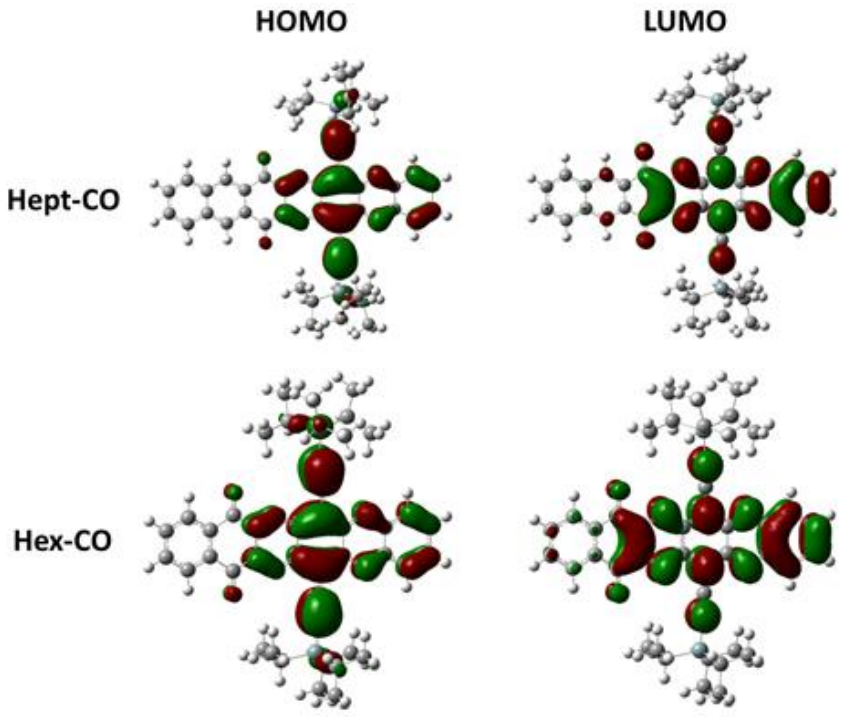

Fig 7.19 The electron density distribution of HOMOs and LUMOs of **Hex-CO** and **Hept-CO** by DFT calculation

The frontier molecular orbitals are theoretically investigated by quantum chemistry calculations performed with Gaussian09 package using density functional theory (DFT) calculation at the B3PW91/6-31G(d) level as shown in Fig 7.19.[22] The electron distribution of HOMOs of **Hex-CO** and **Hept-CO** are mainly delocalized on the azatetraacene parts. Even though the LUMOs are delocalized on the azatetraacenes parts and the quinone units, they still have difficulties getting to the other side of the quinone bridges. This suggests that the quinone units along with the nitrogen atoms have a big contribution in lowering the LUMO levels of the azaacenes derivatives. The calculated energies levels of HOMOs, LUMOs, and band gaps are -5.65 eV, -3.64 eV and 2.01 eV for **Hex-CO**, and -5.60 eV, -3.60 eV and 2.00 eV for **Hept-CO**. The energy of band gap was calculated by the equation of $E_{gap} = E_{LUMO} - E_{HOMO}$.

All the photophysical, electrochemical and DFT calculation data are summarized in Table 7.1. By comparing all these results, it demonstrates that the energy levels of **Hex-CO** and **Hept-CO** are almost the same. This suggests that the energy levels are determined by the azatetraacene parts, and the extended conjugation on the other side of the quinone bridge almost has no influence on the energy levels.

Table 7.1 Photophysical, electrochemical, DFT calculation data and energy levels of **Hex-CO** and **Hept-CO**

	$E_{onset,red}^{1}$ (V)	$E_{onset,red}^{2}$ (V)	$E_{HOMO,DFT}$ (eV)	$E_{HOMO,opt}$ (eV)	$\lambda_{onset,abs}$ (nm)
Hex-CO	-0.53	-1.03	-5.65	-6.13	666
Hept-CO	-0.54	-1.04	-5.60	-6.12	668
	$E_{LUMO,CV}$ (eV)	$E_{LUMO+1,CV}$ (eV)	$E_{LUMO,DFT}$ (eV)	Gap_{DFT} (eV)	Gap_{opt} (eV)
Hex-CO	-4.27	-3.96	-3.64	2.01	1.86
Hept-CO	-4.26	-3.97	-3.60	2.00	1.86

7.3.4 OFET

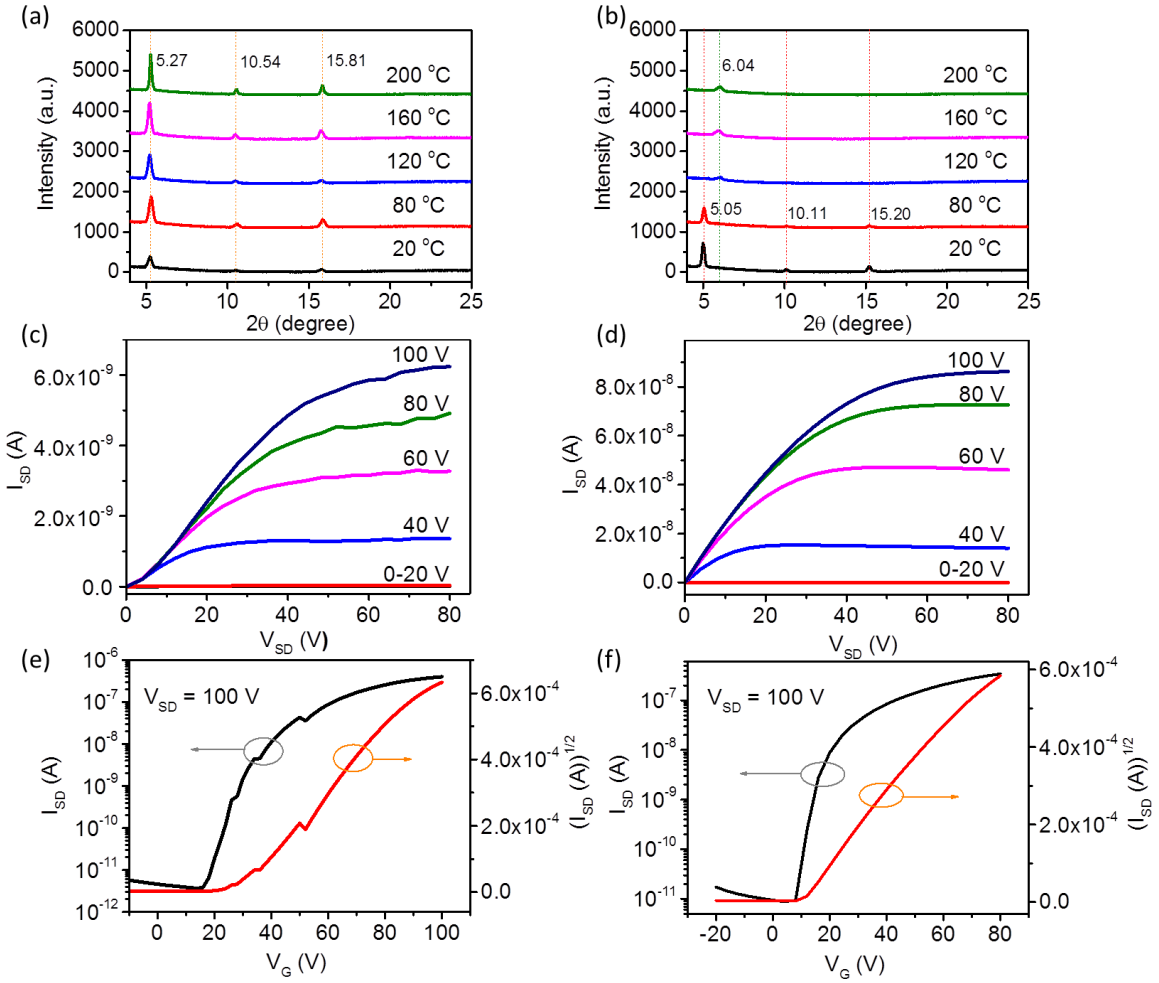

Fig 7.20 X-ray diffraction patterns of spin-coating thin films of (a) **Hex-CO** and (b) **Hept-CO** at different annealing temperatures; (c, d) Representative output and (e, f) transfer characteristics of organic thin-film field effect transistors based on **Hex-CO** (c, e) and **Hept-CO** (d, f) at the optimized temperature (**Hex-CO**, 80 ºC; **Hept-CO**, 80 ºC)

To investigate the charge transport of the **Hex-CO** and **Hept-CO**, the bottom-gate top-contact (BGTC) organic thin-film field effect transistors (OFETs) were fabricated with the spin-coated thin films (40-60 nm) as active layer, the vacuum-evaporated Au (20 nm) as source/drain electrodes, the octadecyltrichlorosilane (OTS)-functionalized SiO_2 (300 nm) and highly n-doped Si as dielectric layer and bottom electrode, respectively. To enhance the molecular re-arrangement, the annealing treatment on the as-fabricated thin films was also done. Fig 7.20 shows the typical output and transfer characteristics of OFETs obtained in vacuum at the optimized annealing temperature and the key cthe

devices exhibit a slightly different electron charge transport with the best electron mobilities of 3.8×10^{-3} cm^2 V^{-1} s^{-1} for **Hex-CO** and 9.3×10^{-3} cm^2 V^{-1} s^{-1} for **Hept-CO**.

Table 7.2 The electrical properties of the thin-film OFET based on **Hex-CO** and **Hept-CO** at different annealing temperatures

Compound	$T_{annealing}$ (°C)	μ ($cm^2V^{-1}s^{-1}$)	V_T (V)	I_{on}/I_{off}
Hex-CO	30	2.3 (3.8) × 10^{-3}	44.6	10^4
	80	2.3 (2.8) × 10^{-3}	23.1	10^4
	120	2.4 (3.5) × 10^{-4}	18.0	10^3
Hept-CO	30	2.3 (2.8) × 10^{-3}	21.4	10^4
	80	5.5 (9.3) × 10^{-3}	21.5	10^5
	120	2.0 (2.3) × 10^{-3}	7.68	10^4
	160	1.8 (2.3) × 10^{-3}	22.1	10^4
	200	1.1 (1.5) × 10^{-3}	11.7	10^4

To further understand the performance difference, the morphology and the molecular packing of the films are characterized by AFM and X-ray diffraction. As well known, higher crystalline morphology has a positive impact on the charge transport for the more ordered molecular packing.[23] As shown in the AFM images and XRD analysis (Fig 7.21 and Fig 7.20), the films of both compounds exhibit good crystallinity with the distinct microstructures and highly ordered diffraction peaks, while the films of **Hex-CO** seem to be rougher and more discontinuous than that of **Hept-CO**, which could lead to its lower mobility. Moreover, calculated from the first intense reflections, the *d*-spacing of the as-spun films for **Hex-CO** and **Hept-CO** are 1.68 nm and 1.75 nm, respectively. In comparison to the estimated molecular length along alky-chain direction (1.74 nm for **Hex-CO**, 1.76 nm for **Hept-CO**, in Fig 7.22), it is supposed that the molecules of **Hept-CO** own a more compact packing along the charge transport direction as they stand perpendicularly on the substrate with a smaller title angle than that of **Hex-CO**. This may be another reason for the performance difference. Besides, the influence of the annealing temperature on the film morphology and the device performance was also investigated. For **Hex-CO**, the increasing annealing temperature can cause the molecular aggregation

and form the discontinuous film, which results in the loss of the effective charge transport path and thus in the loss of the mobility. In comparison, for the film of **Hept-CO**, the morphology exhibits a distinct change from granular grains to clustered nanorods when the temperature goes up to 120 °C. Correspondingly, the XRD also shows an apparent peak shift from 5.18° to 6.02°, indicating a phase change has happened. This may disturb the efficient charge transport and result in lower performance.

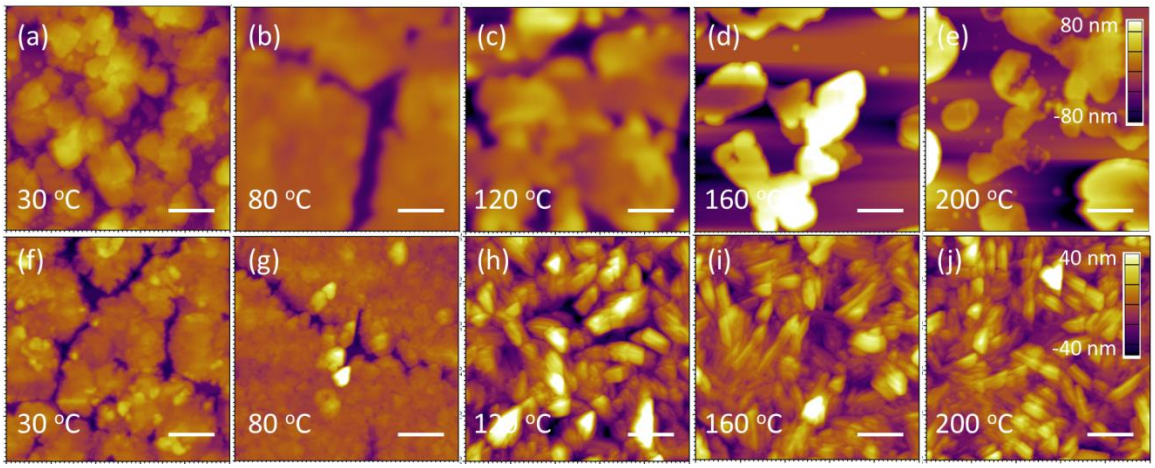

Fig 7.21 AFM images of thin films of (a-e) compounds **Hex-CO** and (f-j) **Hept-CO** at annealing different temperatures

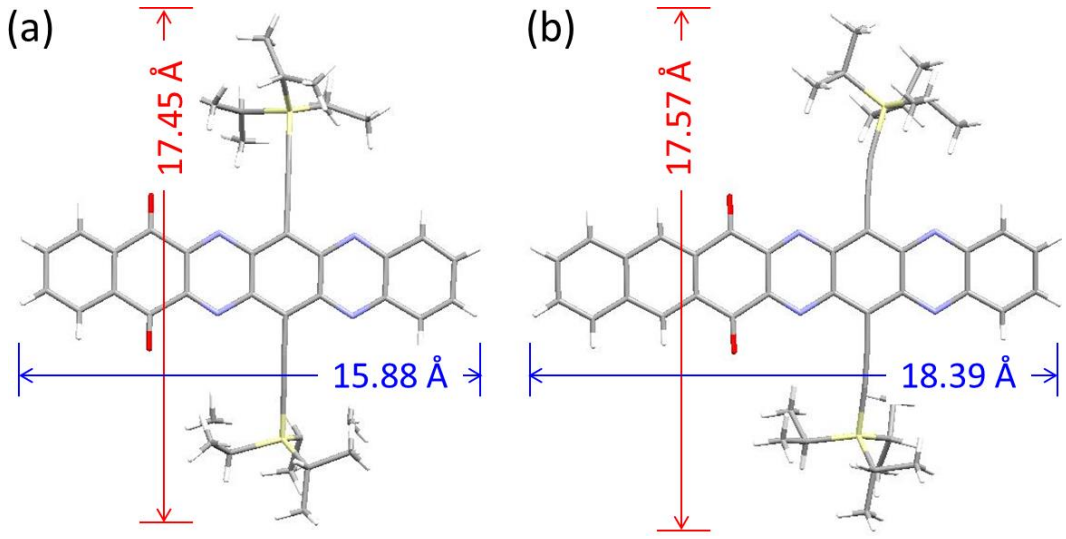

Fig 7.22 The estimated molecular length of (a) **Hex-CO** and (b) **Hept-CO**

To further understand how the molecular structures affect the OFET performance, theoretical calculations based on the single-crystal structure with the Marcus electron transfer theory and an incoherent random walk model were carried out to evaluate the hole and electron mobility.[24] The hole and electron reorganization energies were calculated to be 240.0 meV and 222.9 meV for **Hex-CO** and 243.8 meV and 212.0 meV for **Hept-CO**, respectively, at the DFT/B3LYP/6-31G(d) level. The transfer integrals were also calculated as shown in Fig 7.23 and Fig 7.24, as well as summarized in Table 7.3 and Table 7.4. Very large electron transfer integrals can be observed inside the dimers (64.91 eV for **Hex-CO** and 96.54 eV for **Hept-CO**) which are consistent with the strong π-π interactions in the dimers. The electron transfer integrals between the dimers in the π-π stacking directions are also very large (61.71 meV and 33.10 meV for **Hex-CO**, and -51.14 meV for **Hept-CO**) which are similar with and even higher than that of the classic n-type semiconductor TIPS-TAP (-57.12 meV).[25]

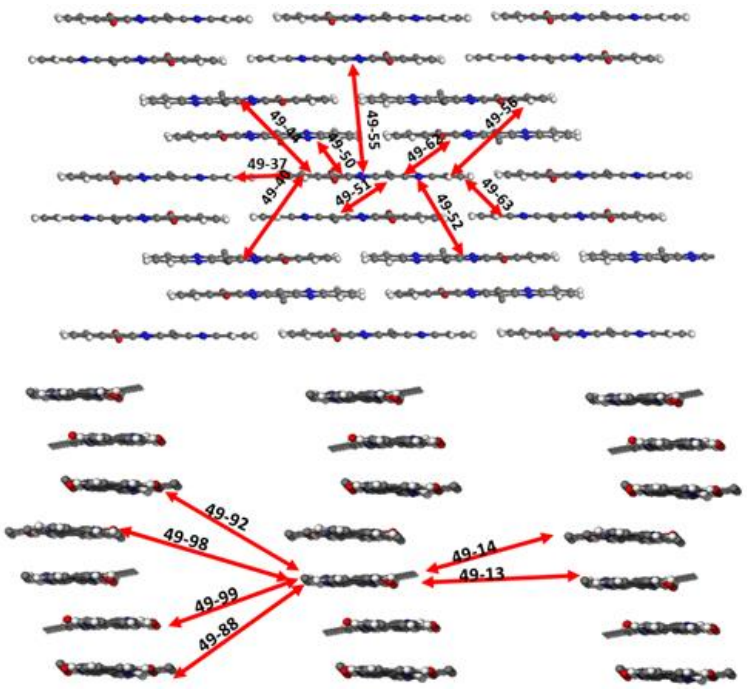

Fig 7.23 Hoping route of **Hex-CO** in the crystal (the hydrogen atoms are omitted for clarification); The intermolecular electronic couplings of hole transfer (V_h) and electron transfer (V_e) for the center molecule **49** are calculated at DFT/B3LYP/6-31G(d) level, which were obtained through a direct evaluation of the coupling element between frontier orbitals using the unperturbed density matrix of the dimer Fock operator[26]

Table 7.3 The electronic couplings for all the hopping pathways of **Hex-CO**

Pathway	center-center/Å	V_h/meV	V_e/meV
49-13	18.54000	-0.05264	-0.01507
49-14	18.23855	0.06780	0.01242
49-37	18.32299	0.00187	2.75964
49-40	14.64957	0.00004	-0.01632
49-44	15.11292	0.00003	-0.01906
49-50	9.59044	8.03378	33.09652
49-51	6.42003	1.24167	64.90778
49-52	8.72079	1.05133	0.15240
49-55	10.22879	0.01801	-0.00035
49-56	8.89166	0.02832	0.03702
49-62	9.19673	23.62718	61.70732
49-63	15.19850	0.08386	13.70639
49-88	16.51413	6.33952	0.12215
49-92	16.53417	3.48570	-0.04805
49-98	17.94120	0.42835	-0.03586
49-99	17.92299	-5.66182	0.02745

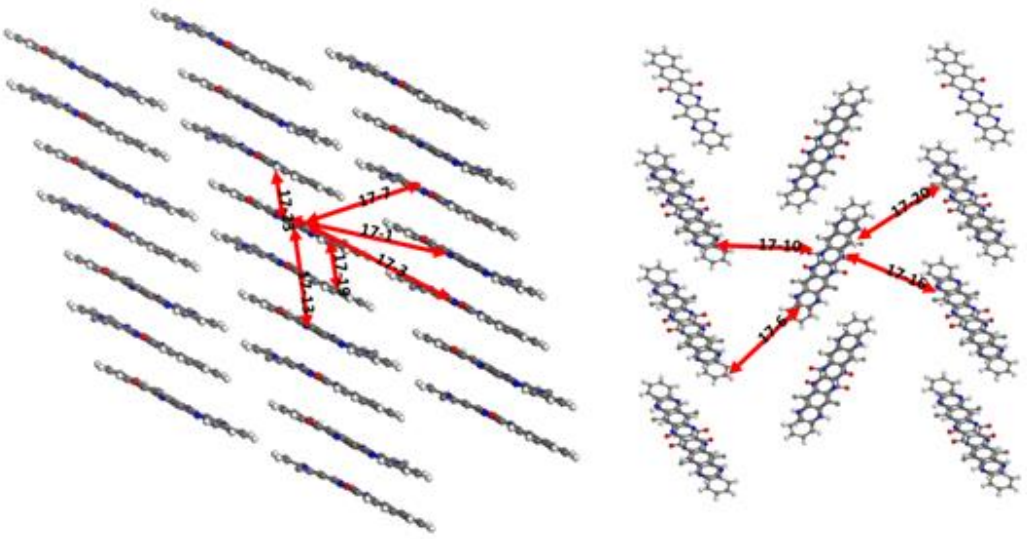

Fig 7.24 Hoping route of **Hept-CO** in the crystal (the hydrogen atoms are omitted for clarification); The intermolecular electronic couplings of hole transfer (V_h) and electron transfer (V_e) for the center molecule **17** are calculated at DFT/B3LYP/6-31G(d) level, which were obtained through a direct evaluation of the coupling element between frontier orbitals using the unperturbed density matrix of the dimer Fock operator.[26]

Table 7.4 The electronic couplings for all the hopping pathways of **Hept-CO**

Pathway	center-center/Å	V_h/meV	V_e/meV
17-1	16.84221	0.00963	-0.45449
17-3	15.45878	0.00780	0.02369
17-6	16.58695	0.02024	0.17297
17-7	10.17935	0.29044	0.78468
17-10	17.01898	-3.59167	-0.88859
17-13	9.46209	4.28320	2.55473
17-16	19.00192	0.23908	-0.22320
17-19	5.62160	51.62460	96.54010
17-20	17.34167	0.14136	-0.04044
17-23	8.67819	-22.30476	-51.13719

7.4 Conclusion

The quinone embedded large azaacene derivatives **Hex-CO** and **Hept-CO** were synthesized through palladium-catalyzed coupling reactions in good yields. This method shows great potential in synthesizing more novel azaacene derivatives. The quinone bridges extend the conjugation length on one side, increase the π-π interactions and change the molecules stacking mode in the solid state. Both **Hex-CO** and **Hept-CO** form dimers through strong π-π interactions in the crystal structures. The dimers of **Hex-CO** show lamellar 2-D π-stacking mode and the dimers of **Hept-CO** adopt lamellar 1-D π-stacking mode with an angle of 90º between the adjacent layers. **Hex-CO** and **Hept-CO** have almost the same behavior in CV, UV, DFT calculation and molecular orbital energy levels. The quinone units offer **Hex-CO** and **Hept-CO** low LUMO energy levels of -4.27 eV and -4.26 eV. The electron reorganization energy of **Hex-CO** and **Hept-CO** are calculated to be 222.9 meV and 212.0 meV, respectively. The largest transfer integrals for electron transport of **Hex-CO** and **Hept-CO** are 61.71 meV and -51.14 meV respectively, excluding that inside the dimers (64.91 meV for **Hex-CO** and 96.54 meV for **Hept-CO**). **Hex-CO** and **Hept-CO** show the best electron mobilities of 3.8×10^{-3} cm^2 V^{-1} s^{-1} and 9.3×10^{-3} cm^2 V^{-1} s^{-1} in the film OFET devices, respectively. Though the mobilities are not among the highest values have been reported, the large transfer integrals suggest that extending the conjugation of the azaacene derivatives through the quinone bridge is a promising way to achieve high performance organic semiconductors, especially for OFET applications.

References

[1] P.-Y. Gu, Z. Wang, Q. Zhang, *Journal of Materials Chemistry B* **2016**, *4*, 7060-7074.

[2] M. Ganschow, S. Koser, S. Hahn, F. Rominger, J. Freudenberg, U. H. F. Bunz, *Chemistry – A European Journal* **2017**, *23*, 4415-4421.

[3] P.-Y. Gu, F. Zhou, J. Gao, G. Li, C. Wang, Q.-F. Xu, Q. Zhang, J.-M. Lu, *Journal of the American Chemical Society* **2013**, *135*, 14086-14089.

[4] P.-Y. Gu, Z. Wang, F.-X. Xiao, Z. Lin, R. Song, Q.-F. Xu, J.-M. Lu, B. Liu, Q. Zhang, *Materials Chemistry Frontiers* **2017**, *1*, 495-498.

[5] a) V. Lami, D. Leibold, P. Fassl, Y. J. Hofstetter, D. Becker-Koch, P. Biegger, F. Paulus, P. E. Hopkinson, M. Adams, U. H. F. Bunz, S. Huettner, I. Howard, A. A. Bakulin, Y. Vaynzof, *Solar RRL* **2017**, *1*, 1700053-n/a; b) P.-Y. Gu, N. Wang, C. Wang, Y. Zhou, G. Long, M. Tian, W. Chen, X. W. Sun, M. G. Kanatzidis, Q. Zhang, *Journal of Materials Chemistry A* **2017**, *5*, 7339-7344.

[6] Q. Miao, *Advanced materials* **2014**, *26*, 5541-5549.

[7] X. Xu, Y. Yao, B. Shan, X. Gu, D. Liu, J. Liu, J. Xu, N. Zhao, W. Hu, Q. Miao, *Advanced materials* **2016**, *28*, 5276-5283.

[8] a) U. H. F. Bunz, *Accounts of Chemical Research* **2015**, *48*, 1676-1686; b) A. H. Endres, M. Schaffroth, F. Paulus, H. Reiss, H. Wadepohl, F. Rominger, R. Krämer, U. H. F. Bunz, *Journal of the American Chemical Society* **2016**, *138*, 1792-1795; c) B. Kohl, F. Rominger, M. Mastalerz, *Angewandte Chemie International Edition* **2015**, *54*, 6051-6056; d) P.-Y. Gu, Z. Wang, G. Liu, H. Yao, Z. Wang, Y. Li, J. Zhu, S. Li, Q. Zhang, *Chemistry of Materials* **2017**, *29*, 4172-4175; e) A. Mateo-Alonso, *Chemical Society reviews* **2014**, *43*, 6311-6324.

[9] U. H. F. Bunz, J. U. Engelhart, B. D. Lindner, M. Schaffroth, *Angewandte Chemie International Edition* **2013**, *52*, 3810-3821.

[10] U. H. F. Bunz, J. U. Engelhart, *Chemistry – A European Journal* **2016**, *22*, 4680-4689.

[11] C. Wang, J. Zhang, G. Long, N. Aratani, H. Yamada, Y. Zhao, Q. Zhang, *Angewandte Chemie International Edition* **2015**, *54*, 6292-6296.

[12] J. E. Anthony, *Chemical reviews* **2006**, *106*, 5028-5048.

[13] Z. Liang, Q. Tang, J. Xu, Q. Miao, *Advanced materials* **2011**, *23*, 1535-1539.

[14] I. Kaur, W. Jia, R. P. Kopreski, S. Selvarasah, M. R. Dokmeci, C. Pramanik, N. E. McGruer, G. P. Miller, *Journal of the American Chemical Society* **2008**, *130*, 16274-16286.

[15] D. Matsumura, K. Kitazawa, S. Terai, T. Kochi, Y. Ie, M. Nitani, Y. Aso, F. Kakiuchi, *Organic letters* **2012**, *14*, 3882-3885.

[16] Y.-Y. Liu, C.-L. Song, W.-J. Zeng, K.-G. Zhou, Z.-F. Shi, C.-B. Ma, F. Yang, H.-L. Zhang, X. Gong, *Journal of the American Chemical Society* **2010**, *132*, 16349-16351.

[17] D. Cortizo-Lacalle, C. Gozalvez, M. Olano, X. Sun, M. Melle-Franco, L. E. Hueso, A. Mateo-Alonso, *Organic letters* **2015**, *17*, 5902-5905.

[18] J. U. Engelhart, F. Paulus, M. Schaffroth, V. Vasilenko, O. Tverskoy, F. Rominger, U. H. F. Bunz, *The Journal of organic chemistry* **2016**, *81*, 1198-1205.

[19] B. D. Lindner, J. U. Engelhart, O. Tverskoy, A. L. Appleton, F. Rominger, A. Peters, H.-J. Himmel, U. H. F. Bunz, *Angewandte Chemie International Edition* **2011**, *50*, 8588-8591.

[20] I. Pochorovski, C. Boudon, J.-P. Gisselbrecht, M.-O. Ebert, W. B. Schweizer, F. Diederich, *Angewandte Chemie International Edition* **2012**, *51*, 262-266.

[21] C. Wang, H. Dong, W. Hu, Y. Liu, D. Zhu, *Chemical reviews* **2012**, *112*, 2208-2267.

[22] M. Frisch, G. Trucks, H. Schlegel, G. Scuseria, M. Robb, J. Cheeseman, G. Scalmani, V. Barone, B. Mennucci, G. Petersson, *Gaussian Inc., Wallingford CT* **2009**.

[23] H. Dong, X. Fu, J. Liu, Z. Wang, W. Hu, *Advanced materials* **2013**, *25*, 6158-6183.

[24] a) R. A. Marcus, *Reviews of Modern Physics* **1993**, *65*, 599; b) J.-L. Brédas, D. Beljonne, V. Coropceanu, J. Cornil, *Chemical reviews* **2004**, *104*, 4971-5004; c) W.-Q. Deng, W. A. Goddard, *The Journal of Physical Chemistry B* **2004**, *108*, 8614-8621.

[25] X.-K. Chen, L.-Y. Zou, J.-X. Fan, S.-F. Zhang, A.-M. Ren, *Organic Electronics* **2012**, *13*, 2832-2842.

[26] a) E. F. Valeev, V. Coropceanu, D. A. da Silva Filho, S. Salman, J.-L. Brédas, *Journal of the American Chemical Society* **2006**, *128*, 9882-9886; b) A. Troisi, G. Orlandi, *The Journal of Physical Chemistry B* **2002**, *106*, 2093-2101.

Chapter 8

Discussion and Future Work

In this chapter, a summary of this thesis is elaborated in three parts: the synthesis of large azaacenes for PEC cells and water splitting, the synthesis of longest azacene derivatives confirmed by single crystal structure and the synthesis of azaacenes for OFET application. Research in some other systems is introduced afterward, including ladder-type azaacenes and bent azaacenes. Finally, some future work about the large azaacenes are proposed including designing the nitrogen doped two-dimensional π-conjugated materials for PEC cells and water splitting, large azaacenes for single molecular device and azaacenes for high performance OFET application.

8.1 General discussion and summary

This thesis focuses on the design and synthesis of novel large N-heteroacenes. This thesis also explores and develops the applications of N-heteroacenes as n-type and ambipolar semiconductors in PEC cells, water splitting, and OFET. All these research can be summarized in three parts as briefly concluded in the following.

8.1.1 Large azaacenes for PEC cells and water splitting

In chapter 4, two large pyrene bridged azaacenes **TAOA** and **OADA** with eight and ten annulated six-membered rings in one row were synthesized and fully characterized. **TAOA** and **OADA** show repeatable positive photocurrents and negative photovoltage in the PEC cell and positive slopes in the Mott-Schottky measurement. All these results suggest both of them are n-type semiconductors. However, the current densities of both **TAOA** and **OADA** are quite low, and they are only at 10^{-9}A level. By analyzing the crystal structure, it can be surmised that the main problem causing the low current densities is the undesirable molecules stacking structures. **TAOA** shows no π-π stacking. The C-H···π interactions are the main force to stabilize the stacking structure. With a longer conjugation, OADA adopts lamellar 2-D π-stacking motif through the π-π interactions. However, the π-π interactions are still weak, because the overlap of the conjugation plane is small. The electrons are hard to transfer in such stacking structures, therefore the current densities of **TAOA** and **OADA** are quite low.

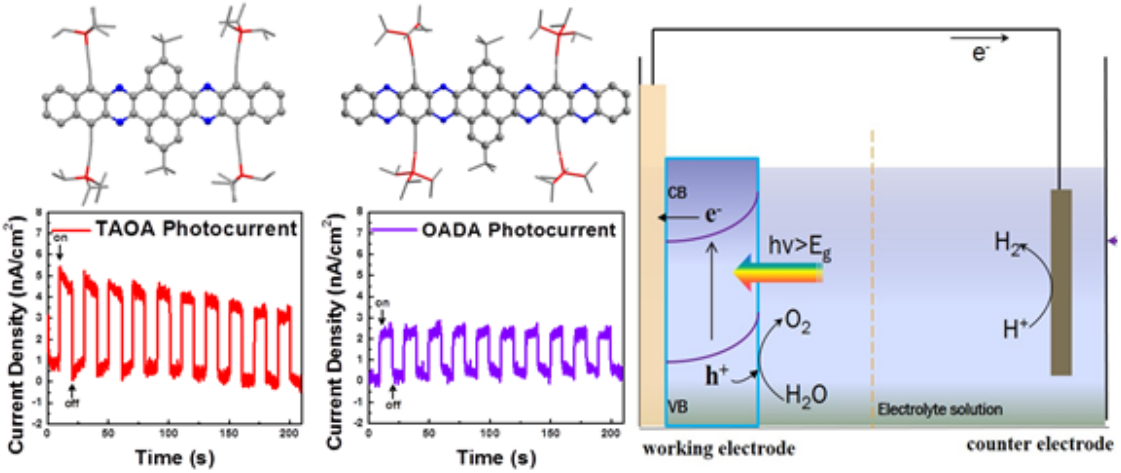

Fig 8.1 A schematic diagram summary of chapter 4

Therefore, an improvement is proposed in chapter 5. The main factor interfering the π-π interactions of such large conjugation of **OADA** is the steric hindrance of the substituents. To decrease steric hindrance and increase π-π interactions, the tert-butyls in the middle are removed and the pyrene bridge is replaced by the pyracyclene unit. Subsequently, molecule **DQNDN** is obtained. **DQNDN** is insoluble in the common solvents, and that is probably caused by the strong π-π interactions. It is hard to study its crystal structure, because of its insolubility. It is speculated that **DQNDN** adopts a closely π-π stacking with the TIPS groups of adjacent molecules cross-aligned as simulated in Fig 8.2. This close π-π stacking with a big conjugation plane overlap is beneficial to current transfer. **DQNDN** shows the largest current density of 0.81 μA cm^{-2} as a photoanode and 0.13 mA cm^{-2} as a photocathode, which is much larger than that of **TAOA** and **OADA**.

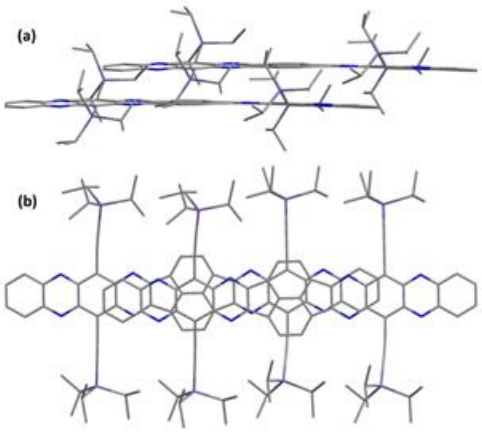

Fig 8.2 Simulated molecules stacking structure of **DQNDN**: (a) side view; (b) top view

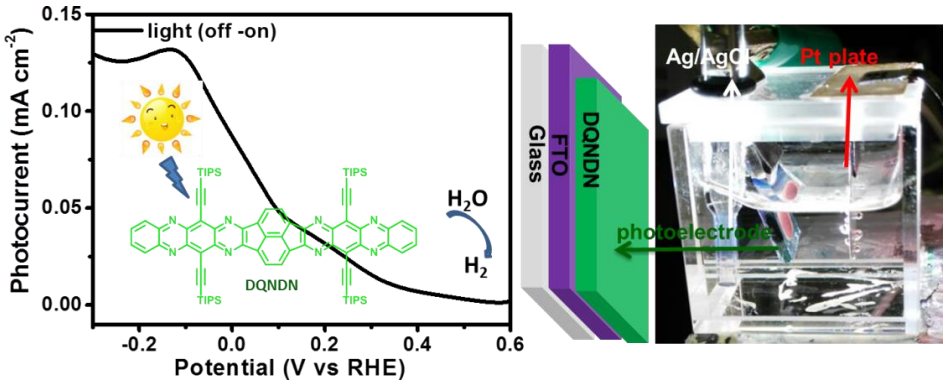

Fig 8.3 A schematic diagram summary of chapter 5

8.1.2 The longest crystal structure confirmed N-heteroacene derivatives

In chapter 4, it is confirmed that pyrene is a suitable bridge to build up large acenes derivatives. With a suitable arrangement of the TIPS group, the large acenes derivatives can have both good solubility and crystallinity. Based on that, it is possible to challenge the record of the longest N-heteroacene confirmed by the crystal structure, which is a research hot spot recently. In chapter 6, two novel pyrene bridged acenes derivatives **15RINGS** and **20RINGS** with 15 and 20 six-membered rings linearly annulated in one row were synthesized, respectively. The crystal of **20RINGS** still cannot be obtained. **15RINGS** has been successfully confirmed by single crystal X-ray diffraction analysis. This is the longest acene derivative confirmed by single-crystal X-ray diffraction so far. The conjugation backbone of **15RINGS** does not adopt a plane conformation as that of **OADA** and **TAOA**, however, it possesses a dual-bending structure (the bending angle is about 13.2°). This bending structure may be a help to stabilize such a large π-conjugated system by release some tension. **15RINGS** is a candidate n-type semiconductor with a LUMO energy level of -3.74 eV and a narrow bandgap of 1.85 eV.

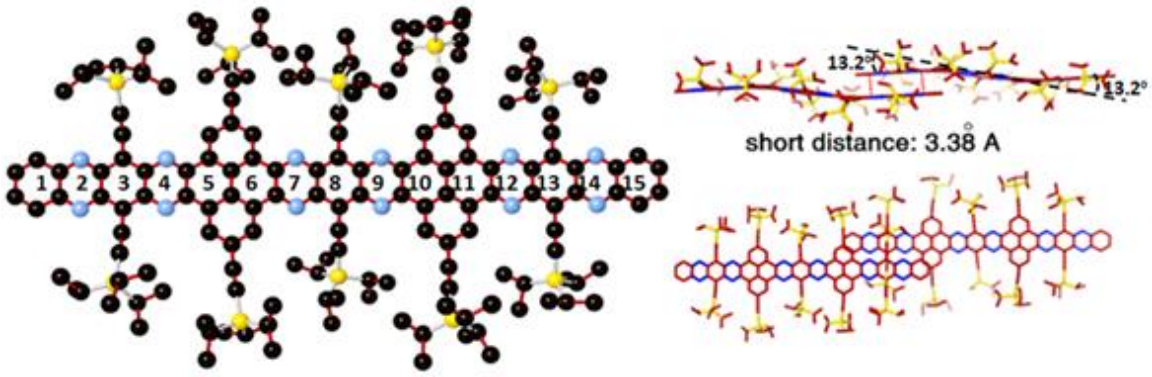

Fig 8.4 A schematic diagram summary of chapter 6

8.1.3 Large N-heteroacenes for OFET application

In chapter 4 and chapter 5, it is confirmed that the molecules stacking structure and π-π interactions can be controlled by arranging the quantity and position of TIPS substituents. In OFET applications, the closely π-π stacking is generally beneficial to charge transfer. However, if the π-π interactions are too strong, the solubility of the material will drastically decrease. That will be a problem in device fabrication. Hence, in chapter 7,

Hex-CO and **Hep-CO** with six and seven six-membered rings conjugated in one row were designed and synthesized. The extended conjugations can increase the π-π interactions and both **Hex-CO** and **Hep-CO** form dimers in the crystal structures through the strong π-π interactions. Strong π-π interactions also exist between dimers which induce **Hex-CO** dimers and **Hep-CO** dimers adopt lamellar 2-D π-stacking mode and lamellar 1-D π-stacking mode, respectively. The extended conjugations affect the molecules stacking structures greatly. However, they almost have no influence on the molecular orbital levels. **Hex-CO** and **Hep-CO** have almost the same energy level. The quinone units offer **Hex-CO** and **Hep-CO** deep low LUMO energy levels about -4.27 eV. **Hex-CO** and **Hep-CO** show very high value of largest transfer integrals because of the strong π-π interactions. **Hex-CO** and **Hept-CO** show the best electron mobilities of 3.8 × 10^{-3} cm^2 V^{-1} s^{-1} and 9.3 × 10^{-3} cm^2 V^{-1} s^{-1} in the film OFET devices, respectively. This research suggests that extending the conjugation of the azaacene derivatives through the quinone bridge is a promising way to achieve high performance organic semiconductors, especially for OFET applications.

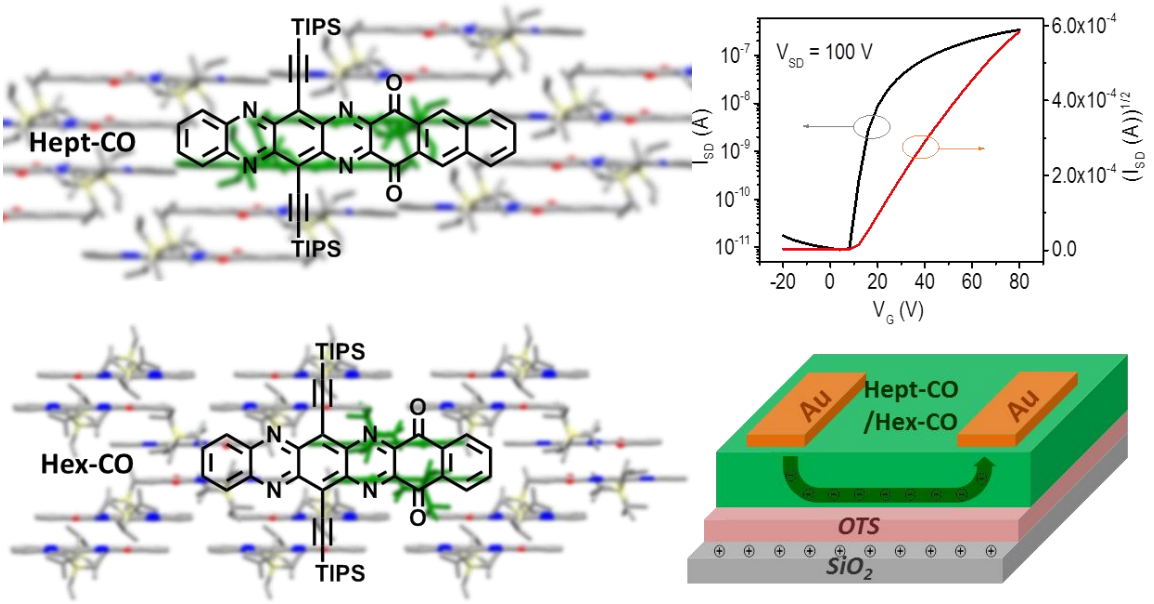

Fig 8.5 A schematic diagram summary of chapter 7

8.2 Reconnaissance work not included in the main chapter

8.2.1 Ladder-Type N-heteroacene

The linear N-heteroacenes have been studied extensively, while the ladder-type heteroacenes are not studied so much. Fig 8.6 shows some examples of the ladder-type acenes derivatives, and they have shown some interesting properties.[1]

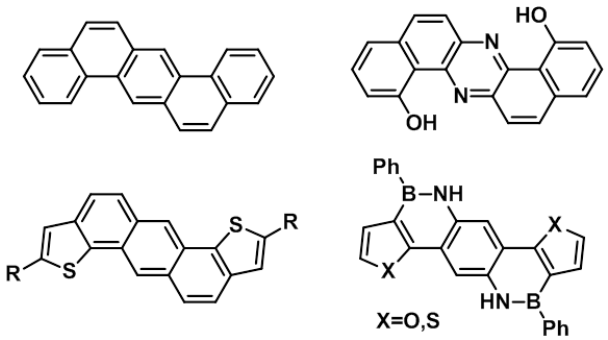

Fig 8.6 Examples of the ladder-type heteroacenes

Based on that, some research about the ladder-type N-heteroacene was conducted. Molecule 2,4,9,11-tetramethoxybenzo[1,2-c:4,5-c']dicinnoline (**TMBDC**) was designed and synthesized as shown in Scheme 8.1. The nitrogen atoms can lower the LUMO energy levels and make **TMBDC** a candidate n-type semiconductor.

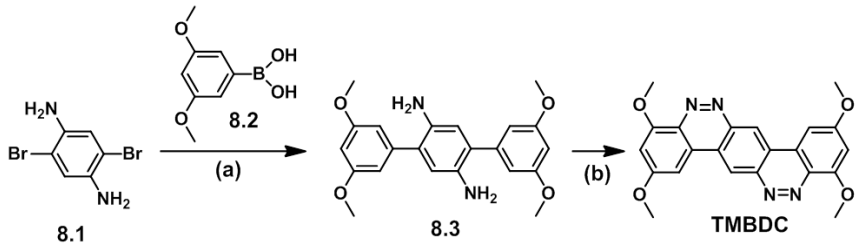

Scheme 8.1 Synthesis route of **TMBDC**: (a): $Pd(PPh_3)_4$, K_2CO_3, Tol, EtOH, H_2O, 100 ºC. (b): $NaNO_2$, AcOH, CH_2Cl_2

The synthesis route is shown in Scheme 8.1. Compound **8.1** can be synthesized according to the literature.[2] Compound **8.3** was synthesized through the Suzuki coupling reaction between compound **8.1** and compound **8.2**. **TMBDC** cannot dissolve in the common solvents. The poor solubility severely limits its application. Employing more and longer

alkoxy chain substituents may improve the solubility, therefore molecule **8.7** is designed. To further decrease the LUMO energy levels and increase the conjugation, molecule **8.12** is designed. The possible synthesis routes are also shown in Scheme 8.2.

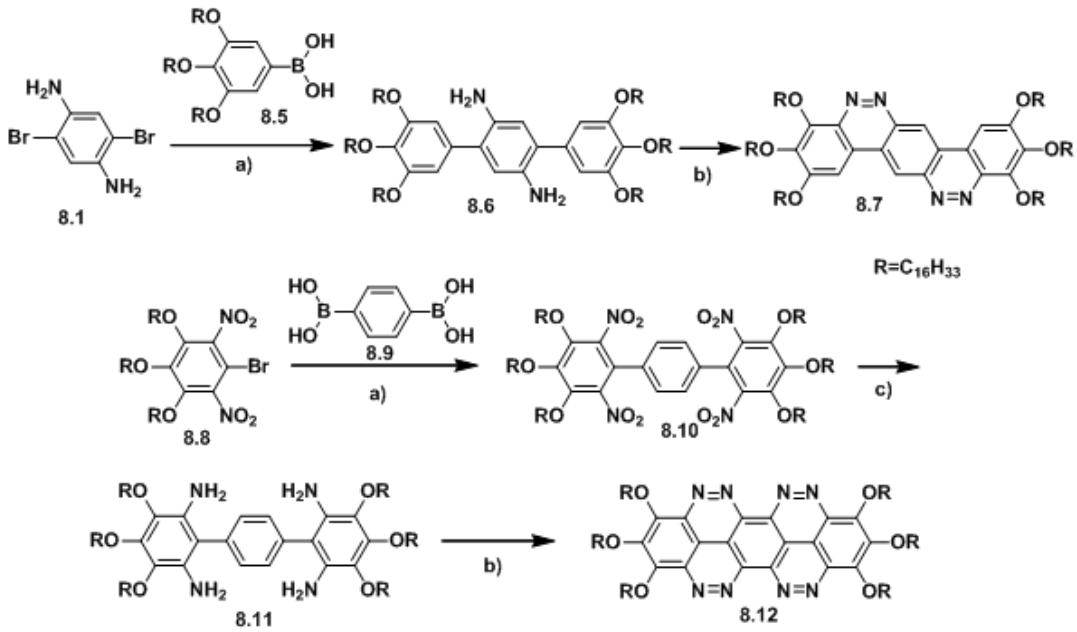

Scheme 8.2. Molecule structures of compounds **8.7** and **8.12**, and the possible synthesis routes. (a): $Pd(PPh_3)_4$, K_2CO_3, Tol, EtOH, H_2O, 100 ºC. (b): $NaNO_2$, AcOH, CH_2Cl_2. (c): Zn, AcOH, reflux.

Synthesis of 3,3'',5,5''-tetramethoxy-[1,1':4',1''-terphenyl]-2',5'-diamine (compound 8.3)

Compound **8.1** (263.9 mg, 1mmol), compound **8.2** (455.0 mg, 2.5 mmol), Tetrakis(triphenylphosphine)palladium(0) ($Pd(PPh_3)_4$) (23.12 mg 0.02 mmol), and potassium carbonate (0.55g) were added into a mix solvent of toluene (10 mL), water (5 mL) and ethanol (2.5 mL) in argon. The mixture was further bubbled with argon for 5 min, and then stirred at 100 ºC for 24 h. Subsequently the reaction mixture was cooled to room temperature, and 30 mL saturated ammonium chloride solution was added. Subsequently, the mixture was extracted by CH_2Cl_2 (3 x 20 mL), the organic phase was wash with water (30 mL) and $NaHCO_3$ (mL) saturated solution, dried with $NaSO_4$. After filtration and removing the solvent, the residue was purified by silica gel column chromatography (Eluent: CH_2Cl_2 : Hex = 4 : 1). The pure compound **8.3** was obtained as

yellow solid (200 mg, 53%). ^{1}H NMR (400 MHz, $CDCl_3$) δ = 6.70 (s, 2H), 6.63 (s, 4H), 6.45 (s, 2H), 3.82 (s, 12H). ^{13}C NMR (100 MHz, $CDCl_3$) δ = 161.02, 141.33, 135.59, 128.66, 117.94, 106.95, 99.59, 55.42.

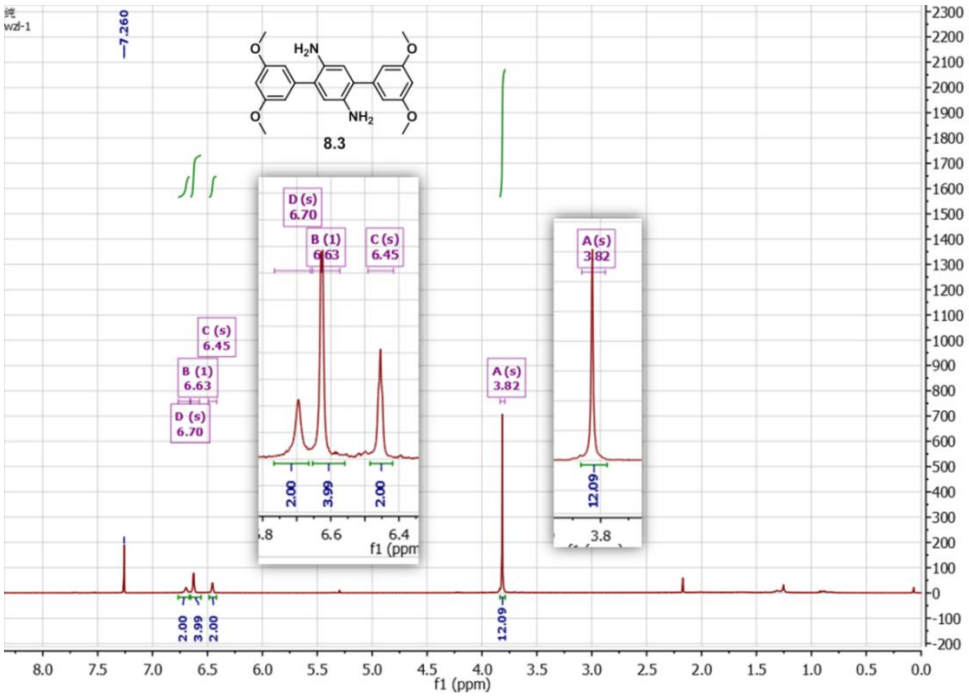

Fig 8.7 ^{1}H NMR spectrum of compound **8.3**, 300 MHz, $CDCl_3$, room temperature

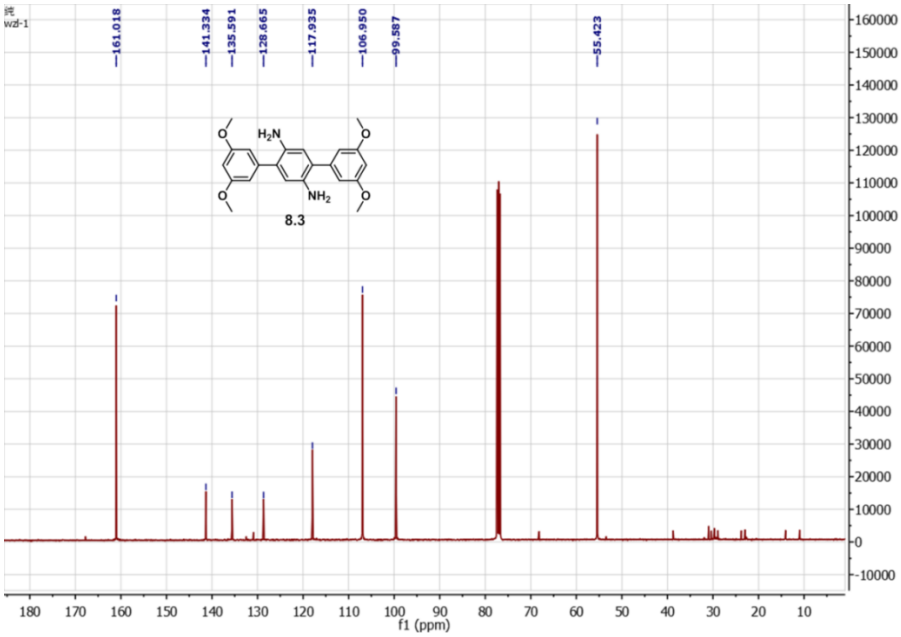

Fig 8.8 ^{13}C NMR spectrum of compound **8.3**, 75 MHz, $CDCl_3$, room temperature

Synthesis of 2,4,9,11-tetramethoxybenzo[1,2-c:4,5-c']dicinnoline (TMBDC)

Compound **8.3** (28.5 mg, 0.075 mmol) was stirred in a mix solvent of acetic acid (5 mL) and CH_2Cl_2 (10 mL) at 0 ºC. Sodium nitrite (48 mg, 0.7 mmol) in 1 mL of water was added slowly. After that, the mixture was stirred at room temperature for 30 min and at 40 ºC for 2 h. Yellow precipitation can be observed in this procedure. Subsequently, the precipitation was collected by filtrate and washed with methanol, THF, Acetone, and CH_2Cl_2 affording the pure **TMBDC** as yellow solid (25.3 mg, 80%) ^{1}H NMR (400 MHz, TFA) δ = 9.90 (s, 2H), 8.09 (d, *J*=1.7, 2H), 7.29 (s, 2H), 4.41 (s, 6H), 4.36 (s, 6H). ^{13}C NMR (100 MHz, TFA) δ = 176.34, 163.60, 135.83, 131.83, 129.73, 125.87, 118.09, 102.80, 100.74, 57.64, 57.24.

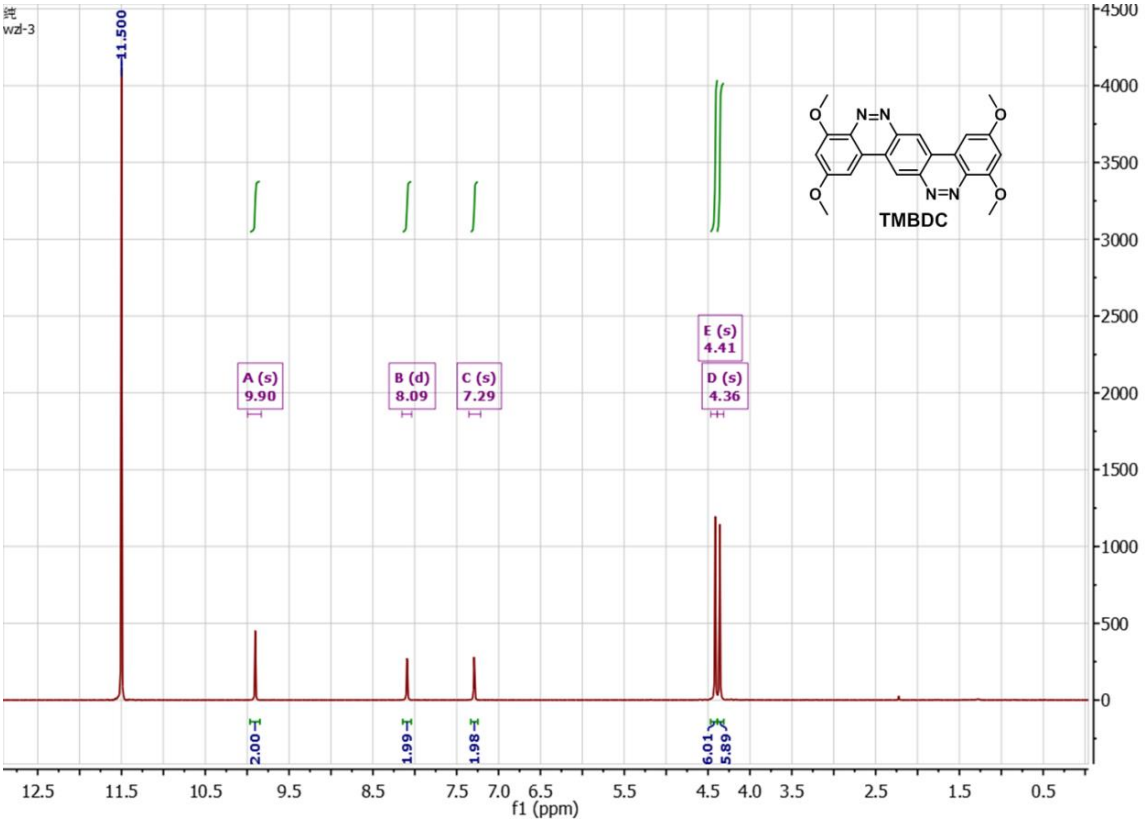

Fig 8.9 ^{1}H NMR spectrum of compound **TMBDC**, 300 MHz, $CDCl_3$, room temperature

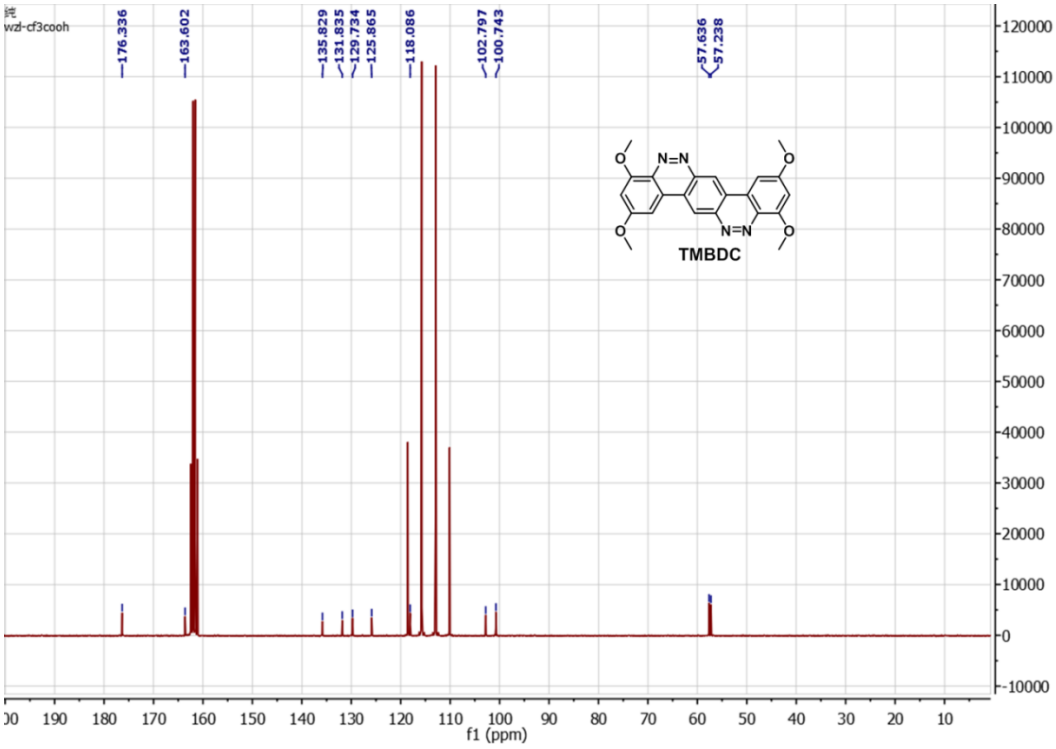

Fig 8.10 ^{13}C NMR spectrum of compound **TMBDC**, 75 MHz, $CDCl_3$, room temperature

8.2.2 Bent N-heteroacene

Comparing to the liner N-heteroacenes, the bent N-heteroacenes are rarely studied. The bent N-heteroacenes may show some unique property. Therefore some research about these molecules was conducted. Molecule **TCDO** is designed by using a five-membered ring in the middle to provide an angle. The synthesis route is shown in Scheme 8.3.

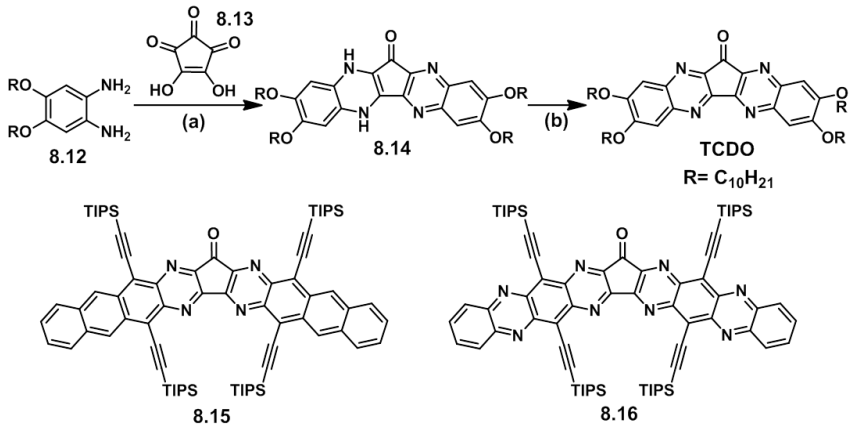

Scheme 8.3 The synthesis route of **TCDO** and the designed molecular structures of **8.15** and **8.16**: (a) AcOH, IBX, reflux; (b) MnO_2, CH_2Cl_2

TCDO may have a performance in the memory devices because of its donor-acceptor structure. However, it shows poor performance in the OFET device, probably because its aromaticity is interrupted by the ketone unit in the middle. Two modified molecules **8.15** and **8.16** are shown in Scheme 8.3, the extended conjugation may improve the performance in the OFET.

Synthesis of 2,3,8,9-tetrakis(decyloxy)-5H-cyclopenta[1,2-b:3,4-b']diquinoxalin-12(13H)-one (compound 8.14)

Compound **8.12** (126.2 mg, 0.3 mmol), croconic acid (compound **8.13**) (14.1 mg, 0.1 mmol) and IBX (5 mg) were added into AcOH (15 mL) in argon. The mixture was further bubbled with argon for 5 min, and then stirred and refluxed for 24 h. Subsequently, the solvent was removed, the residue was purified by silica gel column chromatography (Eluent: CH_2Cl_2 : MeOH = 300 : 1). The pure compound **8.14** was obtained as yellow solid (60 mg, 66%). ^{1}H NMR (300 MHz, $CDCl_3$) δ = 13.03 (s, 1H), 7.57 (s, 1H), 7.55 (s, 1H), 7.52 (s, 1H), 7.46 (s, 1H), 4.30 – 4.12 (m, 9H), 2.06 – 1.81 (m, 9H), 1.60 – 1.47 (m, 9H), 1.44 – 1.22 (m, 52H), 0.93 – 0.82 (m, 13H). ^{13}C NMR (75 MHz, $CDCl_3$) δ = 174.66, 154.06, 153.75, 153.56, 153.40, 147.89, 147.57, 147.35, 145.02, 140.36, 140.26, 140.22, 138.34, 135.94, 108.34, 108.25, 107.65, 69.59, 69.31, 69.18, 31.93, 29.66, 29.61, 29.45, 29.37, 28.91, 28.89, 28.81, 26.04, 22.69, 20.03, 14.10.

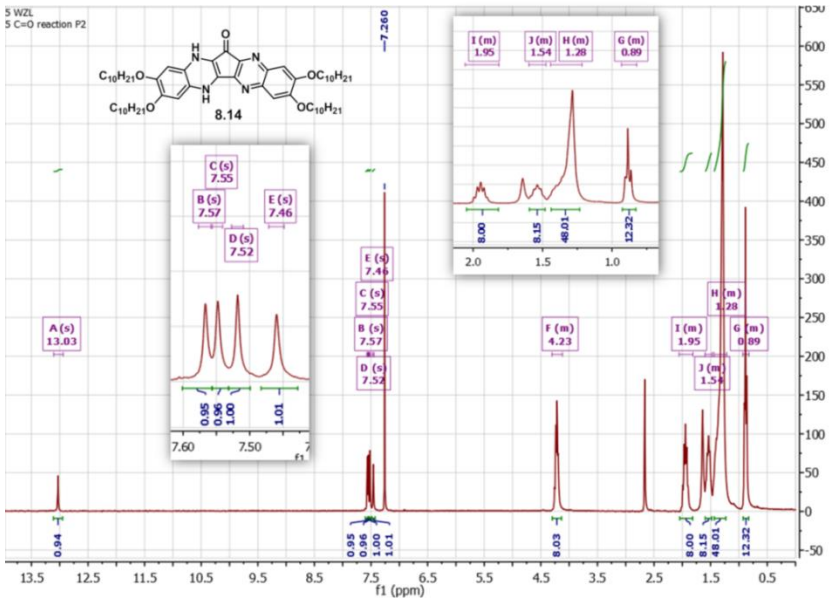

Fig 8.11 ^{1}H NMR spectrum of compound **8.14**, 300 MHz, $CDCl_3$, room temperature

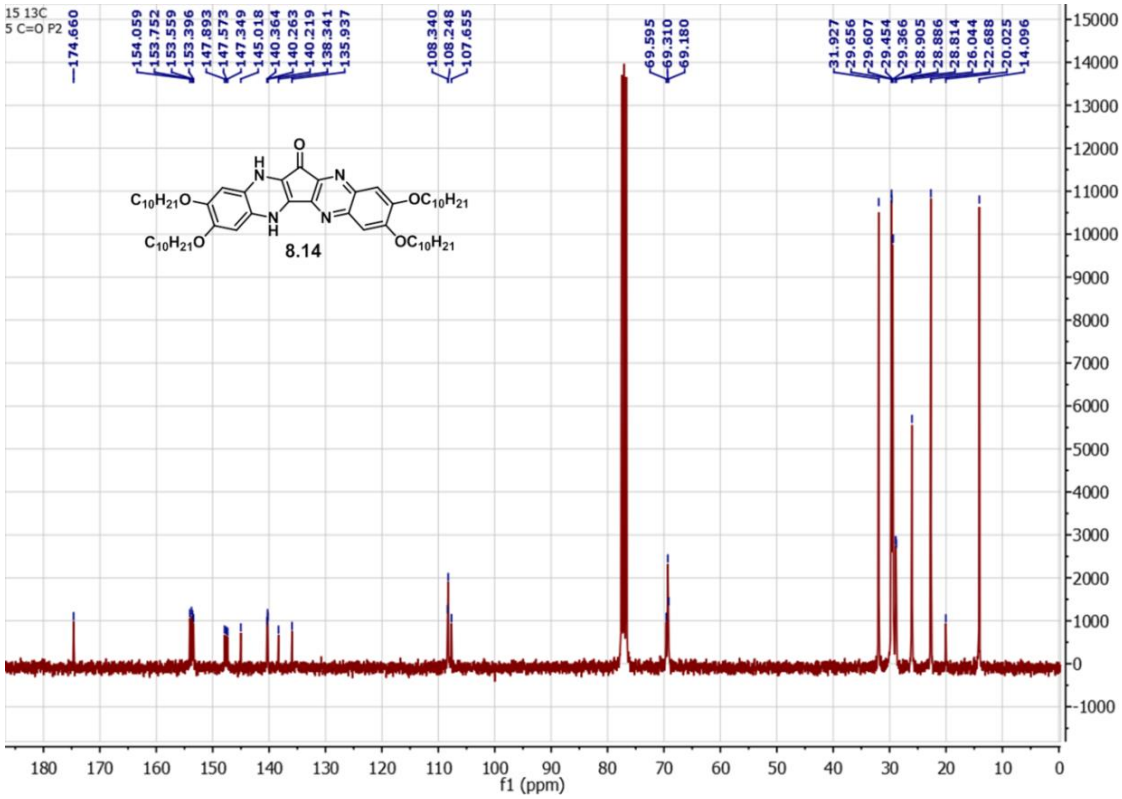

Fig 8.12 ^{13}C NMR spectrum of compound **8.14**, 75 MHz, $CDCl_3$, room temperature

Synthesis of 2,3,8,9-tetrakis(decyloxy)-12H-cyclopenta[1,2-b:3,4-b']diquinoxalin-12-one (compound TCDO)

Compound **8.14** (45 mg, 0.49 mmol) was treated with an excess amount of active MnO_2 in dry methylene chloride (20 mL) at room temperature for about 2 h. The reaction completion of the reaction was confirmed by thin layer chromatography (TLC). Subsequently, MnO_2 was removed by filtrated through celite and washed with methylene chloride until the filtrate was colorless. After removing the solvent, the pure **TCDO** were obtained as red solid (41 mg, 0.44 mmol, 90%). ^1H NMR (300 MHz, $CDCl_3$) δ = 7.52 (s, 2H), 7.47 (s, 2H), 4.36 – 4.05 (m, 8H), 2.08 – 1.78 (m, 8H), 1.57 – 1.46 (m, 8H), 1.41 – 1.19 (m, 48H), 0.95 – 0.78 (m, 12H).

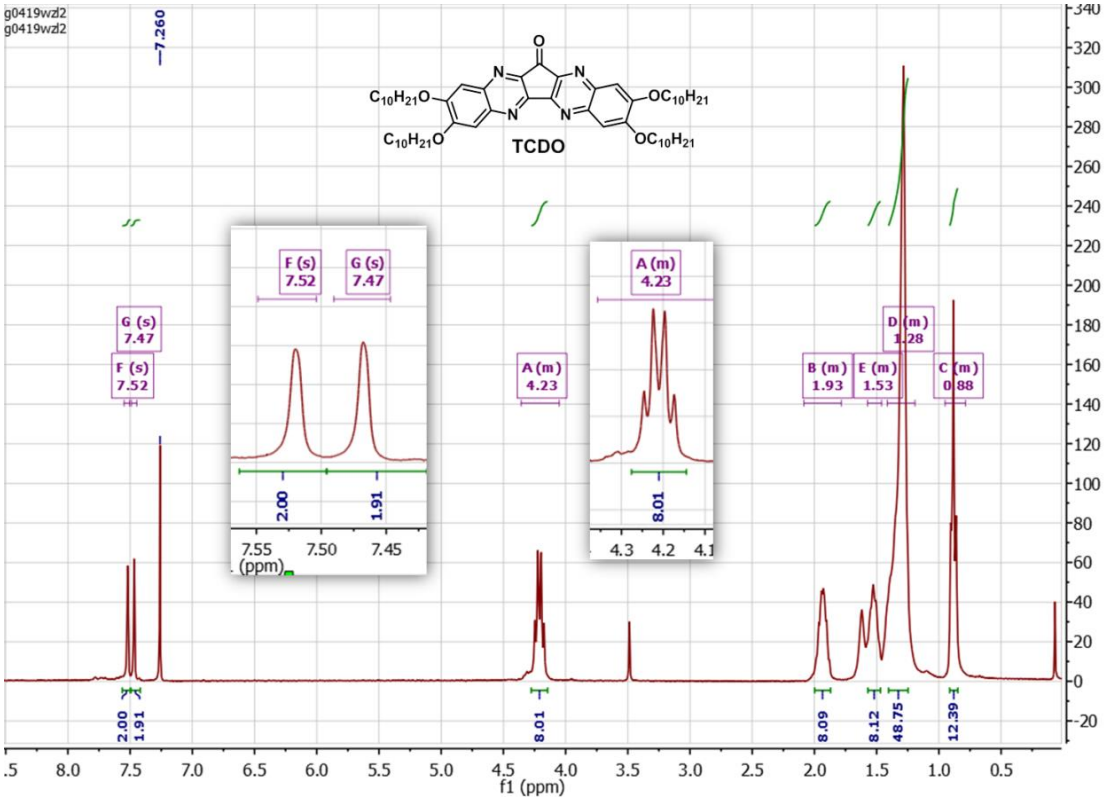

Fig 8.13 ^{1}H NMR spectrum of compound **TCDO**, 300 MHz, $CDCl_3$, room temperature

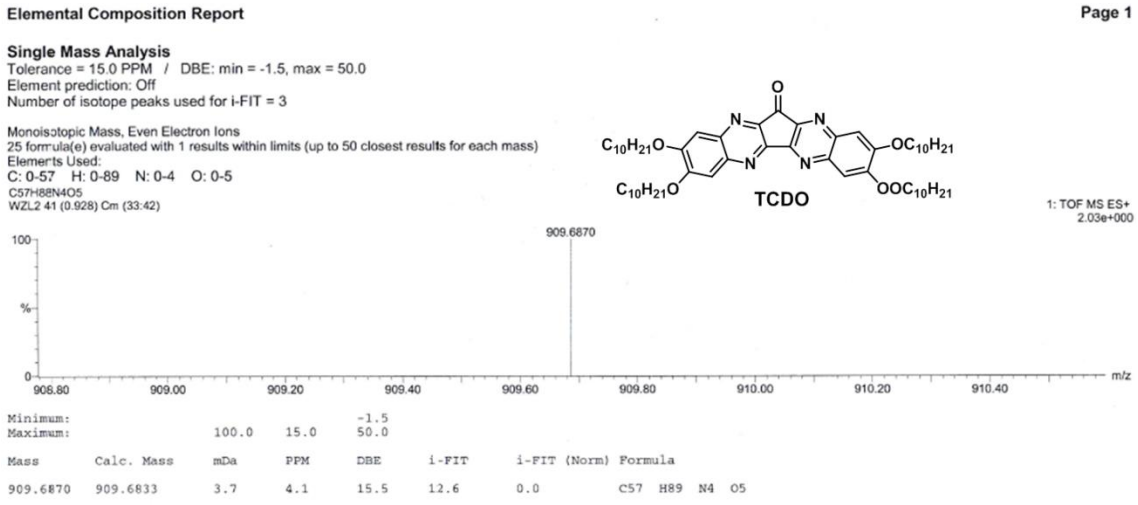

Fig 8.14 HR-MS(ESI) spectrum of compound **TCDO**

8.3 Outstanding questions and future work

8.3.1 Design nitrogen doped porous aromatic frameworks (PAF) for PEC cells and water splitting

In chapter 4 and 5, several N-heteroacenes are designed and the performance in PEC cells and water splitting are tested. The performance is still slightly weaker than the inorganic materials and g-C_3N_4 (as introduced in chapter 2). The morphology of the N-heteroacenes may be an important constraint: the closely stacking structure decreases the surface area. With a large surface area, the materials can contact and split water more efficiently. Therefore, the two-dimensional π-conjugated nitrogen doped **PAF** material **8.19** is designed as shown in Scheme 8.4. The N-heteroacene structure in the framework makes sure the energy levels are suitable for PEC cells and water splitting application. The pores can allow more water moving into this mesoporous material, contacting with the material and getting split subsequently. The π-conjugated structure makes sure the photocurrent can transfer unimpededly in the framework.

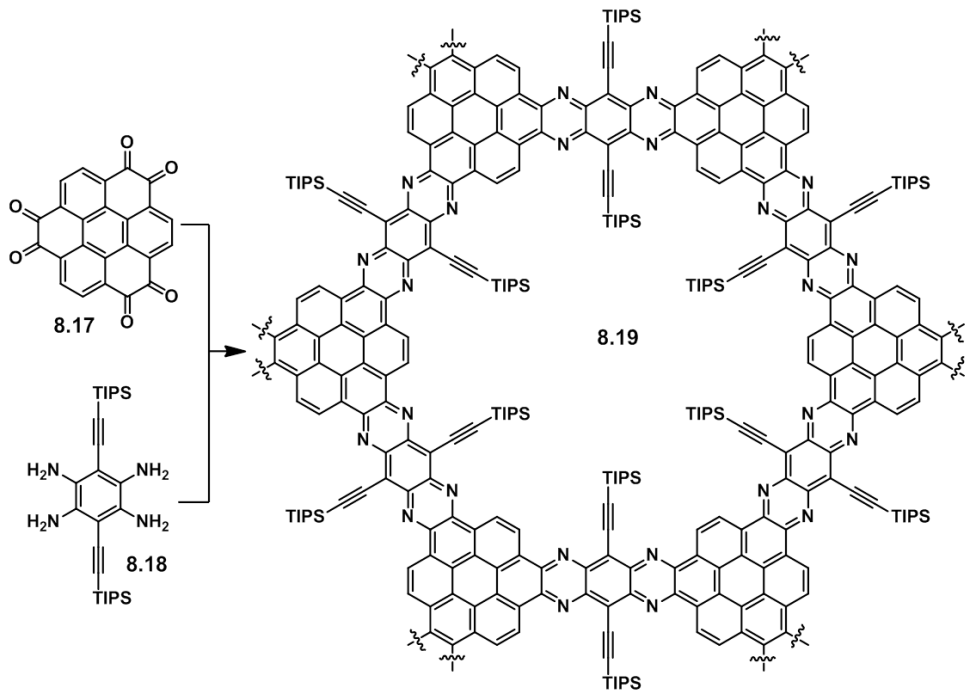

Scheme 8.4 The molecule structure of the two-dimensional π-conjugated nitrogen doped mesoporous graphene material **8.19**, and a possible synthesis route

8.3.2 Large N-heteroacenes for single molecular device

In chapter 4 and 6, several pyrene bridged large N-heteroacenes are synthesized. These molecules are suitable materials for the single molecular device after modification because of the large conjugations length. Therefore, the large N-heteroacenes modified by methanethiol groups are designed as shown in Fig 8.15. With different molecular lengths and quantities of pyrene bridges, these molecules should have different conductivities. It is meaningful to study the relationship between the conductivity and the molecular length and/or the quantity of pyrene bridges.

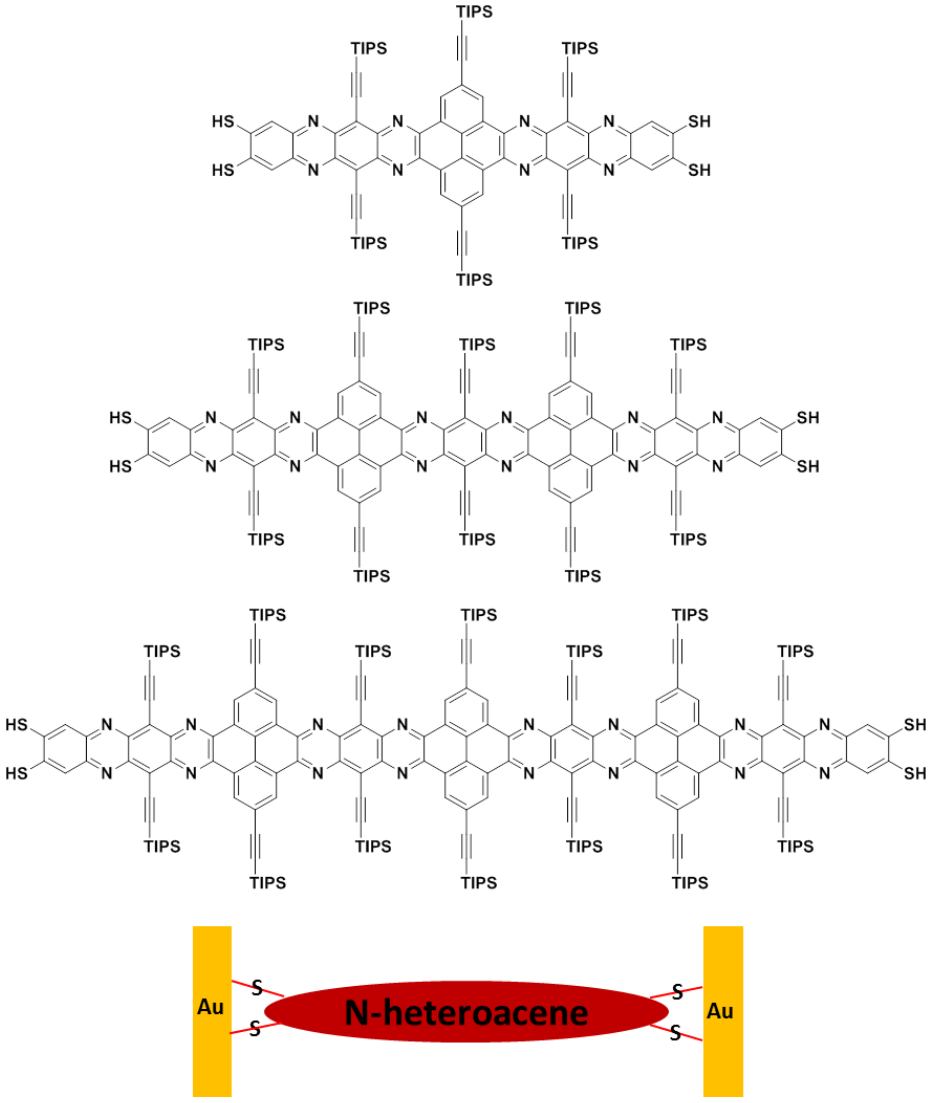

Fig 8.15 Methanethiol modified large N-heteroacene and the single molecule device schematic diagram

8.3.3 Design large N-heteroacenes for OFET application

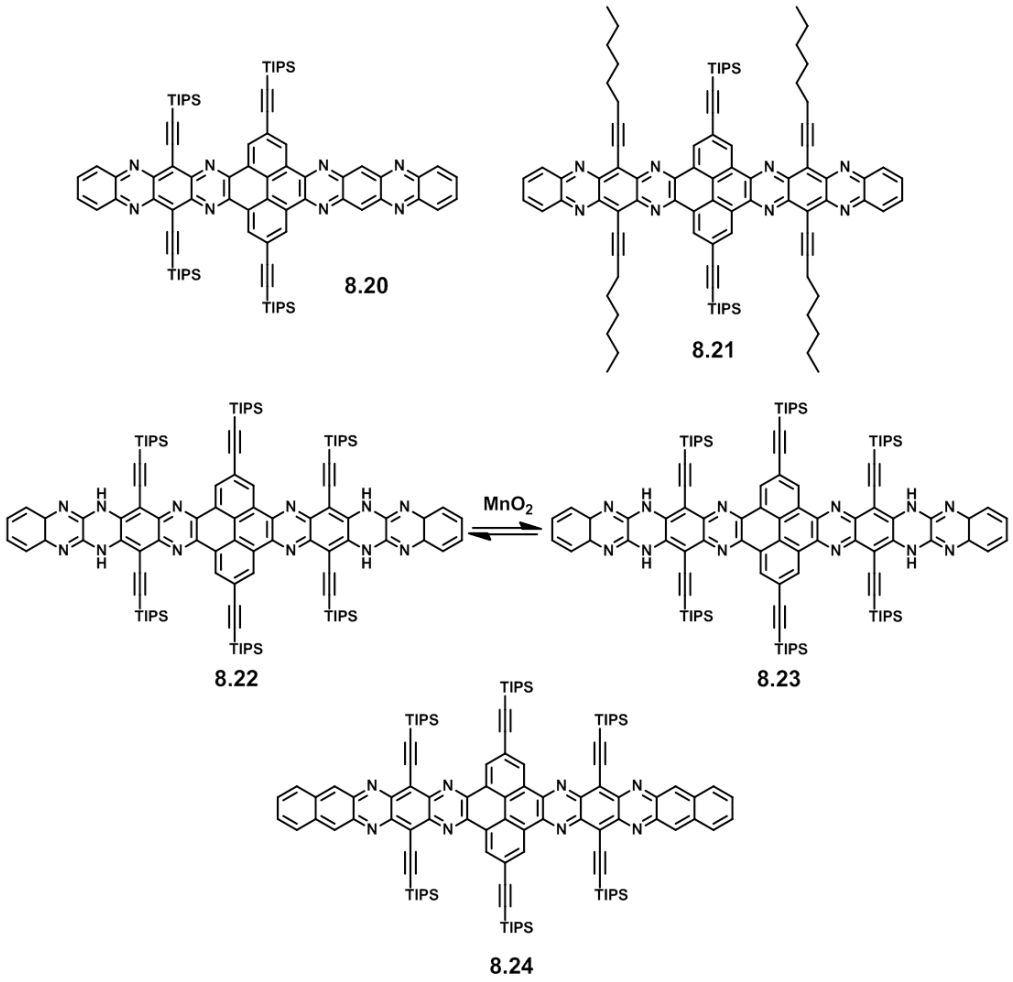

Fig 8.16 Molecular structures of some N-heteroacenes

In chapter 7, it has been well confirmed that increasing the π-π interaction can increase the transfer integral which is conducive to improve the OFET performance. Based on that, **OADA** (synthesized in chapter 4) have great potential in OFET application, because it has large conjugation. However, its π-π interaction was weakened by the steric hindrance of the substituents. Therefore the quantity of the substituents needs to be rearranged to increase the π-π interaction. Molecule **8.20** (as shown in Fig 8.16) was designed and synthesized, firstly. However, molecule **8.20** shows very poor solubility, probably because the π-π interaction is too strong. Hence, the π-π interaction must be carefully controlled. Based on that, molecule **8.21** is designed by changing four TIPS groups of **OADA** with smaller steric hindrance substituents to suitably increasing the π-π

interaction. Molecule **8.21** should be a good material for OFET application. Another way to suitably increasing the π-π interaction is to gradually extend the conjugation of **OADA** at two terminals. Therefore molecule **8.23** was designed and synthesized. However, molecule **8.23** is not stable, and it will change back to its dihydro-analogue **8.22** in minutes in ambient. This is probably because its LUMO energy level is too low. Hence, molecule **8.24** with an extended conjugation and probably suitable energy level was designed. It may be a good material for OFET application.

References

[1] a) X. Wang, F. Zhang, J. Liu, R. Tang, Y. Fu, D. Wu, Q. Xu, X. Zhuang, G. He, X. Feng, *Organic letters* **2013**, *15*, 5714-5717; b) A. Pietrangelo, B. O. Patrick, M. J. MacLachlan, M. O. Wolf, *The Journal of organic chemistry* **2009**, *74*, 4918-4926; c) A. Pietrangelo, M. J. MacLachlan, M. O. Wolf, B. O. Patrick, *Organic letters* **2007**, *9*, 3571-3573; d) J. Piechowska, K. Virkki, B. Sadowski, H. Lemmetyinen, N. V. Tkachenko, D. T. Gryko, *The Journal of Physical Chemistry A* **2014**, *118*, 144-151.

[2] T. Nakamura, S. Furukawa, E. Nakamura, *Chemistry – An Asian Journal* **2016**, *11*, 2016-2020.